Improving Quantification in Lung PET/CT for the Evaluation of Disease Progression and Treatment Effectiveness

Elise Claudine Emond

A dissertation submitted in partial fulfillment

of the requirements for the degree of

Doctor of Philosophy

of

University College London.

Division of Medicine

University College London

April 23, 2020

I, Elise Claudine Emond, confirm that the work presented in this thesis is my own. Where information has been derived from other sources, I confirm that this has been indicated in the work.

"Memento audere semper" (Remember to always dare)

Gabriele d'Annuzio

Abstract

Positron Emission Tomography (PET) allows imaging of functional processes in vivo by measuring the distribution of an administered radiotracer. Whilst one of its main uses is directed towards lung cancer, there is an increased interest in diffuse lung diseases, for which the incidences rise every year, mainly due to environmental reasons and population ageing. However, PET acquisitions in the lung are particularly challenging due to several effects, including the inevitable cardiac and respiratory motion and the loss of spatial resolution due to low density, causing increased positron range.

This thesis will focus on Idiopathic Pulmonary Fibrosis (IPF), a disease whose aetiology is poorly understood while patient survival is limited to a few years only. Contrary to lung tumours, this diffuse lung disease modifies the lung architecture more globally. The changes result in small structures with varying densities. Previous work has developed data analysis techniques addressing some of the challenges of imaging patients with IPF. However, robust reconstruction techniques are still necessary to obtain quantitative measures for such data, where it should be beneficial to exploit recent advances in PET scanner hardware such as Time of Flight (TOF) and respiratory motion monitoring.

Firstly, positron range in the lung will be discussed, evaluating its effect in density-varying media, such as fibrotic lung. Secondly, the general effect of using incorrect attenuation data in lung PET reconstructions will be assessed. The study will compare TOF and non-TOF reconstructions and quantify the local and global artefacts created by data inconsistencies and respiratory motion. Then, motion compensation will be addressed by proposing a method which takes into account the changes of density and activity in the lungs during the respiration, via the estimation of the volume changes using the deformation fields. The method is evaluated on late time frame PET acquisitions using ^{18}F-FDG where the radiotracer distribution has

stabilised. It is then used as the basis for a method for motion compensation of the early time frames (starting with the administration of the radiotracer), leading to a technique that could be used for motion compensation of kinetic measures. Preliminary results are provided for kinetic parameters extracted from short dynamic data using ^{18}F-FDG.

Impact Statement

One of the main advantages of PET imaging is usually seen as the possibility of obtaining "fully quantitative" activity images, as opposed to so-called anatomical images. Such quantitative measures have great potential for disease staging, and monitoring disease progression and treatment effectiveness. The pursuit of this paradigm has been accelerated in recent years, by the means of new scanner specifications (for example, better detector designs especially in terms of time resolution or longer axial field of view), new reconstruction algorithms (mainly penalised reconstruction) and methods to correct for respiratory motion. However, these methods have mainly been proposed for oncological studies.

This thesis concentrates on imaging diffuse lung diseases, where PET imaging is still challenging for research and clinical studies. This work investigates the impact on quantification of the radiotracer distribution due to several effects including positron range and motion, and proposes novel methods for respiratory motion correction. Particular emphasis is given to the non-uniform radiotracer and density distribution and their changes in the lung. This work will allow a better design of future research studies and ultimately could lead to increased accuracy and precision in PET imaging of the lung and therefore patient benefit.

The results on positron range raise awareness of the caveats of using radiotracers labelled with certain (high–energy) positron emitters, where a large bias in the apparent radioactivity in the fibrotic lung could be observed (up to 61.6% if we assume that the true radioactivity distribution is uniform between low–density and high–density lungs). The proposed Monte Carlo method provides a methodology to establish if observed PET image values reflect underlying radiotracer concentrations or are due to local changes in density. This could be used when deciding on the radioisotope used for labelling a new radiotracer.

The two novel methods to improve existing respiratory motion correction in PET imaging proposed in this thesis could lay the foundation of further research or commercial software. A first method extends joint reconstruction of PET emission images and motion estimation to dynamic PET reconstructions, via summation of dynamic data. This will increase the feasibility of deriving radiotracer kinetic measures, an area with resurgence in interest, in the lung. Indeed, additionally to recovering respiratory motion adequately, the residuals from standard compartment model fit in the lung are reduced by more than 18% on average. This could allow estimation of additional clinically relevant parameters from the PET data. The second proposed method incorporates the previously discussed changes in lung density and radiotracer concentration due to respiration into the correction method. As these changes can be up to 30%, this method has the potential to have large impact by increasing the reliability of the PET-derived measures. In future, the benefits of combining the two methods will be necessary.

While the proposed methods for respiratory motion correction have been designed and evaluated for PET, they are directly extendable to other imaging modalities including SPECT, CT and certain MRI sequences.

Acknowledgements

I acknowledge funding support from GlaxoSmithKline to UCL (BIDS3000030921) and research support from the National Institute for Health Research, University College London Hospitals Biomedical Research Centre.

First of all, I would like to thank my two supervisors, Prof. Kris Thielemans and Prof. Brian Hutton. Kris has always found a way to take some of his time to give me advice when I most needed him to, despite his very busy schedule. The trust that he gave me was important for me and motivated me to outdo myself. Brian has been attentive to my needs since the beginning and given some precious directions to my project.

I also want to thank all the people who are or were directly involved in my work, either with technical and collaborative help, in particular Maria Machado for all the help with the patient data, or with supervision – Fred Wilson, Ashley Groves, Sarah Lee. A special thank you goes to my fellow countryman Alexandre Bousse, who has helped for the motion compensation and other parts of my PhD. Another thank-you goes to Joanna Porter, Helen Garthwaite and Francesco Fraioli, for providing me with clinical data. I would also like to thank all the people with whom I have bonded during my entire PhD and everyone in the clinical office. A particular thank you to Ludovica and Ade, who have been close to me since the beginning of my PhD. Ludovica has been an amazing help with this thesis, particularly in careful proofreading. I would also like to thank Robert Shortman for research governance and administration and Maria Machado for the help with data transfer and analysis.

I would also like to thank my family and my friends back in France, whom I have missed greatly during this adventure. My parents and siblings have always been supportive to me and cheering me up when I most needed it. A huge thank you to my boyfriend Joel, who has been here for me for quite a long time now and

helped me so much in some very difficult time and motivated me to get past it, and rebound. His constant support allows me to stay focused on my work no matter what. I also thank two of my best friends, Mélanie and Sokha, who have visited me in London several times and brought me some sunshine (and French food) when I was homesick. The last thank you, but not least, is to my grandparents without whom this adventure would not have been possible, and in particular to my granddad Robert. His generosity and humility are huge motivation for me, he who worked so hard to bring to his children and grandchildren the comfort he did not have when he was younger. I know he is so proud and wish he could read this work.

Contents

List of Figures

List of Tables

Acronyms

2D 2-dimensional 116

3D 3-dimensional 45

4D 4-dimensional 98

AC attenuation corrected 24

APD avalanche photo-diode 43

BFGS Broyden-Fletcher-Goldfarb-Shanno 52

BSREM block sequential regularized expectation maximization 60

CoM centre of mass 97

COPD chronic obstructive pulmonary disease 33

CT computerised tomography 38

FBP filtered back-projection 55

FOV field of view 38

FWHM full-width at half maximum 44

HU Hounsfield unit 46

IDIF image-derived input function 139

IF input function 62

ILD interstitial lung disease 33

IPF idiopathic pulmonary fibrosis 33

JRM joint image reconstruction and motion estimation 95, 103

LNCC local normalised cross correlation 61

LOR line of response 44

MCIR motion-compensated image reconstruction 101

MLAA maximum likelihood reconstruction of activity and attenuation 102

MLEM maximum-likelihood expectation-maximisation 28

MLTR maximum likelihood preconditioned gradient ascent for transmission reconstruction 102

MSE mean squared error 166

NCC normalised cross correlation 121

NRMSD normalised root mean squared deviation 117

OSEM ordered subsets expectation maximisation 58

PCA principal component analysis 97

PET positron emission tomography 34

PMT photo-multiplier tube 43

QP quadratic penalty 107

RD relative difference 59

ROI region of interest 112

RPM real-time position management 19

SAM spectral analysis method 97

SiPM silicon photo-multiplier 43

SNR signal-to-noise ratio 44

SSD sum of squared differences 95

SSPM solid-state photo-multiplier 43

SSS single scatter simulation 49

STV smoothed total variation 107

SUV standardised uptake value 45

TAC time activity curve 70

TOF time of flight 43

Chapter 1

Introduction

The lung can undergo multiple types of diseases. The most common pulmonary disease is lung cancer, one of the main causes of death in the world and the main cause of cancer mortality worldwide (Postmus et al. 2017).

Although, not as common as lung cancer, two other main types of diseases can affect the lung: chronic obstructive pulmonary disease (COPD) and interstitial lung disease (ILD), as described in Chen et al. 2017.

COPD is a major health issue, with a rising incidence, resulting for instance from smoke or air pollution. It is characterised by airflow limitation, usually progressive, and inflammatory response (Martinez et al. 2011). It leads to lung injury, which involves a structure remodelling.

ILD, or diffuse parenchymal lung disease (DPLD), is a disease group affecting the tissue and space around the lung alveoli ("interstitium"). idiopathic pulmonary fibrosis (IPF) is the most common pathology among ILDs, characterised by progressive scarring in the lung, leading to an irreversible loss of breathing capacity (Spagnolo et al. 2015). IPF had a prevalence of $20.2/100,000$ and $13.2/100,000$ for men and women respectively as of 1998 in the USA (Coultas et al. 1994), and the mean age at diagnosis was around 66 years old. The mortality is high, the mean survival is approximately 3 years after first diagnosis (Meltzer and Noble 2008). According to a study published in 2011 (Navaratnam et al. 2011), the incidence of IPF is rising every year in the UK, and was estimated in 2008 at $7.44/100,000$, with more than 5000 new cases diagnosed every year.

The first signs of IPF are breathlessness during physical exercise and a chronic dry cough. At a microscopic level, the disease is characterised mainly by scarring

within the air sacs of the lungs, which leads to localised lung structure remodelling, including a larger fraction of collagen. The pathology is usually restricted to specific areas of the lung, most commonly at the base, and results in regions with an increased rigidity and density and some large air pockets. Due to the increasing loss of elasticity of the lungs, the patient loses the ability to breathe, and eventually succumbs to respiratory failure.

The mechanism and origins of IPF are yet to be understood, although some studies suggested that it could be a result of an abnormal healing response, following a lung injury (Spagnolo et al. 2015). Several therapies have been tested on IPF patients (pirfenidone, nintedanib) and have shown promising results with a reduced progression and functional decline (Raghu et al. 2015; Spagnolo et al. 2015).

As stated in the guidelines of diagnosis of IPF (Raghu et al. 2011), when any other type of ILD is excluded, IPF can be diagnosed using spirometry, bronchoalveolar lavage, a chest x-ray scan or high resolution computerised tomography (high resolution CT or HRCT), and then confirmed by a surgical biopsy. HRCT is nowadays the preferred method for IPF diagnosis, as its sensitivity exceeds 90%. The main patterns of IPF on HRCT are reticular opacities, such as honeycombing or ground-glass opacities.

However, a single HRCT image can be used to detect anatomical changes only, and not the physiological changes, that are therefore likely to be useful on longer time scale.

An alternative to CT scans could lie in the use of positron emission tomography (PET). PET is a medical imaging technique providing "functional" information, i.e. it enables the imaging of metabolic processes in a tissue or organ. It measures the spatial distribution of a positron-emitting radiotracer administrated to a patient, either via injection in the blood or via inhalation. Using a PET acquisition could provide "early information" on the disease, in order to have a better understanding of its aetiology (Chen et al. 2017). Whereas PET imaging is essential for tumour staging and follow-up, particularly via measurement of ^{18}F-FDG uptake (Nakamura et al. 2015), it is rarely used for diffuse lung diseases.

Originally, PET scanners were stand-alone but dual-modality scanner systems (combining PET and CT or PET and Magnetic Resonance Imaging (MRI)) are

now predominant. This report will focus on PET and PET/CT scanners. Despite the increasing influence and use of PET/MRI scanners, the technique is still to be improved in the case of lung imaging and will not be discussed in this work.

Although PET/CT imaging is widely used, especially in oncology, where staging and localisation of the tumours are essential, issues related to quantification of lung PET images still need to be addressed, especially in the context of pathologies such as IPF, which affect the lung architecture more globally than lung tumours. For example, the image resolution becomes spatially-variant, especially for radiotracers labelled with high-energy radionuclides. Current techniques to compensate for respiratory motion might also be inadequate and need to be assessed carefully. The aim of this thesis is therefore to address issues related to lung PET/CT imaging and improving the robustness of quantitative measures for IPF patient data.

The physics and detection techniques in PET will be discussed in Chapter 2. An introduction to optimisation and compartmental modelling will be provided, as well as a brief overview of the reconstruction principles in PET and some of the challenges of PET imaging in the lung and more specifically of imaging IPF. They will be mainly addressed in the following chapters.

Firstly, positron range, which contributes to resolution degradation, will be addressed in Chapter 3. The effect is linked to the inherent resolution of PET imaging and is worsened in the lung, because of its low density.

Secondly, in Chapter 4, an introduction to respiratory motion in medical imaging will be provided, discussing the volume changes and fluid exchanges occurring within the lungs during respiration. The mass-preserving model for respiratory motion used in the rest of the thesis will be described and used within a preliminary image registration, to show its validity in PET/CT imaging. The effect of respiratory motion on static and dynamic PET images will also be demonstrated on patient data.

Then, in Chapter 5, the use of inconsistent data in the reconstruction (due solely to errors in the attenuation map) will be discussed. The quantification errors will be shown to demonstrate the importance of an accurate knowledge of the attenuation map in PET reconstruction, especially in lung imaging, where the attenuation in the lung can vary between two extreme respiratory states.

Finally, Chapter 6 will give an overview of existing motion-compensating methods for lung PET imaging, priot to introducing new methods. On one hand, a preliminary method aimed at tackling motion for dynamic PET acquisitions will be described and assessed on patient data. On the other hand, following the results of Chapters 4 and 5 and their implications for motion correction techniques in PET/CT imaging, the mass-preserving model will be incorporated within a scheme of PET joint reconstruction and motion estimation. The latter method will be validated using simulations and used for static PET acquisitions.

PET/CT data from an IPF cohort will be used throughout this work, and most particularly for the motion compensation work of Chapter 6. The nine patients of the cohort are part of a study to assess the role of coagulation in IPF, the patients undergoing a first PET/CT acquisition before starting an anticoagulation treatment (dabigatran, a direct thrombin inhibitor), and a second PET/CT acquisition takes place at the end of it, about one month later (clinical trial ID: NCT02885961). Additionally to these "treatment patients", two "control patients" were also acquired. The study will be referred as the "Coagulation Study" in the following work and the details of the acquisitions will be given in Section 6.4.1. Only data involving no anticoagulation treatment will be used in this thesis, i.e., the data corresponding to the control patients and the pre-treatment scans of the treatment patients.

Chapter 2

Positron Emission Tomography in the Lung

2.1 Introduction

This chapter introduces the main principles of PET/CT imaging, from data acquisition and physical principles to the reconstruction of PET images and their analysis. An emphasis is given to the clinical analysis of IPF PET images, which suffers from various limitations, and therefore requires careful investigation and reconstruction techniques to obtain robust quantitative measures.

2.2 Positron Emission Tomography

2.2.1 Generalities

2.2.1.1 History of PET

PET is a nuclear medicine technique that uses positron annihilation to image biological metabolism. PET enables "functional" imaging, as opposed to "anatomical" imaging.

The development of PET is based on the discovery of the positron and radioactivity, as well as the invention of the cyclotron between the late 1920s and the late 1940s. Between the 1950s and the 1970s, the ideas and preliminary designs of PET scanners were conceived. Since the 1970s, PET is increasingly used in clinical institutions and their design and performance have improved. PET is mainly dedicated for oncology ($\approx 95\%$ of PET clinical use), but is also used in neurology and cardiology studies (see Rich 1997).

2.2.1.2 Typical PET Examination

The first step in a PET exam consists of the injection (or inhalation) of a radiotracer. A radiotracer is the combination of a biologically active molecule, targeting a specific biological metabolism, and a radionuclide, which allows imaging of the process.

The most common radiotracer is ^{18}F-fluoro-2-deoxy-D-glucose, usually abbreviated as ^{18}F-FDG or simply FDG. The active molecule is a glucose analogue in which the hydroxyl group on the 2-carbon of a glucose molecule is replaced by a fluoride atom. FDG provides an indicator of glucose uptake. It is mainly used for oncology, as tumours generally show larger FDG uptake than surrounding healthy tissue. ^{18}F is the radionuclide, whose half-life is 109.77 min (Delbeke et al. 2006). This enables the production of FDG in an off-site facility, making it widely available.

Other radionuclides and biological ligands can be used for PET tracers (see Section 2.5.1.1 and Chapter 3 for more examples).

In current clinical practice, PET is almost always combined with computerised tomography (CT) (see Section 2.2.3). A PET/CT scanner is composed of two separate systems, that are placed next to one another (see Figure 2.1).

The field of view (FOV) of a scanner is defined by the area in which the activity can be measured by the detectors. Current typical clinical scanners have an axial FOV between 15 cm and 25 cm (Pan et al. 2019), although "whole-body" scanners are under study to improve sensitivity (Cherry et al. 2018). The transaxial FOV is usually between 50 cm and 70 cm.

2.2.2 Physical Principles of PET

2.2.2.1 Radioactive Decay and Annihilation

β^+-radioactivity :

The radionuclide, incorporated in the tracer used in a PET exam, is a positron-emitting radioisotope (β^+-decay), i.e., it is lacking a neutron. The nucleus is therefore not stable and its lifetime is described with a decreasing exponential law:

$$N(t) = N(0) \exp\left(-\lambda_{\mathrm{D}} t\right)$$

where the decay constant $\lambda_{\mathrm{D}} = \frac{\log 2}{t_{1/2}}$, $N(t)$ is the number of radioactive nuclei at a time t in a sample, $t_{1/2}$ is the radionuclide half-life and $\log(\cdot)$ will represent the

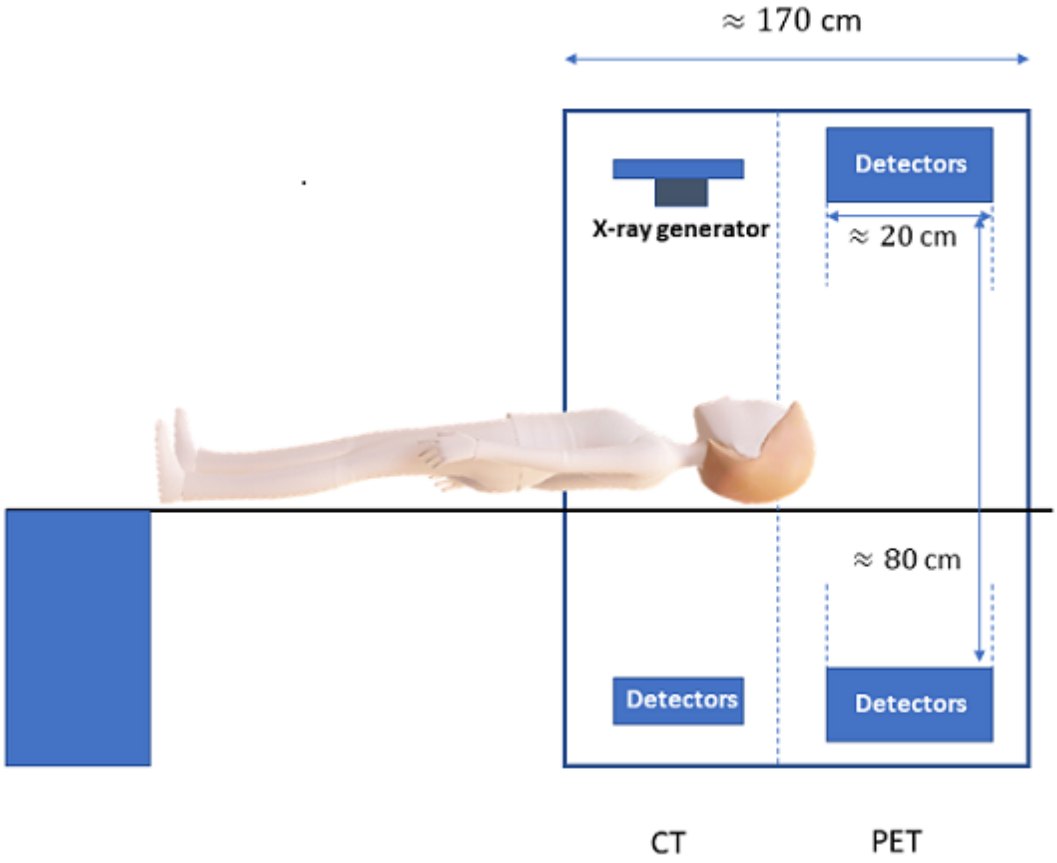

Figure 2.1: Schematic of a PET/CT scanner

natural logarithm in this thesis.

During the β^+-decay, a proton of the nucleus ${}^{A}_{Z}\mathrm{Y}$ is converted into a neutron, which releases a positron e^+ and an electron neutrino ν_e. As a result, a "daughter" nucleus ${}^{A}_{Z-1}\mathrm{X}$ is created, accompanied with an energy release E^* (see Equation (2.1)).

$$ {}^{A}_{Z}\mathrm{Y} \rightarrow {}^{A}_{Z-1}\mathrm{X} + e^+ + \nu_e + E^* \tag{2.1} $$

The energy spectrum of the emitted positrons depends on the radionuclide (see Equation (3.2) in Chapter 3).

Annihilation and Positron Range:

Once the positron is emitted within the tissue, its kinetic energy decreases through sequential collisions with bound electrons of the medium, until the final collision during which the "annihilation" interaction occurs. This results usually in the creation of 2 γ photons of 511 keV that travel almost back-to-back (Evans 1955).

$$e^- + e^+ \rightarrow 2\gamma \tag{2.2}$$

A PET scan will therefore image the annihilation locations instead of the positron emission locations.

The distance between the positron emission location and the annihilation location is known as "positron range" and will be discussed further in Chapter 3.

2.2.2.2 Photon Interactions in Matter

Compton Scattering:

Compton scattering, also known as incoherent scattering, is the predominant interaction at 511 keV in tissue.

The incoming γ-ray photon is deflected through an angle θ with respect to its original direction, when its path gets close to an electron at rest. A part of its energy is transferred to the electron, known as a "Compton electron" or "recoil electron".

The energy E' of the scattered photon can be expressed in terms of the energy of the original photon E and the scatter angle θ: $E' = \frac{E}{1+\alpha(1-\cos\theta)}$, where $\alpha = \frac{E}{m_0c^2}$ and m_0c^2 is the electron rest energy.

The probability of Compton scattering is proportional to electron density and decreases as the photon energy increases.

Rayleigh Scattering:

Rayleigh scattering, also known as "coherent scattering", occurs mainly for low-energy photons or high atomic number Z. Unlike Compton scattering, it happens without loss of energy ("elastic scattering"). However, the probability of Rayleigh scatter is negligible at 511 keV and is usually neglected in PET.

Photoelectric Absorption:

A photon interacts with an atom in which the photon completely vanishes, and it creates an energetic photoelectron. It is the predominant form of interaction at low photon energy and high atomic number Z. It is one of main processes at the base of detectors in PET, in the scintillation crystals (see Section 2.2.2.3).

Pair Production:

For high-energy photons, the inverse process to annihilation can occur, i.e., $\gamma \rightarrow e^+ + e^-$. However, as the γ photon needs to have an energy of at least 1.022 MeV

(conservation of energy), this process cannot happen for photons created in an annihilation event.

2.2.2.3 Detection Principles

Coincidences in PET :

PET is based on the detection of "coincidences", which are pairs of photons from the same annihilation event, whose energies fall into the scanner energy window (typically between 425 keV and 650 keV, like for the GE Discovery PET/CT 690 (Bettinardi et al. 2011)) and the difference of their arrival times at the detectors is in the coincidence window ($\approx$ 5 ns). Because of the different types of photon interactions in the body (Section 2.2.2.2), four types of coincidences are defined in PET:

- true coincidences, or "trues", correspond to a photon pair both emitted in the same annihilation event and whose directions were not modified during their travel to the detectors.
- scattered coincidences, or "scatters", is when at least one of the detected photons is a scattered photon.
- random coincidences, or "randoms", correspond to two photons which were emitted in two distinct annihilation events.
- multiple coincidences, or "multiples", when more than three photons are detected within the same coincidence window, making it impossible to distinguish annihilation photons from the same event.

The "prompts" are defined as the recorded in-time coincidences in a PET scan. In this case, the total number of prompts P is equal to:

$$P = T + S + R$$

where T, S and R are the number of trues, scatters and randoms, respectively. An illustration of the four types of coincidences can be found in Figure 2.2. These types of coincidences need to be accounted for when PET images are reconstructed. The standard method to estimate the amount of scatter events in the prompts is discussed in Section 2.2.5.

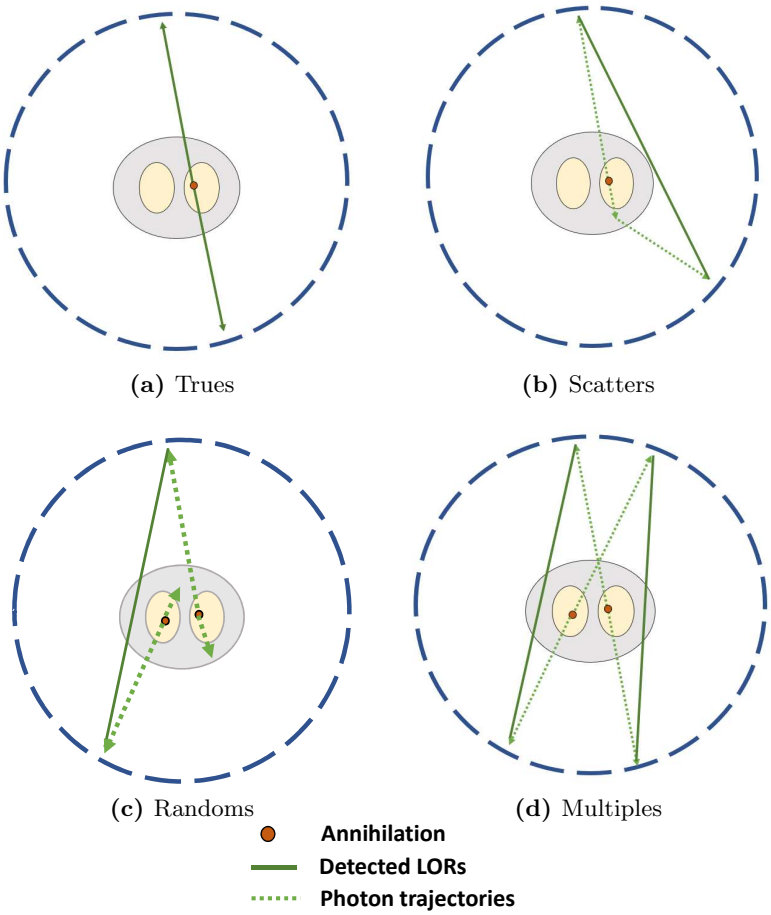

Figure 2.2: Different types of coincidences in PET: (a) Trues, (b) Scatters, (c) Randoms and (c) Multiples.

Photo-detection :

The annihilation photon detector in PET is composed of a scintillation crystal and a signal detector, usually known as the photo-detector; the high-energy photons first lose energy and become light (scintillations). The light pulse produced by the scintillation crystal is then converted to an electrical signal by the photo-detector.

For PET imaging, desirable characteristics for the scintillation crystals are the following:

- a high atomic number Z, as photoelectric absorption is favoured, to achieve good sensitivity and a high stopping power, defined as the inverse of the mean distance travelled by the photons before depositing energy, to overcome the limited size of the crystals.

- a high light output (fraction of incident γ photons converted into scintillation

photons), leading to a good energy resolution (the fraction of scintillation photons is proportional to the energy brought by the annihilation photon), crucial to discriminate the true events from the scattered events (2.2.2.3).

- a low light decay constant, to allow detecting higher photon rates and a precise measurement of time arrival of the photons.

In the first PET scanners, the crystals were made of NaI, but they were replaced by BGO and nowadays mostly LSO/LYSO crystals, as they have a better overall efficiency, time resolution and are not hygroscopic (see Melcher 2000).

The main types of photo-detectors used for PET scanners are:

- Photo-multiplier tubes (PMTs). They consist of a photocathode and of a series of dynodes in an evacuated glass enclosure. Even though they have a high amplification of the signal, the conversion of incoming light photons into electrons ($\approx 25\%$, "quantum efficiency") and its bulky shape are drawbacks for PET detectors (Roncoli and Cherry 2011).

- Avalanche photo-diodes (APDs), silicon device based on a modified p-n junction structure, providing a better quantum efficiency (up to 80%). They however require careful maintaining of operating conditions, including a cooling system, and the signal amplification and the timing resolution is poorer than for PMTs. (Shah et al. 2002)

- Silicon photo-multipliers (SiPMs), or solid-state photo-multipliers (SSPMs), combine the advantages of both PMTs and APDs, with high signal amplification, quantum efficiency and time resolution. They are the new standard for photo-detectors (Roncoli and Cherry 2011).

Time-of-Flight :

As stated above, PET is based on the detection of two photons in a coincidence timing window. Additionally, the time information can predict the position of the annihilation event from the arrival times of the photons at the detectors. Even though this concept, called time of flight (TOF), was proposed in the very beginning of PET development (1960s), it was only first clinically available in the 1980s (Surti 2015).

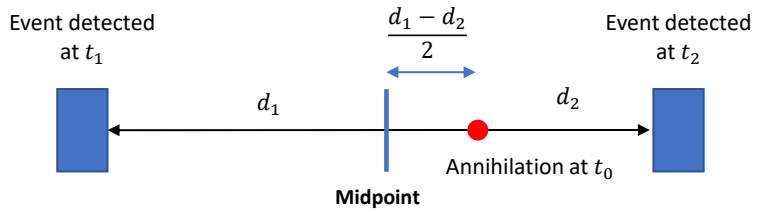

Figure 2.3: Principle of Time-of-Flight

If two annihilation photons created at t_0 are detected by two separate detectors adjoined by a line at time t_1 and time t_2, the distance between the line midpoint and the annihilation location is equal to $\frac{|d_1-d_2|}{2}$ where $|d_1 - d_2| = c \cdot |t_2 - t_1|$ (Figure 2.3).

There is however an uncertainty on the location of the event, which can be characterised by a time resolution Δt. This is usually modelled with a normal distribution along the line of response (LOR) where the full-width at half maximum (FWHM) of the function is equal to $\frac{c\Delta t}{2}$.

The TOF capability of a scanner requires an accurate evaluation of the arrival time of the photons at each detector (Spanoudaki and Levin 2010). Some types of scintillation crystals cannot provide the minimal time resolution required for TOF, therefore it is only used in clinical practice for LSO/LYSO detector scanners at the moment (Moses and Derenzo 1999). Better photomultipliers can improve the time resolution of the scanners, as it is the case for new PET scanners, using SiPMs instead of PMTs. The manufacturers are currently pushing towards higher time resolution, in order to improve the signal-to-noise ratio (SNR) of the PET images (Lecoq 2017; Cates and Levin 2018). Recent Siemens PET/CT Vision has a reported time resolution FWHM of approximately 210 ps/3.15 cm (Van Sluis et al. 2019), whereas GE PET/CT Discovery MI has a lower resolution of FWHM 382 ps/5.73 cm (Pan et al. 2019). The TOF-ready scanner in this project is the GE PET/CT Discovery 710 (Bettinardi et al. 2011), for which the time resolution FWHM is only of 550 ps/8.25 cm.

Data Output :

The data output of a PET acquisition is a file storing the collection of all prompts (see Section 2.2.2.3). An annihilation event is primarily characterised by the detector pair where the photons arrived. For each of them, we define a LOR, connecting the centres of the two detectors. The time information, when it can be measured, is

stored in a number of "TOF bins", the TOF bin index being an additional coordinate to an event in TOF PET. The "TOF bin size" is equal to the coincidence window divided by the number of TOF bins. The output can be stored as:

- a "listmode" file. The file encompasses the main information about the detected events, such as the arrival time, the detector and annihilation event coordinates or the detected energy.
- a "sinogram". The events are histogrammed during the acquisition process. Although less flexible than the listmode files, sinograms are still largely used in routine image reconstructions and for data display.

In order to obtain a 3-dimensional (3D) representation of the radiotracer concentration in the body, the PET data needs to be reconstructed. The resulting images often show the concentration in $kBq.mL^{-1}$ but the values are often normalised to represent the activity within the body, such as standardised uptake value (SUV) dividing the activity values by a factor related to the patient morphology and by the injected activity.

We can distinguish two main types of PET acquisitions:

- Static PET: these are the most common acquisitions, the (short) acquisition takes place when the radiotracer is considered "stable" in the body during the duration of the acquisition, therefore the patient needs to wait a certain duration between the time the tracer was given to him and the acquisition time. This waiting time before the acquisition depends on the radiotracer metabolism. In clinical practice, it is approximated to 60 min for ^{18}F-FDG and only a few minutes for ^{15}O-CO.
- Dynamic PET: the acquisition starts just before the radiotracer is given to the patient. Measures on radiotracer kinetics can be obtained from such acquisitions (Lammertsma 2017a), for example from compartmental modelling. This will be introduced in Section 2.3.4.

2.2.2.4 Factors influencing PET Resolution

The resolution of PET is limited by several factors. The three main factors (Moses 2011) are the following:

- Limitations linked to the detectors such as inter-crystal scatter and crystal finite dimension (Rahmin et al. 2013).

- Positron Range; as discussed in 2.2.2.1, PET detects the annihilation events instead of the positron emission events (Levin and Hoffman 1999). This will be discussed in more details in Chapter 3.

- Non-collinearity of annihilation photons; the centre of gravity of the positron and atomic electron system ("positronium") is not always at rest at their annihilation. Therefore the annihilation photons are not always emitted back-to-back (i.e., exactly 180 ° apart), due to conservation of energy and momentum. In the case of a PET scan with a ^{18}F-labelled radiotracer (e.g., FDG), there is a collinearity error of approximately 0.54 ° (Shibuya 2007).

2.2.3 CT Physical Principles

CT, or more appropriately "X-ray" CT, measures the attenuation of X-rays by tissues from different angles.

During the CT acquisition, an X-ray generator rotates around the patient, usually along a helical trajectory. It emits X-rays in a given direction, using a photoguide. A part of the X-ray beam is attenuated within the body, mainly because of photoelectric effect. The remaining X-rays are collected by photodetectors on the other side of the patient.

The energy spectrum of a X-ray source is polychromatic (mixture of several wavelengths) and depends on the scanner settings, mainly its peak kilovoltage (kVp) and the electric current applied (in mA). The energy spectrum of CT acquisitions (for a PET/CT scanner) is typically comprised in a range from 40 keV to 140 keV (Alvarez and Macovski 1976), for which Compton scattering and photoelectric absorption are considered as the main physical interactions in soft tissue and bones.

For PET/CT scanners, the CT acquisition used for attenuation correction (see next Section 2.2.4) normally takes place before the PET acquisition. For a standard helical CT acquisition, the scan is very fast (of the order $\approx 2-3$ s for a thoracic coverage,Goerres et al. 2003). The resulting CT image is usually expressed in Hounsfield

units (HUs), defined, at a location x as:

$$\mathrm{HU}(x) = 1000 \times \left(\frac{\mu(x) - \mu_{\mathrm{water}}}{\mu_{\mathrm{water}} - \mu_{\mathrm{air}}} \right)$$

where $\mu(x)$, μ_{water} and μ_{air} are the linear attenuation coefficients of the tissue at the location x, the water and the air, respectively.

2.2.4 Attenuation in PET and PET/CT

2.2.4.1 Physical Properties

Attenuation is defined as the loss of (true) coincidences as a result of the photon interactions occurring within the body of the patient, as described in Section 2.2.2.2.

In CT imaging, the attenuation of a photon ray of energy E along the line between the X-ray generator and a detector follows the Beer-Lambert's law:

$$I(x, E) = I_0 \exp\left(- \int_{l=0}^{x} \mu(l, E)\, \mathrm{d}l \right) , \tag{2.3}$$

where $\mu(l, E)$ is the linear attenuation coefficient for a photon of energy E in the tissue located at a distance l from the X-ray generator, I_0 is the photon ray intensity at distance 0 and $I(x, E)$ is the photon ray intensity at distance x along the line, for a monochromatic X-ray source. Considering the polychromatic nature of the X-ray source used in CT acquisition, the resulting photon ray intensity at distance x becomes:

$$I(x) = \int_{0}^{E_{\max}} I_0(E) \exp\left(- \int_{l=0}^{x} \mu(l, E)\, \mathrm{d}l \right) \mathrm{d}E , \tag{2.4}$$

where $E_{\max}$ is the maximal energy of the X-ray source and $I_0(E)$ is the photon ray intensity for a given energy E at distance 0 (i.e., as emitted from the source). As the energy spectral distribution of the X-ray source $I_0 : 0 \rightarrow E_{\max}$ is unknown, the integral in (2.4) cannot be calculated directly. However, according to the mean value theorem, we can prove that there exists an energy E_{eff} such that it is possible to rewrite (2.4) as (2.3). Although this energy depends on the photon paths, in practice CT reconstruction uses an "effective" linear attenuation coefficient $\mu_{\mathrm{eff}}(l)$ (Baur et al. 2019), which can cause beam hardening artefacts in CT images.

Whereas photon attenuation is the foundation of X-ray imaging, it represents an issue in PET. The fraction of photons attenuated in a tissue is proportional to

the tissue density. For large patients in PET, the fraction can be up to 95% (Mettler and Guiberteau 2012), or more for obese patients, and needs to be accounted for.

As for CT, attenuation in PET can also be described using the Beer-Lambert's Law (Equation (2.3) for $E = 511\,\text{keV}$):

$$I(x, E = 511\,\text{keV}) = I_0 \exp\left(-\int \mu(l, E = 511\,\text{keV})\,\text{d}l\right) , \tag{2.5}$$

where $\mu(l, E = 511\,\text{keV})$ is the linear attenuation coefficient at the distance l, for photons of energy 511 keV.

In order to achieve good quantification of the physiological processes in PET, the attenuation needs to be estimated and taken into account. In this thesis, we will refer to attenuation map or μ map as an image representation of the linear attenuation coefficients μ, which are used to reconstruct PET images corrected for attenuation.

2.2.4.2 Attenuation Estimation using Transmission Scans

In the case of a stand-alone PET scanner, attenuation is estimated using a "transmission" scan, acquired prior to the injection or inhalation of the main radiotracer (Bailey 2004). It usually consists of a radioactive positron-emitting rod source (usually a ^{68}Ge / ^{68}Ga source) rotating around the patient.

A blank exam, i.e., without the patient, is also acquired routinely to correct for detection efficiencies in the transmission scan. The quotient sinogram of the two gives the attenuation correction factors. This method, since the arrival of PET/CT scanners, is not used routinely anymore, as it requires an additional external source and lengthy scan, which is subject to intrastudy motion.

2.2.4.3 Attenuation Estimation using a CT Acquisition

When a CT attenuation image is available, it can be used to derive the PET attenuation image. However, the two images are not directly comparable: PET uses monoenergetic 511 keV annihilation photons while CT uses polychromatic low-energy photons (energy spectrum from 40 keV to 140 keV). The relative importance of photon interactions in matter (see Section 2.2.2.2) is therefore different.

However, rescaling the CT image, often via a bilinear or trilinear conversion, to assess the attenuation coefficient factors in PET (see Part 2.3.2), has proved to be

an efficient method. Using a CT-based attenuation image has the advantage of not needing extra scans and being quasi-instantaneous, reducing the motion uncertainty and providing more comfort for the patient and a higher patient throughput (cf P.E. Kinahan et al. 1998; Alessio et al. 2004).

The use of CT-based attenuation maps in PET relies on an accurate alignment between the PET and CT images, which is normally the case in integrated PET/CT systems. However, in presence of motion during the acquisition (mostly for cardiac and lung imaging) or when the attenuation of a material is wrongly estimated (e.g., because of metallic implants or contrast medium), some artefacts can appear on the emission images (streaking artefact, blurring of lung lesions or heart, breathing artefact, etc.) and are difficult to eliminate (Sureshbabu et al. 2005).

2.2.5 Estimation of Scatters in Detected Prompts

Scatter events (Section 2.2.2.3) represent a large part of the detected prompts and depend on the attenuation of the medium— approximately equal to 36% according to Spinks et al. 1992. Therefore, to achieve good quantification, scatter sinograms are commonly estimated either to pre-correct the prompts (usually for analytical reconstructions, see Section 2.3.2.2) or to incorporate within the system model (see Equation (2.19) of next Section 2.3.2.4).

Currently, the most common method is an iterative estimation of the scatter component, by using single scatter simulation followed tail fitting. The single scatter simulations (SSS) (Watson et al. 1996; Ollinger 1996) are based on calculating the probability of scattering to the PET detectors, by integrating the Klein-Nishina equation (Evans 1955). These simulations assess the single scatter only sinogram (i.e., for a detected pair of photons, one photon was not scattered along its path and the other photon was scattered only once). Multiple and out of the FOV scatters are added to the previously estimated sinogram by scaling it up, via tail fitting (Thielemans et al. 2007). This method was extended to TOF data (Watson 2007).

2.3 Data Processing

This section will give a brief overview of the main techniques and algorithms used to process PET/CT data. This includes an introduction to general optimisation and its use in three domains:

- *PET activity image reconstruction*: the main reconstruction algorithms nowadays rely on optimising a given cost function to obtain the most likely activity image. This will be developed in Section 2.3.2.

- *Medical image registration*: it is often necessary to register/realign images, for example for patient follow-up or more generally to compensate for motion within image reconstruction. An introduction will be given in Section 2.3.3 and some results presented in Chapter 4.

- *Compartmental modelling*: it is possible to extract kinetic parameters from dynamic PET acquisitions. Some details are provided in Section 2.3.4 and in Appendix A.

2.3.1 Parameter Estimation through Optimisation in Medical Imaging

As introduced in Section 2.2.2.3, the output of a PET acquisition is not directly representative of the radiotracer distribution, the data needs to be "reconstructed".

2.3.1.1 Introduction to Optimisation

An optimisation problem (Nocedal and S. Wright 2006) finds the optimal solution for a specific problem given a vector $\boldsymbol{x} \in A$. It relies usually on the minimisation of an objective function (or cost function) $\Psi : A \to \mathbb{R}$ for a vector $\boldsymbol{x} \in A$ i.e., in finding:

$$\bar{\boldsymbol{x}} \in \arg\min_{\boldsymbol{x} \in A} \Psi(\boldsymbol{x}) \,. \tag{2.6}$$

The optimisation domain A can be $\mathbb{R}^n$ (where n is the number of variables) or can incorporate equality or inequality constraints. Note that it is sometimes easier to pose a problem as a maximisation, hence the equivalent formulation:

$$\bar{\boldsymbol{x}} \in \arg\max_{\boldsymbol{x} \in A} -\Psi(\boldsymbol{x}) \,. \tag{2.7}$$

Optimisation is used in several fields of medical imaging, among which image denoising, image segmentation, image registration, image reconstruction or compartmental modelling. The objective function is often written as:

$$\Psi(x) = \text{Similarity}(x) + \beta \, \text{Roughness}(x) \,, \tag{2.8}$$

where Similarity indicates the goodness of model fit and β Roughness is the "regularisation" term, usually relying on prior knowledge on the image distribution (Roughness is the penalising function and β is its penalty weight). Similarity measures and regularisation penalties for image reconstruction and image registration will be discussed in Section 2.3.2 and 2.3.3.

2.3.1.2 Optimisation Methods

Iterative Optimisation :

An iterative optimisation scheme is usually as follows, starting from an iterate $\boldsymbol{x}_k$:

1. *Convergence test*: If the previous iterate (or initial iterate when $k = 1$) satisfies the convergence criteria, the optimisation stops.
2. Computation of a *search direction* p_k.
3. Computation of the *step length* $\alpha_k > 0$ (depending on optimisation method): usually using a line search
4. *Update* following Equation (2.9), increment k and return to step 1.

$$\boldsymbol{x}_{k+1} = \boldsymbol{x}_k + \Delta\boldsymbol{x}_k, \quad \text{where} \quad \Delta\boldsymbol{x}_k = \alpha_k p_k \,. \tag{2.9}$$

Other update rules (e.g., multiplicative) are sometimes used, but can often be rewritten as in Equation (2.9).

In gradient-based optimisation, the search direction corresponds to the gradient of the objective function. This section will focus on this type of methods.

When a direction p_k is chosen, a line search strategy is usually applied to find the step length α_k. In a steepest gradient descent, it is set as: $\alpha_k \in \arg\min_{\alpha>0} \Psi(x_k + \alpha p_k)$. Instead of finding the exact minimiser, in practice many line search algorithms find a close estimate of the optimal step size.

Newton method :

If we consider the second-order Taylor's expansion of a function f with values in $\mathbb{R}$:

$$f(\boldsymbol{x}) \approx f(\boldsymbol{x}_0) + f'(\boldsymbol{x}_0)(\boldsymbol{x} - \boldsymbol{x}_0) + \frac{1}{2} f''(\boldsymbol{x} - \boldsymbol{x}_0)^2 \tag{2.10}$$

and rewrite the equation for a vector $\boldsymbol{x}_k + \Delta\boldsymbol{x}_k$, using the gradient vector $\nabla f(\boldsymbol{x}_k)$ and the Hessian matrix $\nabla^2 f(\boldsymbol{x}_k)$, we obtain:

$$f(\boldsymbol{x}_k + \Delta\boldsymbol{x}_k) \approx f(\boldsymbol{x}_k) + \nabla f(\boldsymbol{x}_k)^\intercal \Delta\boldsymbol{x}_k + \frac{1}{2}\Delta\boldsymbol{x}_k{}^\intercal \nabla^2 f(\boldsymbol{x}_k)\Delta\boldsymbol{x}_k \tag{2.11}$$

where $[\,\cdot\,]^\intercal$ denotes the transpose of a matrix.

When differentiating Equation (2.11) and setting the derivative $\frac{\partial}{\partial\Delta\boldsymbol{x}_k} f(\boldsymbol{x}_k + \Delta\boldsymbol{x}_k)$ to 0 (signifying that f has a local extremum in $\boldsymbol{x}_k + \Delta\boldsymbol{x}_k$), we obtain the following equation:

$$\nabla^2 f(\boldsymbol{x}_k)\Delta\boldsymbol{x}_k = -\nabla f(\boldsymbol{x}_k) \tag{2.12}$$

Provided the Hessian $\nabla^2 f(\boldsymbol{x}_k)$ is positive definite, we can rewrite Equation (2.12) to obtain the "Newton step":

$$\Delta\boldsymbol{x}_k = -\nabla f(\boldsymbol{x}_k) \cdot \left(\nabla^2 f(\boldsymbol{x}_k)\right)^{-1} \tag{2.13}$$

where $\left(\nabla^2 f(\boldsymbol{x}_k)\right)^{-1}$ is the inverse of the Hessian. One disadvantage of using such step is the computation time of the Hessian matrix ($n(n+1)/2$ unique elements where n is the number of variables), its storage and the inversion of it, therefore quasi-Newton methods are often used to reduce the complexity of the optimisation. Instead of computing (and inverting) Hessian matrices, the latter methods use either approximate Hessian matrices or even approximate inverse Hessian matrices, using the values of the cost function and gradients from previous iterations. Quasi-Newton methods can also be used when the Hessian is not positive definite, as the constructed inverse Hessian matrix will be constructed as positive definite (Nocedal and S.J. Wright 1999).

Broyden-Fletcher-Goldfarb-Shanno (BFGS) :

The Broyden-Fletcher-Goldfarb-Shanno (BFGS) method is a widely-used quasi-Newton method (Dennis, Jr. et al. 1977; Nocedal and S.J. Wright 1999). The approximation V_{k+1} at an iteration of the inverse of the Hessian matrix $\nabla^2 f(\boldsymbol{x}_{k+1})$, from the previous iterate V_k:

$$V_{k+1} = \left[I_n - \frac{\Delta\boldsymbol{x}_k \boldsymbol{y}_k{}^\intercal}{\Delta\boldsymbol{x}_k{}^\intercal \boldsymbol{y}_k}\right] V_k \left[I_n - \frac{\boldsymbol{y}_k \Delta\boldsymbol{x}_k{}^\intercal}{\boldsymbol{y}_k{}^\intercal \Delta\boldsymbol{x}_k}\right] + \frac{\Delta\boldsymbol{x}_k \Delta\boldsymbol{x}_k{}^\intercal}{\Delta\boldsymbol{x}_k{}^\intercal \boldsymbol{y}_k} \tag{2.14}$$

where $\boldsymbol{y}_k = \nabla f(\boldsymbol{x}_k + \Delta\boldsymbol{x}_k) - \Delta f(\boldsymbol{x}_k)$

Variations of BFGS, including Limited-memory BFGS (L-BFGS) (Matthies and Strang 1979; Nocedal and S. Wright 2006) and L-BFGS-B (Nocedal 1980), with additional boundary constraints, are commonly used to speed up the optimisation: instead of storing the entire approximate to the inverse of the Hessian matrix, only a portion of it is stored.

2.3.1.3 Discretisation

The activity and attenuation distributions are usually discretised in medical imaging. A given distribution f can be discretised as a 3D image $\boldsymbol{f} = [f_i]$ such that, at a location $(x, y, z) \in \mathbb{R}^3$:

$$f(x, y, z) = \sum_{j=1}^{n_\text{v}} f_j b_j(x, y, z) \tag{2.15}$$

where n_v is the number of elements of the image volume and f_j is the contribution for each basis function.

Several types of basis functions exist in literature, among which two will be used throughout this work:

- Rectangular voxels/cuboid representation, for standard image reconstruction (see Section 2.3.2). In this case, $\forall j \in [\![1, n_\text{v}]\!]$, the contributions f_j are the voxel values and b_j is a rectangular function.

- Cubic B-splines (they will be used to parameterise deformation fields, see Chapters 4 and 6). B-splines are commonly used as they are $\mathcal{C}^\infty$ functions with explicit and simple derivatives (piecewise polynomials).

2.3.2 Image Reconstruction in PET

An overview of the main algorithms used in PET reconstruction will be given in this part.

2.3.2.1 Motivation

The data acquired on a PET scanner can be sinograms (or projection data) or listmode (see 2.2.2.3). The reconstructed images are composed of volume elements, or "voxels" (see discretisation in previous Section 2.3.1.3).

Two main types of reconstruction algorithms exist in PET: analytical and iterative reconstruction algorithms.

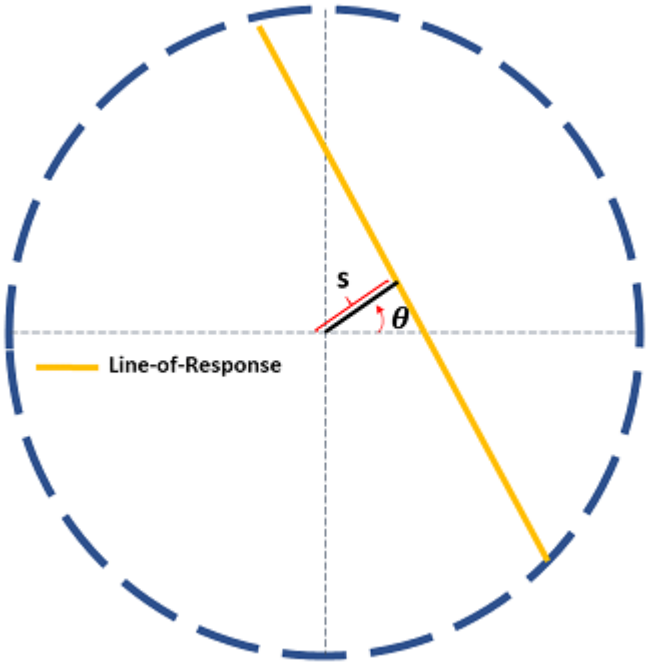

Figure 2.4: Line-of-response 2D parameterisation in PET

2.3.2.2 Analytical Reconstruction

Each LOR of the PET scanner (see Section 2.2.2.3) can be parameterised with spatial coordinates (see in 2D in Figure 2.4).

The X-ray transform of a 2D distribution λ, also known as Radon transform, can be written as:

$$\mathcal{R}\lambda(s,\theta) = \int_{-\infty}^{\infty} \lambda(s\cos\theta - \xi\sin\theta, s\sin\theta + \xi\cos\theta)\,\mathrm{d}\xi \tag{2.16}$$

In the case of TOF data (2.2.2.3), the annihilation along the LOR defined by (s,θ) is approximately located at a TOF time τ, the uncertainty being defined by a temporal blurring kernel $h(\tau)$ (usually defined as Gaussian). The previous Equation (2.16) is modified and the line integral is replaced by a convolution along the LOR:

$$\mathcal{R}^{\mathrm{TOF}}\lambda(s,\theta,\tau) = \int_{-\infty}^{\infty} \lambda(s\cos\theta - \xi\sin\theta, s\sin\theta + \xi\cos\theta)h(\tau-\xi)\,\mathrm{d}\xi\,. \tag{2.17}$$

The parameterisation using X-ray transforms can be extended in 3D to LORs in oblique planes (Defrise et al. 1989).

The most common analytical reconstruction method is the filtered backprojection (FBP) reconstruction and relies on X-ray transforms and the associated "Central Slice theorem", relating the Fourier transform of a projection to the Fourier transform of the image. A ramp filter is first applied to the sinogram (which is usually pre-corrected for attenuation, scatter and randoms). The filtered sinogram is then backprojected to construct the PET image. The reconstruction is fast, and used to be the gold standard of PET reconstruction. However it has important limitations as it does not account for the stochastic variability in photon detection or degrading factors such as detector size or positron range (see Section 2.2.2.4). The use of FBP reconstruction has decreased over the years (P.E. Kinahan et al. 2004; Tong et al. 2010).

2.3.2.3 Statistic Model for PET Detection

The Poisson distribution is used to describe the probability of events occurring within a period of time at a certain rate, all events occurring independently. For PET acquisitions, the positron emission and the photon detection (within the photodetectors) are usually described as Poisson statistics. For each detector pair of a PET scanner, the number of coincidence events detected is a Poisson variable.

The likelihood $\mathcal{L}(\boldsymbol{g} \,|\, \lambda)$ describes the probability of a set of events $\boldsymbol{g}$ to occur for an emission distribution λ. For a Poisson distribution, it is given by:

$$\mathcal{L}(\boldsymbol{g} \,|\, \lambda) = \prod_{i=1}^{n_\mathrm{d}} \frac{\bar{g_i}^{g_i} \cdot \exp(-\bar{g_i})}{g_i!} \,, \tag{2.18}$$

where n_d is the number of detection bins, g_i is the number of events detected by a detection bin i, $\bar{g_i}$ is the expected number of events detected by the detection bin i, depending on the emission distribution λ (see following Equation (2.19)). In PET, a detection bin corresponds either to the set of events for a detector pair (in the non-TOF case) or to the set of events for a detector pair and a TOF bin (in the TOF case).

2.3.2.4 Iterative Emission Image Reconstruction

An iterative emission image reconstruction algorithm is a specific type of optimisation problem (Section 2.3.1), where an emission image is updated to fit a given cost function. Unlike the analytical reconstructions, these iterative methods can

take into consideration the statistical noise and the physical effects of the imaging system, which improves the reconstruction performance.

For a known emission distribution λ, when the system response $\boldsymbol{M}$ and the expected values of randoms $\bar{\boldsymbol{r}}$ and scatters $\bar{\boldsymbol{s}}$ are given, we can calculate the expected value for the projection data:

$$\bar{\boldsymbol{g}} = \boldsymbol{M}\lambda + \bar{\boldsymbol{r}} + \bar{\boldsymbol{s}}\,, \tag{2.19}$$

where for a detection bin i

$$M_i\lambda = \int_\Omega \lambda(\boldsymbol{r})\, m_i(\boldsymbol{r})\, \mathrm{d}\boldsymbol{r}\,,$$

$\Omega \subset \mathbb{R}^3$ is a compact set for the field of view of the scanner and $m_i : \mathbb{R}^3 \to \mathbb{R}^+$ is the system response function corresponding to the detection bin i.

When the distribution is discretised as $\boldsymbol{\lambda} = [\lambda_j]_{j\in[\![1,n_\mathrm{v}]\!]}$ (as introduced in Section 2.3.1.3), the previous equation 2.19 becomes for a projection data of a detection bin i:

$$\bar{g}_i = \sum_{j=1}^{n_\mathrm{v}} M_{ij}\lambda_j + \bar{r}_i + \bar{s}_i\,, \tag{2.20}$$

where M_{ij} is the element (i,j) of the system matrix $\boldsymbol{M}$ and $\bar{g}_i$ (respectively $\bar{r}_i$, $\bar{s}_i$) is the i-th element of $\bar{\boldsymbol{g}}$ (respectively $\bar{\boldsymbol{r}}$, $\bar{\boldsymbol{s}}$), i.e., its value for the detection bin i.

M_{ij} is the probability that a pair of unscattered photons created in a voxel j is detected by the detector bin i, and incorporates the attenuation and all detection uncertainties. $\boldsymbol{M}$ can be factorised as: (Qi et al. 1998; Leahy and Qi 2000a)

$$\boldsymbol{M} = \boldsymbol{M}_\text{sensitivity} \cdot \boldsymbol{M}_\text{blurring} \cdot \boldsymbol{M}_\text{attenuation} \cdot \boldsymbol{M}_\text{geometry} \cdot \boldsymbol{M}_\text{positron range}\,, \tag{2.21}$$

where $\boldsymbol{M}_\text{sensitivity}$ and $\boldsymbol{M}_\text{blurring}$ are matrices to account for detector effects, $\boldsymbol{M}_\text{attenuation}$ is composed of the attenuation correction factors, as discussed in Part 2.2.4, $\boldsymbol{M}_\text{geometry}$ incorporates a geometrical mapping between the source and the data (the element (i,j) of $\boldsymbol{M}_\text{geometry}$ would correspond to the probability that a photon pair created in a voxel j is detected by the detector pair corresponding to the bin i in the absence of any attenuation or any blurring effects unrelated to detection) and $\boldsymbol{M}_\text{positron range}$ is a blurring matrix, accounting for positron range.

The operation of forward-projection of a 3D emission image relies in applying (2.19) to an emission $\boldsymbol{\lambda}$ image. Backprojection is the adjoint operator of forward-projection.

The likelihood (Equation (2.18)) is used in iterative reconstruction algorithms to define the optimisation cost function (Section 2.3.1). The most common scheme in PET is the "Maximum Likelihood estimation", in which $\mathcal{L}(\boldsymbol{g} \,|\, \boldsymbol{\lambda})$ is maximised to obtain an estimate of $\boldsymbol{\lambda}$, fitting the projection data.

As an alternative to maximising directly the likelihood $\mathcal{L}$, the log-likelihood L is generally used, as it is easier to take the derivative of a sum instead of a product and then maximise (log is a strictly increasing function on $\mathbb{R}^{+*}$):

$$L(\boldsymbol{g} \,|\, \boldsymbol{\lambda}) = \sum_{i=1}^{n_\mathrm{d}} g_i \log \bar{g}_i - \bar{g}_i \; . \tag{2.22}$$

Maximum-likelihood estimation in PET is most commonly of the form: $\hat{\boldsymbol{\lambda}}_\mathrm{ML} = \arg\max_{\boldsymbol{\lambda} \geq 0} L(\boldsymbol{g} \,|\, \boldsymbol{\lambda})$, imposing a non-negativity constraint on $\boldsymbol{\lambda}$, considering that radioactivity concentration cannot be negative.

The emission image estimate $\hat{\boldsymbol{\lambda}}_\mathrm{ML}$ is often updated using an "Expectation Maximisation" (EM) algorithm. Instead of maximising directly $L(\boldsymbol{g} \,|\, \boldsymbol{\lambda})$, the expected value $\mathbf{E}\left[L(\boldsymbol{g} \,|\, \boldsymbol{\lambda}) \,|\, \boldsymbol{g}, \hat{\boldsymbol{\lambda}}\right]$ is maximised, where $\hat{\boldsymbol{\lambda}}$ is an estimate of $\boldsymbol{\lambda}$. At an iteration k, the algorithm combines an Expectation (E) step, which computes $\bar{\boldsymbol{g}}^{(k)}$ from the previous estimate $\hat{\boldsymbol{\lambda}}^{(k-1)}$, and a Maximisation (M) step, which provides a new estimate $\hat{\boldsymbol{\lambda}}^{(k)}$ via maximisation of the expected value of the log-likelihood $L(\boldsymbol{g} \,|\, \hat{\boldsymbol{\lambda}}^{(k-1)})$ (Dempster et al. 1977; Shepp and Vardi 1982; Lange and Carson 1984). Because of the non-negativity constraint on $\boldsymbol{\lambda}$, in the absence of any *a priori* estimation, $\hat{\boldsymbol{\lambda}}^{(0)}$ is generally initialised as a matrix of 1s. These iterative algorithms are known as MLEM. For a Poisson log-likelihood, the standard MLEM algorithm can be simplified as:

$$\begin{aligned} \hat{\lambda}_j^{(k+1)} &= \frac{\hat{\lambda}_j^{(k)}}{\sum_{i=1}^{n_\mathrm{d}} M_{ij}} \sum_{i=1}^{n_\mathrm{d}} M_{ij} \frac{g_i}{\bar{g}_i^{(k)}} \\ &= \frac{\hat{\lambda}_j^{(k)}}{\sum_{i=1}^{n_\mathrm{d}} M_{ij}} \sum_{i=1}^{n_\mathrm{d}} M_{ij} \frac{g_i}{\sum_{l=1}^{N} M_{il} \hat{\lambda}_l^{(k)} + r_i + s_i} \end{aligned} \tag{2.23}$$

This is a special case of gradient-based optimisation (Section 2.3.1), where the cost

function to maximise is $L(\boldsymbol{g} \,|\, \boldsymbol{\lambda})$. The update rule is here multiplicative, as we can write $\boldsymbol{\lambda}^{(k+1)} = \boldsymbol{\lambda}^{(k)} \Delta\big(\boldsymbol{\lambda}^{(k)}\big)$, where $\Delta\big(\boldsymbol{\lambda}^{(k)}\big) = \frac{1}{\sum_{i=1}^{n_\mathrm{d}} M_{ij}} \sum_{i=1}^{n_\mathrm{d}} M_{ij} \frac{g_i}{\bar{g}_i^{(k)}}$.

Note that for projection data with TOF bins, a detection bin is often noted as $g_{i,t}$ where i now corresponds to the detector pair and t the TOF bin, and in the previous Equation (2.23), the sum over $i \in [\![1, n_\mathrm{d}]\!]$ is replaced by a double sum over $\{i, t\} \in [\![1, D]\!] \times [\![1, T]\!]$, where D is the number of detector pairs (i.e., LORs) and T is the number of TOF bins, and in this case $g_i = \sum_{t=1}^{T} g_{i,t}$.

In the case of realistic data, the MLEM methods yield noisy reconstructed images and converge slowly. In PET, the iteration is usually terminated early to have a good trade-off between acceptable noise level and quantitative values (see Chapter 5). A smoothing filter is also usually applied to the reconstructed images. (Llacer 1993; Johnson 1994)

To overcome the problem of slow convergence, the use of "ordered subsets" within the reconstruction was introduced in 1994 (Hudson and Larkin 1994) and clinically validated in 1997 (Hutton, Hudson, and Beekman 1997). In this type of algorithms, the projection data is "binned" into different ordered subsets (which are commonly chosen to be disjoint) and the MLEM algorithm is applied for each of these subsets in a specific order. In practice, subsets are taken in terms of sets of LORs/detector pairs, however other schemes exist. Provided there are not too many subsets, this strategy speeds up the reconstructions, without impacting much on the quantification or detectability (Morey and Kadrmas 2013). It is now used as a clinical routine. This type of iterative reconstruction is referred as ordered subsets expectation maximisation (OSEM) and accelerate the process by about B times compared with MLEM (B is the number of subsets). If more than 2 subsets are used in OSEM, the reconstruction will however not converge to a single solution but to a limit cycle (Mettivier et al. 2011).

Some reconstruction algorithms allow negative values in the reconstructed images, such as Erlandsson et al. 2001; Bousse, Courdurier, et al. 2020. Although the radioactivity distribution cannot be negative physically, allowing the algorithm to locally reconstruct negative values can improve the problems linked with biases in low-activity regions, especially in the presence of a "hot" surrounding area.

In order to control the noise level within the PET reconstructions, in lieu of

early stopping and/or filtering the reconstructed images, the log-likelihood can be penalised with a prior (Fessler and Hero 1995; De Pierro 1995; Fessler 1994). Instead of maximising the log-likelihood $L(\boldsymbol{g}\,|\,\boldsymbol{\lambda})$, the penalised-likelihood (PL) algorithms will maximise $\Phi(\boldsymbol{\lambda})$:

$$\Phi(\boldsymbol{\lambda}) = L(\boldsymbol{g}\,|\,\boldsymbol{\lambda}) - \beta R(\boldsymbol{\lambda})$$

where $L(\boldsymbol{g}\,|\,\boldsymbol{\lambda})$ was defined in Equation (2.22) and $R(\boldsymbol{\lambda})$ is the regularisation penalty (or prior), with a penalty weight β.

The regularisation penalty can be written as:

$$R(\boldsymbol{\lambda}) = \sum_{j=1}^{n_\mathrm{v}} \sum_{k \in \mathcal{N}_j} w_{jk} V(\lambda_j, \lambda_k)\,, \tag{2.24}$$

where n_v is the number of image voxels, w_{jk} are weights related on the distance between the two voxels j and k, $\mathcal{N}_j$ is the neighbourhood of a voxel j and V is the penalty function. $R(\boldsymbol{\lambda})$ is usually chosen to penalise absolute differences between pixels in a neighbourhood. Three penalties will be of interest here:

- the quadratic penalty (Mumcuoğlu et al. 1996):

$$R(\boldsymbol{\lambda}) = \sum_{j=1}^{n_\mathrm{v}} \sum_{k \in \mathcal{N}_j} w_{jk} \left(\lambda_j - \lambda_k\right)^2 . \tag{2.25}$$

- Relative difference (RD) penalty (Nuyts et al. 2002):

$$R(\boldsymbol{\lambda}) = \sum_{j=1}^{n_\mathrm{v}} \sum_{k \in \mathcal{N}_j} w_{jk} \frac{\left(\lambda_j - \lambda_k\right)^2}{(\lambda_j + \lambda_k) + \gamma|\lambda_j - \lambda_k|} . \tag{2.26}$$

- smoothed total variation penalty (Rudin et al. 1992): (differentiable total variation) For α a smoothing parameter, we have:

$$R(\boldsymbol{\lambda}) = \sum_{j=1}^{n_\mathrm{v}} \sqrt{||\nabla\lambda_j||_2^2 + \alpha^2}, \quad \alpha > 0\,, \tag{2.27}$$

where $||\cdot||_2$ is the $\mathcal{L}_2$-norm and $\nabla\lambda_j$ the gradient of λ at a voxel j. $\nabla\lambda_j$ is usually approximated with finite differences between λ_j and voxels in $\mathcal{N}_j$. We will use forward differences in this work (cf. Section 4.5.2).

Modified versions of MLEM and OSEM can be implemented using those priors. In this work, two versions will be used:

- "De Pierro modified MLEM/OSEM" (De Pierro 1995), which utilises surrogates within the image reconstruction. It requires concave priors, for which a "surrogate" can be found. This (separable) surrogate function is indeed simpler to optimise but will mathematically lead to the same optimum in the optimisation. This will be referred as "modified OSEM" hereafter.

- Block sequential regularized expectation maximization (BSREM) (De Pierro et al. 2001; Ahn et al. 2003), which only needs the gradient of the penalty function, therefore is more generally applicable than the previous modified OSEM.

2.3.2.5 Implementation of Reconstruction Algorithms

Several software packages allow to reconstruct projection or listmode data, either via analytical or iterative reconstruction algorithms. In the case of iterative reconstruction, the scanner type must be known, and the user needs to provide the reconstruction parameters (reconstruction scheme, number of iterations, subsets, sub-iterations, optional filters, etc.).

In the following work, two software packages will be used to reconstruct the data: on one hand the open-source STIR and on the other hand a MATLAB implementation relying on proprietary GE projectors (Appendix B).

2.3.3 Image Registration

Image registration is a processing technique which aims to spatially align a set of images to a single referential. It is usually based on optimisation (Section 2.3.1), and considers two images: one of the two images is deformed in order to increase correspondences with the second "target" image. The images can be from the same modality (for example CT-CT or PET-PET) or from different modalities (for example PET-CT).

The deformation can be rigid (e.g., rotation and translation) or non-rigid (including compression, dilation, etc.). Several similarity functions are commonly used in medical imaging, to register the images either based on voxel similarity measures (assuming there is a relation between the two image intensities) or on geometrical

features (e.g., from the extraction of points/surfaces). In this work, all deformation fields are parameterised using cubic B-splines (see Section 4.5.1).

For a voxel-similarity measure, we can write the objective function Ψ as a function of f_1, f_2, φ, where f_1 is the "target" image, f_2 is the "moving" image and φ is the deformation transforming f_2 to f_1. Two objective functions for image registration will be of interest here:

- Sum of Squared Differences (SSD) (Hill et al. 2001):

$$\Psi(f_1, f_2, \varphi) = \frac{1}{N} \sum_{\boldsymbol{r}_n \in \Omega_\varphi} \left(f_1(\boldsymbol{r}_n) - f_2(\varphi(\boldsymbol{r}_n))\right)^2 .$$

  where r_n is a voxel of f_1 and N is the number of elements in the voxel overlap domain Ω_φ between the (discretised) target image and the (discretised) moving image transformed by φ. When the two images are from the same modality and only differs by Gaussian noise (i.e., $\forall \boldsymbol{r} \in \Omega_\varphi$, $f_2(\varphi(\boldsymbol{r})) = f_1(\boldsymbol{r}) + \eta$, where η is a random variable with a Gaussian distribution), SSD-based registration provide robust results. However, when global or local intensity changes between the two images can be observed, it might not provide good deformation fields (Hill et al. 2001). This cost function will be used for the in-house registration of monomodality images of Chapter 4.

- Normalised Cross Correlation (NCC):

$$\Psi(f_1, f_2, \varphi) = \frac{\sum_{\boldsymbol{r}_n \in \Omega_\varphi} (f_1(\boldsymbol{r}_n) - \bar{f}_1)(f_2(\varphi(\boldsymbol{r}_n)) - \bar{f}_2)}{\sqrt{\sum_{\boldsymbol{r}_n \in \Omega_\varphi} (f_1(\boldsymbol{r}_n) - \bar{f}_1)^2 \sum_{\boldsymbol{r}_n \in \Omega_\varphi} (f_2(\varphi(\boldsymbol{r}_n)) - \bar{f}_2)^2}} ,$$

  where $\bar{f}_1$ (respectively $\bar{f}_2$) is the mean value of image $\boldsymbol{f}_1$ (respectively $\boldsymbol{f}_2 \circ \varphi$) in Ω_φ. A modified version of this cost function – local normalised cross correlation (LNCC) (Cachier et al. 2003) – is used for lung image registration within NiftyReg (Modat et al. 2010) for lung registration of clinical data corresponding to the Coagulation Study (Section 6.4.1). It differs from the standard NCC measure by the use of a moving window function (usually Gaussian) within the cost function, thereby computing local measures.

Both cost functions will be discussed in more details in Section 4.6.3 of Chapter 4.

In contrast to PET image reconstruction, the stochastic nature of the data used to generate the images is often not taken into account in the cost functions used for image registration. This will be further discussed in Chapter 4.

Other types of cost function include histogram-based registration (via joint histograms of image intensities, usually for multi-modality registration) or feature-based (Hill et al. 2001; Oliveira et al. 2014). They will not be discussed in this thesis.

2.3.4 Compartmental Modelling

Although static scans are the standard clinical procedure in PET, the measures obtained from the reconstructed images cannot give any information on the radiotracer uptake rate and even standardised measures, such as the most commonly used measure SUV which takes into account the patient weight and the injected activity, are prone to large uncertainties (Fletcher and P.E. Kinahan 2010). Another technique in PET, which we refer as a "dynamic" acquisition, acquires short time frames to characterise the change of radiotracer concentration over time in a tissue (Lammertsma 2017b). From these data, it is possible to achieve better quantitative measures using a "kinetic analysis" approach (Castell and Cook 2008).

A compartment model is based on the decomposition of a physiological system into a number of "compartments", each of them representing a simplified component of the radiotracer transport and binding process.

The change of tracer concentration in one of the compartments is related to the concentrations in all other compartments, i.e., $\forall i \in [\![0, n]\!]$, where $n+1$ is the number of compartments, there is a linear function Φ_i such as:

$$\frac{\mathrm{d}C_i(t)}{\mathrm{d}t} = \Phi_i(C_0(t), C_1(t), ..., C_n(t))$$

By convention, when there is a blood input to the model, the first compartment (0) is the plasma (or blood) compartment, and $C_0(t)$ is its concentration of tracer at a time t. It is usually referred as the input function (IF), and $C_0(t)$ will be noted $\mathrm{IF}(t)$ in the following.

A representation of a compartmental model comprising a sequence of compartments is given in Figure 2.5. The rate constants $K_1, k_2, \ldots, k_n$ represent unidirec-

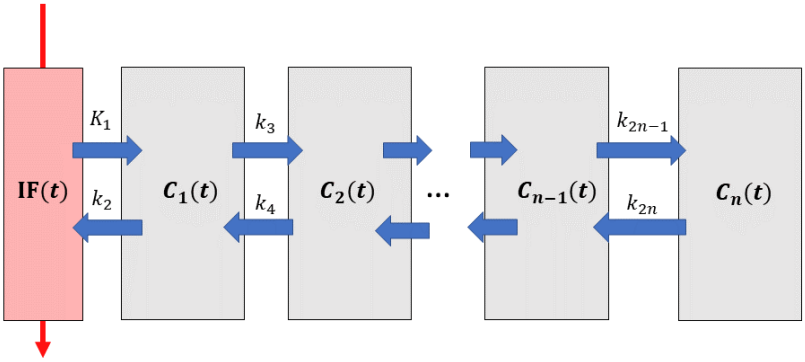

Figure 2.5: Representation of a sequential compartmental model

tional transport of the tracer from one compartment to another (where K_1 is the rate from the plasma or blood compartment to the first tissue compartment). It is to note that, although not as common, other configurations exist.

If we use Laplace transforms to solve the system, for a plasma IF, we obtain a general solution $C_{\text{ROI}}(t)$, the concentration of a ROI at a time t, such as: (Gunn et al. 2001; Gunn et al. 2002)

$$C_{\text{ROI}}(t) = V_{\text{B}} \cdot \text{IF}(t) + (1 - V_{\text{B}}) \sum_{i=1}^{n} \phi_i e^{-\theta_i t} \otimes \text{IF}(t) \tag{2.28}$$

where:

$$\begin{cases} n \text{ is the number of compartments.} \\ \phi_i \text{ is the weighting factor for a compartment } i. \\ \theta_i \text{ is the clearance parameter for a compartment } i. \\ \text{IF}(t) \text{ is the input function at a time } t. \\ \otimes \text{ is the convolution operator.} \end{cases}$$

The clearance parameters $\{\theta_i\}_{i \in [\![1,n]\!]}$ can be expressed in terms of the rate constants $\{k_i\}_{i \in [\![1,n]\!]}$.

Fitting dynamic PET values to a given compartment model corresponds usually in finding a set of kinetic parameters such that the optimisation minimises

$$\sum_{t \in \Psi} (C_{\text{ROI}}(t) - [\text{ROI}]_t)^2$$

where Ψ corresponds to the set of frame mid-times of the dynamic PET acquisition and $[\text{ROI}]_t$ is the average activity concentration in the ROI at time t. Details on kinetic parameters for some compartment models are provided in Appendix A.

2.4 Challenges of PET in the Lungs

Comparatively to other regions in the body, imaging the lung in PET suffers more largely from uncertainties and artefacts. Some aspects will be introduced here and discussed in following chapters.

2.4.1 Patient Motion

Three main types of motion can affect a PET acquisition: respiratory, cardiac and involuntary (bulk) motion. A lung acquisition is highly affected by patient motion, as all three types occur during the acquisition time. Cardiac motion (due to heartbeats) is expected not to impact much PET images for pulmonary investigations, when not in close proximity to the mediastinum, therefore it will not be investigated here. The issue of respiratory motion will be addressed in details in Chapters 4 and 6.

2.4.2 Complex Composition of the Lung

Whereas tissue accounts for about 95% of the brain with most of the remaining 5% being blood, the lung has a more diverse composition, which needs to be taken into account especially in the case of pulmonary diseases inducing composition changes. As previously described in a review co-led by UCL (Chen et al. 2017), the lung is composed of air, blood and "tissue" (defined as anything in the lung except air and blood). Any potential increased build-up of collagen will be included in the "tissue" component in this work.

2.4.2.1 Disease-dependent and Locally-variant Composition

The review in Chen et al. 2017 gives a diverse composition of the lung in the presence of different pulmonary pathologies:

The results in Figure 2.6 are shown for the whole lung. However, it does not represent the local changes in the fibrotic area of the lung of an IPF patient, especially since the fibrotic areas take up only a fraction of the lung volume, the local changes are expected to be much higher there. In previous work (Holman 2017), two regions (either normal-appearing or fibrotic) were defined, using a thresholding mask determined on CT and subsequent manual editing. The fractions of air, blood

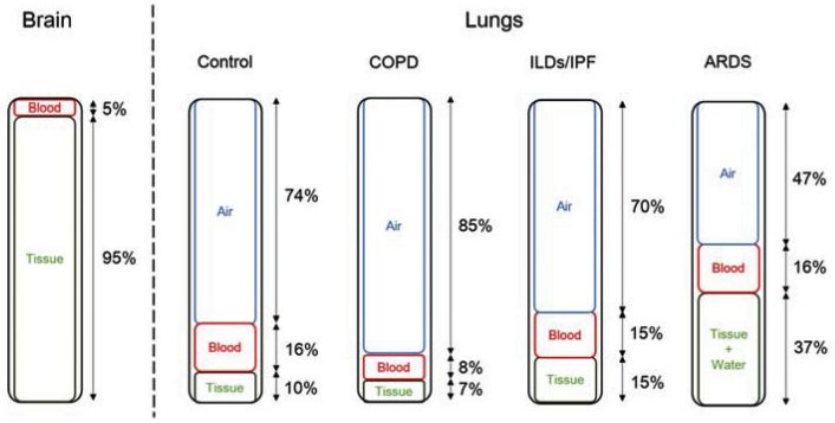

Figure 2.6: Fractions of air, blood and tissue in the whole lung for healthy, COPD, ILD/IPF and Acute Respiratory Distress Syndrome (ARDS) on average during respiration, compared to the brain (Chen et al. 2017).

Table 2.1: Fractions of air, blood and tissue in the different regions of the IPF lung (Holman 2017)

Fraction (%)	Air	Blood	Tissue
Normal-appearing	70	15	15
Fibrotic	40	16	44

and tissue proved quite different (see a summary of the results in Table 2.1), resulting from the major structural change in the fibrotic region of the IPF lungs and the increased build-up of collagen.

2.4.2.2 Varying Composition and Positron Range

The varying composition in the lung affects positron range, as introduced in Section 2.2.2.1.

The lower the density, the longer the positron range, and because air has a very low density compared to the other components of the lung, its fraction has a direct effect on the positron range. This issue will be assessed in details in Chapter 3.

2.4.2.3 Tissue Fraction Effect in the Lung

As discussed previously, the lung is in fact composed of multiple components, the main one being air. The composition is changing on a microscopic level, so the images in PET show an average activity in a voxel of all the lung components.

We can decompose the radiotracer concentration in a lung voxel C_{Lung} as:

$$C_{\text{Lung}} = V_{\text{A}} \cdot C_{\text{A}} + V_{\text{B}} \cdot C_{\text{B}} + V_{\text{T}} \cdot C_{\text{T}} \tag{2.29}$$

where V_A is the fractional air volume, C_A the concentration of radiotracer in the air in the lung, V_B the fractional blood volume, C_B the concentration of radiotracer in the blood, V_T the fractional tissue volume and C_T the concentration of radiotracer in the tissue.

Considering $C_A = 0$ (no activity in the air component) and $V_A + V_B + V_T = 1$, one can simplify the previous Equation (2.29) with:

$$C_{\text{Lung}} = V_B \cdot C_B + (1 - V_A - V_B) \cdot C_T \tag{2.30}$$

If the activity of the lung tissue needs to be estimated, it is necessary to determine the fractional volumes V_A and V_B, as well as C_B.

If one wants to dissociate the fraction of air in a voxel, i.e., compute V_A, it is possible to derive its value directly from the CT image (Lambrou et al. 2011b):

$$\text{HU}_{\text{Lung}} = V_A \cdot \text{HU}_A + V_{\text{Lung}\backslash\text{Air}} \cdot \text{HU}_{\text{Lung}\backslash\text{Air}} \tag{2.31}$$

where HU_{Lung} is the measured lung density in Hounsfield units, $V_{\text{Lung}\backslash\text{Air}}$ and $\text{HU}_{\text{Lung}\backslash\text{Air}}$ are respectively the fractional volume and the density in Hounsfield units of everything in the lung except the air.

As $V_A + V_{\text{Lung}\backslash\text{Air}} = 1$ and $\text{HU}_A = -1000$, under the assumption that the density of everything in the lung except air is close to the one of the thoracic muscle in IPF, i.e., $\text{HU}_{\text{Lung}\backslash\text{Air}} \approx 45$ (Yilmaz et al. 2011), the previous equation can be rearranged as:

$$V_A \approx \frac{\text{HU}_{\text{Lung}} + 1000}{1045} \tag{2.32}$$

2.5 Current Imaging Techniques of IPF

2.5.1 High Resolution CT

High-resolution CT (HRCT) is considered to be the reference standard for ILD patients. The structures in the lung parenchyma, supported by some histology, provides information on the pathology and its origin. Figure 2.7 shows an axial view of an HRCT acquisition for an IPF patient of the Coagulation Study cohort (Section 6.4.1).

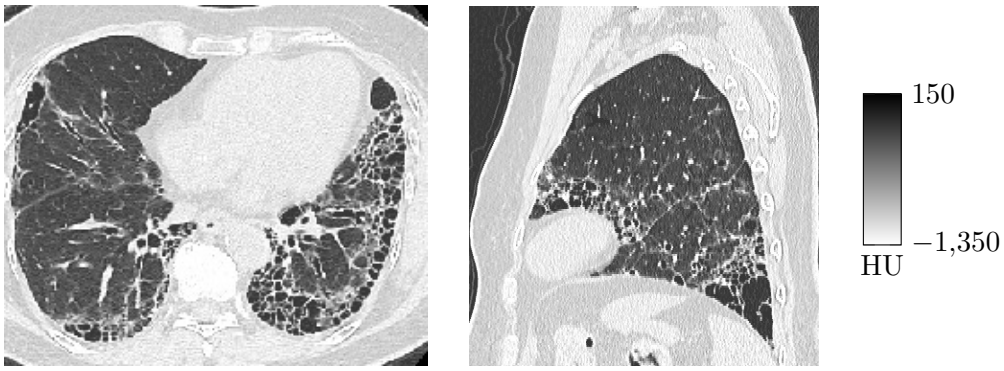

(a) Axial view **(b)** Sagittal view

Figure 2.7: (a) Axial and (b) sagittal views of an HRCT acquisition for an IPF patient of the Coagulation Study cohort (Section 6.4.1), showing honeycombing at the base of the lungs and near the heart.

The pathological areas are usually situated at the base of the lungs (Spagnolo et al. 2015), as can be visualised in Figure 2.7.

2.5.1.1 PET Radiotracers under Consideration for IPF

- ^{18}F-FDG: As introduced in Section 2.2.1.2, FDG images glucose consumption within the body. In addition to tumours, FDG can be used to image inflammation, as activated neutrophils have a higher glucose metabolism (Jones et al. 1998; Jones et al. 2002). Studies on IPF patients have shown an increased concentration in regions where fibrosis was observed on the CT image (Groves et al. 2009; Inoue et al. 2009; Win et al. 2012a).

- ^{18}F-Fluoromisonidazole, or "FMISO": The radiotracer was used to image the distribution of hypoxia in tumours (Bruehlmeier et al. 2004), due to its lipophilic nature, it diffuses through the cell membranes in a high-oxygen environment, but gets trapped within the cell when the fraction of oxygen is not sufficient (Thorwarth et al. 2005). In the case of tumours, hypoxia (i.e., lack of oxygen) is a factor of poor survival for the patients. In IPF lungs, there is an overexpression of a hypoxia-inducible factor-1 (HIF-1α), activated in presence of hypoxia. HIF-1α has been shown to accelerate wound healing, and its mechanism could be essential to understand IPF pathogenesis, and could be used in the treatment of IPF (Ruthenborg et al. 2014; Tzouvelekis et al. 2014).

- ^{18}F-Fluciclatide: This tracer targets angiogenesis (i.e., the formation of new

blood vessels), and has shown promising results in oncology (Sharma et al. 2015), as angiogenesis is essential for tumour growth. It is also present in other pathologies, including wound repair. The tracer targets integrins, which participate in the adhesion of the new tumour vasculature to the extracellular matrix (see Gaertner et al. 2012).

- ^{18}F-Proline: Its active molecule, proline, is an amino acid found in collagen, which is the main constituent of the extracellular matrix in IPF. Even though it showed promising results in rabbits, a study with IPF human patients did not show any changes between fibrotic and non-fibrotic areas of the lungs (Wallace et al. 2002; Lavalaye et al. 2009).

- ^{68}Ga-PSMA: The tracer targets tumour neovasculature, mainly for prostate cancer (see Chang et al. 1999; Wang et al. 2015). Accidental findings on patients demonstrating both IPF and lung cancer have shown an increased uptake in the fibrotic areas, as for FDG, and this tracer might be investigated within the institute for IPF.

2.5.2 Static FDG PET Results

Groves et al. 2009 showed increased FDG uptake in fibrotic regions versus normal-appearing regions for ILD patients (including IPF cases). They concluded that there was a increased glucose metabolism in both ground-glass and honeycombing (as visualised in the HRCT). The pulmonary FDG uptakes were correlated with global health score and other physiological measurements.

The increase in FDG uptake was also visually confirmed for the patients from the Coagulation Study (Section 6.4.1), as can be seen in Figure 2.8.

However, Lambrou et al. 2011b and Holman et al. 2015 demonstrated that the previous results should be interpreted with caution, as the lung has a very diverse composition, which varies throughout fibrotic and normal-appearing regions (discussed in Section 2.4.2.1). This leads to varying tissue fraction effect, which could potentially change the interpretation of measures taken from a PET study. Figure 2.9 shows the differences in perceived SUVs when no correction is applied compared to SUVs with air only or air and blood fraction correction.

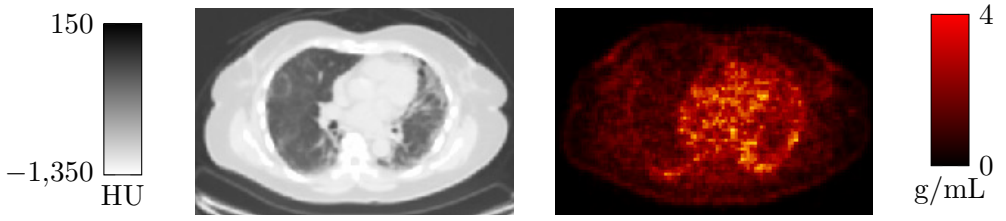

Figure 2.8: Apparent FDG uptake increase in fibrotic lung compared to normal-appearing lung in an axial view of (a) CT image versus (b) PET image, for one patient of the Coagulation Study cohort (Section 6.4.1).

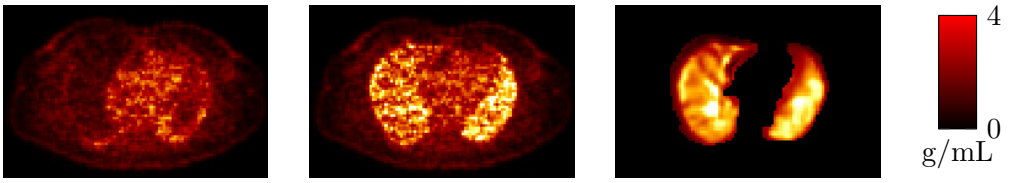

Figure 2.9: Axial views of the reconstructed PET image (a) with no correction, (b) with air fraction correction and (c) with air and blood fraction correction (only computed in the lung), for one patient of the Coagulation Study cohort (Section 6.4.1).

2.5.3 Dynamic PET Studies

For IPF patients, studies have shown that using FDG kinetic analysis can help to understand the mechanism of lung injury (Schroeder et al. 2008; Schroeder et al. 2011; Dittrich et al. 2012). Kinetic parameters of interest include the influx rate constant K_i or the delivery rate of the tracer from the plasma or blood to the first compartment K_1 (related to perfusion).

Using kinetic analysis can also provide information on the fractional blood volume, in order to correct an important component of the Tissue Fraction Effect (see Section 2.4.2.3). Holman 2017 determined that it was necessary to incorporate a voxel-wise time delay dt for IPF, as the travel arrival in normal-appearing or fibrotic lungs can be very different. In the initial stage of this PhD, a validation study was performed on porcine data to derive the blood volume fractions in the lung using a reversible 1-tissue compartment model (against a gold standard technique). The results are presented in Appendix A.

2.5.4 Combining Static and Dynamic PET Results

Recalling Formula (2.30), when V_{A}, V_{B} and C_{B} are known, it is possible to determine C_{T}, the concentration in radioactivity in the lung tissue (defined as everything but air and blood).

$$C_{\mathrm{T}} = \frac{C_{\mathrm{Lung}} - V_{\mathrm{B}} \cdot C_{\mathrm{B}}}{1 - V_{\mathrm{A}} - V_{\mathrm{B}}} \,, \tag{2.33}$$

where C_{Lung} is the radioactivity in the static PET image, V_{B} is determined from compartmental modelling applied to the dynamic images, V_{A} from a given CT image corresponding to the static referential and C_{B} is the blood concentration (which can be approximated by using a time activity curve (TAC) in a blood vessel, e.g., the descending aorta).

In order to apply Formula (2.33), it is required to either maintain the patient on the scanner bed for the entire study (from the injection to the end of the dynamic acquisition) or to register the dynamic images to the static images.

IPF patients corresponding to the Coagulation Study (Section 6.4.1) and other IPF studies within our institute were allowed to get off the bed between the dynamic and static acquisitions, in order to stretch and relax, to prevent discomfort of severely ill patients. The CT images (acquired before the dynamic and static acquisitions) are therefore aligned using image registration (Section 2.3.3) to align the PET results.

2.5.5 Current Caveats and Limitations in the Analyses

The precise origin of the increased or decreased uptake in the fibrotic lung compared to normal-appearing lung is yet to be fully understood. A possible source of misquantification could arise from high positron range in the lung. This will be studied in Chapter 3.

Additionally, the pathological regions of the IPF lungs being predominantly situated in basal lungs, i.e., near the diaphragm where large respiratory motion is appreciated, IPF quantification measures (arising from both static and dynamic studies) are highly affected by motion. Although some techniques can help to diminish the impact of motion on the measures (to minimise the impact of data misalignment between PET and the attenuation map, see Chapter 4), currently (to the author's knowledge) no motion-compensating technique has been applied in PET studies of IPF. This further complicates the realignment of dynamic and static re-

sults, discussed in Section 2.5.4, especially when two separate days of acquisitions (or more) are used to follow the progression of a disease.

A previously developed strategy for IPF in terms of motion compensation used in our clinical settings is only linked to reducing the artefacts linked to misalignment between the attenuation map and PET data (AC mismatch will be discussed in Chapter 5). An averaging attenuation map is computed from as many attenuation maps as possible to reduce quantitative errors. More details are given in following Section 4.3.1. Such a method however does not address two critical points:

- The displacement of tissues and organs, especially near the diaphragm, resulting in blurring/mis-localisation.
- The difficulty of realigning two different PET acquisitions.

Using such averaged CT image also cannot solve the issue raised in Section 2.5.4 related to aligning results from dynamic and static acquisitions. A more robust method to correct for motion is necessary in the Coagulation Study (more information in Section 6.4.1), where "post-treatment" measures are compared to "pre-treatment" measures. Doing such analysis involves several image registrations, which ultimately propagate errors.

Respiratory motion in PET imaging will be discussed and addressed in Chapters 4 and 6 of this thesis, where motion-compensating methods for image registration and reconstruction will be proposed.

Chapter 3

Evaluation of Positron Range in the Diseased and Normal Lungs

3.1 Introduction

PET images are meant to be a representation of the tissue radioactivity concentration. However as discussed in Part 2.2.2.1, the measured PET data do not actually correspond to the locations of the positron emission (hence, the actual radioactivity location), but to the locations of the annihilation events (Lehnert et al. 2011; Derenzo 1979). PET images are indeed formed using the detection of annihilation γ photons. A few methods exist to compensate for positron range, some will be introduced in Section 3.2.2.

In many tissues and with the most common radionuclides, the positron range effect is relatively small compared to other sources of image degradation (Moses 2011). However, for low-density regions, such as the lung, it has a larger effect and could potentially be important for some tracers. The study of positron range in this work is motivated by the premise of clinical studies using novel radiotracers, for which the effect of positron range is mostly unknown. For example, a seemingly significant specific uptake in the fibrotic lung of IPF patients was observed clinically on ^{68}Ga-PSMA images. The specificity of this uptake needs to be determined in order to discard false positives. As discussed in Section 2.4.2.1, the architecture of an IPF lung is very diverse. This introduces spatially-varying Tissue Fraction Effect (Section 2.4.2.3), which might indicate a higher percentage of lung parenchyma rather than a specific uptake in the fibrotic parenchyma. These differences will need to be investigated. Such a varying lung composition should also lead to spatially-

varying positron range effect on the images. Although some studies of positron range in heterogeneous media exist (B. Bai et al. 2003; Szirmay-Kalos et al. 2012; Rahmim et al. 2008; Cal-González et al. 2015), they are usually limited to simple boundaries.

Contrary to Section 2.4.2.3, in this chapter we will refer to lung "tissue" as being everything in the lung except the air, similarly as in Lambrou *et al.* (Lambrou et al. 2011a), i.e., we will neglect the blood component (the blood mass density should be close to the one of the lung parenchyma).

Several radionuclides will be studied here: ^{18}F, ^{68}Ga, ^{82}Rb, ^{15}O, ^{89}Zr, ^{64}Cu and ^{124}I. Besides ^{18}F, ^{68}Ga is increasingly used to label biological ligands such as DOTATATE which targets somatostatin receptors. Another example is prostate-specific membrane antigen (^{68}Ga-PSMA) which targets tumour neovasculature and has shown promising results, mainly for prostate cancer but also more recently in the lung (Chang et al. 1999; Wang et al. 2015). ^{68}Ga has the disadvantage of having a larger positron range than ^{18}F. ^{82}Rb or ^{15}O are less commonly used in PET lung imaging, however these can be used to evaluate perfusion, for example of lung tumours. Other radionuclides of recent interest in PET are ^{89}Zr, ^{64}Cu and ^{124}I which, because of their relatively long half-life, are potentially useful for imaging lung cancers using radiolabelled monoclonal antibodies, for which the circulation half-life is generally on the order of days (Reichert and Valge-Archer 2007).

This chapter is organised as follows. We briefly discuss the effect of positron range in uniform media, then describe the Monte Carlo methodology of this chapter in detail. Last, we present results of the effect of positron range in the lungs, in the presence of small high-density structures within the healthy lung, such as tumour, localised fibrosis or blood vessels.

This chapter is largely based on Emond et al. 2019.

3.2 Theory and Methodology

3.2.1 Radionuclide-Dependent and Spatially-Variant Properties

The probability of annihilation increases as the kinetic energy of the positron decreases due to collisions with electrons. The positron range depends therefore on the initial kinetic energy of the positron at emission and the density and composition of the media crossed by the positron before it annihilates. Its effect on the overall resolution is usually small for ^{18}F, the clinically most commonly used radionuclide.

However, the resolution degradation linked to positron range is greater for radionuclides emitting higher energy positrons and in tissues of low density, such as the lung. Estimated values will be given for some common radionuclides in Table 3.2.

Whereas the density of healthy lungs is relatively uniform (aside from airways and blood vessels), some pulmonary diseases can affect local structure and density, for example in the case of lung cancer or interstitial lung diseases such as IPF. In these cases, the effect of positron range is spatially variant and image quantification can be impacted. In order to establish whether a local apparent increase in radioactivity corresponds to a specific tracer uptake, the effect must be studied carefully.

In this chapter, we will focus on two pathologies that can modify the lung architecture: lung cancer and IPF. Usually, lung tumours have a density close to that of soft tissue ($\approx 1\,\mathrm{g}\cdot\mathrm{cm}^{-3}$, Xu et al. 2008), whereas the rest of the lung has a far lower density ($\approx 0.26\,\mathrm{g}\cdot\mathrm{cm}^{-3}$). This means that there is usually an abrupt change of density at the interface of the tumour with the rest of the lung. In the case of IPF, the fibrotic regions of the lungs have an increased density compared to the healthy parts of the lungs. Localised high-density structures, such as honeycombing, increase in extent as disease progresses (Spagnolo et al. 2015).

3.2.2 Compensating Methods for Positron Range

If we consider a positron-emitting point source, the probability of annihilation can be expressed as a 3D distribution. The image corresponding to the annihilation events ("annihilation image") can be viewed as the convolution by a blurring kernel of the image corresponding to the positron emission events ("emission image").

In absence of any magnetic field, in isotropic media, the positron range distribution is isotropic. For this reason, a 1D blurring kernel q linked to positron range was introduced in Derenzo 1979 to describe the 3D annihilation density p at a point $\boldsymbol{r}$ over a volume $\mathcal{V}$, assuming we have an emission density λ:.

$$p(\boldsymbol{r}) = \iiint_{\mathcal{V}} q(\|\boldsymbol{r}'\|)\lambda(\|\boldsymbol{r}-\boldsymbol{r}'\|)\,\mathrm{d}\boldsymbol{r}' \tag{3.1}$$

where $\|\cdot\|$ is the Euclidean norm in $\mathbb{R}^3$. More generally, in uniform media, previous work on estimating positron range involved computation of 1D or 2D annihilation range distributions from the actual distribution (Blanco 2006; Levin and Hoffman

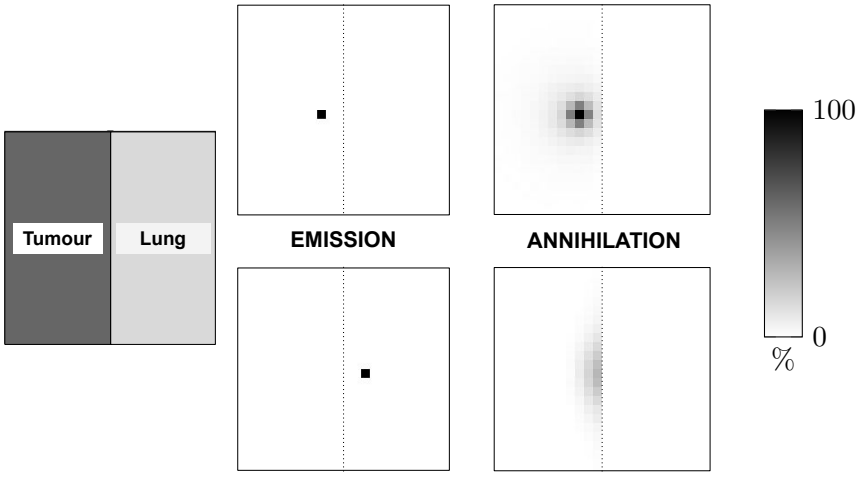

Figure 3.1: Illustration of positron range effect for a radioactive ^{82}Rb emission source placed in close proximity (6 mm) to an abrupt density change, showing the number of emission and annihilation events - emission either in the tumour (top) or in the (healthy) lung (bottom). The annihilation images (image size of $72 \times 72 \times 72\,\text{mm}^3$ with voxel of size: $3 \times 3 \times 3\,\text{mm}^3$) were scaled to 1% of the total number of emitted positrons ($\approx 918,000$ for both simulations).

1999; Derenzo 1979; Cal-González et al. 2010; L. Jødal et al. 2012; Cal-González et al. 2013). Although using one of the previous methods is satisfactory in a relatively uniform medium, it may be inaccurate in highly heterogeneous media or near a boundary between two regions with very different densities. In fact, a noticeable difference compared to a homogeneous medium is that the centre of gravity for activity is not located at the emission source point, i.e. a shift occurs. We illustrate this here with a boundary between a high-density medium and a low-density medium (tumour and healthy lung), obtained from a GATE (Jan et al. 2004) Monte Carlo simulation (see later in this chapter for more details), in Figure 3.1. In non-homogeneous tissue, the positron range can be modelled using spatially-variant anisotropic kernels. A good model should take into account the difference of densities in a neighbourhood. Several strategies already exist (B. Bai et al. 2003; Szirmay-Kalos et al. 2012; Alessio and MacDonald 2008; Cal-González et al. 2015), but have not been validated in humans and may not be applicable to heterogeneous lungs or for all radionuclides. Furthermore it might be impractical in clinical settings due to rather lengthy processing.

Another possibility for non-homogeneous media is to use Monte Carlo simulations (Lehnert et al. 2011) to obtain the positron range distribution via simulations

of all possible physical interactions given a radioactivity distribution. The latter are also computationally expensive and unsuitable for routine use, but represent a gold standard to assess the effect of positron range on PET images.

(3.2)

3.2.3 Monte Carlo Simulation Settings

In this work, we used GATE (version 8.2), Monte Carlo simulation software dedicated to medical imaging (Jan et al. 2004), to simulate the effect of positron range in the lung. GATE is based on the GEANT4 toolkit (version 10.5.1), which simulates the particle behaviour through physical matter (Agostinelli et al. 2003); the GATE physics list "*empenelope*" accounts for most of the physical interactions involved in PET imaging to obtain an accurate model of the path an emitted positron takes before annihilating with an electron, including multiple scattering, ionisation, annihilation or production of bremsstrahlung. The energy distribution function, for a single β^+ transition, can be approximated as (Levin and Hoffman 1999):

$$N(E)\,\mathrm{d}E = p\,F(Z-1,E)\left(1+\frac{E}{0.511}\right)(E_{\max}-E)^2\,\mathrm{d}E \tag{3.3}$$

where:

- Z is the atomic number of the mother nucleus, prior beta decay.
- E is the kinetic energy of the positron in MeV.
- $E_{\max}$ is the maximum kinetic energy for the radionuclide, in MeV.
- $p = \sqrt{\left(1+\frac{E}{0.511}\right)^2 - 1}$ is the momentum of the positron.
- $F(Z,E) = \frac{2\pi\eta}{1-e^{-2\pi\eta}}$ is the Fermi function, where:
  - $\eta = -\frac{Z\alpha}{p} \times (1+\frac{E}{0.511})$, for positron decay.
  - $\alpha \approx 1/137$ the fine-structure constant, used in fundamental physics.

Mathematica (Wolfram Research 2017) was used to obtain histograms corresponding to the energy distribution of the studied radionuclides, using the values of Z and $E_{\max}$ in Table 3.1. Whereas the decay schemes of ^{18}F, ^{15}O, ^{68}Ga, ^{89}Zr, ^{64}Cu

Table 3.1: Maximum kinetic energy and atomic number of the studied PET radionuclides (Bé et al. 2016; Brookhaven National Laboratory 2019)

Radionuclide	$E_{\max}$	Z
^{18}F	0.635	9
^{64}Cu	0.653	29
^{89}Zr	0.902	40
^{15}O	1.723	8
^{68}Ga	1.899	31
^{124}I (1)	1.535	53
^{124}I (2)	2.138	53
^{82}Rb (1)	2.605	37
^{82}Rb (2)	3.381	37

are simple (only one β^+ transition), ^{82}Rb and ^{124}I have several β^+ transitions. For both radionuclides, the previous formula 3.3 was applied to the two transitions with the highest probabilities to create a total energy distribution as a weighted sum of the separate energy spectra. The resulting energy spectra are shown in Figure 3.2. The histogrammed spectra were incorporated in GATE as user-defined spectra.

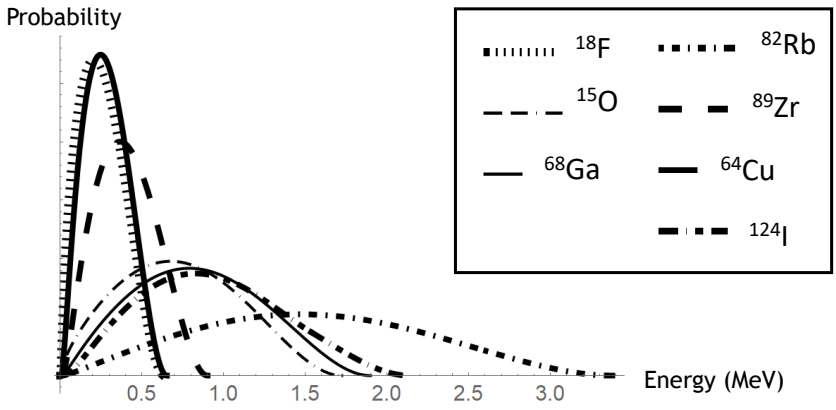

Figure 3.2: Positron emission energy spectra for the different radioisotopes of this study

Simple point source simulations in water were performed to assess the validity of the settings by calculating the mean and maximal positron ranges (R_{mean} and $R_{\max}$ respectively) from the GATE output, see Table 3.2. The values were in good agreement with Lehnert et al. 2011 for both ^{18}F and ^{15}O, as well as with other more sophisticated positron range models, although slightly lower.

In addition to the definition of radioactive sources, "materials" need to be defined in GATE to create the simulation phantom. These are defined by the physical elements comprising them, their fractions, as well as their corresponding mass density. The default GATE material database comprises only one "Lung" material,

Table 3.2: Positron ranges estimated and in literature, in water for the studied radionuclides.

	Estimated		Literature	
Radionuclide	R_{mean} (mm)	R_{max} (mm)	R_{mean} (mm)	R_{max} (mm)
^{18}F	0.44	2.31	0.48[a],0.57[b],0.6[c]	2.27[a],1.85[b],2.6[c]
^{64}Cu	0.51	2.54	0.56[d]	2.9[d]
^{89}Zr	0.87	3.76	1.27[d]	4.2[d]
^{15}O	2.00	8.01	2.21[a],2.34[b],2.5[c]	7.96[a],7.70[b],9.1[c]
^{68}Ga	2.39	9.57	2.69[b],2.9[c]	8.86[b],10.3[c]
^{124}I	2.70	10.57	3.4[d]	11.7[d]
^{82}Rb	5.03	16.80	5.33[b],5.9[c]	17.6[b],18.6[c]
a: Lehnert et al. 2011, b: Cal-González et al. 2010, c: L. Jødal et al. 2012, d: Jødal et al. 2014				

which corresponds to the average composition and density of 'normal' lung. A material corresponding to a malignant lung tumour was added to the database with an average CT value of 11 ($\approx 1.028\,\text{g}\cdot\text{cm}^{-3}$, Xu et al. 2008) (see C.1). In the case of the fibrotic lung, as its composition is spatially variant depending on the degree of fibrosis, the material database was modified to incorporate a range of fibrotic lung materials, that correspond to lung tissues between $-800\,\text{HU}$ ($\approx 0.26\,\text{g}\cdot\text{cm}^{-3}$, healthy lung) to $-200\,\text{HU}$ ($\approx 0.615\,\text{g}\cdot\text{cm}^{-3}$, severely fibrotic lung), with a step of $50\,\text{HU}$ ($\approx 0.3\,\text{g}\cdot\text{cm}^{-3}$). This was achieved by creating first a "lung tissue" GATE material (corresponding to "everything but the blood and air in the lung"), from the lung fractions for the normal-appearing lung given in Chen et al. 2017—also in Table 2.1—and the "Blood", "Lung" and "Air" materials pre-defined in the GATE database. Intermediary fibrotic lung materials are then defined by interpolating the lung fraction values between the normal-appearing and the fibrotic lungs. The details of the fibrotic lung materials are given in C.2.

3.2.4 Additional Factors Affecting Resolution in PET

Aside from positron range, PET resolution also depends on other factors such as detection uncertainties, acolinearity or the reconstruction method (Moses 2011, as introduced in Section 2.2.2.4). The typical spatial resolution for a clinical scanner, characterised for a very small object source in air comparable to a point source (negligible positron range effect), is approximately 5 mm (Bettinardi et al. 2011; Jakoby et al. 2011; Kolthammer et al. 2015). In addition, postfiltering is generally used in PET reconstruction. In clinical practice, a Gaussian postfilter of FWHM

$\approx 6\,\text{mm}$ is typically applied, resulting in a global spatial blurring that we can model via a normal distribution of FWHM equal to $\sqrt{5^2+6^2} \approx 8\,\text{mm}$. In the following simulations, the raw results will be either filtered via a Gaussian filter of FWHM 5 mm or 8 mm to be able to study the effect of positron range on quantification of reconstructed images in more realistic conditions.

3.2.5 Simulation Processing

From the output from a GATE Monte Carlo simulation, the locations of all positron emission events and the locations of all annihilation events were recorded.

The emission events corresponding to annihilations occurring outside of the phantom were discarded. In our simulations, the "emission image" $\boldsymbol{E}$ and "annihilation image" $\boldsymbol{A}$ are computed. These two images were either used directly or postfiltered in order to mimic measures on PET reconstructed images (see Section 3.2.4), using two different Gaussian filter FWHM: 5 mm (unfiltered reconstructed images) and 8 mm (filtered reconstructed images). From these images, the "apparent recovery ratio" α of a volume-of-interest (VOI) can be computed, measuring the increase or decrease in activity within the volume due solely to positron range and postfiltering (if any). In a VOI $\mathcal{V}$, we denote:

$$\alpha_{\mathcal{V},i} = \frac{A_{\mathcal{V},i}}{E_{\mathcal{V},i}} \tag{3.4}$$

where $A_{\mathcal{V},i}$ (respectively $E_{\mathcal{V},i}$) is the mean number of events in the annihilation image (respectively the emission image) within $\mathcal{V}$, after postfiltering with a Gaussian of FWHM i mm. In addition to the apparent recovery ratio, the "apparent contrast" $\mathcal{C}_{\mathcal{V}_1/\mathcal{V}_2,i}$, defined as the ratio of $A_{\mathcal{V}_1,i}$ and $A_{\mathcal{V}_2,i}$ is calculated to compare the uptake of a VOI $\mathcal{V}_1$ to that of a VOI $\mathcal{V}_2$, after a postfilter of FWHM i mm was applied on the images.

The same definitions are extended to ensembles of VOIs $\{\mathcal{V}_k\}_{k\in\mathbb{N}}$ and $\{\mathcal{W}_k\}_{k\in\mathbb{N}}$, where $\alpha_{\mathcal{V},i} = \overline{\alpha_{\mathcal{V}_k,i}}$ and $\mathcal{C}_{\mathcal{V}/\mathcal{W},i} = \sum_k \alpha_{\mathcal{V}_k,i} \Big/ \sum_k \alpha_{\mathcal{W}_k,i}$, in which $\overline{\cdot}$ represents the "mean" operator.

When comparing the effect of positron range between two complementary media (i.e. there are only two types of material in the simulation and all events are emitted and annihilated in either of those), we also compute the fraction $\mathcal{S}_{\mathcal{R}_1/\mathcal{R}_2}$ of the

number of emission events emitted from one medium $\mathcal{R}_2$ but annihilated in the other medium $\mathcal{R}_1$ over the number of emission events emitted from $\mathcal{R}_1$ but annihilated in $\mathcal{R}_2$. This measure will be described as the "spillover" ratio of $\mathcal{R}_1$ in $\mathcal{R}_2$. If the ratio is > 1 (resp. < 1), this means that the apparent uptake of the entire $\mathcal{R}_1$ is overestimated (resp. underestimated) because of positron range effects.

3.3 Simulations

Two pulmonary pathologies were considered in this work, for which two different radioactivity distributions were simulated. The different phantoms and scenarios are presented in this section.

3.3.1 Simulations of a Spherical Lung Tumour of Variable Radius

Spherical tumours ($d = 1.028\,\mathrm{g \cdot cm^{-3}}$) with three different diameters (10 mm, 20 mm and 30 mm) were simulated in the normal lung ($d = 0.26\,\mathrm{g \cdot cm^{-3}}$). The VOIs corresponding to the tumours are denoted as $\mathcal{T}_{10}$, $\mathcal{T}_{20}$ and replaced$\mathcal{T}_{30}\mathcal{T}_3$ (corresponding to diameters of 10 mm, 20 mm and 30 mm, respectively). The images of annihilation and emission were computed using voxels of dimension $1 \times 1 \times 1\,\mathrm{mm^3}$.

3.3.2 Simulations of a Fibrotic Lung

A diagnostic CT image volume from an IPF patient (see Section 6.4.1) was used to perform a realistic simulation of a fibrotic lung. The latter was obtained from a GE Discovery 690, multislice helical CT acquisition at breathhold covering 27.5 cm with a 1.25 mm slice thickness and a pitch of 0.516, with 120 kVp, 149 mA and 0.6 s revolution time. The image was segmented into several fibrotic lung materials, according to their Hounsfield values (Section 3.2.3). The outside of the lung was considered as liquid water for the simulation (GATE default database: $d = 1\,\mathrm{g \cdot cm^{-3}}$). For computational reasons, the original CT image was cropped to a volume of $100 \times 100 \times 100\,\mathrm{mm^3}$ for the simulation. In order to avoid issues with border effects, the emission and annihilation events occurring near the edges of the input CT image were not considered and the measurements were made within a volume of $60 \times 60 \times 60\,\mathrm{mm^3}$. A slice through the CT image is presented in Figure 3.3.

The images of annihilation and emission were computed using voxels of dimension $0.5 \times 0.5 \times 0.5\,\mathrm{mm^3}$ and were analysed using two VOI sizes - small

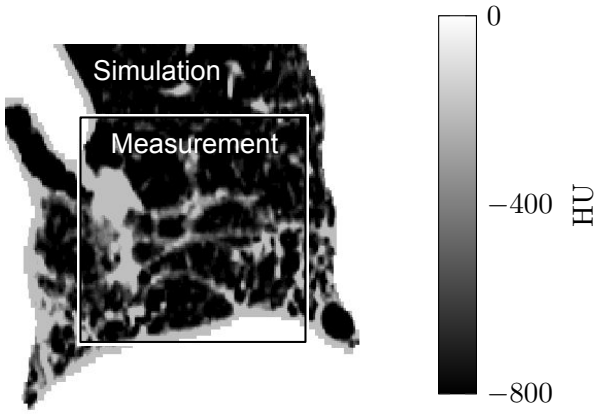

Figure 3.3: Coronal view of the density image used in the simulation showing the simulation volume (all image) and measurement volume (within the box).

($3 \times 3 \times 3\,\mathrm{mm}^3$) and medium-sized ($9 \times 9 \times 9\,\mathrm{mm}^3$) – at 20 locations – determined on the density map:

* 10 predominantly normal lung
  - small VOIs "$\mathcal{N}_1$": mean density ± standard deviation = $0.263 \pm 0.016\,\mathrm{g \cdot cm^{-3}}$
  - medium-sized VOIs "$\mathcal{N}_2$": mean density ± standard deviation = $0.274 \pm 0.045\,\mathrm{g \cdot cm^{-3}}$
* 10 predominantly fibrotic lung
  - small VOIs "$\mathcal{F}_1$": mean density ± standard deviation = $0.574 \pm 0.171\,\mathrm{g \cdot cm^{-3}}$
  - medium-sized VOIs "$\mathcal{F}_2$": mean density ± standard deviation = $0.431 \pm 0.224\,\mathrm{g \cdot cm^{-3}}$

3.3.3 Radioactivity Distributions

For each simulation presented above, two radioactivity distributions were assessed:

- *Scenario 1*: the radioactivity concentration is uniform throughout the whole lung.
- *Scenario 2*: the radioactivity concentration is uniform in the "tissue" (as defined here as everything in the lung except for the air) and that there is no radioactivity in the air. The resulting radioactivity concentration in each voxel

Table 3.3: Lung Tumour - Scenario 1 - Apparent recovery computed from the emission and annihilation images for the studied radionuclides in the tumour (diameters: 10 mm, 20 mm and 30 mm). $\alpha_{\mathcal{T}_k,i}$ is the apparent recovery for a tumour of diameter k mm, after a postfilter of FWHM i mm.

Radionuclide	$\alpha_{\mathcal{T}_{10},0}$	$\alpha_{\mathcal{T}_{10},5}$	$\alpha_{\mathcal{T}_{10},8}$	$\alpha_{\mathcal{T}_{20},0}$	$\alpha_{\mathcal{T}_{20},5}$	$\alpha_{\mathcal{T}_{20},8}$	$\alpha_{\mathcal{T}_{30},0}$	$\alpha_{\mathcal{T}_{30},5}$	$\alpha_{\mathcal{T}_{30},8}$
^{18}F	1.116	1.029	1.011	1.060	1.018	1.010	1.040	1.013	1.007
^{64}Cu	1.146	1.041	1.017	1.073	1.024	1.014	1.049	1.017	1.010
^{89}Zr	1.292	1.097	1.042	1.147	1.059	1.036	1.098	1.041	1.027
^{15}O	1.766	1.348	1.179	1.403	1.224	1.157	1.269	1.156	1.115
^{68}Ga	1.918	1.434	1.229	1.490	1.284	1.203	1.329	1.199	1.149
^{124}I	2.072	1.525	1.284	1.497	1.290	1.209	1.379	1.237	1.182
^{82}Rb	2.705	1.915	1.513	2.038	1.717	1.550	1.718	1.520	1.421

is therefore obtained by multiplying with $1 - V_a$, where V_a is the air fraction in the lung medium (given in C.2).

The minimal numbers of emission/annihilation events retained are the following: (1) Lung Tumours: $\approx 2 \cdot 10^8$ for Scenario 1 and $\approx 5 \cdot 10^7$ for Scenario 2, (2) Fibrotic Lung: $\approx 8 \cdot 10^7$ for Scenario 1 and $\approx 3 \cdot 10^7$ for Scenario 2. In both scenarios, the neighbouring soft tissue does not have any radioactivity. For conciseness, only images corresponding to the simulations of ^{18}F, ^{68}Ga and ^{82}Rb will be shown. Note that ^{89}Zr and ^{64}Cu have similar energy spectra to ^{18}F and ^{15}O and ^{124}I to ^{68}Ga 3.2, therefore similar positron ranges.

In the case of the lung tumour simulations, in order to study the effect of the "background" level (i.e., the relative amount of activity in the healthy lung respectively to the tumour), intermediary apparent recovery values were found from the results of Scenario 1, by rescaling the annihilation and emission images corresponding to emission events occurring in the healthy tissue.

3.4 Results

3.4.1 Simulation of Spherical Lung Tumours

3.4.1.1 Scenario 1

The apparent recovery α measured from the different tumours $\mathcal{T}_{10}$, $\mathcal{T}_{20}$ and $\mathcal{T}_{30}$ for scenario 1 can be found in Table 3.3, including measures made before and after postfiltering.

Before any postfiltering, a halo can be seen on the outside edge of the tumour, see images corresponding to $\mathcal{T}_{20}$ in Figure 3.4. After postfiltering, the halo either

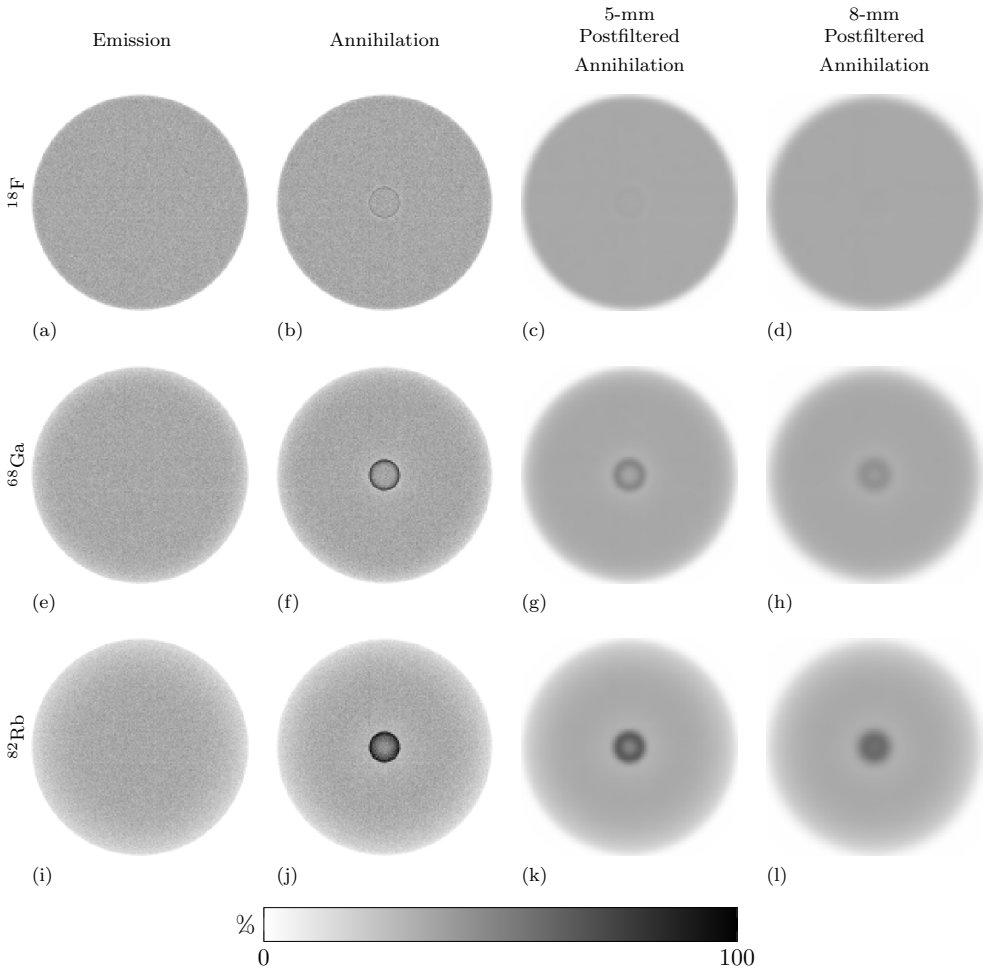

Figure 3.4: Lung Tumour (20 mm) - Scenario 1 - (a) (resp. (e), (i)) emission events, (b) (resp. (f), (j)) annihilation events, (c) (resp. (g), (k)) 5 mm postfiltered annihilation events and (d) (resp. (h), (l)) 8 mm postfiltered annihilation events computed for ^{18}F (top row) (resp. ^{68}Ga (middle row), ^{82}Rb (bottom row)). All images are scaled using the same colourbar (maximal value of the unfiltered ^{82}Rb annihilation image).

almost disappears (^{18}F, ^{89}Zr and ^{64}Cu) or is blurred out to appear as an increased uptake in the tumour compared to the healthy lung background (^{82}Rb, ^{124}I, ^{68}Ga and ^{15}O). The effect is amplified for ^{82}Rb where the tumour resembles a hot spot on the image.

The spillover ratios for the tumours $\mathcal{T}_{10}$, $\mathcal{T}_{20}$ and $\mathcal{T}_{30}$ in the background $\mathcal{N}$ are given in Table 3.4, where $\mathcal{N}$ represents the outside of the tumour, comprising normal lung.

All measures show that the shift of radioactivity from the outside of the tu-

Table 3.4: Lung Tumours - Scenario 1 - Spillover ratios corresponding to the tumour, computed from the emission and annihilation images for the studied radionuclides in the tumour (diameters: 10 mm, 20 mm and 30 mm). $\mathcal{T}_k$ represents the tumour of diameter k mm.

Radionuclide	$\mathcal{S}_{\mathcal{T}_{10}/\mathcal{N}}$	$\mathcal{S}_{\mathcal{T}_{20}/\mathcal{N}}$	$\mathcal{S}_{\mathcal{T}_{30}/\mathcal{N}}$
^{18}F	1.987	1.680	1.840
^{64}Cu	2.111	1.801	1.941
^{89}Zr	2.498	2.239	2.351
^{15}O	3.102	2.977	3.046
^{68}Ga	3.198	3.087	3.161
^{124}I	3.344	3.116	3.247
^{82}Rb	3.482	3.442	3.494

Table 3.5: Lung Tumours - Scenario 2 - Apparent recovery computed from the emission and annihilation images for the studied radionuclides in the tumour (diameters: 10 mm, 20 mm and 30 mm). $\alpha_{\mathcal{T}_k,i}$ is the apparent recovery for a tumour of diameter k mm, after a postfilter of FWHM i mm.

Radionuclide	$\alpha_{\mathcal{T}_{10},0}$	$\alpha_{\mathcal{T}_{10},5}$	$\alpha_{\mathcal{T}_{10},8}$	$\alpha_{\mathcal{T}_{20},0}$	$\alpha_{\mathcal{T}_{20},5}$	$\alpha_{\mathcal{T}_{20},8}$	$\alpha_{\mathcal{T}_{30},0}$	$\alpha_{\mathcal{T}_{30},5}$	$\alpha_{\mathcal{T}_{30},8}$
^{18}F	1.002	0.998	0.997	1.001	1.000	0.999	1.001	1.000	1.000
^{64}Cu	1.002	0.999	0.998	1.001	1.000	0.999	1.001	1.000	1.000
^{89}Zr	1.006	0.999	0.996	1.003	1.000	0.999	1.001	1.000	1.000
^{15}O	1.004	0.997	0.990	1.005	1.003	1.001	1.003	1.002	1.001
^{68}Ga	1.011	1.003	0.993	1.004	1.002	1.000	1.003	1.002	1.001
^{124}I	1.017	1.009	0.999	1.006	1.004	1.002	1.004	1.003	1.002
^{82}Rb	1.013	1.006	0.995	1.006	1.005	1.010	1.004	1.004	1.003

mours, that is low-density lung, to the tumour is greater than the opposite, i.e. the shift from the tumour to the normal lung.

3.4.1.2 Scenario 2

The recovery ratios were all close to 1 (with and without postfiltering), see in Table 3.5. The images for $\mathcal{T}_{20}$ are shown in Figure 3.5.

Visually the images for ^{18}F, ^{68}Ga and ^{82}Rb are almost identical. However, the measured values show that the effect observed in Scenario 2 is dominated by the "spill-out", i.e. there are more positrons emitted from the tumours that are annihilated in the normal lung than the opposite. This can be verified by computing, on the unfiltered images, the spillover ratios of the tumours. The results are given in Table 3.6 for all radionuclides (where $\mathcal{N}$ represents the outside of the tumour, comprising normal lung). The spillover ratios are indeed all inferior to 1.

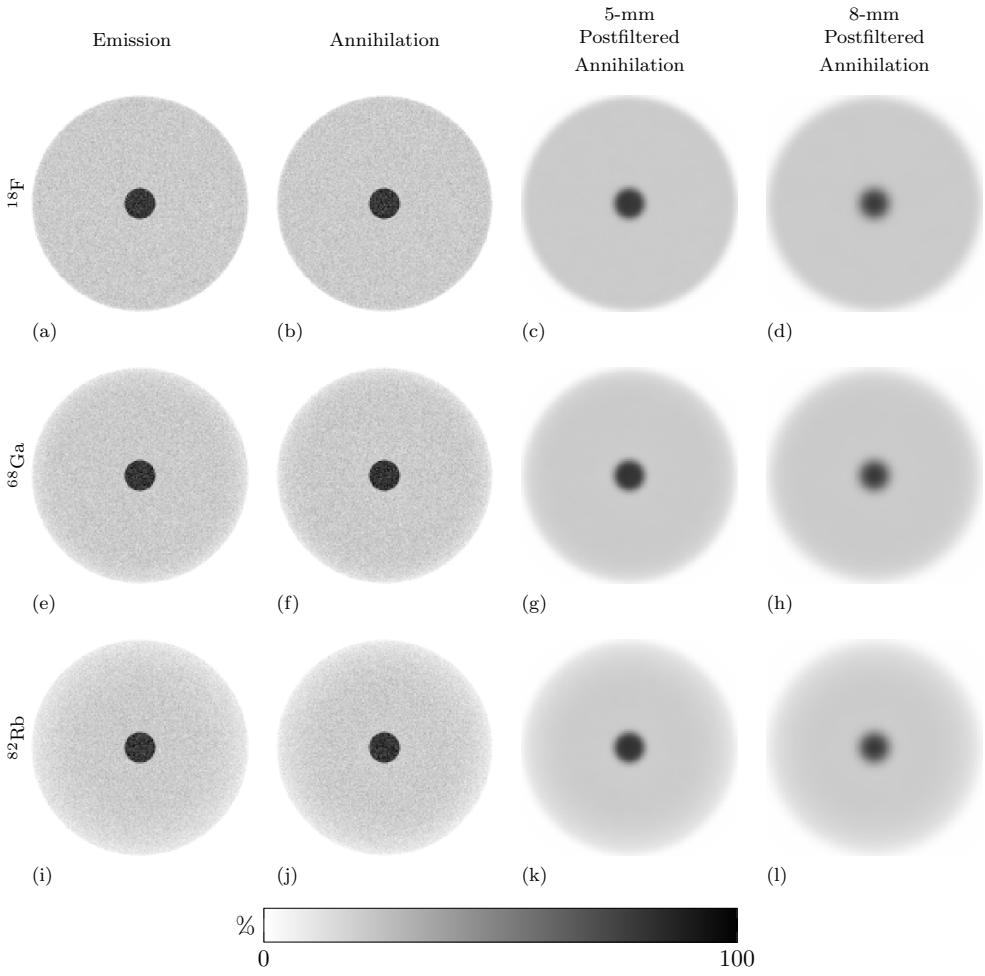

Figure 3.5: Lung Tumour (20 mm) - Scenario 2 - (a) (resp. (e), (i)) emission events, (b) (resp. (f), (j)) annihilation events, (c) (resp. (g), (k)) 5 mm postfiltered annihilation events and (d) (resp. (h), (l)) 8 mm postfiltered annihilation events computed for ^{18}F (top row) (resp. ^{68}Ga (middle row), ^{82}Rb (bottom row)). All images are scaled using the same colourbar (maximal value of the unfiltered ^{82}Rb annihilation image).

Table 3.6: Lung Tumours - Scenario 2 - Spillover ratios corresponding to the tumour, computed from the emission and annihilation images for the studied radionuclides in the tumour (diameters: 10 mm, 20 mm and 30 mm). $\mathcal{T}_k$ represents the tumour of diameter k mm.

Radionuclide	$\mathcal{S}_{\mathcal{T}_{10}/\mathcal{N}}$	$\mathcal{S}_{\mathcal{T}_{20}/\mathcal{N}}$	$\mathcal{S}_{\mathcal{T}_{30}/\mathcal{N}}$
^{18}F	0.523	0.441	0.480
^{64}Cu	0.556	0.469	0.504
^{89}Zr	0.660	0.588	0.612
^{15}O	0.800	0.775	0.793
^{68}Ga	0.843	0.805	0.821
^{124}I	0.865	0.827	0.844
^{82}Rb	0.904	0.897	0.911

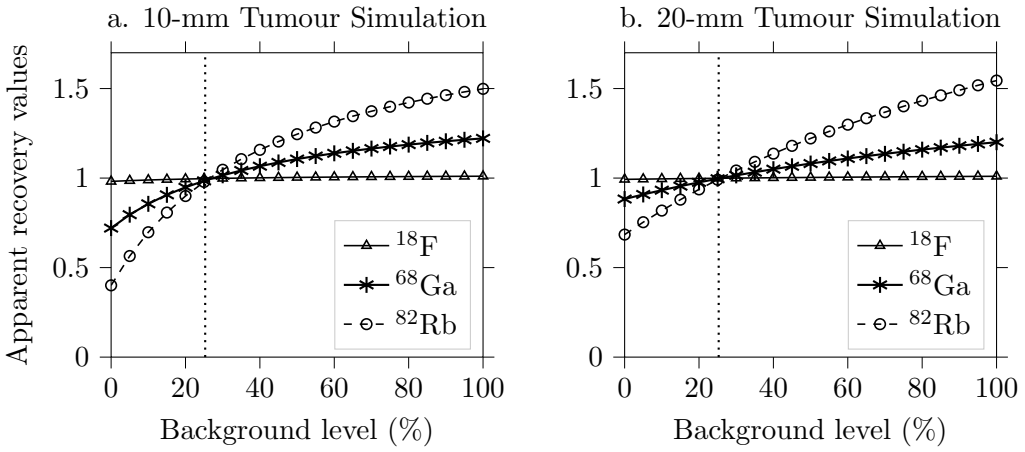

Figure 3.6: Plots showing the apparent recovery values (a.) $\alpha_{\mathcal{T}_{10},8}$ (tumour of diameter 10 mm) and (b.) $\alpha_{\mathcal{T}_{20},8}$ (tumour of diameter 20 mm), for different background levels (8-mm Gaussian postfiltering). The vertical dotted line indicates the threshold value for which the apparent recovery values are ≈ 1 for all radionuclides.

3.4.1.3 Intermediary Scenarios

The change of balance between spill-in and spill-out can be observed in Figure 3.6 (for ^{18}F, ^{68}Ga and ^{82}Rb and tumours of 10 mm and 20 mm). The plots show the apparent recovery values for different levels of activity in the healthy lung ("background") after a 8-mm postfilering. For this type of small tumours, it appears that the apparent recovery are ≈ 1 when $\lambda_{\mathcal{T}}/d_{\mathcal{T}} \approx \lambda_{\mathcal{N}}/d_{\mathcal{N}}$ (where $\lambda_{\mathcal{T}}$ (resp. $\lambda_{\mathcal{N}}$) is the activity concentration in the tumour (resp. the healthy lung) and $d_{\mathcal{T}}$ (resp. $d_{\mathcal{N}}$) is the mass density of the tumour (resp. the healthy lung)), i.e., which is equivalent to Scenario 2. Below that threshold (indicated by the vertical dotted line in Figure 3.6) the change in spill-in/spill-out fractions leads to a negative bias in the apparent recovery of the tumour. This is also the case for other radionuclides and tumour of 30 mm.

3.4.2 Simulation of a Fibrotic Lung

3.4.2.1 Scenario 1

The emission images and the unfiltered and filtered annihilation images for the seven studied radionuclides can be found in Figure 3.7, with the corresponding measures of apparent recovery and apparent contrast for different postfiltering in Tables 3.7 and 3.8.

This case is similar to Scenario 1 of the tumour simulations: when the ra-

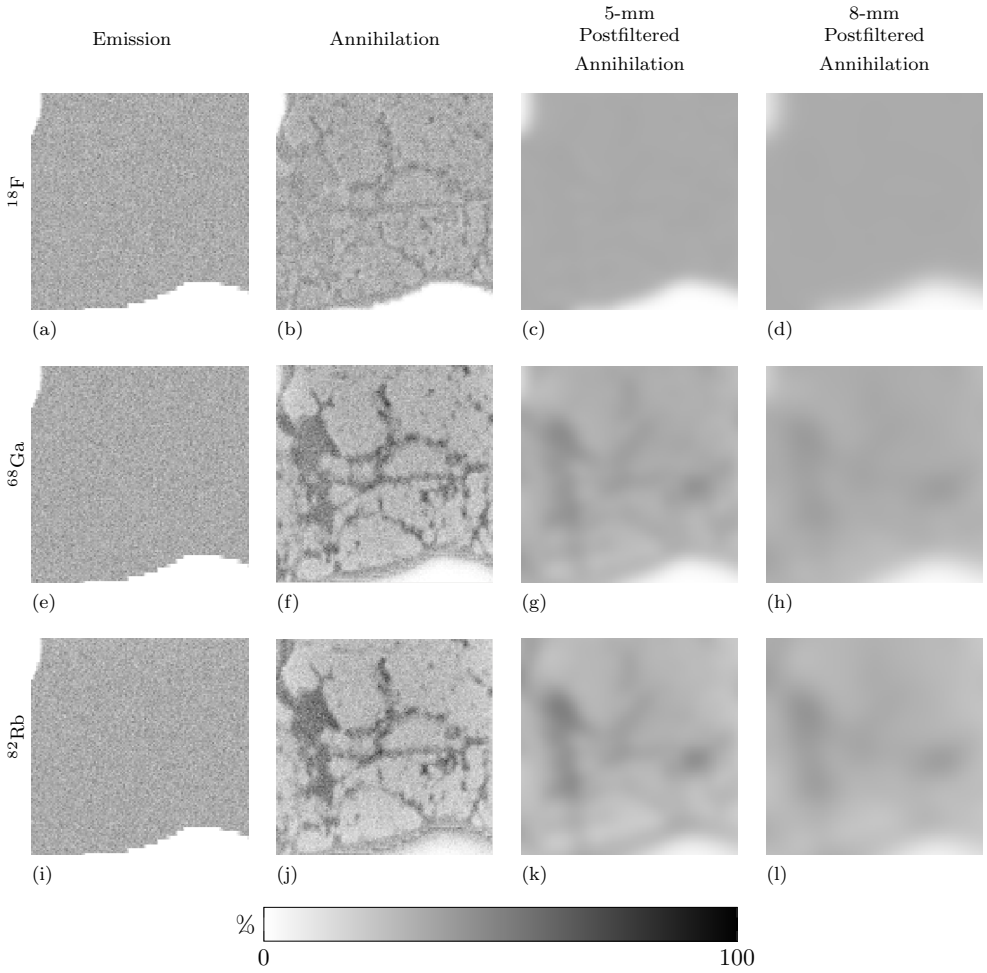

Figure 3.7: Fibrotic Lung - Scenario 1 - (a) (resp. (e), (i)) emission events, (b) (resp. (f), (j)) annihilation events, (c) (resp. (g), (k)) 5 mm postfiltered annihilation events and (d) (resp. (h), (l)) 8 mm postfiltered annihilation events computed for ^{18}F (top row) (resp. ^{68}Ga (middle row), ^{82}Rb (bottom row)). All images are scaled using the same colourbar (110% of the maximal value of the unfiltered ^{82}Rb annihilation image).

Table 3.7: Fibrotic Lung - Scenario 1 - Mean apparent recovery values computed from the original emission and annihilation images for all studied radionuclides. $\alpha_{\mathcal{V},i}$ is the apparent recovery for a VOI $\mathcal{V}$ (description in 3.3.2), after a postfilter of FWHM i mm.

Measure	^{18}F	^{64}Cu	^{89}Zr	^{15}O	^{68}Ga	^{124}I	^{82}Rb
$\alpha_{\mathcal{N}_1,0}$	0.987	0.970	0.976	0.924	0.918	0.896	0.820
$\alpha_{\mathcal{N}_2,0}$	0.997	0.995	0.987	0.953	0.942	0.927	0.850
$\alpha_{\mathcal{F}_1,0}$	1.073	1.089	1.196	1.513	1.515	1.557	1.619
$\alpha_{\mathcal{F}_2,0}$	1.016	1.022	1.049	1.168	1.166	1.182	1.172
$\alpha_{\mathcal{N}_1,5}$	0.995	0.992	0.984	0.948	0.937	0.921	0.848
$\alpha_{\mathcal{N}_2,5}$	0.997	0.995	0.989	0.959	0.948	0.933	0.858
$\alpha_{\mathcal{F}_1,5}$	1.026	1.035	1.075	1.195	1.224	1.247	1.248
$\alpha_{\mathcal{F}_2,5}$	1.010	1.014	1.031	1.094	1.109	1.119	1.097
$\alpha_{\mathcal{N}_1,8}$	0.997	0.996	0.990	0.961	0.951	0.937	0.863
$\alpha_{\mathcal{N}_2,8}$	0.998	0.997	0.992	0.965	0.956	0.942	0.868
$\alpha_{\mathcal{F}_1,8}$	1.010	1.014	1.087	1.116	1.101	1.111	1.087
$\alpha_{\mathcal{F}_2,8}$	1.006	1.008	1.051	1.051	1.059	1.063	1.028

Table 3.8: Fibrotic Lung - Scenario 1 - Mean apparent contrasts computed from the original emission and annihilation images for all studied radionuclides. $\mathcal{C}_{\cdot,i}$ is the apparent contrast between VOIs (description in 3.3.2), after a postfilter of FWHM i mm.

Measure	^{18}F	^{64}Cu	^{89}Zr	^{15}O	^{68}Ga	^{124}I	^{82}Rb
$\mathcal{C}_{\mathcal{F}_1/\mathcal{N}_1,0}$	1.073	1.103	1.195	1.511	1.581	1.645	1.862
$\mathcal{C}_{\mathcal{F}_2/\mathcal{N}_2,0}$	1.015	1.021	1.051	1.167	1.199	1.231	1.322
$\mathcal{C}_{\mathcal{F}_1/\mathcal{N}_1,5}$	1.028	1.039	1.082	1.232	1.272	1.312	1.419
$\mathcal{C}_{\mathcal{F}_2/\mathcal{N}_2,5}$	1.011	1.016	1.036	1.119	1.143	1.169	1.239
$\mathcal{C}_{\mathcal{F}_1/\mathcal{N}_1,8}$	1.011	1.016	1.083	1.116	1.139	1.163	1.230
$\mathcal{C}_{\mathcal{F}_2/\mathcal{N}_2,8}$	1.006	1.009	1.047	1.076	1.093	1.111	1.163

dioactivity is evenly distributed among the different lung types, the fibrotic parts of the lung (corresponding to the regions with higher density) appear to have higher radioactivity concentration than the normal lung.

3.4.2.2 Scenario 2

The emission images and the unfiltered and filtered annihilation images for the seven studied radionuclides can be found in Figure 3.8, with the corresponding measures of apparent recovery values for different amounts of postfiltering in Table 3.9. Similarly as Scenario 2 for the tumours, especially ^{82}Rb, the apparent recovery ratio values do not demonstrate a positive quantitative bias in the high-density medium (here the fibrosis) due to positron range, but a negative bias; this suggests that more positrons emitted from the fibrotic lung are annihilated in the normal lung than the opposite.

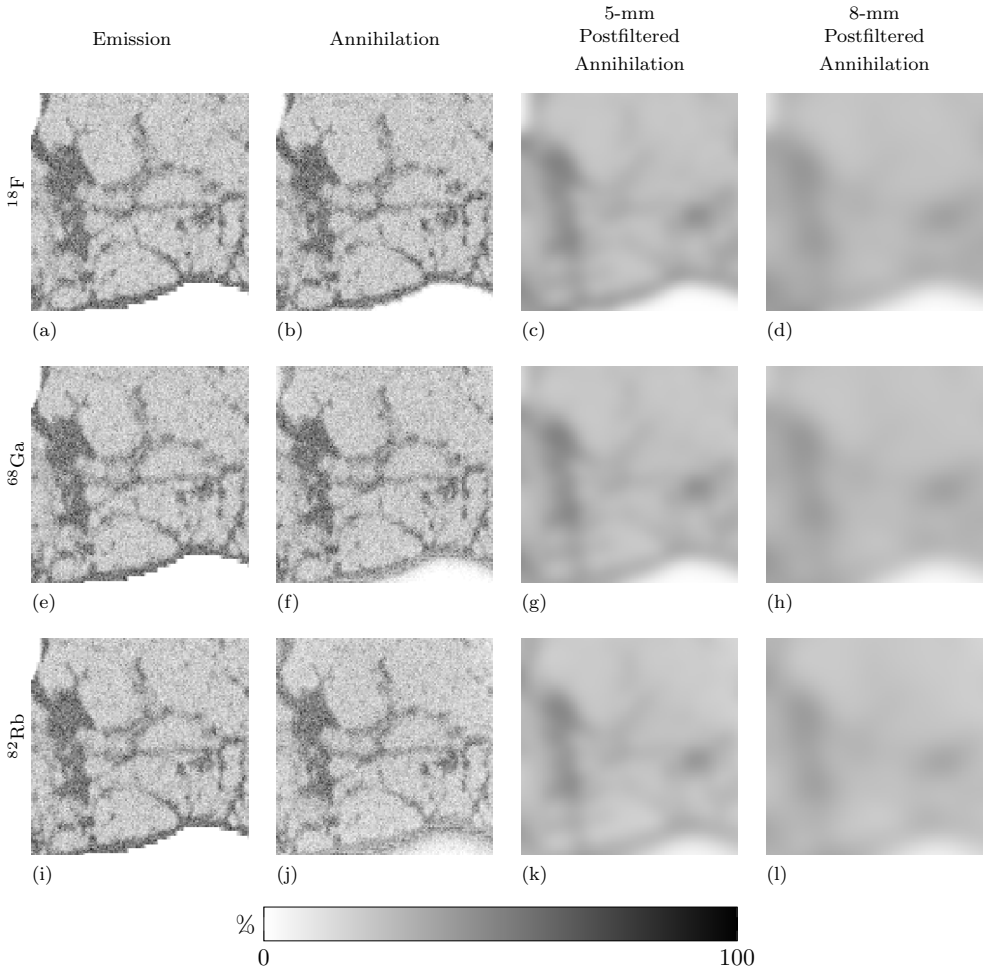

Figure 3.8: Fibrotic Lung - Scenario 2 - (a) (resp. (e), (i)) emission events, (b) (resp. (f), (j)) annihilation events, (c) (resp. (g), (k)) 5 mm postfiltered annihilation events and (d) (resp. (h), (l)) 8 mm postfiltered annihilation events computed for ^{18}F (top row) (resp. ^{68}Ga (middle row), ^{82}Rb (bottom row)). All images are scaled using the same colourbar (maximal value of the unfiltered ^{82}Rb annihilation image).

Table 3.9: Fibrotic Lung - Scenario 2 - Mean apparent recovery values computed from the original emission and annihilation images for all studied radionuclides. $\alpha_{\mathcal{V},i}$ is the apparent recovery for a VOI $\mathcal{V}$ (description in 3.3.2), after a postfilter of FWHM i mm.

Measure	^{18}F	^{64}Cu	^{89}Zr	^{15}O	^{68}Ga	^{124}I	^{82}Rb
$\alpha_{\mathcal{N}_1,0}$	1.003	1.001	1.006	1.014	1.002	1.009	0.975
$\alpha_{\mathcal{N}_2,0}$	1.000	1.000	1.001	1.005	1.002	1.000	0.966
$\alpha_{\mathcal{F}_1,0}$	1.011	1.004	1.009	1.006	1.000	0.993	0.956
$\alpha_{\mathcal{F}_2,0}$	1.001	0.999	0.999	0.995	0.991	0.987	0.939
$\alpha_{\mathcal{N}_1,5}$	1.001	1.001	1.002	1.007	1.002	1.001	0.968
$\alpha_{\mathcal{N}_2,5}$	1.000	1.000	1.001	1.003	1.001	0.999	0.964
$\alpha_{\mathcal{F}_1,5}$	1.001	1.000	0.999	0.995	0.989	0.984	0.938
$\alpha_{\mathcal{F}_2,5}$	1.000	0.999	0.999	0.995	0.991	0.986	0.936
$\alpha_{\mathcal{N}_1,8}$	1.000	1.000	1.001	1.003	1.000	0.999	0.963
$\alpha_{\mathcal{N}_2,8}$	1.000	1.000	1.001	1.001	1.000	0.998	0.959
$\alpha_{\mathcal{F}_1,8}$	1.000	0.999	0.999	0.993	0.988	0.982	0.932
$\alpha_{\mathcal{F}_2,8}$	1.000	1.000	0.999	0.994	0.990	0.984	0.932

3.5 Discussion and Conclusion

In this chapter, we have simulated in the lung two different scenarios. In the first scenario, the entire lung (comprising of healthy lung, lung tumour or fibrotic lung) was considered to have the same radioactivity concentration. In the second scenario, the air in the lung was assumed to contain no radioactivity, meaning the radioactivity was evenly distributed over the "tissue" in the lung (defined as "everything but the air" here). The latter scenario corresponds to the situation where the normal lung tissue has the same radiotracer uptake as the tumour or fibrotic tissue.

The results of the simulations show that, although positron range is usually perceived as a blurring effect, in heterogeneous media it should rather be considered as a more complex change in the apparent radioactivity distribution, as high-density structures are more likely to "capture" some of the activity from the neighbouring lower density structures, than the opposite.

In the case of a high-density tumour located within a healthy lung, a part of the activity of the surrounding low-density area will be transferred to the tumour ("spill-in"), as well as some activity from the tumour to the healthy lung ("spill-out"). In the first scenario (even distribution), the tumour will appear hotter on the PET images, as the spill-out is largely dominated by the spill-in. However, in the second scenario (air containing no radioactivity), the spill-out now balances the

spill-in, which leads to apparent recovery values ≈ 1. When varying the level of activity in the surrounding healthy lung (see Figure 3.6), the changes of spill-in and spill-out fractions lead to either positive or negative biases in the apparent recovery values. The radioactivity distribution of Scenario 2 acts as a "threshold": when the radioactivity of the healthy lung is lower than the one of Scenario 2, the recovery values will be negatively impacted, if higher, positively impacted. When there is no activity in the healthy lung, the observations are consistent with Kemerink et al. 2011, where a similar experiment was performed using syringes of various sizes containing activity in water (water density $\approx$ lung tumour density). They were placed in cellular polyethylene foam (density $0.164\,\mathrm{g}\cdot\mathrm{cm}^{-3}$) to mimic a healthy lung. As no background activity was used (therefore observing only spill-out from the syringe), only spill-out was observed, which led to a negative bias in the tumour recovery values.

The spill-in effect of the positron range is mostly noticeable at the edges of the tumour, with the "penetration depth" depending on the radionuclide and expected to be related to the "mean positron range in water", with $R_{\mathrm{mean}} \approx 5\,\mathrm{mm}$ for ^{82}Rb, i.e. half the radius). That implies that the spill-in effects need to be considered for structures of about twice the mean positron range – the magnitude depending on the radioactive concentration in the background. In this study, lung tumours were modelled with a uniform density and a spherical shape. The composition of a lung tumour is usually more diverse (e.g., with necrotic regions, see Travis et al. 2015) and could lead to more complex positron range effects.

The results from the simulation of a fibrotic lung show the same trend as for the tumour. In the first scenario (uniform distribution), a large bias in the apparent radioactivity of the fibrotic lung is observed (up to $\approx +61.9\%$ for unfiltered ^{82}Rb images), with a highly heterogeneous distribution overall. In the second scenario (air containing no activity), the apparent recovery ratio is slightly less than 1 for high-energy radionuclides, meaning that the spill-out is now dominant (minimum found of 0.939 in a VOI of dimension $9 \times 9 \times 9\,\mathrm{mm}^3$ for ^{82}Rb).

The observations shown here have implications for other situations. For example, the shift in measured radionuclide concentration to the higher density medium could be observed in the case of a metal implant or prosthetic in close proximity

to a low-density medium. Such effect could be expected for cardiac imaging near the lung, however the effect of cardiac motion might prevail. Also, Chronic Obstructive Pulmonary Disease, one of the main causes of global mortality (Martinez et al. 2011) is mainly characterised by emphysema and air trapping, which leads to a locally lower density of the lung, meaning that positron range effects may be more prominent for this pathology. More generally the spill-in dominance is most relevant for cold-spot imaging, such as the detection of myocardial defects in PET (Rahmim et al. 2008). However for most purposes, PET tracers are more likely to have higher uptake in high-density regions (as expected for ^{18}F-FDG in IPF, Win et al. 2012b). The second scenario is therefore more realistic and the increase of apparent recovery in the high-density regions due to spill-in from the background healthy regions should be limited in the case where spill-out dominates, e.g., in tumour imaging. Our aim in this study was to better understand the possible effects that may be introduced in lung studies due to positron range, with particular emphasis on the quantitative bias that may be introduced. Our simulations therefore were conducted without noise so that the source of bias could be easily visualised. In practice, when noise is present, the underlying distribution of annihilation locations may not be visually observed, however, bias in quantitative measurements would remain. We therefore consider that the noise-free illustrative examples are useful. The effect of positron range will also be more visible for pre-clinical systems, because of better spatial resolution (Yang et al. 2016). Note that positron ranges were found to be lower than ranges estimated with alternative models (Cal-González et al. 2010; L. Jødal et al. 2012; Jødal et al. 2014), suggesting that the positron range effect might be underestimated in this work. Nonetheless, the results of the simulations presented in this chapter (without postfiltering) may provide an indication of the magnitude of this effect, although additional simulations with appropriate object size as well as phantom acquisitions would be necessary to assess this in detail.

This work was aimed at providing some insights on the effect of positron range in heterogeneous media. Anisotropic kernels (B. Bai et al. 2003; Alessio and MacDonald 2008; Rahmim et al. 2008; Szirmay-Kalos et al. 2012; Cal-González et al. 2015) or Monte Carlo simulations (Lehnert et al. 2011) could be used for positron range compensation within iterative reconstruction: the effects and bias observed

here could potentially be reduced by incorporating one of these strategies, however the high computational cost might be a limiting factor in clinical settings (especially for the fibrotic lung where no clear uniform region can be used for correction). In the absence of an accurate positron range compensation method, when measuring the radioactivity concentration of a tumour or localised high-density regions in the lung, the reported radioactivity concentration values should be evaluated with caution when using of a tracer labelled with a radionuclide that emits high-energy positrons.

In this chapter, an overview of positron range, its effect on reconstructed PET images and some correction techniques was given. Monte Carlo simulations were run to evaluate the effect of positron range in the normal lung, fibrotic lung and in presence of a lung tumour.

Positron range is often assimilated to a spill-out "blurring". We have demonstrated that the effect is however more complex, especially for IPF patients. Its effect leads indeed to a quantitative bias in the annihilation images (in addition to the apparent blurring), resulting from the probability of positron annihilation being higher in high-density regions. If we consider that low-density and high-density regions have a similar radioactivity concentration, an important bias could be observed for imaging radionuclides emitting high-energy positrons such as ^{68}Ga, ^{124}I or ^{82}Rb. However, for low-energy positrons, such as ^{18}F, or when the high-density medium has a higher radioactivity than low-density medium, e.g., due to a different fraction of air, the spill-out becomes more predominant and other types of image degradation (e.g., due to data acquisition and reconstruction inaccuracies) are expected to have a larger impact on the quantification. Other radionuclides could have been studied, such as ^{11}C or ^{13}N. The former can also be used to radiolabel carbon monoxide to image blood (see Appendix A). The latter can be used to label ammonia, usually for myocardial imaging (Driessen et al. 2017), instead of using ^{82}Rb imaging, although perfusion studies in the lung might be useful with ^{13}N-ammonia. It would however be preferable to use ^{18}F-based radiotracers (Werner et al. 2019). In what follows, we will therefore neglect all effect resulting from positron range as only ^{18}F-FDG data will be studied. For these data, we will consider motion occurring in the chest area to be of greater impact for the PET quantification. This will be assessed in the

following Chapter 4.

Chapter 4

Respiratory motion for pulmonary PET/CT: effects and compensation strategies

4.1 Introduction

Respiratory motion is an important cause of quantification errors and artefacts in lung imaging. The main components of the motion are:

- **Tissue Displacement**, due to the lungs being compressed or dilated during respiration.
- **Density Changes**, created by the compression and expansion of the lung during respiration. PET activity concentration changes are correlated with density changes.

An overview of the physical principles involved in the respiratory motion is given in Section 4.2, including the two components of respiratory motion. Following that, existing techniques to correct for respiratory motion—including compensation of displacement and/or density changes—will be introduced in Section 4.3.

The density occurring during the respiration will be approximated to (local) volume changes between respiratory states in this thesis. They can be estimated from the deformation fields obtained in motion estimation by computing the Jacobian determinant of the transformation. This will be introduced in Section 4.4, where different mathematical assumptions for motion estimation will be also discussed. The activity concentration ratios between respiratory gates will be assumed to be

the same as the density ratios.

Afterwards, in Section 4.6, a preliminary evaluation of respiratory motion on static and dynamic PET will be performed, to show the artefacts caused by respiratory motion in both cases.

Finally, a simple mass-preserving registration will be introduced in this chapter. The mathematical formulation of mass preservation will be incorporated in a standard cost function: sum of squared differences (SSD) (introduced in Section 2.3.2.4). When the images to register only differ with Gaussian noise, sum of squared differences (SSD) provides optimal results. This cost function is however not robust when differences in image intensities are observed between the target and the source images, such as for multi-modality registration or when a region has a different uptake/intensity (Hill et al. 2001). In CT registration, this can be the case when registering images with different settings (mA, kVp) or when one of the images is a contrast CT. This is also the case of respiratory-gated chest PET/CT images, where the image intensities depend on the respiratory state. A mass-preserving SSD image registration could potentially overcome the issue and is investigated in this chapter for PET and μ images. The registration technique presented is aimed at laying the foundations for a joint image reconstruction and motion estimation (JRM) implementation (discussed in following section 4.3.6), using a motion-dependent log-likelihood including density and activity concentration changes. The results of the mass-preserving registration will determine the feasibility of such technique, including discussing adequate regularisation for the optimisation.

4.2 Respiratory Motion and the Lung

4.2.1 Tissue Displacement

During respiration, oxygenated air is taken out of the ambient environment into the alveoli, which ensures the gas exchange, essential for survival. Physically, this is performed by the mechanical movement of the lungs. During inhalation, the contraction of the diaphragm (the main muscle of respiration) is what contributes mostly to the breathing mechanics, combined with the enlargement of the rib cage, caused by the anterior-posterior motion of the intercostal muscles. This leads to an increase of the volume within the thorax cavity and pushes the organs situated in the abdomen downwards. As the tissue in the lungs is elastic, it expands to fill the

cavity. As the intra-thoracic pressure decreases, the air flows in the lungs, via the respiratory airways. Exhalation is the inverse process, where the diaphragm relaxes and the rib cage returns to its rest state. The diaphragm moves about 15-20 mm during the respiration (Schwarz and Leach 2000).

At full-expiration, the lung volume is at its lowest and at full-inspiration its highest. For an average healthy adult in a supine position at rest, the tidal volume (mean displaced volume during the respiratory cycle) is approximately of 0.46 L out of a total lung capacity of 4.9 L (Moreno and Lyons 1961).

4.2.2 Density Changes

Due to the compression and dilation of the lungs during the respiration, as described in 4.2.1, the lung tissue displacement is accompanied by density changes.

In a good first approximation, we consider a mass conservation in the lung during the respiratory cycle, neglecting fluid and gas exchanges occurring within the respiratory cycle (Cuplov et al. 2018), i.e., we have $m_{\text{ins}} = m_{\text{exp}}$. In this case: $d_{\text{ins}}V_{\text{ins}} \approx d_{\text{exp}}V_{\text{exp}}$ and $d_{\text{ins}}/d_{\text{exp}} \approx V_{\text{exp}}/V_{\text{ins}}$, where m_{ins} (respectively m_{exp}) is the lung average mass, d_{ins} (respectively d_{exp}) is the average lung density and V_{ins} (respectively V_{exp}) is the lung volume, at full-inspiration (respectively at full-expiration).

However, the motion is position-dependent, and this results in variable density changes over the lungs (Simon 2000; Verschakelen et al. 1993); the change of density may be higher in regions where most of the mechanical stress is applied, and particularly near the diaphragm, i.e., at the base of the lungs. It has been suggested (Jahani et al. 2014) that the local density changes are correlated with the local volume changes, which can be estimated if the spatial transformation is known by the computation of the Jacobian determinant of the deformation field (Cuplov et al. 2018). There is some evidence that second-order effects actually occur in the lungs, such as fluid movement in and out of the lungs (blood, lymph), which may contribute to a change of total lung tissue mass of up to 10% over the respiratory cycle (Guerrero et al. 2006; El-Chemaly et al. 2008). Although this mass change has an effect on both density and PET value, it will be neglected here as it would need further work to specifically image the lymphatic and blood components in the lung during respiration,e.g., using CO imaging for blood imaging (Appendix A),

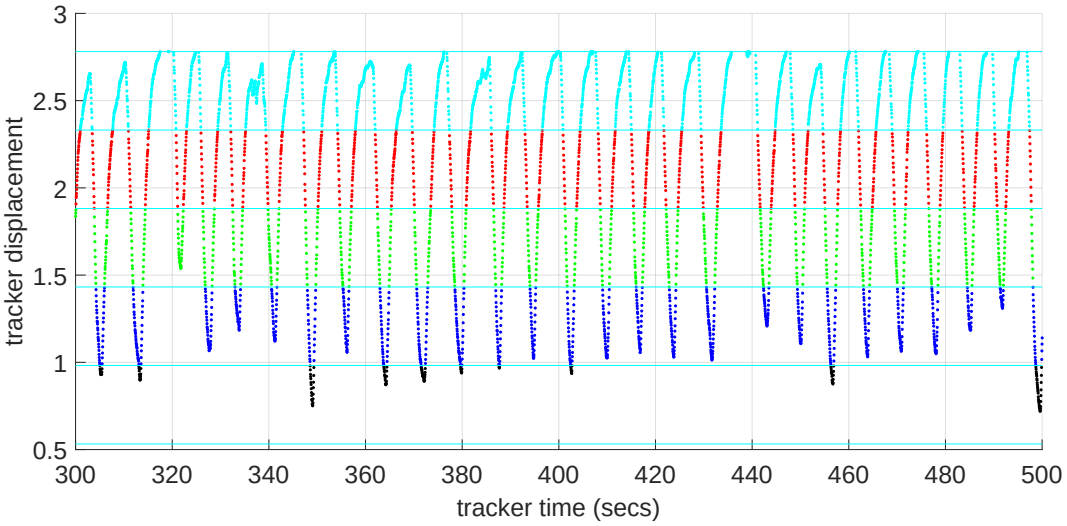

Figure 4.1: RPM respiratory signal of one of the PET acquisitions of the Coagulation Study (Section 6.4.1). The five different colours correspond to distinct respiratory gates, using displacement gating.

which could contribute to assessing with higher precision the total mass change from PET imaging. The mass-preserving model presented in this thesis is therefore not exact for PET/CT lung imaging, however it should provide a better representation compared to the standard model.

4.2.3 4D Data Binning for Respiratory Motion

Listmode PET and 4D-CT data (capturing the entire breathing cycle) can be binned into several respiratory motion "gates" (corresponding to different respiratory states), using a surrogate respiratory signal. The latter can be derived from a measure (e.g., the elevation of the chest captured by a infrared camera, pressure belts, see Nehmeh and Erdi 2008) or directly from the PET acquisition, referred as "data-driven" signals, using methods such as principal component analysis (PCA) (Thielemans et al. 2011; Bertolli et al. 2017), centre of mass (CoM) (Bundschuh et al. 2007) or the spectral analysis method (SAM) (Schleyer et al. 2009).

For PET acquisitions, 5 gates are often used, one for full-inspiration, one for full-expiration and the others for intermediate states. An illustration using displacement gating can be found in Figure 4.1, for respiratory gating of a PET examination of the Coagulation Study (see Section 6.4.1). When no gating is used to bin the data, we usually refer to these images or acquisitions as "ungated" data.

Similarly, CINE-CT acquisitions (also called 4D-CT acquisitions) can be used to

capture the entire respiratory cycle (Pan et al. 2004). The entire lung is acquired using step-and-shoot short CT acquisitions, each consisting in a rotating X-ray source around a stationary bed. The total acquisition duration is typically longer than the average respiratory cycle. The 4-dimensional (4D)-CT data is reconstructed into several images and sorted into respiratory bins.

As presented in Yamamoto et al. 2008, CINE-CT images usually present artefacts. Additionally, the binning between the CT respiratory gates and PET respiratory gates is most of the time inconsistent, meaning that PET and CT gates do not match perfectly.

In the following of this thesis, we will refer to lung PET acquisitions without any data binning using motion gating as "ungated" acquisitions.

4.2.4 Artefacts linked to Motion

Lung static PET acquisitions typically take about 2 or 3 min and contain information from multiple respiratory cycles, during which the size of the lungs is variable. Therefore when no motion compensation is used, the reconstructed images do not represent only one respiratory state. In a non-attenuation corrected reconstructed PET image, a blurring (gradient of estimated activity) can be observed, especially at the base of the lung near the diaphragm, see Section 4.2.1: this is expected as the image represents an average over time of the PET data. When using an attenuation image corresponding to a single respiratory state in the AC reconstruction of an ungated PET acquisition, the inconsistency will cause quantification errors in the image. The most conspicuous artefact is often referred as "banana artefact" (W. Bai and Brady 2004). An example will be provided in the following Section 4.6.1 for a static FDG acquisition.

Tissue displacement caused by the respiration is the main cause of visual artefacts for PET lung imaging and has been documented extensively in the literature (Beyer et al. 2003; Sureshbabu et al. 2005), mainly regarding the wrong cold areas which can appear near the diaphragm or for tumour delineation (see below). It is usually referred to "respiratory motion", although this is somewhat misleading as changes in density affect at a similar level the quantification in PET reconstructed images of the lung (Holman et al. 2016; Cuplov et al. 2018).

Respiratory motion can induce a diagnostic misinterpretation (e.g., when a

lung tumour is identified as being located within the liver), as described in Erdi et al. 2004. The size of the lung tumours is also overestimated and their activity underestimated, which can be a problem in cancer staging and follow-up. In the case of lung diseases such as IPF, the effect of respiratory motion is more complex and will be discussed below.

Aside from potential errors in localisation and overall blurring due to displacement, respiratory motion brings another problems for quantification: AC mismatch, created by the use of an incorrect attenuation map in the reconstruction. Some simple techniques can be utilised to diminish the extent of AC mismatches (e.g., via an averaged CT image for the attenuation map or having the patients perform shallow or free-breathing, Nyflot et al. 2015a).

Other more complex techniques are susceptible to compensate for displacement blurring and reduce AC mismatches. They will be discussed in more detail in Section 4.3.

4.3 Existing Reconstruction Strategies

All strategies presented in this section require a surrogate respiratory signal (see Section 4.2.3). A review of the main strategies for motion-compensated reconstruction algorithms in PET/CT can be found in Pépin et al. 2014. The following subsections will focus on the main approaches, relevant in lung imaging.

4.3.1 Reconstructions with an Averaged CT Image

gAs the PET acquisition represents an average over time of the activity distribution and the CT acquisition is quasi-instantaneous, hence representing all the respiratory states in PET versus only one in CT, the idea of the "averaged CT volume" is to obtain a CT volume which corresponds to the entire PET acquisition, without any motion correction.

Several research groups have used a modified CT, created from averaging CT images corresponding to different respiratory states, in order to improve the quantification of ungated PET reconstruction (Pan et al. 2005; Nehmeh and Erdi 2008). The best technique would be to use an average of gated CT volumes, which are CT images corresponding to different respiratory gates from the surrogate respiratory signal.

At the Institute of Nuclear Medicine, University College London Hospital (London, UK), current IPF studies comprise two or three PET/CT acquisitions ("study sections"), starting at different time points after the tracer injection. Using a cine-CT for each of these sections is not possible due to patient dose limits, although in some studies one cine-CT is available. Therefore, the current image reconstruction process involves the computation of an averaged CT image for each section (Holman et al. 2018). The CT images, usually including CT images from a cine-CT if present, are registered to a reference CT of each of the study sections. "Combined CT" images are created from averaging the registered images and are used for attenuation correction for each section. However, the implementation was unsatisfactory, as the registration involved aligning the lungs, therefore not representing a true average. During this work, this registration process was refined for clinical data, in order to distinguish body movement from respiratory movement. This is not discussed in this thesis. The benefit of using an averaged CT image in the emission image reconstruction is the reduction of the attenuation mismatch (see results in Section 4.6.1 and Chapter 5), as the averaging attempts to correct for the errors linked to density changes in the lungs during respiration. However, the averaging process can only work well if a sufficient number of CTs is present, which is often not the case. In addition, clearly, the reconstructed PET image is still affected by the blurring due to the displacement.

4.3.2 Gated Reconstructions

A second type of reconstruction involves the use of a single"gated" sinogram, created from the original listmode data using the surrogate respiratory signal. The part of the listmode data corresponding to a single gate is binned into a sinogram. Ideally, the gate coincides with the attenuation image. In practice, usually data corresponding to end-expiration are used (Liu et al. 2010; Grootjans et al. 2014), although a breath-hold CT can also be used (Nehmeh et al. 2007).

The major drawback of this method is that a large fraction of the acquired counts is discarded. The reconstruction is very noisy as a result, unless the acquisition time is extended (Nehmeh and Erdi 2008), which is not ideal for patient comfort and throughput. Furthermore, respiratory-gated reconstructions cannot be used for dynamic PET studies, as the early dynamic frames are usually very short (gates

might be missing) and might not contain information on radiotracer concentration (before injection).

4.3.3 Registered and Summed Reconstructions

Another strategy, in order to use all the counts from the PET acquisition, is to use gated reconstructions (Section 4.3.2) for all the respiratory phases and to move all reconstructed images to the same reference by using image registration (Klein et al. 1996; P. Kinahan et al. 2006).

All respiratory gates are reconstructed separately from one another, using either the corresponding CT image for the respiratory gate, if a cine-CT acquisition is available, or using a single CT image (this will lead to attenuation artefacts, which are discussed in detail in Chapter 5). As a result, deformation fields obtained from gated PET reconstructed with the corresponding gated μ maps are usually more robust (W. Bai and Brady 2009), at the expense of higher dose delivered to the patient.

4.3.4 Motion-Compensated Image Reconstruction

When the respiratory motion can be estimated, for example from gated CT images, magnetic resonance (MR) images or gated reconstructed emission images (without attenuation correction), the deformation model can be incorporated within the emission image reconstruction to obtain a motion-free reconstructed image (Qiao et al. 2006; Li et al. 2006; Manjeshwar et al. 2006,Gillman et al. 2017; Rakvongthai et al. 2017). Motion-compensated image reconstruction (MCIR) has the benefit, over the previously discussed gated reconstruction (Section 4.3.2), that it uses all of the data in the PET acquisition. This leads to less noisy images. Additionally, MCIR can be used for both static and dynamic PET acquisitions.

The Equation (2.19) introduced in Section 2.3.2.4 becomes, for a time bin t of the respiratory cycle:

$$\bar{\boldsymbol{g}}(t) = \boldsymbol{M}\mathcal{W}_{t\to 0}\boldsymbol{\lambda}(0) + \bar{\boldsymbol{r}}(t) + \bar{\boldsymbol{s}}(t)$$

where $\mathcal{W}_{t\to 0}$ is a (discrete) warping operator defined from the bin t to the reference time bin 0 and $\boldsymbol{\lambda}(0)$ is the reconstructed activity image at the reference time bin 0.

$\bar{\boldsymbol{r}}(t)$ and $\bar{\boldsymbol{s}}(t)$ are the random and scatter sinograms at bin t. In practice the scatter sinograms $\bar{\boldsymbol{s}}(t)$ use either a rescaled version of the scatter sinogram estimated from the entire acquisition with a given attenuation map or are re-estimated from the gated projection data and the deformed attenuation maps. These two possibilities will be discussed in Sections 6.2.1 and 6.4.3.2.

Examples of warping operators will be introduced in Section 4.4.1.

4.3.5 Maximum Likelihood for Attenuation and Activity

The reconstruction algorithms of type maximum likelihood reconstruction of activity and attenuation (MLAA) are a combination of two reconstructions: emission image reconstruction from known attenuation (e.g., OSEM) as described in Section 2.3.2, and attenuation image reconstruction, which estimates the attenuation image from the measured data and a known emission image. The latter uses maximum likelihood preconditioned gradient ascent for transmission reconstruction (MLTR) (Van Slambrouck et al. 2014).

It was proposed first in Nuyts et al. 1999 in the non-TOF case, however the solution is non-unique and can lead to "cross-talk artefacts": the reconstructed attenuation images can mimic structures or be quantitatively affected by errors in emission values and vice versa. The method was then extended to TOF data (Salomon et al. 2011; Rezaei et al. 2012a); the non-uniqueness of the solution in the case is reduced to a constant attenuation sinogram offset (Defrise et al. 2012).

Although MLAA is rarely used when a CT-based μ map is available, it is now commonly used in research to reconstruct data from PET scanners combined with a MR imaging gantry (instead of a CT gantry). As standard techniques used to derive MR-based μ maps are usually not fully accurate (Lillington et al. 2019), TOF-MLAA represents a potential solution to obtain quantitative PET images, provided it is possible to derive the previously discussed constant offset (Mehranian et al. 2017; Heußer et al. 2017; Rezaei et al. 2019).

The advantage of using MLAA is that it is possible to re-estimate the attenuation image while reconstructing the emission data. Similarly as using an averaged CT technique (Section 4.3.1), MLAA allows one to reduce effects of using an incorrect attenuation map within the PET reconstruction. The method is still under evaluation for clinical data, with some difficulties associated to scatter estimation

and sensitivity to errors in the TOF kernels (Rezaei et al. 2017); recently, in Rezaei et al. 2019, MLAA has shown better results when scatter is re-estimated within the reconstruction.

MLAA has also not been properly evaluated on respiratory-gated data yet, which will lead to noisier reconstructions. A recent study (Hwang et al. 2019a) has used MLAA on gated PET data. The noisy attenuation maps are then enhanced using a convolutional neural network, to obtain deformation fields. The estimated motion and the enhanced attenuation maps are then used in MCIR.

4.3.6 Joint Image Reconstruction Motion Estimation

Rather than using the reconstruction technique in Section 4.3.3, the motion can be estimated directly from the acquired PET data. Joint image reconstruction and motion estimation (JRM) (Jacobson and Fessler 2003; Rezaei et al. 2012b; Bousse et al. 2016a) is a reconstruction strategy which uses gated PET data and a single CT image $\boldsymbol{\mu}$ to estimate an emission image $\boldsymbol{\lambda}$ (accumulating all of the PET data) and warping operators $\mathcal{W}_\ell$ defined at each gate. The input single CT image does not need to correspond to one of the PET gates; the computed $\boldsymbol{\lambda}$ corresponds then to the same state as the CT. The estimated warping operators $\mathcal{W}_\ell$ can warp both $\boldsymbol{\lambda}$ and $\boldsymbol{\mu}$ to the emission and attenuation images corresponding to each gate of the PET data.

JRM has only been recently developed. It has been shown to recover the lung outline appropriately, especially if TOF information is available (Bousse et al. 2016b). However, it is still unclear whether the internal lung tissue displacement is properly estimated. The method implemented by Bousse et al. 2016a will be the base of the methods developed in this work and described in detail in Section 6.2.

4.4 Mass Preservation in Motion Estimation

As discussed in Section 4.2.2, in the case of compressible organs, density and concentration changes can be approximated via the local volume changes. The use of the Jacobian determinant within mass-preserving optimisation will be formally introduced in this section.

4.4.1 Mathematical Formulation of Volume Changes and Mass Preservation

From physiological considerations, we can intuitively consider there is a relation between how a volume moves, its volume changes and its density changes (in absence of any exchanges which would modify the mass).

In Chapters 4 and 6, we denote:

- the (continuous) tracer concentration distribution $\lambda \in \mathcal{C}^0(\mathbb{R}^3, \mathbb{R}^+)$.
- the (continuous) density distribution $\mu \in \mathcal{C}^0(\mathbb{R}^3, \mathbb{R}^+)$.

To describe the deformation between one motion state to another motion state, we define the standard warping operator $\mathcal{W}_\varphi : \mathcal{C}^0(\mathbb{R}^3, \mathbb{R}^+) \to \mathcal{C}^0(\mathbb{R}^3, \mathbb{R}^+)$ associated with a diffeomorphism [1] $\varphi : \mathbb{R}^3 \to \mathbb{R}^3$ such that:

$$\mathcal{W}_\varphi : f \mapsto f \circ \varphi \quad \text{where } f = \lambda \text{ or } f = \mu \,. \tag{4.1}$$

When applying the warping operator to h, the distribution is transformed without accounting for any volume changes, which translate into either changes of density (therefore attenuation coefficients) when $f = \mu$ or changes of activity when $f = \lambda$.

The previous warping operator can therefore be modified to account for the volume/mass changes. We define a mass-preserving warping operator $\widetilde{\mathcal{W}}_\varphi$: $\mathcal{C}^0(\mathbb{R}^3, \mathbb{R}^+) \to \mathcal{C}^0(\mathbb{R}^3, \mathbb{R}^+)$ such that:

$$\widetilde{\mathcal{W}}_\varphi : h \mapsto |\det(J_\varphi)| \cdot h \circ \varphi \,. \tag{4.2}$$

where $\det(J_\varphi(\boldsymbol{r}))$ is the determinant of $J_\varphi(\boldsymbol{r})$ the Jacobian matrix, which contains the partial derivatives of φ at a point $\boldsymbol{r} \in \mathbb{R}^3$.

The definition of the latter operator is motivated by the consideration of local mass preservation: if we consider a diffeomorphic deformation φ which transforms a non-negative continuous distribution f_1 into f_2 (i.e., $f_2 = f_1 \circ \varphi$), the integrals of f_1 and f_2 over $\mathbb{R}^3$ are given by:

$$\int_{\mathbb{R}^3} f_1(\boldsymbol{r})\,\mathrm{d}\boldsymbol{r} = \int_{\mathbb{R}^3} |\det(J_\varphi(\boldsymbol{r}))|\, f_2(\boldsymbol{r})\,\mathrm{d}\boldsymbol{r}$$

[1] A transformation function is diffeomorphic if it is invertible and if the function and its inverse are both differentiable.

where $\det(J_\varphi(\boldsymbol{r}))$ consequently reflects the volume changes.

4.4.2 Mass-Preserving Motion Estimation in PET/CT

4.4.2.1 Motivation

While it might not be necessary to use mass preservation to obtain accurate deformation fields for histogram-based registration or registration that accounts for changes in intensity (such as cross correlation or mutual information, Hill et al. 2001; Cao et al. 2012), we do not want to use such cost functions in this thesis. The aim of this preliminary is to use a mass-preserving model directly within the Poisson log-likelihood in PET reconstruction, for which it is impossible to use such techniques.

4.4.2.2 Previous Work

Incorporating the Jacobian determinant into the cost function of an optimisation problem (as introduced in Section 2.3.1) has already been done in the past (Reinhardt et al. 2008; Yin et al. 2009; Thielemans et al. 2009; Gigengack et al. 2012; Gorbunova et al. 2012), but the results were not satisfying for PET image registration.

Mass-preserving registration is indeed non-trivial and therefore regularisation and similarity measures need to be optimised especially in the presence of noisy data.

In Thielemans et al. 2009, a mass-preserving registration was tested on noiseless and noisy simulated PET images. The author highlighted the importance of choosing a robust regularisation, otherwise the noise difference between two images can be partly compensated by changes in the Jacobian determinant. The optimisation however did not include the analytical derivatives of the Jacobian and Jacobian determinants. This assumes that the change in Jacobian stays small at every optimisation update.

The registration methods in Reinhardt et al. 2008 and Gigengack et al. 2012 are very similar and both include a mass-preserving SSD cost function and the same regularisation, however the former is aimed at CT registration and the latter at PET registration of cardiac images. The hyperelastic regularisation used consisted of 3 terms, which might be complicated to tune for joint image reconstruction and motion estimation (JRM), where more parameters are necessary. Here a more simple

regularisation is desired.

In Yin et al. 2009, a mass-preserving CT image registration via SSD minimisation is performed, using a multi-level optimisation and an L-BFGS-B line search (cf Section 2.3.1). Apart from the multi-level registration and the difference in cost function, the motion estimation scheme is similar to the implementation of JRM on which the methods presented in Chapter 6 will be based. However, there is no mention of regularisation in the paper, which is crucial to be able to translate the method to PET data.

Here, we aim to find a simple regularisation penalty that could be sufficient at PET resolution, in view of using it in PET reconstruction with a log-likelihood cost function. This will be the subject of Chapter 6.

4.4.2.3 Image Registration

In the standard and mass-preserving image registrations, the optimisation problem consists in finding a deformation $\hat{\varphi}$ such that the similarities between two images f and g are increased, e.g., via minimisation of a cost function $\mathcal{C}$. Examples for $\mathcal{C}$ were given in the introductory image registration Section 2.3.3. For a given warping operator $\dot{\mathcal{W}}_\varphi$ associated with a deformation φ, we have:

$$\hat{\varphi} \in \arg\min_{\varphi} \left\{ \mathcal{C}(\dot{\mathcal{W}}_\varphi f, g) + \beta \mathcal{R}(\varphi) \right\} , \tag{4.3}$$

where $\mathcal{R}$ is the regularisation penalty and β its associated weight to ensure the estimation of a realistic deformation field. Choices of the penalty $\mathcal{R}$ will be discussed in Section 4.5.2.

4.5 Warping Operators in the Optimisation Cost Functions

When estimating deformation fields between two or more different motion states (images or projection data), it is usually necessary to express the partial derivatives of the motion-dependent cost function for the optimisation (see Section 2.3.1 for gradient-based search). This involves the mathematical formulation of the deformation fields (depending on the parameterisation chosen, 4.5.1) and the choice of a discretisation scheme (4.5.3).

4.5.1 Parameterisation of the Deformation

In this work, the deformation φ is parameterised by the B-spline coefficients $\boldsymbol{\alpha} = \left\{\boldsymbol{\alpha}^X = (\alpha_n^X)_{n=1}^{n_c}, \boldsymbol{\alpha}^Y = (\alpha_n^Y)_{n=1}^{n_c}, \boldsymbol{\alpha}^Z = (\alpha_n^Z)_{n=1}^{n_c}\right\}$ on a subgrid of the original image grid comprising n_c control points:

$$\varphi(\boldsymbol{r}) = \boldsymbol{r} + \begin{pmatrix} \sum_{n=1}^{n_c} \alpha_n^X \mathcal{B}\left(\frac{\boldsymbol{r}-\boldsymbol{r}_n}{D}\right) \\ \sum_{n=1}^{n_c} \alpha_n^Y \mathcal{B}\left(\frac{\boldsymbol{r}-\boldsymbol{r}_n}{D}\right) \\ \sum_{n=1}^{n_c} \alpha_n^Z \mathcal{B}\left(\frac{\boldsymbol{r}-\boldsymbol{r}_n}{D}\right) \end{pmatrix} \tag{4.4}$$

where D is the distance between the control points, $\boldsymbol{r}_n$ is the n-th control point and $\mathcal{B}(\boldsymbol{r}) = b(x)b(y)b(z)$ where $\boldsymbol{r} = (x, y, z)$ are the coordinates of a point in the image grid (n_v voxels) and b is the cubic B-spline function, given for a value $v \in \mathbb{R}$ as:

$$b(v) = \begin{cases} \frac{1}{6}(4 - 6v^2 + 3\,|v|^3), & \text{if } 0 \leq |v| < 1 \\ \frac{1}{6}(2 - |v|)^3, & \text{if } 1 \leq |v| < 2 \\ 0, & \text{if } 2 \leq |v| \end{cases} \tag{4.5}$$

Cubic B-spline parameterisation is regularly employed for deformations, because of the differentiability and relative ease of use (efficient computation because of the limited support and only a few parameters are used to parameterise), while managing to obtain accurate estimates (Bardinet et al. 1996; Rueckert et al. 1999; Mattes et al. 2003; Jacobson and Fessler 2003).

In the following, the warping operators, as well as the Jacobian determinant, will be indexed with the corresponding B-spline coefficients instead of the deformation field, i.e. $\mathcal{W}_{\boldsymbol{\alpha}} \triangleq \mathcal{W}_\varphi$, $\widetilde{\mathcal{W}}_{\boldsymbol{\alpha}} \triangleq \widetilde{\mathcal{W}}_\varphi$ and $\det \mathcal{J}_{\boldsymbol{\alpha}} \triangleq \det \mathcal{J}_\varphi$.

4.5.2 Regularisation on Jacobian Determinant Images

Two penalties will be evaluated in this chapter: quadratic penalty (QP) and smoothed total variation (STV) penalty (as introduced in Section 2.3.2.4). For motion estimation, they will be applied on the Jacobian determinant image (instead of the activity image), to ensure that the problem noticed by Thielemans et al. 2009 is avoided.

Mathematically, the quadratic penalty (QP) on the Jacobian determinant image

$\mathcal{R}_{\mathrm{QP}}$ can be expressed as:

$$\mathcal{R}_{\mathrm{QP}} : \boldsymbol{\alpha} \mapsto -\frac{1}{2} \sum_{j=1}^{n_{\mathrm{v}}} \sum_{k \in \mathcal{N}_j} \omega_{j,k} \left(|\det \boldsymbol{\mathcal{J}}_{\boldsymbol{\alpha}}|_j - |\det \boldsymbol{\mathcal{J}}_{\boldsymbol{\alpha}}|_k \right)^2 ,$$

where $\omega_{j,k}$ is the inverse distance between the centre of a voxel j and the centre of a voxel k and $\mathcal{N}_j$ is the neighbourhood of voxel j.

The smoothed total variation (STV) penalty $\mathcal{R}_{\mathrm{STV}}$ is formulated as:

$$\mathcal{R}_{\mathrm{STV}} : \boldsymbol{\alpha} \mapsto \sum_{j=1}^{n_{\mathrm{v}}} \sqrt{||\nabla |\det \mathcal{J}_{\boldsymbol{\alpha}}|_j ||_2^2 + \zeta^2}, \quad \zeta > 0$$

where $\nabla |\det \mathcal{J}_{\boldsymbol{\alpha}}|_j$ is the (image) gradient of the absolute value of the Jacobian determinant at a voxel j (the gradient approximation uses forward differences in $\mathcal{N}_j$ on $|\det \boldsymbol{\mathcal{J}}_{\boldsymbol{\alpha}}|$ the discretised Jacobian determinant image – see following 4.5.3 for details on discretisation) and ζ is used as a smoothing factor, enabling differentiation when the gradient is 0.

For both penalties, the neighbourhood size was set to $3 \times 3 \times 3$. The values at the image borders were handled by adding padding to the image, using the nearest voxel values.

Furthermore, to be able to compare the two penalties with equivalent weighting, we consider the following function g (where $\zeta \neq 0$):

$$g : x \mapsto \sqrt{x^2 + \zeta^2} = |\zeta| \cdot \sqrt{\left(\frac{x}{\zeta}\right)^2 + 1} \tag{4.6}$$

The first-order Taylor expansion of g in 0 gives:

$$g(x) = |\zeta| + |\zeta| x^2 + o(x) \tag{4.7}$$

We can therefore derive the weights for the STV prior from the quadratic prior weights, as $\beta_{\mathrm{STV}} = \beta_{\mathrm{QP}} |\zeta|$, where ζ was chosen as 0.3 in order to preserve larger changes of Jacobian determinant while smoothing smaller ones.

In image registration, preservation of topology is desired, which means that the connected structures remain connected after warping and that the neighbourhood relationship remains the same, e.g., ensuring a one-to-one mapping of structures. It

is the case when the Jacobian determinant $\det \mathcal{J}_{\boldsymbol{\alpha}}$ is strictly positive everywhere in $\mathbb{R}^3$ (Musse et al. 2001; Ashburner et al. 1999). In initial experiments, we have found that the above penalties were not sufficient to ensure that the deformation is diffeomorphic. Therefore, we need to introduce an additional penalty encouraging smooth deformation fields: a standard quadratic regularisation $\mathcal{R}_{\text{def}}$ is applied directly on the B-spline coefficients:

$$\mathcal{R}_{\text{def}} : \boldsymbol{\alpha} \mapsto -\frac{1}{2} \sum_{n=1}^{n_c} \sum_{m \in \widetilde{\mathcal{N}}_n} \widetilde{\omega}_{n,m} \sum_{C \in \{X,Y,Z\}} \left(\alpha_n^C - \alpha_m^C\right)^2 , \tag{4.8}$$

where $\widetilde{\omega}_{n,m}$ is the inverse distance between the control points n and m, $\widetilde{\mathcal{N}}_n$ is the neighbourhood of a control point n. The size of the neighbourhoods $\widetilde{\mathcal{N}}_n$ was set to $3 \times 3 \times 3$. The values at the image borders were handled by adding padding to the image, using the nearest values.

We write the total regularisation on the deformation as:

$$\mathcal{R}(\boldsymbol{\alpha}) = \mathcal{R}^*(\boldsymbol{\alpha}) + \xi \cdot \frac{n_{\text{v}}}{n_c} \mathcal{R}_{\text{def}}(\boldsymbol{\alpha}) \tag{4.9}$$

where $\mathcal{R}^*$ corresponds to either $\mathcal{R}_{\text{quad}}$ or $\mathcal{R}_{\text{STV}}$. ξ is a small scalar > 0. In this chapter, ξ was chosen as 0.005 when $\mathcal{R}^* = \mathcal{R}_{\text{quad}}$ or $0.005 \cdot \zeta$ when $\mathcal{R}^* = \mathcal{R}_{\text{STV}}$ (where ζ is the smoothing scalar in the STV prior). In the rest of the thesis, we will refer to QP and STV on the Jacobian determinant image for the above combinations (i.e., with the added quadratic regularisation on the B-spline coefficients).

4.5.3 Discretisation Scheme

The discretisation is performed after warping of the continuous distributions λ and μ, similarly to the scheme proposed in Jacobson and Fessler 2003. It can be summarised as follows, for a given continuous distribution f:

1. Image Interpolation: We assume a distribution f can be decomposed using basis functions (see Section 2.3.1.3), which are centred on a voxel grid $\mathcal{G} = \{\boldsymbol{r}_i, i \in [\![1, n_v]\!]\}$:

$$f(\boldsymbol{r}) = \sum_{i=1}^{n_v} f_i w(\boldsymbol{r} - \boldsymbol{r}_i)$$

where f_i denotes the scalar coefficients at a voxel $i \in [\![1, n_v]\!]$ for an interpolation function $w : (x, y, z) \to e(x)e(y)e(z)$, where e is a 1D interpolator

(positive, definite and continuously differentiable). e is typically chosen as a 1D linear interpolation function, however here a B-spline interpolation will be used within the optimisation, using recursive filtering algorithms introduced in Unser et al. 1993.

2. Warping: Use a warping operator $\dot{\mathcal{W}}_{\boldsymbol{\alpha}}$ to obtain the warped image (in continuous space):

$$\dot{\mathcal{W}}_{\boldsymbol{\alpha}} f(\boldsymbol{r}) = \sum_{i=1}^{n_v} f_i \dot{\mathcal{W}}_{\boldsymbol{\alpha}} w(\boldsymbol{r})$$

3. Discretisation: Finally, resample the warped image to obtain the image at voxel values:

$$\forall j \in [\![1, n_{\mathrm{v}}]\!], \quad \left[\dot{\boldsymbol{\mathcal{W}}}_{\boldsymbol{\alpha}} \boldsymbol{h}\right]_j = \dot{\mathcal{W}}_{\boldsymbol{\alpha}} f(\boldsymbol{r}_j)$$

The discretised images corresponding to a distribution f (e.g., f or μ) will be denoted $\boldsymbol{f}$ and the discretised warped images associated with a warping operator $\dot{\mathcal{W}}_{\boldsymbol{\alpha}}$ (e.g., $\mathcal{W}_{\boldsymbol{\alpha}}$ or $\widetilde{\mathcal{W}}_{\boldsymbol{\alpha}}$) denoted $\dot{\boldsymbol{\mathcal{W}}}_{\boldsymbol{\alpha}} \boldsymbol{f}$. Additionally, $|\det \mathcal{J}_{\boldsymbol{\alpha}}|$ will be discretised to $|\mathbf{det}\, \boldsymbol{\mathcal{J}}_{\boldsymbol{\alpha}}|$.

4.5.4 Jacobian Matrix and Jacobian Determinant for a B-Spline Deformation

The element (k, l) of the matrix $\mathcal{J}_{\boldsymbol{\alpha}}(r)$ is given by:

$$[\mathcal{J}_{\boldsymbol{\alpha}}(r)]_{k,l} = \delta_{kl} + \sum_{n=1}^{n_c} \frac{\alpha_n^{C_k}}{D} \frac{\partial \mathcal{B}}{\partial x_l} \left(\frac{\boldsymbol{r} - \boldsymbol{r}_n}{D} \right) \tag{4.10}$$

where δ_{kl} is the Kronecker delta for k, l and $\frac{\partial \mathcal{B}}{\partial x_l}$ is the partial derivative of $\mathcal{B}$ with respect to x_l, where C_k is equal to X, Y, Z for $k = 1$, $k = 2$, $k = 3$, respectively, and x_l is x, y or z for $l = 1$, $l = 2$, $l = 3$ respectively.

The determinant of the Jacobian matrix corresponding to the transformation at a point $\boldsymbol{r}$ can be computed as the determinant of the 3×3 matrix.

4.5.5 Analytical Derivatives of the Jacobian Determinant

Optimising a cost function in which the Jacobian determinant appears (i.e., in mass-preserving optimisation) requires the knowledge of its derivatives in terms of the deformation parameters, i.e., here the B-spline coefficients $\boldsymbol{\alpha}$. The partial derivative of $\det \mathcal{J}_{\boldsymbol{\alpha}}(\boldsymbol{r})$ with respect to a given B-spline coefficient $\alpha_n^{C_k}$ can be obtained via

Jacobi's formula:

$$\frac{\partial \det \mathcal{J}_{\boldsymbol{\alpha}}(\boldsymbol{r})}{\partial \alpha_n^{C_k}}(\boldsymbol{\alpha}) = \operatorname{tr}\left(\operatorname{adj}\left(\mathcal{J}_{\boldsymbol{\alpha}}(\boldsymbol{r})\right)\right) \frac{\partial \mathcal{J}_{\boldsymbol{\alpha}}(\boldsymbol{r})}{\partial \alpha_n^{C_k}}(\boldsymbol{\alpha}) ,$$

where $\operatorname{tr}(\cdot)$ denotes the trace [2] of a matrix, $\operatorname{adj}(.)$ is its adjugate [3] and the partial derivative of $\det \mathcal{J}_{\varphi}(\boldsymbol{r})$ with respect to $\alpha_n^{C_k}$ is equal to:

$$\frac{\partial \mathcal{J}_{\boldsymbol{\alpha}}(\boldsymbol{r})}{\partial \alpha_n^{C_k}}(\boldsymbol{\alpha}) = \frac{1}{D} \sum_{l=1}^{3} \frac{\partial \mathcal{B}}{\partial x_l} \left(\frac{\boldsymbol{r} - \boldsymbol{r}_n}{D} \right) \tag{4.11}$$

where C_k is equal to X, Y, Z for $k = 1$, $k = 2$, $k = 3$, respectively, and x_l is x, y or z for $l = 1$, $l = 2$, $l = 3$ respectively.

By composition, the partial derivative of $|\det \mathcal{J}_{\boldsymbol{\alpha}}(\boldsymbol{r})|$ with respect to $\alpha_n^{C_k}$ is therefore:

$$\frac{\partial \, |\det \mathcal{J}_{\boldsymbol{\alpha}}(\boldsymbol{r})|}{\partial \alpha_n^{C_k}}(\boldsymbol{\alpha}) = \operatorname{sgn}(\det \mathcal{J}_{\boldsymbol{\alpha}}(\boldsymbol{r})) \operatorname{tr}\left(\operatorname{adj}\left(\mathcal{J}_{\boldsymbol{\alpha}}(\boldsymbol{r})\right)\right) \frac{\partial \mathcal{J}_{\boldsymbol{\alpha}}(\boldsymbol{r})}{\partial \alpha_n^{C_k}}(\boldsymbol{\alpha}) ,$$

where $\operatorname{sgn}(\cdot)$ is the sign function. The non-differentiability of $|\cdot|$ function in 0 is handled by adding a small number to the Jacobian determinant. The analytical derivatives of $|\det(\mathcal{J}_{\varphi})|$ were validated against finite differences in terms of absolute percentage error between the gradient and the finite differences, normalised with respect to the maximum absolute value of the gradient, for random B-spline coefficients and $\epsilon = 0.00001$ used in finite differences. The mean and maximum errors were found to be less than $3 \cdot 10^{-11}$ and $4 \cdot 10^{-10}$ respectively.

4.6 Evaluation on Patient Data

4.6.1 Motion during Static Acquisitions

In this part, data corresponding to a static acquisition were reconstructed with three different μ maps, to evaluate the impact of the attenuation map on quantification. Both non-TOF and TOF reconstructions were performed to demonstrate the dependency of the errors on the reconstruction algorithm.

A 76-year-old male patient from the Coagulation Study (see Section 6.4.1) un-

[2] The trace $\operatorname{tr}(\cdot)$ of a matrix is equal to the sum of its diagonal elements.

[3] The adjugate $\operatorname{adj}(\cdot)$ of a matrix is equal to the transpose of its cofactor matrix. For a 3×3 matrix, its elements are easy to compute, as $\pm D_{ij}$, where D_{ij} are 2×2 matrix determinants.

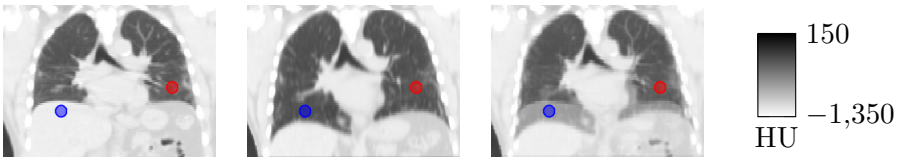

Figure 4.2: CT images used to create the attenuation maps used in this study: (a) end-expiration CT for $\boldsymbol{\mu}_{\text{exp}}$, (b) deep-inspiration CT for $\boldsymbol{\mu}_{\text{insp}}$ and (c) average CT for $\boldsymbol{\mu}_{\text{ave}}$. The spherical ROIs used in the analysis are overlayed in blue and red for the liver and the lung, respectively. The data correspond to one patient from the Coagulation Study (Section 6.4.1).

derwent a static FDG acquisition (injected activity: 170.8 MBq), on a GE Discovery 690.

Two different CT acquisitions were available: one at end-expiration (CTAC acquisition, multislice helical acquisition at shallow breathing, slice thickness: 3.75 mm, pitch: 1.375, voltage: 120 kVp, current: 40 mA, revolution time: 0.8 s) and one at end-inspiration (HRCT, multislice helical acquisition at breathhold, slice thickness: 1.25 mm, pitch: 0.516, voltage: 120 kVp, current: 149 mA, revolution time: 0.6 s). A third averaged CT image was formed by averaging the end-expiration CTAC and the (filtered) HRCT images (method presented in Section 4.3.1).

The (ungated) PET data were reconstructed using the 3 following attenuation maps:

- $\boldsymbol{\mu}_{\text{exp}}$, from the end-expiration CTAC image.
- $\boldsymbol{\mu}_{\text{insp}}$, from the end-inspiration HRCT image.
- $\boldsymbol{\mu}_{\text{ave}}$, from the averaged CT image.

The estimated scatter term also depended on the attenuation map used (Section 2.2.5).

For the quantitative analysis, two spherical regions of interest (ROIs) were drawn on the CT input images (volume 4189 mm^3): the first one is located in the lung at both end-expiration and end-inspiration and the second is in the liver at end-expiration but in the lung at end-inspiration. Coronal views of the CT images, overlayed with the ROIs, are given in Figure 4.2.

In addition, the listmode data was amplitude-gated into 4 respiratory bins (no cardiac gating) based on the respiratory trace from a Varian RPM system. The end-

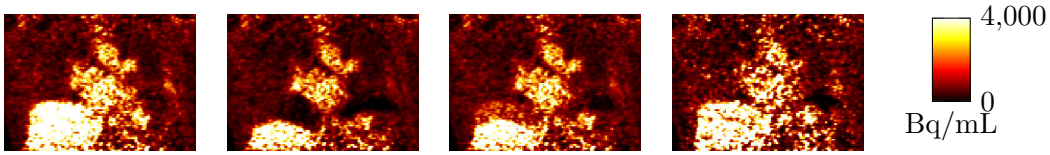

Figure 4.3: Non-TOF reconstructed images corresponding to the entire ungated acquisition, using (a) $\boldsymbol{\mu}_{\text{exp}}$, (b) $\boldsymbol{\mu}_{\text{insp}}$ and (c) $\boldsymbol{\mu}_{\text{ave}}$ as attenuation maps. The reference non-TOF end-expiration reconstruction is displayed in (d).

ROI	$\boldsymbol{\mu}_{\text{exp}}$	$\boldsymbol{\mu}_{\text{insp}}$	$\boldsymbol{\mu}_{\text{ave}}$	Reference
Lung	981 (+2.7%)	744 (−22.1%)	863 (−9.6%)	955
Liver	4645 (+3.6%)	518 (−88.5%)	1951 (−56.5%)	4485

Table 4.1: Measured radioactivity (in Bq/mL) and relative errors in the the two ROIs, for non-TOF reconstructions.

expiration gated PET data were reconstructed using $\boldsymbol{\mu}_{\text{exp}}$ and will be considered as the reference for quantification (Liu et al. 2010). The alignment between the end-expiration PET data and end-expiration CTAC image was visually assessed using non-AC TOF gated images.

All data in this chapter were reconstructed using GE proprietary software in MATLAB (Matlab 2016b), with OSEM using 8 subsets with 200 iterations for non-TOF data and 100 iterations for TOF data.

4.6.1.1 Non-TOF Quantitative Results

Coronal views of the non-TOF recontructed images are shown in Figure 4.3. The AC artefacts are conspicuous when both end-inspiration and averaged attenuation maps are used. The reconstructed image with the end-expiration μ map is similar to the reference gated reconstruction.

The visual assessments are also confirmed from measured tracer concentration and relative errors in the ROIs are in Table 4.1. The results in non-TOF reconstructions show that—when no motion correction is applied—the quantification is very dependent on the attenuation map.

4.6.1.2 TOF Quantitative Results

Coronal views of the TOF reconstructed images are shown in Figure 4.4. Visually, the images are similar to the non-TOF images of Figure 4.3, although activity values appear slightly different where the diaphragm displaces.

The measured uptakes and relative errors in the ROIs are in Table 4.2. The

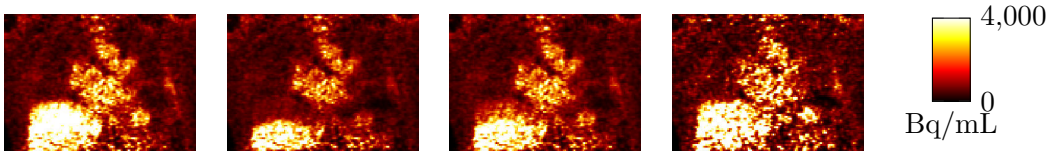

(a) (b) (c) (d)

Figure 4.4: TOF reconstructed images corresponding to the entire ungated acquisition, using (a) $\boldsymbol{\mu}_{\text{exp}}$, (b) $\boldsymbol{\mu}_{\text{insp}}$ and (c) $\boldsymbol{\mu}_{\text{ave}}$ as attenuation maps. The reference TOF end-expiration reconstruction is displayed in (d).

ROI	$\boldsymbol{\mu}_{\text{exp}}$	$\boldsymbol{\mu}_{\text{insp}}$	$\boldsymbol{\mu}_{\text{ave}}$	Reference
Lung	925 (+1.5%)	800 (−12.2%)	863 (−5.3%)	911
Liver	3860 (−5.9%)	1145 (−72.1%)	2149 (−47.6%)	4101

Table 4.2: Measured radioactivity (in Bq/mL) and relative errors in the the two ROIs, for TOF reconstructions.

differences between reconstructions in the ROIs are lower than for non-TOF reconstructions.

4.6.2 Motion during Dynamic Acquisition

Short non-AC images (duration: 1 s) were reconstructed at the start of a dynamic acquisition (for one patient of the Coagulation Study cohort), to demonstrate the motion during the early part of a dynamic acquisition.

Images corresponding to 6 consecutive frames at the start of the acquisition are shown in Figure 4.5; in addition to the changes due to kinetics within the thorax – we can observe the tracer coming from the veins, passing through the lungs to the aorta – motion is visible, especially near the diaphragm, as outlined using dotted lines.

This observation implies that changes in radioactivity concentration due to motion and due to kinetics cannot be dissociated in highly mobile regions such as the base of the lungs, where the fibrotic regions are usually located in IPF.

4.6.3 Image Registration

The possibility of obtaining accurate Jacobian determinant maps is studied here. Registration was performed on gated μ maps and PET images using the two similarity measures introduced in Section 2.3.3:

- SSD, using an in-house implementation in MATLAB. Both mass-preserving and non-mass-preserving versions were tested. The optimisation uses an L-

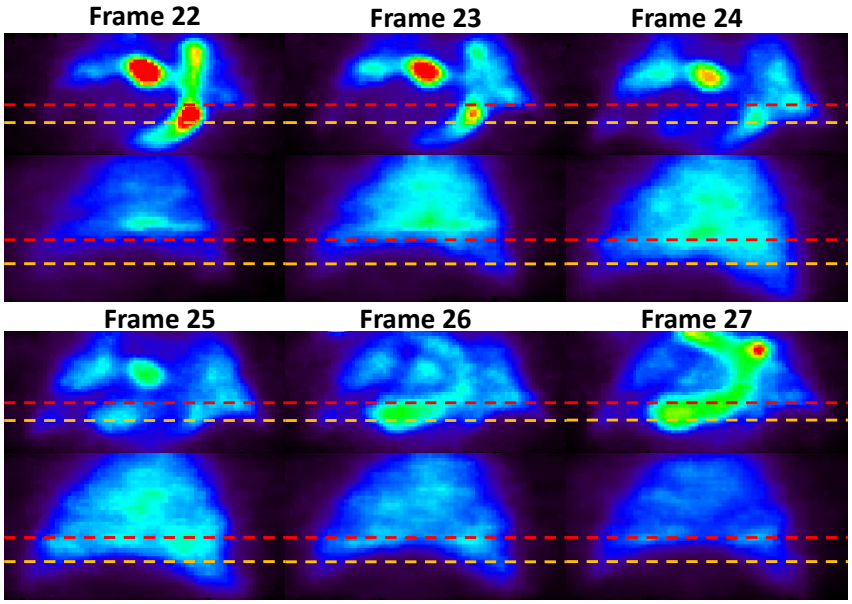

Figure 4.5: Coronal and sagittal views of 6 early consecutive 1 s long frames of a dynamic PET acquisition, reconstructed without attenuation correction. The displacement of the diaphragm is characterised using dotted lines to show its extent between end-expiration (red) and end-inspiration (yellow).

BFGS-B line search (Section 2.3.1). This will be also used in JRM presented in Chapter 6.

- LNCC, using NiftyReg (Modat et al. 2010). The Jacobian determinant is not included in the NiftyReg similarity measure. However, the LNCC cost function should not be too sensitive to variations of image intensity.

Both registrations here use B-spline parameterised deformations. The same distance between control points (3 voxels along each direction) was used in both types of registration however the grids do not coincide because of differences in implementation.

The NiftyReg registration is included here as it is a well-validated package to make sure the SSD registration gives realistic results. Note however that NiftyReg could not be used in Chapter 6, because no registration on projection data is implemented.

4.6.3.1 Patient Data

FDG-PET listmode and cine-CT data (Cuplov et al. 2018) were acquired on a GE Discovery STE 134 min after injection, with monitoring using the Varian RPM system (Nehmeh and pthers 2002). Both PET and cine-CT data were gated into 5 bins based on the RPM displacement (see Section 4.2.3). These data will be referred

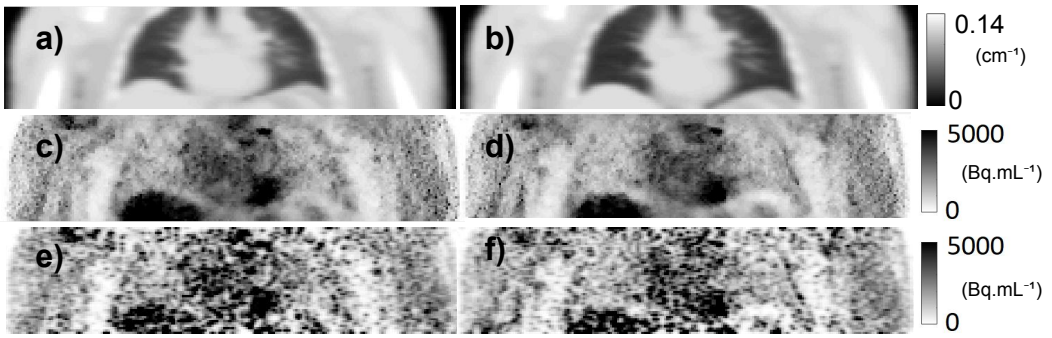

Figure 4.6: Input images: a) end-expiration μ-map, b) end-inspiration μ-map, c) end-expiration BSREM PET, d) end-inspiration BSREM PET, e) end-expiration OSEM PET, f) end-inspiration OSEM PET.

as the "gated entire PET acquisitions". The PET data were reconstructed with two different reconstruction algorithms:

- 60 iterations of OSEM (7 subsets) + 6-mm FWHM 2-dimensional (2D) Gaussian postfilter + 1-4-1 weighted z-axis postfilter.
- BSREM (Ahn et al. 2003), using the relative difference (RD) penalty (introduced in Section 2.3.2.4) to regularise the images. Details on the implementation of BSREM (max iteration number, step size, etc.) are given in Section B.3 (Appendix B).

Both reconstructions included scatter and randoms modelling. The gated attenuation maps matched the PET gates according to the RPM trace. The input μ, OSEM PET images and BSREM PET images used as input images are displayed in Figure 4.6.

Unlike standard methods developed for mass-preserving CT image registration (Reinhardt et al. 2008; Yin et al. 2009), the gated CT images were here first converted to μ maps, in units $\text{mm}^{-1} \cdot \Delta_Z^{-1}$, where Δ_Z is the voxel Z-dimension—the μ maps are therefore in volume units, implying that there is no need to multiply the Jacobian determinant by a slope as in Yin et al. 2009. The images were also resampled to PET resolution: Jacobian determinant images from PET and CT registrations will be readily comparable.

Additionally, in order to verify the stability of the registration, the PET data were divided into 4 parts (random gating), each part also gated into 5 respiratory bins, according to the RPM signal. These data will be referred as "gated partial

PET acquisitions". Because of the limited number of counts, only BSREM was used to reconstruct the latter partial gated data, with a higher RD penalty weight.

For all types of registration in this chapter, the end-expiration images were registered to the end-inspiration images, to avoid problems with structures moving in the FOV. We denote $\boldsymbol{\lambda}_{\text{insp}}^{\text{BSREM}}$ and $\boldsymbol{\lambda}_{\text{insp}}^{\text{OSEM}}$ the end-inspiration activity image for BSREM and OSEM reconstructions, respectively. Similarly at end-expiration the activity images are denoted $\boldsymbol{\lambda}_{\text{exp}}^{\text{BSREM}}$ and $\boldsymbol{\lambda}_{\text{exp}}^{\text{OSEM}}$. The two μ maps used in the registration are denoted $\boldsymbol{\mu}_{\text{insp}}$ and $\boldsymbol{\mu}_{\text{exp}}$ for end-inspiration and end-expiration, respectively.

Three penalty weights (for both priors) were tested, normalised across PET and μ registrations. They were expressed as a % of the cost function at iteration 0 (i.e., initial value) divided by the number of image voxels): weak regularisation (1%), medium regularisation (10%) and strong regularisation (100%).

4.6.3.2 Evaluation Methods

Gated Entire PET Acquisitions :

The registrations of the images corresponding to gated entire acquisitions were assessed by computing the normalised root mean squared deviation (NRMSD) between the warped end-expiration images and the end-inspiration images. Normalisations use the mean image value $M = \frac{1}{N}\sum_i [\boldsymbol{f}_{\text{insp}}]_i$ in the lung at end-inspiration, where $\boldsymbol{f}$ designates either the μ maps, the OSEM activity images or the BSREM activity images. The measure can be expressed as:

$$\text{NRMSD}\,(\boldsymbol{f}) = \frac{1}{M}\sqrt{\frac{\sum_{i\in\Omega_\varphi}\left(\left[\dot{\mathcal{W}}_\varphi \boldsymbol{f}_{\text{exp}}\right]_i - [\boldsymbol{f}_{\text{insp}}]_i\right)^2}{N}}$$

where N is the number of elements in the voxel overlap domain Ω_φ between the (discretised) target image and the (discretised) moving image transformed by a deformation φ.

Gated Partial PET Acquisitions :

The registrations of gated partial PET data were evaluated by plotting the variances in the Jacobian determinant images against the squared biases in the activity images. The variances in the activity image cannot be used as introducing the Jacobian determinant in the registration will tend to overfit the image noise, and therefore

to lower variances (as discussed in Thielemans et al. 2009). Here $\boldsymbol{\lambda}_{\text{insp}}$ and $\boldsymbol{\lambda}_{\text{exp}}$ denote the BSREM images $\boldsymbol{\lambda}_{\text{insp}}^{\text{BSREM}}$ and $\boldsymbol{\lambda}_{\text{exp}}^{\text{BSREM}}$. The Jacobian image variances Var is given as

$$\text{Var} = \frac{1}{K-1}\frac{1}{N}\sum_{j\in\Omega_\varphi}\sum_{\kappa=1}^{K}\left(\left[|\det \boldsymbol{\mathcal{J}}_\varphi|^{[\kappa]}\right]_j - m_j\right)^2 ,$$

where $K = 16$ is the number of realisations and $|\det \boldsymbol{\mathcal{J}}_\varphi|^{[\kappa]}$ corresponds to the Jacobian determinant image from the κ-th realisation and

$$m_j = \frac{1}{K}\sum_{\kappa=1}^{K}\left[|\det \boldsymbol{\mathcal{J}}_\varphi|^{[\kappa]}\right]_j .$$

The (image) activity squared bias Bias^2 is defined as

$$\text{Bias}^2 = \frac{1}{K}\frac{1}{N}\sum_{j\in\Omega_\varphi}\left(\sum_{\kappa=1}^{K}\left[\dot{\mathcal{W}}_\varphi \boldsymbol{\lambda}_{\text{exp}}^{[\kappa]}\right]_j - [\boldsymbol{\lambda}_{\text{insp}}]_j\right)^2 ,$$

where $\dot{\mathcal{W}}_\varphi \boldsymbol{\lambda}_{\text{exp}}^{[\kappa]}$ corresponds to the end-expiration image $\boldsymbol{\lambda}_{\text{exp}}^{[\kappa]}$ warped using the warping obtained from the κ-th registration and $\boldsymbol{\lambda}_{\text{insp}}^{[\kappa]}$ is the input end-inspiration image from the κ-th realisation.

4.6.3.3 In-house SSD

For a given warping operator $\dot{\mathcal{W}}$, we want to solve Equation 4.3, where $\mathcal{R}$ is one of the penalties introduced in Section 4.5.2 and $\mathcal{C}$ is the SSD cost function.

Including mass preservation :

The Figures 4.7 and 4.8 show the Jacobian determinant maps obtained from the mass-preserving registration, using as input images either the μ maps, the PET BRSEM images or the PET OSEM images, with the STV and quadratic priors, respectively. The corresponding NRMSD values for the different types of registration are given in Table 4.3.

We now verify whether the incorporation of the Jacobian determinant in the similarity measure can compensate the density changes during respiration in the μ map. To do so, for each mass-preserving μ registration, the relative difference images $(\mu_{\text{exp}} \circ \varphi - \mu_{\text{insp}})/\mu_{\text{insp}}$ and $(|\det \boldsymbol{\mathcal{J}}_\varphi|\, \mu_{\text{exp}} \circ \varphi - \mu_{\text{insp}})/\mu_{\text{insp}}$ are shown in Figure 4.9.

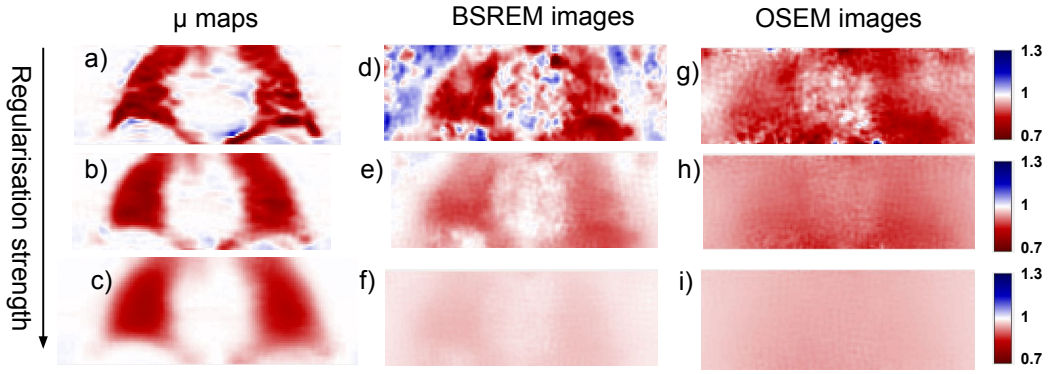

Figure 4.7: Jacobian maps obtained with STV regularisation, for μ images: a) weak, b) average, c) strong; for BSREM PET images: d) weak, e) average, f) strong; for OSEM PET images: g) weak, h) average and i) strong. The PET regularisation uses the activity images from the gated entire PET acquisitions.

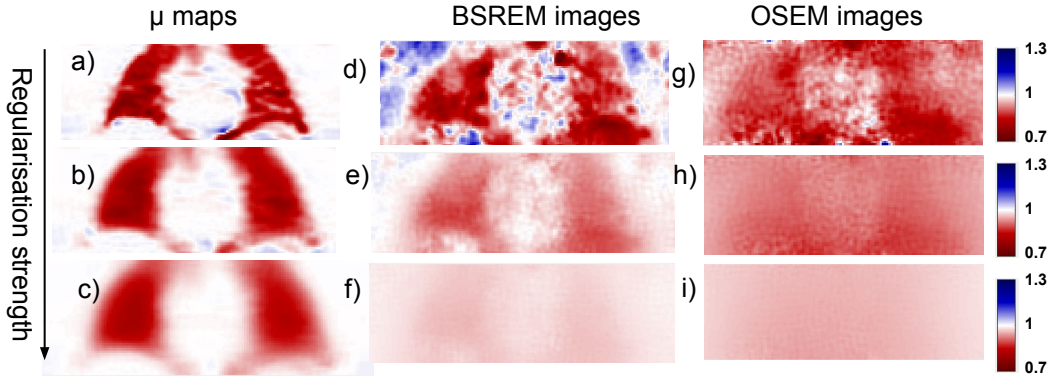

Figure 4.8: Jacobian maps obtained with quadratic regularisation, for μ images: a) weak, b) average, c) strong; for BSREM PET images: d) weak, e) average, f) strong; for OSEM PET images: g) weak, h) average and i) strong. The PET regularisation uses the activity images from the gated entire PET acquisitions.

Table 4.3: NRMSD between the end-inspiration images and the warped images (including the multiplication by $\mathbf{det}\,\mathcal{J}_\varphi$) for weak, average and strong regularisations.

STV	Weak	Average	Strong
BSREM PET	20.66%	26.42%	31.96%
OSEM PET	65.36%	72.45%	76.64%
μ	3.66%	6.19%	13.29%
Quadratic	Weak	Average	Strong
BSREM PET	20.74%	26.46%	32.01%
OSEM PET	65.42%	72.48%	76.64%
μ	3.60%	6.26%	13.47%

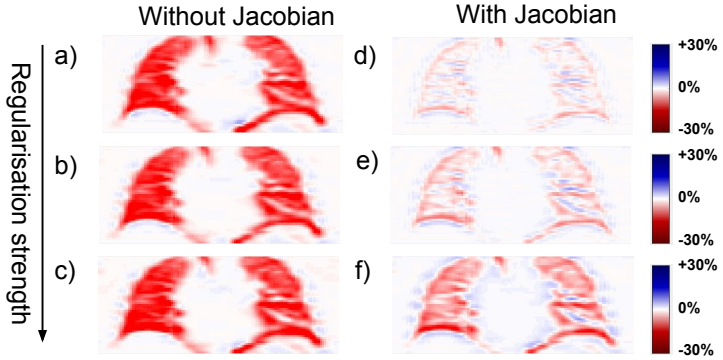

Figure 4.9: Relative difference images between $\mu_{\text{exp}} \circ \varphi$ and μ_{insp} (left) and between $|\det \mathcal{J}_\varphi| \cdot \mu_{\text{exp}} \circ \varphi$ and μ_{insp} (right), for (a), (b) weak regularisation, (c), (d) average regularisation and (e), (f) strong regularisation using the STV penalty.

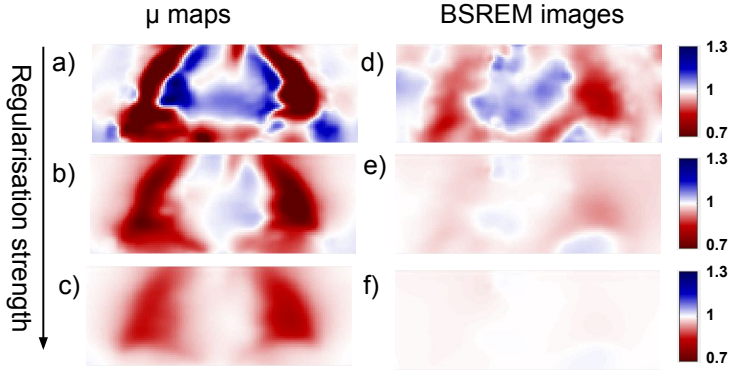

Figure 4.10: Jacobian maps obtained with STV regularisation, for μ images: a) weak, b) average, c) strong; for BSREM PET images: d) weak, e) average. The PET regularisation uses the activity images from the gated entire PET acquisitions.

Without mass preservation :

As expected, in the absence of any way to compensate for local image intensity changes, the standard SSD registration performs worse than its mass-preserving counterpart. Whereas the μ map registration manages to realign coarsely the lung images, the PET registration provides poor results, hindered by both high level of image noise and global intensity changes. The Jacobian determinant images for the μ and BSREM images are displayed in Figure 4.10.

4.6.3.4 Validation of Regularisation

The plots of the variance in the Jacobian maps against the bias in the activity images confirmed better results in the BSREM PET image registrations. As expected,

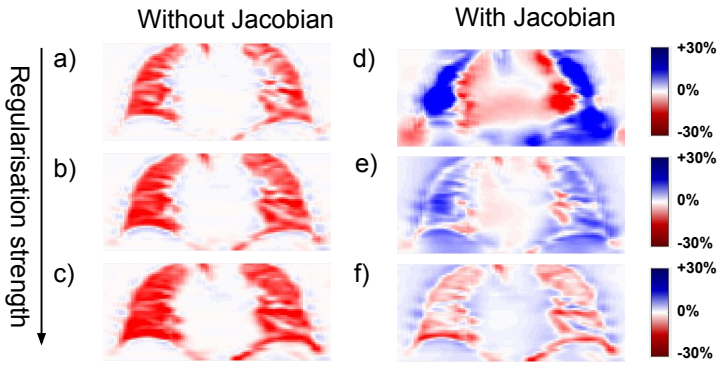

Figure 4.11: Relative difference images between $\mu_{\text{exp}} \circ \varphi$ and μ_{insp} (left) and between $|\det \mathcal{J}_\varphi| \cdot \mu_{\text{exp}} \circ \varphi$ and μ_{insp} (right), for (a), (b) weak regularisation, (c), (d) average regularisation and (e), (f) strong regularisation using the STV penalty.

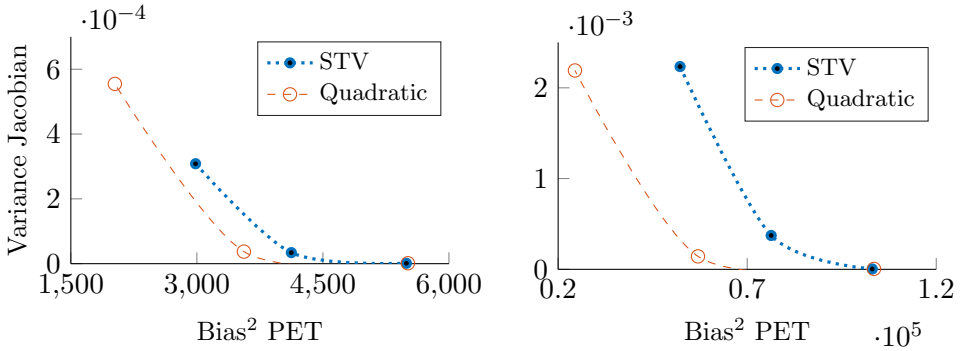

(a) Entire image **(b)** Lung only

Figure 4.12: Tradeoff between variance in the Jacobian determinant images and the (squared) bias in the activity images (in Bq^2/mL^2), in (a) the entire image and in (b) the lung only, for the BSREM sampled PET data.

using a stronger regularisation diminishes the variances but increases the biases (see Figure 4.12 for BSREM). STV prior showed smaller variances in the entire image, although the variances in the lung were similar for both priors. The biases for the quadratic prior were slightly lower.

4.6.3.5 Comparison with NiftyReg LNCC

Similarly as in Cuplov et al. 2018, a 2-step registration scheme was used in the NiftyReg optimisation, in the following order:

1. Affine registration (using NiftyReg's *reg_aladin* executable, Modat et al. 2014), using block-matching normalised cross correlation (NCC) (i.e., NCC calculated between "blocks", which are parts of the source and target images). This allows a global realignment of two images.

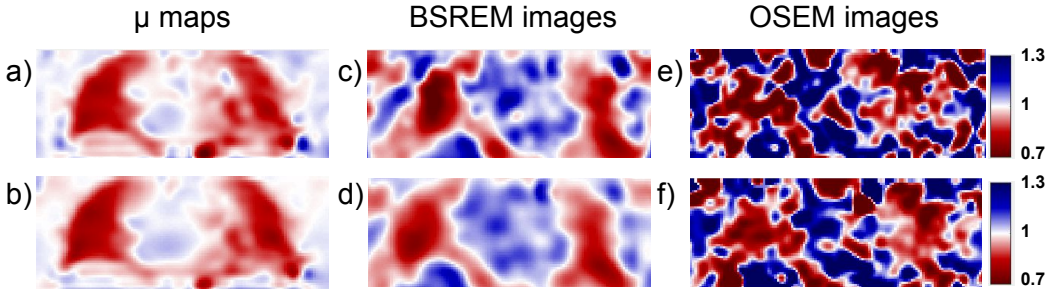

Figure 4.13: Jacobian maps obtained from NiftyReg LNCC registration, from μ maps (a) and b)), BSREM PET images (c) and d)) and OSEM PET images (e) and f)). Jacobian maps in a), c) and e) were obtained using a standard deviation of 5 voxels and in b), d) and f) a standard deviation of 10 voxels for the LNCC Gaussian window.

2. Non-rigid registration (using NiftyReg's *reg_f3d* executable, Modat et al. 2010). The similarity measure was chosen to be local normalised cross correlation (LNCC) (Cachier et al. 2003) using a Gaussian window to compute the local statistics. Two standard deviations σ_G were tested here: 5 voxels and 10 voxels along each axis. A larger standard deviation implies a more global registration, which could help for noisy images but the registration might be more sensitive to localised changes in intensity.

No lung mask was used in the non-rigid registration in order to compare with the previous registration technique using SSD. The regularisation penalties (and corresponding weights) were chosen as the default options given by NiftyReg, i.e., the bending energy penalty (sum of squared second derivatives of the transformation) and a linear elastic penalty (both penalties favour smooth warping).

We compare the results from the in-house mass-preserving SSD registration with the results from the open-source registration package NiftyReg.

The Jacobian determinant maps, corresponding to the different registrations on μ maps and PET images, are shown in Figure 4.13. The Jacobian maps depend only slightly on the choice of LNCC Gaussian windows. The Jacobian maps from the μ map registration are visually similar to the Jacobians map obtained with the in-house mass-preserving SSD registration. However, in the default settings, the NiftyReg LNCC registration seems more sensitive to the noise in the reconstructed PET images.

4.7 Discussion and Conclusion

In this chapter, we have evaluated the effect of motion and more particularly respiratory motion for PET/CT imaging, and introduced basic PET reconstruction methods to compensate for motion. In PET reconstruction, large motion artefacts can be observed for thorax acquisitions, due to both displacement of the radioactivity and changes of density and activity, due to compression and dilation of the lungs. These affect chest PET images visually and quantitatively, for both static and dynamic acquisitions. Lung image registration is also affected by density and activity concentration changes. In order to obtain good results, the optimisation needs to cope with those changes by either allowing local changes in the cost function (e.g., using LNCC as used in this chapter with NiftyReg) or modify the registration to incorporate a mass-preserving model (as performed here with our in-house SSD), which was the strategy adopted here.

In this chapter, we have concentrated on the effect and feasibility of including the Jacobian determinant in the cost function, prior to introducing it within the PET system model. To do so, a regularisation on the Jacobian determinant images and on the B-spline parameters was used. The image registration results could possibly have been better using a stationary velocity field (Christensen et al. 1996), which should lead to smoother deformation fields, especially for the OSEM PET images presented in Figure 4.13. However, we wanted to compare with the same type of deformation parameterisation as what was already implemented, therefore velocity fields were not investigated in this part.

At CT resolution, sliding motion (e.g., interlobar or intercostal) can lead to localised registration issues. Regularisation can be modified in order to accommodate better discontinuities due to sliding motion (Pace et al. 2011), however localised issues will still be present. Some authors have suggested to estimate different motion fields in different regions, for example using an automated lung mask for motion estimation (Vandemeulebroucke et al. 2012). Sliding motion was neglected here, but could be added to PET motion estimation in future work.

In Section 4.6.1, we have observed artefacts due to lung motion with the current scanner, with and without TOF. However, the errors near the diaphragm seemed to diminish in TOF reconstructions, therefore the question arises as to whether

artefacts can be resolved in the future, thanks to TOF scanners, with improved time resolutions. In recent years, TOF reconstructions have indeed gained popularity, thanks to better performance, especially in terms of image SNR (Conti 2011). The reconstructed images are also assumed to be more reliable in presence of model inconsistencies, such as errors in the attenuation map (Ahn et al. 2003). This was indeed the case in regions where the attenuation map was known accurately, in Section 4.6.1. Lung motion creates AC errors for non-gated PET reconstructions or gated reconstructions where the CT acquisition does not correspond perfectly to the PET gate. The effect of utilising TOF reconstruction versus non-TOF reconstruction in presence of attenuation errors will be discussed in the following chapter 5.

Chapter 5

Evaluation of the Effect of Attenuation Mismatches in TOF

5.1 Introduction

Reconstructing PET images from inconsistent data is common, particularly in lung imaging. The causes can be multiple: mis-estimation of the background sinogram, mis-alignment of the PET acquisition with the attenuation map, use of a wrong data model (e.g., due to changes in distribution), etc. Depending on the optimisation used to create the images, the effect on quantification will be different.

TOF PET reconstructions incorporate time information from a coincidence pair to estimate more accurately the localisation of the originating annihilation event (see Section 2.2.2.3). The optimisation problem becomes better determined, with more equations to solve, which usually leads to an overall better image quality and better quantification (Conti 2011). Current clinical TOF PET scanners have resolution between 210 ps (Van Sluis et al. 2019; Pan et al. 2019) and $\approx$ 550 ps (Bettinardi et al. 2011; Rausch et al. 2015), but sub-100 ps time resolutions are expected in the future (Lecoq 2017; Cates and Levin 2018). If 10 ps or higher time resolution can be achieved, this would allow for "reconstruction-less" PET images, as the detected events could be placed directly in the images, although effects such as photon attenuation and scatter will still have to be taken into account.

In this chapter, we will focus only on "attenuation mismatches", which are defined as the use of a wrong attenuation map to calculate the attenuation coefficients, use in the image reconstruction of PET data.

The use of "mismatched" attenuation maps in the PET reconstruction can

induce large quantification errors in the reconstructed images, as discussed theoretically in Thielemans et al. 2008, B. Bai et al. 2003 and Ahn et al. 2014 and clinically in Geramifar et al. 2013 and Nyflot et al. 2015b.

Apart from potential artefacts in the CT images acquired for attenuation (Sureshbabu et al. 2005), a common cause of such attenuation mismatch is motion in PET/CT imaging, as introduced in the previous Chapter 4. Indeed, when a single CT image is used to to calculate attenuation coefficients, unless the PET and the CT are perfectly aligned, there is an inherent mismatch because of respiratory motion. To deal with motion and reduce attenuation mismatches, it is usually common to bin the data into respiratory states, as described in Section 4.2.3. Some techniques to reduce mismatches will be discussed in Section 4.3. However, unless a continuous perfect motion model for event-by-event PET reconstruction is used (via listmode), intra-gate motion is unavoidable.

In non-TOF reconstruction (i.e., when the time information is not used), when far away from the edges, for an "emission object" that is large enough (for example, in the chest), the effect is mostly local and depends on the size of the perturbation area, as well as the amount of activity in the surrounding areas. This was used to derive approximations to quantify the error in the reconstructed PET image in the area where the mismatch occurs (Thielemans et al. 2008). In Ahn et al. 2014, the effect of mismatched attenuation maps in TOF reconstruction was also considered as local, which allowed the authors to obtain an approximation of the quantification errors. Under that assumption, if the object size is considered negligible compared to the time resolution, an estimation close to the one found in Thielemans et al. 2008 can be found, now depending on the time resolution instead of the size of the emission object. In both cases, only the local effect of a perturbation in the attenuation map on the emission image was considered in the analysis.

This chapter will focus on showing the non-local effect of attenuation mismatches for high time resolutions. It will first demonstrate first mathematically the non-local effect and its quantification error for perfect time resolution. Then, simulations and the reconstruction of patient data will demonstrate the quantification error, for different time resolutions.

5.2 Theory

5.2.1 PET Imaging System

As introduced in Section 2.3.2.4, the PET measured data take the form of a random vector $\boldsymbol{g} \in \mathbb{N}^{n_\mathrm{b}}$, where $[\boldsymbol{g}]_i$ is the number of counts at bin $i \in [\![1, n_\mathrm{b}]\!]$ and n_b is the number of detection bins. The imaging system is usually modelled as

$$\boldsymbol{p} = \boldsymbol{M}\boldsymbol{\lambda} + \boldsymbol{n} \tag{5.1}$$

where $\boldsymbol{p} = \mathbb{E}[\boldsymbol{g}]$, $\boldsymbol{\lambda} \in \mathbb{R}_+^{n_\mathrm{v}}$ is the unknown emission image, $\boldsymbol{M} \in \mathbb{R}^{n_\mathrm{b} \times n_\mathrm{b}}$ is the imaging system matrix, $\boldsymbol{n}$ is the background term (comprising randoms and scatter), and n_v is the number of voxels.

In the case of TOF PET systems, events are binned according to the difference of photon arrival time in addition to the detector pair. The time information is known with a temporal uncertainty, which defines the time resolution ΔT of the scanner. The number of detection bins n_b depends on the PET system, i.e., $n_\mathrm{b} = n_\mathrm{d}$ for non-TOF PET and $n_\mathrm{b} = n_\mathrm{d} n_\mathrm{t}$ for TOF PET, n_d and n_t denoting the number of detection bins for non-TOF reconstruction and the number of temporal bins, respectively.

Each entry $[\boldsymbol{M}]_{i,j} = M_{i,j}$ represents the probability that a pair of unscattered photons emitted in a voxel j is detected by the detector pair i, and incorporates the attenuation. In principle, detector blurring should be modelled after attenuation; however, for simplicity, we will consider the factorisation of $\boldsymbol{M}$ as Leahy and Qi 2000b

$$\boldsymbol{M} = \boldsymbol{a}(\boldsymbol{\mu})\boldsymbol{H}\,, \tag{5.2}$$

where $\boldsymbol{a}(\boldsymbol{\mu})$ is a $n_\mathrm{b} \times n_\mathrm{b}$ diagonal matrix containing the attenuation factors corresponding to $\boldsymbol{\mu}$ and $\boldsymbol{H}$ is a system matrix that incorporates a geometrical mapping between the source and the data—each entry $[\boldsymbol{H}]_{i,j} = H_{i,j}$ represents the probability that an emission from voxel j is detected by the detection bin i in the absence of attenuation.

The background term $\boldsymbol{n}$ includes scatter, which in practice can be estimated from the attenuation map (Watson et al. 1996; Ollinger 1996). In the remainder of

this section, we will assume that $\boldsymbol{n} = \boldsymbol{0}$, so that (5.1) becomes

$$\boldsymbol{p} = \boldsymbol{a}(\boldsymbol{\mu})\boldsymbol{H}\boldsymbol{\lambda}\,. \tag{5.3}$$

This can be achieved, for example, by subtracting $\boldsymbol{n}$ from $\boldsymbol{p}$ and zeroing the negative values.

5.2.2 Spatial Extent of Activity Errors due to Local Attenuation Mismatch

We assume the true activity and attenuation images are respectively $\boldsymbol{\lambda}^\star \in \mathbb{R}_+^{n_\mathrm{v}}$ and $\boldsymbol{\mu}^\star \in \mathbb{R}_+^{n_\mathrm{v}}$. Furthermore, we assume that $\boldsymbol{H}$ is full rank with $n_\mathrm{b} \geq n_\mathrm{v}$ such that the mapping $\boldsymbol{H}\colon \boldsymbol{x} \mapsto \boldsymbol{H}\boldsymbol{x}$ is injective. The transmission system matrix—used to generate the attenuation coefficients—is the discretised line integral operator $\boldsymbol{R} \in \mathbb{R}^{n_\mathrm{d} \times n_\mathrm{v}}$.

The attenuation coefficient diagonal matrix $\boldsymbol{a}(\boldsymbol{\mu})$ is of size $n_\mathrm{d}n_\mathrm{t} \times n_\mathrm{d}n_\mathrm{t}$ (in non-TOF PET, $n_\mathrm{t} = 1$) and for each bin detector pair $d \in [\![1, n_\mathrm{d}]\!]$ and time bin $t \in [\![1, n_\mathrm{t}]\!]$, the diagonal element at the detection bin $i = (d-1) \times n_\mathrm{t} + t$ is

$$[\boldsymbol{a}(\boldsymbol{\mu})]_{i,i} = \exp(-[\boldsymbol{R}\boldsymbol{\mu}]_d)\,,$$

that is to say, in TOF PET, the attenuation coefficients are independent of the time bin.

Let $\boldsymbol{p}^\star$ be an idealised noiseless measurement of the true activity $\boldsymbol{\lambda}^\star$ with attenuation $\boldsymbol{\mu}^\star \in \mathbb{R}^{n_\mathrm{v}}$, i.e.,

$$\boldsymbol{p}^\star = \boldsymbol{a}(\boldsymbol{\mu}^\star)\boldsymbol{H}\boldsymbol{\lambda}^\star\,. \tag{5.4}$$

In absence of noise, the PET image reconstruction problem becomes

$$\text{find } \boldsymbol{\lambda} \text{ such that} \quad \boldsymbol{p}^\star = \boldsymbol{a}(\boldsymbol{\mu}^\star)\boldsymbol{H}\boldsymbol{\lambda} \tag{5.5}$$

and has a unique solution $\boldsymbol{\lambda} = \boldsymbol{\lambda}^\star$.

Now assume that the attenuation map $\widetilde{\boldsymbol{\mu}}$ used for reconstruction is a perturbed version of $\boldsymbol{\mu}^\star$, i.e., $\widetilde{\boldsymbol{\mu}} = \boldsymbol{\mu}^\star + \boldsymbol{\eta}$ where $\boldsymbol{\eta}$ is a small perturbation supported on a small

region far from the edges. The reconstruction problem (5.5) is equivalent to solving

$$\begin{aligned} \boldsymbol{a}(\widetilde{\boldsymbol{\mu}})\boldsymbol{H}\boldsymbol{\lambda} &= \boldsymbol{a}(\boldsymbol{\mu}^\star)\boldsymbol{H}\boldsymbol{\lambda}^\star \\ \Leftrightarrow \qquad \boldsymbol{H}\boldsymbol{\lambda} &= \boldsymbol{a}(-\boldsymbol{\eta})\boldsymbol{H}\boldsymbol{\lambda}^\star \end{aligned}$$

Non-TOF PET : Along the lines of Thielemans et al. 2008 and Ahn et al. 2014, using a Taylor expansion around $\boldsymbol{R}\boldsymbol{\mu}^\star$, the problem is approximated in non-TOF PET to:

$$\boldsymbol{H}(\boldsymbol{\lambda} - \boldsymbol{\lambda}^\star) \approx \text{diag}[\boldsymbol{R}\boldsymbol{\eta}]\boldsymbol{H}\boldsymbol{\lambda}^\star \tag{5.6}$$

where diag[·] is the operator that generates a diagonal matrix from a vector.

By introducing some further approximations, Thielemans et al. 2008 derived a formula applicable to non-TOF PET:

$$\boldsymbol{R}(\boldsymbol{\lambda} - \boldsymbol{\lambda}^\star) \approx \rho\boldsymbol{R}\boldsymbol{\eta} \tag{5.7}$$

where ρ is the mean projected activity along the LORs intersecting the support of $\boldsymbol{\eta}$. Approximation (5.7) shows that when $\boldsymbol{\mu}$ and $\boldsymbol{\mu}^\star$ differ from a local perturbation $\boldsymbol{\eta}$, then, by injectivity of $\boldsymbol{R}$, the solution to the approximated reconstruction problem is $\widehat{\boldsymbol{\lambda}} = \boldsymbol{\lambda}^\star + \rho\boldsymbol{\eta}$, which suggests that the error in the reconstructed activity remains localised on the mismatch.

TOF PET : Equation (5.6) can be extended to TOF PET, i.e., for all line of response i intersecting the support of $\boldsymbol{\eta}$ and for all time bin t,

$$[\boldsymbol{H}(\boldsymbol{\lambda} - \boldsymbol{\lambda}^\star)]_i \approx [\boldsymbol{R}\boldsymbol{\eta}]_d[\boldsymbol{H}\boldsymbol{\lambda}^\star]_i \,. \tag{5.8}$$

Approximation (5.8) implies that for all lines of response i intersecting the mismatch area, the error between the reconstructed activity $\hat{\boldsymbol{\lambda}}$ and $\boldsymbol{\lambda}^\star$ propagates to each time bin t by a factor proportional to $[\boldsymbol{R}\boldsymbol{\eta}]_d$, which means the error can no longer be considered local.

The previous equation (5.8) implies that in most cases the system to solve is made of inconsistent equations. For this reason, the solution depends on the cost function used for solving such reconstruction problem.

5.2.3 Maximum-Likelihood Expectation Maximisation

In this section we deepen the analysis from Section 5.2.2 by investigating the effect of the attenuation mismatch from the perspective of MLEM reconstruction. We will consider the highly idealised case of perfect spatial resolution here.

We denote for $(i,j) \in [\![1, n_\mathrm{b}]\!] \times [\![1, n_\mathrm{v}]\!]$ (here i is a TOF bin and $n_\mathrm{b} = n_\mathrm{d} n_\mathrm{t}$):

- $\widehat{\boldsymbol{\lambda}} = \left[\widehat{\lambda}_j\right]$ the activity image reconstructed with the true attenuation map $\boldsymbol{\mu}^\star$, i.e., using $\boldsymbol{M}^\star = \left[M^\star_{i,j}\right] = \boldsymbol{a}(\boldsymbol{\mu}^\star)\boldsymbol{H}$.
- $\widetilde{\boldsymbol{\lambda}} = \left[\widetilde{\lambda}_j\right]$ the activity image reconstructed with a wrong attenuation map $\widetilde{\boldsymbol{\mu}}$, where $\widetilde{\boldsymbol{M}} = \left[\widetilde{M}_{i,j}\right] = \boldsymbol{a}(\widetilde{\boldsymbol{\mu}})\boldsymbol{H}$.

We also define the sets

$$\mathcal{S}_j = \{\, i \in [\![1, n_\mathrm{b}]\!] \mid H_{i,j} \neq 0 \,\}\,.$$

In a hypothetical case of an activity image reconstructed with perfect time resolution as well as perfect spatial resolution, the $\mathcal{S}_j$ are disjoint, so that

$$\forall i \in [\![1, n_\mathrm{b}]\!],\ \exists! j \in [\![1, n_\mathrm{v}]\!],\ i \in \mathcal{S}_j. \tag{5.9}$$

Given a system matrix $\boldsymbol{M}$, which can either be $\boldsymbol{M}^\star$ or $\widetilde{\boldsymbol{M}}$, and the measurement data $\boldsymbol{p} = \{p_i\}_{i \in [\![1, n_\mathrm{b}]\!]}$, the MLEM algorithm $(k+1)$-th iteration at a voxel j is

$$\lambda_j^{(k+1)} = \frac{\lambda_j^{(k)}}{M_j} \sum_{i=1}^{n_\mathrm{b}} M_{i,j} \frac{p_i}{\sum_{l=1}^{n_\mathrm{v}} M_{i,l} \lambda_l^{(k)}} \tag{5.10}$$

where $M_j = \sum_{i=1}^{n_\mathrm{b}} M_{i,j}$ and $\lambda_j^{(k)}$ is the value of the activity image at a voxel j and iteration k (Dempster et al. 1977; Shepp and Vardi 1982; Lange and Carson 1984).

In TOF PET, assuming the temporal resolution is perfect, condition (5.9) holds and therefore $\sum_{l=1}^{n_\mathrm{v}} M_{i,l} \lambda_l^{(k)} = M_{i,j} \lambda_j^{(k)}$. Equation (5.10) simplifies to

$$\lambda_j^{(k+1)} = \frac{\lambda_j^{(k)}}{M_j} \sum_{i \in \mathcal{S}_j} M_{i,j} \frac{p_i}{M_{i,j} \lambda_j^{(k)}} = \frac{\sum_{i \in \mathcal{S}_j} p_i}{\sum_{i \in \mathcal{S}_j} M_{i,j}} \tag{5.11}$$

and convergence is achieved after one iteration. Substituting $\boldsymbol{M}$ with $\boldsymbol{M}^\star$ and $\widetilde{\boldsymbol{M}}$

successively in (5.11) leads to

$$\frac{\widetilde{\lambda}_j}{\widehat{\lambda}_j} = \frac{\sum_{i\in\mathcal{S}_j} M^{\star}_{i,j}}{\sum_{i\in\mathcal{S}_j} \widetilde{M}_{i,j}} \tag{5.12}$$

The quantification of the non-local effect due to a local error in the attenuation map, from Equation (5.8) can therefore be quantified easily for MLEM/OSEM in the case of perfect time resolution by the relative error

$$\frac{\widetilde{\lambda}_j - \widehat{\lambda}_j}{\widehat{\lambda}_j} = \frac{\sum_{i\in\mathcal{S}_j} M^{\star}_{i,j}}{\sum_{i\in\mathcal{S}_j} \widetilde{M}_{i,j}} - 1 \tag{5.13}$$

It is worth noticing that for small attenuation mismatches and using the same first-order Taylor expansion around $\boldsymbol{\mu}^{\star}$, (5.13) resembles an image space version of (5.8).

5.3 Experiments and Results

In this section we will study the quantification errors in TOF reconstruction due to attenuation mismatches for MLEM/OSEM.

5.3.1 Summary of Simulated and Patient Data

We use four different datasets, either simulated for or acquired on a GE Discovery 690 PET/CT scanner (Bettinardi et al. 2011). The PET reconstructions use two different attenuation maps: the true attenuation map $\boldsymbol{\mu}^{\star}$ and a wrong attenuation map $\widetilde{\boldsymbol{\mu}}$.

5.3.1.1 Simulations

The simulated datasets are the following (similar to that of Holman et al. 2016):

Simulation 1: A 28.8-cm diameter uniform cylinder (linear attenuation: $0.916\,\mathrm{cm}^{-1}$) is placed at the centre of the FOV. The wrong attenuation map $\widetilde{\boldsymbol{\mu}}$ is known accurately in the reconstruction except for one small cylinder (diameter = 6 mm) at the centre of the FOV, where the attenuation is overestimated by 15%. This simulation is aimed at studying the impact of a very small attenuation mismatch on the reconstructed activity image. The phantom volumes are shown in Figure 5.1.

Simulation 2: An XCAT PET/CT simulation of an FDG oncological pulmonary acquisition at end-inspiration (tumour of $1\,\mathrm{cm}^3$ situated in the lower right lung).

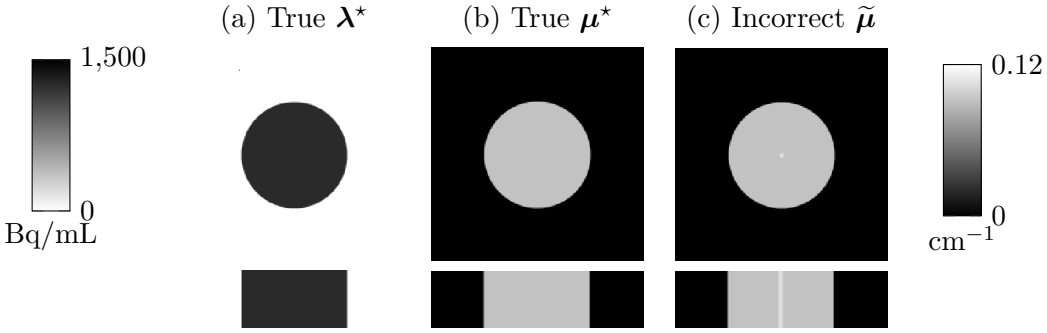

Figure 5.1: Simulation 1 – Axial and coronal views of the input images used: (a) true activity, (b) true attenuation and (c) incorrect attenuation.

Two incorrect input $\widetilde{\boldsymbol{\mu}}$ maps are assessed:

- *Lung density changes only*: The incorrect $\widetilde{\boldsymbol{\mu}}$ map (denoted $\widetilde{\boldsymbol{\mu}}_1$) is aligned with the structures in the PET data, however the density in the lung is not known accurately (overestimation of 15%). Note that the lung tumour density does not change, as the structure is considered rigid. Such simulation is relevant in MCIR or gated reconstruction, when a static $\boldsymbol{\mu}$ map is warped to another respiratory gate (for which intra-motion is negligible), but the changes in density are not considered.

- *Lung density changes + misalignment*: The incorrect $\widetilde{\boldsymbol{\mu}}$ map (denoted $\widetilde{\boldsymbol{\mu}}_2$) corresponds to the end-expiration state, therefore both structure alignment and lung density are wrong. The input simulation images are given in Figure 5.2.

Data Generation: The simulations were performed using STIR with TOF (Efthimiou et al. 2018) in the following order:

1. Forward projection of the true activity image $\boldsymbol{\lambda}^\star$ to obtain the non-attenuated projection data.

2. Calculation of the attenuation coefficient sinogram $\boldsymbol{a}(\boldsymbol{\mu}^\star)$ from the true attenuation map $\boldsymbol{\mu}^\star$ and multiplication by the projection data.

3. Reconstruction of the attenuated projection data using either the true attenuation map $\boldsymbol{\mu}^\star$ or the incorrect attenuation map $\widetilde{\boldsymbol{\mu}}$.

To assess the effect of varying time resolution in the TOF reconstruction, the overall scanner geometry of the GE PET/CT Discovery 690 was used, but some changes were done to the TOF characteristics:

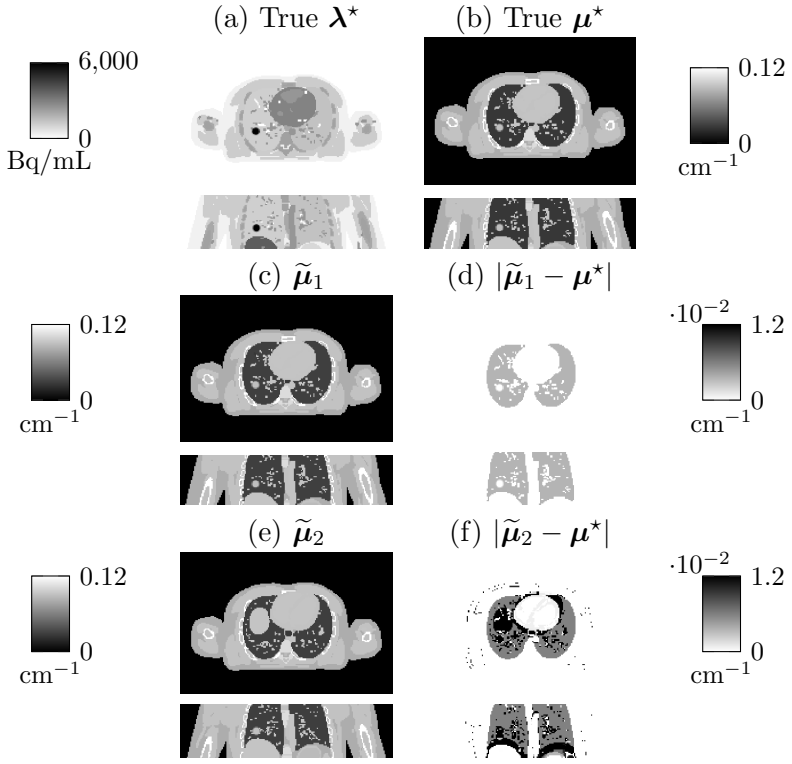

Figure 5.2: Simulation 2 – Axial and coronal views of the input images used: (a) true activity $\boldsymbol{\lambda}^\star$, (b) true attenuation $\boldsymbol{\mu}^\star$, (c) incorrect attenuation $\widetilde{\boldsymbol{\mu}}_1$, (d) absolute difference between $\boldsymbol{\mu}^\star$ and $\widetilde{\boldsymbol{\mu}}_1$ (e) incorrect attenuation $\widetilde{\boldsymbol{\mu}}_2$ and (f) absolute difference between $\boldsymbol{\mu}^\star$ and $\widetilde{\boldsymbol{\mu}}_2$.

- The maximal number of TOF bins extended to 175 (of width equal 28 ps) instead of the original 55 bins (of width ≈ 89 ps).

- The time resolution was modified to test a range of time resolutions, from 70 ps to 550 ps.

Image Reconstruction : For the simulations, the projection data were reconstructed using STIR with MLEM, using a sufficient number of iterations so that the mean difference between the last two iterations was less than 0.1% overall, when the correct attenuation map was used in the reconstruction. The numbers of iterations for the TOF reconstructions, depending therefore on the time resolution, are given in Table 5.1. 1600 iterations were used in non-TOF reconstructions. For computational reasons, TOF "mashing" was used in this work: adjacent TOF bins are summed together to create a new TOF sinogram with larger TOF bins. Only small loss was reported for quantification (Efthimiou et al. 2018).

TOF FWHM	70	100	150	200	250	300	350	400	450	500	550
MLEM iteration #	80	160	160	240	240	240	240	240	240	240	240

Table 5.1: Time resolution FWHM simulated and the corresponding number of MLEM iterations used.

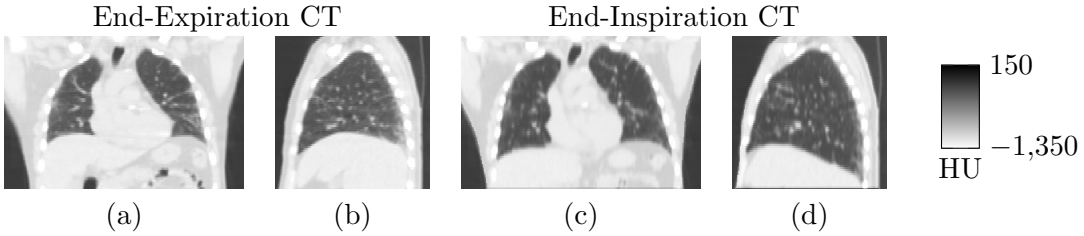

Figure 5.3: Patient Data – (a) Coronal and (b) sagittal view of the end-expiration CT image and (c) coronal and (d) sagittal view of the end-inspiration CT image, used to derive the attenuation maps in this study.

5.3.1.2 Patient Data

The same patient from the Coagulation Study (Section 6.4.1) as in Section 4.6.1 was selected for this study. Two different CT acquisitions were available: one at end-expiration CTAC acquisition and one end-inspiration HRCT. The listmode data was also amplitude-gated into 4 respiratory bins, using the respiratory trace from a Varian RPM system.

The end-expiration gated PET data were reconstructed using two μ maps $\boldsymbol{\mu}^\star$ and $\widetilde{\boldsymbol{\mu}}$, computed from the end-expiration and the end-inspiration CT images, respectively. The patient data were reconstructed using GE proprietary software in MATLAB (Matlab 2016b), with OSEM using 8 subsets with 200 iterations for non-TOF data and 100 iterations for TOF data.

5.3.1.3 Measures

At a given time resolution, we denote $\tilde{\boldsymbol{\lambda}}$ and $\widehat{\boldsymbol{\lambda}}$ the reconstructed images at the final reconstruction iteration, using the true attenuation map $\boldsymbol{\mu}^\star$ and the incorrect attenuation map $\widetilde{\boldsymbol{\mu}}$, respectively.

In the following, we will use the relative errors in absolute value defined in a ROI $\mathcal{R}$ as

$$|\mathrm{RE}|_{\mathcal{R}} = \frac{\left|\underset{\mathcal{R}}{\mathrm{mean}}(\tilde{\boldsymbol{\lambda}}) - \underset{\mathcal{R}}{\mathrm{mean}}(\widehat{\boldsymbol{\lambda}})\right|}{\underset{\mathcal{R}}{\mathrm{mean}}(\widehat{\boldsymbol{\lambda}})}$$

where $\underset{\mathcal{R}}{\mathrm{mean}}(\cdot)$ designates the mean value in $\mathcal{R}$.

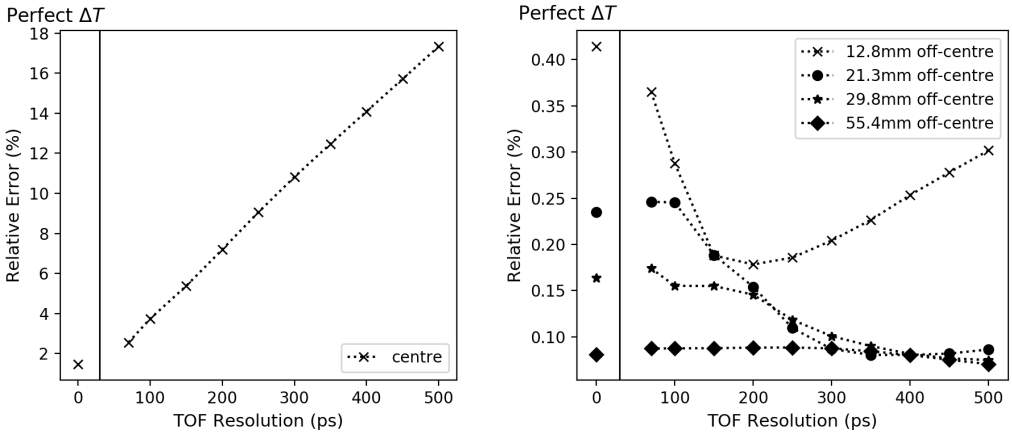

Figure 5.4: Simulation 1 – Relative errors versus time resolution at the centre of the cylinder (left) and for three off-centre ROIs (right), from the reconstructions and from Equation (5.13). We used two subplots due to scale differences.

We also define the relative difference image $\mathbf{RD}_\lambda$ (in absolute values) such that

$$[\mathbf{RD}_\lambda]_{j\in[\![1,n_\mathrm{v}]\!]} = \frac{\left|\widetilde{\lambda}_j - \widehat{\lambda}_j\right|}{\widehat{\lambda}_j}$$

5.3.2 Results

5.3.2.1 Simulation 1

We consider five ROIs. The first one is placed at the centre of the FOV, therefore at the centre of the perturbation area. The four other ROIs are off-centre (distance between the centre of the FOV and the ROIs: 12.8 mm, 21.3 mm, 29.8 mm and 55.4 mm respectively).

We computed the relative error within the perturbation area and in four off-centre ROIs. The plots showing the relative errors with respect to the time resolution are shown in Figure 5.4, where the relative error at perfect time resolution was predicted by Equation (5.13).

The first subplot is consistent with previous results on TOF, where improve time resolution decreases locally errors in the activity images. The second subplot confirms that the errors propagate globally in the image, in agreement with Equation (5.8).

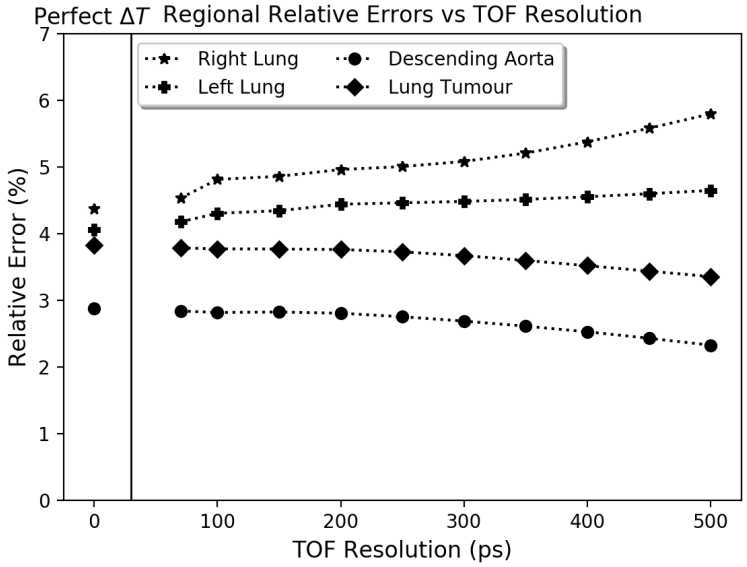

Figure 5.5: Simulation 2 (*Lung density changes only*) – Relative errors versus time resolution in different ROIs: left lung, right lung, lung tumour and descending aorta.

5.3.3 Simulation 2: Lung XCAT Simulation

5.3.3.1 Lung density changes only:

In Figure 5.5, the relative errors are plotted in different ROIs (left and right lungs, descending aorta and lung tumour), relatively to time resolution. Similarly as for Simulation 1, the relative errors within the lungs (where the attenuation mismatch is located) decrease with improved time resolution. However, the errors increase in the lung tumour and the descending aorta. The same behaviour was observed for the right and left ventricles, as well as ascending aorta (results not shown). The results show the propagation of the errors outside of the lungs (where the attenuation mismatches lie), in neighbouring regions, as predicted by Formula (5.13).

5.3.3.2 Lung density changes + misalignment:

In Figure 5.7, the relative difference images in absolute values are shown.

Additionally, the relative errors $\mathrm{RE}_{\mathcal{R}}$ were quantified in different ROIs $\mathcal{R}$: ascending aorta (AA), descending aorta (DA), left ventricle (LV), right ventricle (RV) and liver. The relative differences |RD| between $\widehat{\boldsymbol{\lambda}}$ and $\tilde{\boldsymbol{\lambda}}$ are given in Table 5.2.

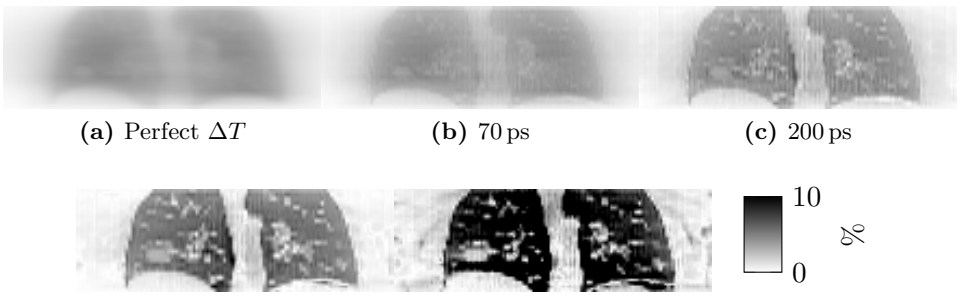

(a) Perfect ΔT **(b)** 70 ps **(c)** 200 ps

(d) 550 ps **(e)** non-TOF

Figure 5.6: Simulation 2 (*Lung density changes only*) – Relative errors in absolute values, in coronal view (a) expected at perfect time resolution and for four reconstructions with different TOF resolution: (b) 70 ps, (c) 200 ps, (d) 550 ps and (e) non-TOF.

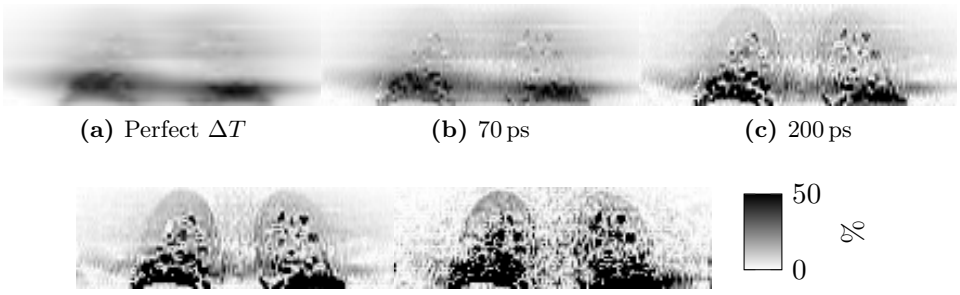

(a) Perfect ΔT **(b)** 70 ps **(c)** 200 ps

(d) 550 ps **(e)** non-TOF

Figure 5.7: Simulation 2 (*Lung density changes + misalignment*) – Relative errors in absolute values, in coronal view (a) expected at perfect time resolution and for four reconstructions with different TOF resolution: (b) 70 ps, (c) 200 ps, (d) 550 ps and (e) non-TOF.

ROI	AA	DA	LV	RV
Perfect TOF	12.8%	3.3%	22.9%	25.5%
70 ps	12%	1.0%	23.0%	26.6%
200 ps	8.8%	1.7%	20.9%	27.9%
550 ps	6.5%	4.5%	14.2%	21.8%
non-TOF	8.3%	5.4%	13.3%	16.6%

Table 5.2: Simulation 2 (*Lung density changes + misalignment*) – Relative errors $|\mathrm{RE}|_{\mathcal{R}}$ for different time resolutions and for non-TOF in different ROIs $\mathcal{R}$: ascending aorta (AA), descending aorta (DA), left ventricle (LV), right ventricle (RV) and liver.

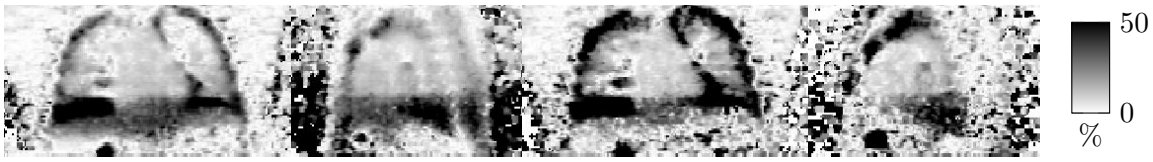

Figure 5.8: Patient Data – Relative errors for TOF reconstruction (550 ps) in (a) coronal and (b) sagittal views and for non-TOF reconstruction in (c) coronal and (d) sagittal views.

ROI	AA	U-DA	L-DA	LV	RV	Liver
TOF	5.1%	2.1%	14.0%	8.2%	5.7%	8.6%
non-TOF	2.7%	0.5%	13.5%	2.8%	3.6%	5.1%

Table 5.3: Patient data – Relative errors $|\mathrm{RE}|_{\mathcal{R}}$ in TOF and non-TOF in different ROIs $\mathcal{R}$: ascending aorta (AA), upper descending aorta (U-DA), upper descending aorta (L-DA), left ventricle (LV), right ventricle (RV) and liver.

5.3.4 Patient Data

The two input CT images and the relative errors images are shown in Figures 5.3 and 5.8, respectively.

Additionally, ROIs were drawn on the end-expiration CT for measurements, using ITK-SNAP (Yushkevich et al. 2006): Ascending Aorta (AA, 1.76 cm^3), Descending Aorta (DA, 1.76 cm^3), Left Ventricle (LV, 1.76 cm^3) and Right Ventricle (RV, 1.54 cm^3).

The relative differences $|\mathrm{RE}|_{\mathcal{R}}$ in different ROI $\mathcal{R}$ between $\widehat{\boldsymbol{\lambda}}$ and $\tilde{\boldsymbol{\lambda}}$ are shown in Table 5.3.

5.4 Discussion and Conclusion

The time information in PET has helped to achieve better image quality and quantification. However, accurate attenuation information is still essential in the reconstruction, as the results from this chapter demonstrates.

Indeed, the effect of using an incorrect attenuation map in the reconstruction on the reconstructed activity image cannot be considered local in TOF reconstructions. The relative errors depend on the optimisation chosen to reconstruct the data and can be quantified for perfect time resolution for algorithms such as MLEM. For high resolutions such as 100 ps or below, the latter should be close to the projected relative errors at perfect time resolution. For intermediate time resolutions however,

obtaining an approximation to link inconsistencies in the attenuation map and errors in the reconstructed activity image for a given reconstruction algorithm would be a hard task in general cases when no symmetry arguments can be used, as the formulation will depend highly on the object/body geometry, as well as the time resolution.

Three simulations were used to show the errors for different time resolutions (using MLEM). The first simulation corresponds to a simple cylinder, with an error in the attenuation map in the middle of the FOV. For improved time resolutions, the error became local and at 70 ps was very close to the formula corresponding to perfect time resolution. Two XCAT lung simulations were also used. The first simulation had no misaligned structures in the attenuation map, however the attenuation values were wrong in the lung. This is relevant for MCIR which does not consider changes in density or activity, see in the next Chapter 6. At higher time resolution, errors were found greater outside of the lungs, for example in the Ascending Aorta or in the heart. The second XCAT simulation is an example of gated PET reconstruction which uses a misaligned attenuation map (i.e., encompassing also changes in density). This extreme case showed the large effect on the quantification. Finally end-expiration patient data were reconstructed using two different μ maps: one close to the PET gate and the second one corresponding to end-inhalation. Both TOF (FWHM: 550 ps) and non-TOF were employed. The results were similar to those observed with the second XCAT simulation. While differences in the lung reduced with increased TOF timing resolution, they increased in most neighbouring ROIs, such as the ascending aorta (from 2.7% to 5.1%) or the left ventricles (from 2.8% to 8.2%), similarly to the 12.8 mm off-centre ROI of the cylindrical simulation.

In addition to problems with quantification in static PET images, the results in this chapter show that using an incorrect attenuation map could have implications in kinetic modelling, especially in the lung. Indeed, nowadays blood samplings are avoided to obtain the input functions used in compartmental modelling (Section A.1 in Appendix A), therefore it is common to draw ROIs in blood vessels such as the aorta to obtain image-derived input functions (IDIFs). However, as those regions are often neighbouring the lungs, at high time resolution the quantification might be less accurate. In Kotasidis et al. 2016, attenuation mismatches were discussed

for kinetic modelling in TOF reconstructions: biases were reduced at high time resolution, but could not be completely resolved; this is consistent with our results.

Additionally to quantification problems, the convergence of the MLEM was also slowed down in presence of attenuation mismatches. This could be a problem when trying to standardise reconstruction parameters.

A possibility to correct the attenuation map is by using an algorithm such as MLAA. This will be further discussed in Section 4.3.5 of the following chapter. When TOF information is available, it is possible to determine, from the prompts and an initial guess of the attenuation map, the corrected attenuation sinogram up to a constant sinogram (Defrise et al. 2012). It becomes therefore possible to compute precisely the entire attenuation sinogram when at least a part of it is known precisely (e.g., when a region of the μ map is known). From this work, one might theorise that this is closely related to the non-local effect of using an incorrect attenuation on the activity image in TOF reconstruction. The cross-talk identified in non-TOF therefore disappears when the error provoked by using a wrong attenuation map in the reconstruction tends to be non-local, therefore MLAA becomes globally more sensitive to any changes.

The work in this chapter only focused on attenuation mismatches. Data inconsistencies due to incorrect background term within the reconstruction (i.e., bad estimations of randoms and scatters) could also be studied. A recent publication demonstrated that an accurate estimation of the scatter sinogram was important in TOF-MLAA to obtain quantitative measures (Rezaei et al. 2019).

The following Chapter 6 is dedicated to reconstruction algorithms that encompass motion compensation, with an overview of the main existing algorithms, accounting for tissue displacement and/or density changes, followed by a presentation of a method to compensate for the two components of the motion.

Chapter 6

Tackling Respiratory Motion in the Lung

6.1 Introduction

Chapters 4 and 5 demonstrated the issues linked to motion in the lung, for both static and dynamic acquisitions, and discussed some methods to compensate for motion in PET reconstruction. They also showed the impact on PET quantification of data inconsistencies between the attenuation map and the acquired PET data in standard PET reconstruction, such as MLEM. This also demonstrates the importance of a robust motion compensation in lung PET imaging, where both tissue displacement and density changes would be accounted for. The problem linked to respiratory motion is even greater in IPF imaging as the pathological fibrosis is usually located at the base of the lungs, where the motion is predominant. Mass preservation assumes that changes in density and activity concentration observed in lung PET/CT imaging can be quantified using a measure obtained from the deformations between respiratory gates, as introduced in the previous chapter 4. This will be developed for joint image reconstruction and motion estimation (JRM) in this chapter.

In this chapter, two motion-compensating methods will be presented for dynamic PET MCIR and mass-preserving (static PET) MCIR, with a view to correct PET images corresponding to IPF patients. They will be tested on simulated data and on parts of the acquisition data corresponding to the Coagulation Study (only results for pre-treatment data or control patients from the Coagulation Study will be demonstrated here). Cardiac contraction motion will not be taken into account

in the motion compensation.

6.2 Joint Motion Reconstruction

6.2.1 Motion-Dependent Log-Likelihood

In Chapter 2, any type of motion or change in distributions was neglected in the log-likelihood L of Equation (2.22). However, as PET acquisitions are longer than the cardiac and respiratory cycles, the log-likelihood corresponding to abdominal PET acquisitions needs to include a dependence on motion state.

In practice, the acquired PET data $\boldsymbol{g} = \{g_i\}_{i \in [\![1, n_\mathrm{b}]\!]}$ can be binned into several "gates" (where n_g is the number of gates), for which intra-gate motion can be considered negligible in comparison to the PET resolution. The Equation 2.22 can be modified to include the motion states/gates $\ell \in [\![1, n_\mathrm{g}]\!]$. Indeed if we denote $\boldsymbol{g}_\ell$ the corresponding "gated" acquired data, we have:

$$\forall \ell \in [\![1, n_\mathrm{g}]\!], \quad \boldsymbol{g}_\ell \sim \mathrm{Poisson}(\bar{\boldsymbol{g}}(\lambda_\ell, \mu_\ell)) \,, \tag{6.1}$$

where $\bar{\boldsymbol{g}}(\lambda_\ell, \mu_\ell)$ is the expected number of counts at the gate ℓ, which depends on the activity distribution λ_ℓ and the attenuation distribution μ_ℓ, corresponding to the activity and attenuation distributions at the gate ℓ, respectively. To follow the notations in Bousse et al. 2016a, for a given detection bin i and a gate ℓ, the expected number of counts is given by:

$$\bar{g}_i(\lambda_\ell, \mu_\ell) = \tau_\ell \, a_i(\mu_\ell) H_i \lambda_\ell + s_{i,\ell} \,, \tag{6.2}$$

where τ_ℓ corresponds to the duration of the binned gate ℓ and $s_{i,\ell}$ is the background term for the ℓ-th gate at the detection bin i (i.e., comprising both scatters and randoms). The corresponding log-likelihood L is such that:

$$L(\lambda, \mu) = \sum_{\ell=1}^{n_\mathrm{g}} \sum_{i=1}^{n_\mathrm{b}} g_{i,\ell} \log \bar{g}_i(\lambda_\ell, \mu_\ell) - \bar{g}_i(\lambda_\ell, \mu_\ell) \,. \tag{6.3}$$

In absence of gross motion during the PET acquisition, a motion state could be defined from distinct cardiac and respiratory states. However, in this thesis, cardiac contraction motion will be ignored. n_g will therefore represent the num-

ber of respiratory bins, which are obtained from a respiratory surrogate signal (see Section 4.3).

In Bousse et al. 2016a, the background sinogram $\boldsymbol{s}$ corresponding to the entire PET acquisition (comprising both randoms and scatters) was first estimated from the input attenuation map, without any deformation. From this estimation, $\forall \ell$, the background sinograms $\boldsymbol{s}_\ell$ were computed as $K_\ell \, \boldsymbol{s}$, where $K_\ell = D_\ell \frac{\tau_\ell}{\sum_l \tau_l}$ for each gate (τ_ℓ is the gate duration and D_ℓ is a factor related to decay factors). This was motivated by Burgos et al. 2016, where small differences in the estimated scatter sinogram resulted in small differences in the reconstructed images. Additionally, the tails from $K_\ell \, \boldsymbol{s}$ were visually assessed against the tails of the gated projection data before using the rescaled background in Bousse et al. 2016a. However, recent work demonstrated the importance of re-estimating the background sinogram for accurate quantification in joint reconstruction (Brusaferri et al. 2019; Rezaei et al. 2019). Therefore the estimation of gated background term will be compared to the previous strategy (see Section 6.4.3.2).

6.2.2 Standard JRM

Bousse *et al.* proposed a JRM scheme where the emission image $\boldsymbol{\lambda}$ and a set of diffeomorphisms φ_ℓ, as in previous Chapter 4, are estimated from the binned projection data $(\boldsymbol{g}_\ell)_{\ell=1}^{n_\mathrm{g}}$ and a single attenuation image $\boldsymbol{\mu}$.

The emission and attenuation images can be defined at each gate $\ell \in [\![1, n_\mathrm{g}]\!]$ as $\boldsymbol{\lambda}_\ell = \boldsymbol{\mathcal{W}}_{\varphi_\ell} \boldsymbol{\lambda}$ and $\boldsymbol{\mu}_\ell = \boldsymbol{\mathcal{W}}_{\varphi_\ell} \boldsymbol{\mu}$, where $\boldsymbol{\mathcal{W}}_{\varphi_\ell}$ is the (discretised) standard warping operator defined in the previous chapter 4. A B-spline parameterisation is used for the motion fields (Bousse et al. 2016a), as described in Section 4.5.1. The B-spline coefficients at gate ℓ are denoted $\boldsymbol{\alpha}_\ell = \left(\boldsymbol{\alpha}_\ell^X, \boldsymbol{\alpha}_\ell^Y, \boldsymbol{\alpha}_\ell^Z\right)$ and the collection of B-spline coefficients for all n_g gates is denoted $\boldsymbol{\theta} = (\boldsymbol{\alpha}_\ell)_{\ell=1}^{n_\mathrm{g}}$.

Using the warping operator, the discretised log-likelihood for multiple gates (Equation 6.3) can be rewritten as:

$$L(\boldsymbol{\lambda}, \boldsymbol{\theta}, \boldsymbol{\mu}) = \sum_{\ell=1}^{n_\mathrm{g}} \sum_{i=1}^{n_\mathrm{b}} g_{i,\ell} \log \bar{g}_i(\boldsymbol{\lambda}, \boldsymbol{\alpha}_\ell, \boldsymbol{\mu}) - \bar{g}_i(\boldsymbol{\lambda}, \boldsymbol{\alpha}_\ell, \boldsymbol{\mu}) \,, \tag{6.4}$$

where $\bar{g}_i(\boldsymbol{\lambda}, \boldsymbol{\alpha}_\ell, \boldsymbol{\mu}) = \tau_\ell \, a(\boldsymbol{\mathcal{W}}_{\varphi_\ell} \boldsymbol{\mu}) \, [\boldsymbol{H} \boldsymbol{\mathcal{W}}_{\boldsymbol{\varphi_\ell}} \boldsymbol{\lambda}]_i + s_{i,\ell}$ (where $\boldsymbol{H}$ is the discretised system matrix, excluding the attenuation corrector factors, similarly as in Section 5.2.1 of

Chapter 4) and $a_i(\boldsymbol{\mathcal{W}}_{\varphi_\ell}\boldsymbol{\mu})$ is the attenuation factor corresponding to the warped attenuation map $\boldsymbol{\mathcal{W}}_{\varphi_\ell}\boldsymbol{\mu}$.

In order to control noise, regularisation has to be added for both the motion estimation and the image reconstruction, resulting in a penalised log-likelihood:

$$\Phi(\boldsymbol{\lambda}, \boldsymbol{\theta}, \boldsymbol{\mu}) \triangleq L(\boldsymbol{\lambda}, \boldsymbol{\theta}, \boldsymbol{\mu}) + \beta U(\boldsymbol{\lambda}) + \gamma V(\boldsymbol{\theta}) \,, \tag{6.5}$$

where β and γ are the penalty weights associated to the penalty terms $U(\boldsymbol{\lambda})$ and $V(\boldsymbol{\theta})$, respectively. Bousse *et al.* used quadratic regularisation for U on the activity image (as in Equation (2.25)) and for V on $\boldsymbol{\theta}$ (more details in Section 6.2.3.2). Regularisation will be further discussed in Section 6.2.3.1. Thus, the discussed JRM is trying to solve the following optimisation problem:

$$\arg\max_{\boldsymbol{\lambda}, \boldsymbol{\theta}} \Phi(\boldsymbol{\lambda}, \boldsymbol{\theta}, \boldsymbol{\mu}) \,. \tag{6.6}$$

In other words, the optimisation consists in maximising the Poisson log-likelihood with respect to $\boldsymbol{\lambda}$ and $\boldsymbol{\theta} = (\varphi_\ell)_{\ell=1}^{n_\mathrm{g}}$.

In Jacobson *et al.* a motion-dependent log-likelihood (Equation (6.5)) is maximised for both the activity image and the motion parameters, alternatively, but neglects any changes in attenuation in the system matrix. The optimisation does not maximise the log-likelihood directly, but via optimisation transfer. This involves finding surrogates for $\Phi(\boldsymbol{\lambda}, \boldsymbol{\theta}, \boldsymbol{\mu})$ such that maximising the surrogates also maximises the log-likelihood.

The method in Rezaei *et al.* (Rezaei et al. 2016) also maximises a motion-dependent log-likelihood for the activity $\boldsymbol{\lambda}$ and a set of deformation parameters (using a different motion parameterisation), but differs mainly in the motion update, which is based on maximum likelihood preconditioned gradient ascent for transmission reconstruction (MLTR) (also used in maximum likelihood reconstruction of activity and attenuation (MLAA), see Section 4.3.5). MLTR approximates the log-likelihood using separable quadratic surrogate functions (using second-order Taylor's expansion of the likelihood). This does not necessarily guarantee the likelihood monotonicity.

As for the strategy of Bousse *et al.* , the optimisation maximises directly

$\Phi(\boldsymbol{\lambda}, \boldsymbol{\theta}, \boldsymbol{\mu})$. The gradients with respect to the deformation parameters were analytically obtained and incorporated within a gradient-based optimisation, using L-BFGS-B (Section 2.3.1). The image reconstruction uses an MCIR version OSEM, based on the algorithm in De Pierro 1995. More details on the implementation are provided in the following section 6.2.3.4.

In all of these algorithms, the input single CT image does not need to correspond to one of the gates of the respiratory signal and the reconstructed $\boldsymbol{\lambda}$ corresponds then to the same respiratory state.

6.2.3 Mass-Preserving JRM

As discussed in Chapter 4, respiration causes changes in displacement as well as in density and radiotracer concentration. However, in the formulation from Bousse et al. 2016a, the latter two effects are ignored. In this section, we introduce a mass-preserving version of JRM, where the Jacobian determinant of the transformation is incorporated within the system model and the regularisation. To the best of the author's knowledge, it has never been done before in a joint reconstruction scheme.

At each gate ℓ, the activity and attenuation images are now obtained with warping operators that take the Jacobian determinant into account, i.e., as $\boldsymbol{\lambda}_\ell = \widetilde{\boldsymbol{\mathcal{W}}}_{\varphi_\ell}\boldsymbol{\lambda}$ and $\boldsymbol{\mu}_\ell = \widetilde{\boldsymbol{\mathcal{W}}}_{\varphi_\ell}\boldsymbol{\mu}$ (see Equation 4.2). As in Chapter 4, the warping operators and the Jacobian determinants will be indexed with their B-spline coefficients, i.e., $\forall \ell \in [\![1, n_\text{g}]\!], \mathcal{W}_{\boldsymbol{\alpha}_\ell} \triangleq \mathcal{W}_{\varphi_\ell}$, $\widetilde{\mathcal{W}}_{\boldsymbol{\alpha}_\ell} \triangleq \widetilde{\mathcal{W}}_{\varphi_\ell}$ and $|\det \boldsymbol{\mathcal{J}}_{\boldsymbol{\alpha}_\ell}| \triangleq |\det \boldsymbol{\mathcal{J}}_{\varphi_\ell}|$.

The gradient of the cost function for the image registration step in Bousse et al. 2016a is modified in a similar way as in Yin et al. 2009, including the analytical derivatives of $|\det \boldsymbol{\mathcal{J}}_{\boldsymbol{\alpha}_\ell}|$ with respect to the B-spline coefficients $\boldsymbol{\alpha}_\ell$, as detailed in Section 4.5.5. In particular, the Jacobian matrix $\boldsymbol{J}(\boldsymbol{\mathcal{W}}_{\boldsymbol{\alpha}_\ell}\boldsymbol{f})$ (where the discretised image $\boldsymbol{f}$ is either $\boldsymbol{\lambda}$ or $\boldsymbol{\mu}$) with respect to $\boldsymbol{\alpha}_\ell$ is replaced by:

$$\boldsymbol{J}(\widetilde{\boldsymbol{\mathcal{W}}}_{\boldsymbol{\alpha}_\ell}\boldsymbol{f}) = \text{diag}\{|\det \boldsymbol{\mathcal{J}}_{\boldsymbol{\alpha}_\ell}|\}\boldsymbol{J}(\boldsymbol{\mathcal{W}}_{\boldsymbol{\alpha}_\ell}\boldsymbol{f}) + \text{diag}\{\boldsymbol{\mathcal{W}}_{\boldsymbol{\alpha}_\ell}\boldsymbol{f}\}\boldsymbol{J}(|\det \boldsymbol{\mathcal{J}}_{\boldsymbol{\alpha}_\ell}|) \tag{6.7}$$

where $\text{diag}\{\boldsymbol{x}\}$ is the diagonal matrix generated from a vector $\boldsymbol{x}$ and $\boldsymbol{J}(|\det \boldsymbol{\mathcal{J}}_{\boldsymbol{\alpha}_\ell}|)$ is the Jacobian matrix of $|\det \boldsymbol{\mathcal{J}}_{\boldsymbol{\alpha}_\ell}|$ with respect to $\boldsymbol{\alpha}_\ell$. More details are provided in Appendix A of Bousse et al. 2016a.

6.2.3.1 Image and Motion Estimation Regularisation

In Bousse et al. 2016a, quadratic priors were used to regularise both the image reconstruction and the motion estimation. In this work, other penalties will be investigated, including edge-preserving penalties.

6.2.3.2 Emission Image Regularisation

Regularisation of image reconstruction is discussed in Section 2.3.2.4. In this chapter, we used two common choices for $U(\boldsymbol{\lambda})$ of Equation (6.5):

- A quadratic regularisation on the emission image $\boldsymbol{\lambda}$, denoted $U_{\text{QP}}(\boldsymbol{\lambda})$. This was previously used in the original publication (Bousse et al. 2016a), and defined in Equation (2.25).

- An edge-preserving regularisation, here the relative difference penalty $U_{\text{RD}}(\boldsymbol{\lambda})$, see Equation (2.26).

6.2.3.3 Deformation Regularisation

In this work, we have only considered regularisation for each gate separately. In that case, $V(\boldsymbol{\theta})$ from Equation (6.5) can be expressed as a sum of penalties over all the gates $\ell \in [\![1, n_{\text{g}}]\!]$:

$$V(\boldsymbol{\theta}) = \sum_{\ell=1}^{n_{\text{g}}} \mathcal{R}(\boldsymbol{\alpha}_\ell) \tag{6.8}$$

where $\mathcal{R}$ is a penalty on the coefficients $\boldsymbol{\alpha}_\ell$.

The original regularisation in Bousse et al. 2016a uses the penalty $\mathcal{R}_{\text{def}}$ on the B-spline parameters of Equation (4.8), defined in Section 4.5.2 (no combination with $\mathcal{R}_{\text{QP}}$ or $\mathcal{R}_{\text{STV}}$ on $|\det \boldsymbol{\mathcal{J}}_{\boldsymbol{\alpha}_\ell}|$). We denote $V_{\text{def}}(\boldsymbol{\theta}) = \sum_{\ell=1}^{n_{\text{g}}} \mathcal{R}_{\text{def}}(\boldsymbol{\alpha}_\ell)$.

Additionally, the same regularisation for the motion estimation as in Chapter 4 was utilised here, except that the parameter ξ was chosen as 0.001 when $\mathcal{R}^* = \mathcal{R}_{\text{QP}}$ or 0.001ζ when $\mathcal{R}^* = \mathcal{R}_{\text{STV}}$ (where ζ is the smoothing scalar in the STV prior). We will denote V_{QP} and V_{STV} the regularisation using the QP and the STV penalty on the Jacobian image, respectively.

6.2.3.4 Summary of JRM Implementation

General Outline :

Standard and mass-preserving JRM, described above, alternate between:

- *Motion Update*: maximising the log-likelihood, with a given activity image, with respect to the B-spline coefficients $\boldsymbol{\theta}$ to estimate the deformations between the reference respiratory state (corresponding to the CT image used to compute the input attenuation map) and the PET respiratory gates (binned using a respiratory surrogate signal). The optimisation is performed for each respiratory gate separately.

- *Image Update*: given the deformation fields estimated during the previous step, MCIR is used to obtain $\boldsymbol{\lambda}$, either with a modified version of OSEM or BSREM, implemented in MATLAB using GE projectors and the same subset ordering as the GE MATLAB reconstruction package (more details in Appendix B.3). Contrary to Bousse et al. 2016a, in this work, the image is always reinitialised to $\mathbf{1}_{n_\mathrm{v}}$ before each reconstruction.

The algorithm is initialised from a gated regularised image reconstruction at end-expiration (according to the respiratory trace). The first motion estimation is chosen to have more iterations than following ones (here twice as many). A concise peudo-code is given in Algorithm 1. A more detailed pseudo-code for standard JRM is given in Bousse et al. 2016a and Bousse et al. 2016b.

Algorithm 1
Joint Reconstruction of Motion and Activity

Input: μ, gated projection data $\boldsymbol{g}$
$\boldsymbol{\theta}^{(0)} \leftarrow \mathbf{0}$
$\boldsymbol{\lambda}^{(0)} \leftarrow$ Gated image reconstruction from $(\boldsymbol{g}_1, \boldsymbol{\mu}, \beta)$
for $r = 1, ..., \text{numJRMIter}$ **do**
  $\boldsymbol{\theta}^{(r)} \leftarrow$ Motion estimation from $(\boldsymbol{g}, \mu, \boldsymbol{\theta}^{(r-1)}, \boldsymbol{\lambda}^{(r-1)}, \gamma)$
  OPTIONAL: scatter re-estimation
  $\boldsymbol{\lambda}^{(r)} \leftarrow$ MCIR from $(\boldsymbol{g}, \mu, \boldsymbol{\theta}^{(r)}, \beta)$
end for
Output: estimated PET image $\hat{\boldsymbol{\lambda}}$, B-spline coefficients $\hat{\boldsymbol{\theta}}$

The parameters in Table 6.1 need to be specified for the reconstruction. In this thesis, JRM will be applied only to TOF data, for which convergence has been shown to be accelerated in standard JRM compared to non-TOF (Bousse et al. 2016b).

Motion Update :

The penalised log-likelihood $\Phi(\boldsymbol{\lambda}, \boldsymbol{\theta}, \boldsymbol{\mu})$ is maximised with respect to $\boldsymbol{\theta}$ in the motion update. Let $\boldsymbol{\theta}^{(k)}$ be a current estimate of $\boldsymbol{\theta}$ at iteration k. $\boldsymbol{\theta}^{(k+1)}$ is obtained by

Parameter	Description
numJRMIter	number of alternations between motion estimation and image update
numMotionEstimation	maximal number of L-BFGS-B updates for each (gated) motion estimation
numSubs	number of subsets used in image reconstruction
numOSEMIter	number of image reconstruction iterations, when the modified OSEM from De Pierro 1995 is used for the reconstruction. When BSREM is used instead, the image update when the stopping criteria are met (either based on the number of iterations or median difference between two updates, as described in Appendix B).
β	penalty weight for the image reconstruction
γ	penalty weight for the motion estimation

Table 6.1: Main parameters needed for JRM.

performing an (approximate) maximisation along a search direction $\boldsymbol{t}^{(k)}$:

$$\boldsymbol{\alpha}^{(k+1)} = \boldsymbol{\theta}^{(k)} + \delta^{(k)}\boldsymbol{t}^{(k)} \tag{6.9}$$

where $\delta^{(k)} = \arg\max_{\delta \geq 0} \Phi(\boldsymbol{\lambda}, \boldsymbol{\theta}^{(k)} + \delta \boldsymbol{t}^{(k)}, \boldsymbol{\mu})$ and $\boldsymbol{t}^{(k)}$ is computed with a limited-memory Broyden-Fletcher-Goldfarb-Shanno quasi-Newton algorithm (Nocedal 1980). The step length has to satisfy the Wolfe conditions (More et al. 1994), i.e., guarantying sufficient increase of (6.5). A Fortran implementation (Zhu et al. 1994) was used to compute $\boldsymbol{t}$ and $\delta^{\star}$ at each motion estimation iteration.

To simplify the notation, dependencies on $\boldsymbol{\lambda}$ and $\boldsymbol{\mu}$ will be omitted in this part. The expected number of counts at a given gate ℓ $\bar{\boldsymbol{g}}_\ell(\boldsymbol{\lambda}, \boldsymbol{\alpha}_\ell, \boldsymbol{\mu})$ will be written as $\bar{\boldsymbol{g}}_\ell(\boldsymbol{\alpha}_\ell)$. The likelihood $L(\boldsymbol{\lambda}, \boldsymbol{\theta}, \boldsymbol{\mu})$ will be denoted $L(\boldsymbol{\theta})$ and $\boldsymbol{J}(\cdot)$ will represent the Jacobian matrix in $\boldsymbol{\alpha}_\ell$.

Using the chain rule, the gradient of the log-likelihood in $\boldsymbol{\alpha}_\ell$ is:

$$\nabla_{\boldsymbol{\alpha}_\ell} L(\boldsymbol{\theta}) = \boldsymbol{J}(\bar{\boldsymbol{g}}_\ell(\boldsymbol{\alpha}_\ell))^\top \nabla_\ell(\bar{\boldsymbol{g}}_\ell(\boldsymbol{\alpha}_\ell)) \tag{6.10}$$

where $\nabla_\ell(\bar{\boldsymbol{g}}_\ell(\boldsymbol{\alpha}_\ell)) = \boldsymbol{g}_\ell / \bar{\boldsymbol{g}}_\ell(\boldsymbol{\alpha}_\ell) - \mathbf{1}_{\mathbb{R}^{n_c}}$.

The latter is modified with the incorporation of the mass-preserving warping

operator $\widetilde{\boldsymbol{\mathcal{W}}}$ instead of the regular warping operator $\boldsymbol{\mathcal{W}}$ used in Bousse et al. 2016a:

$$\begin{aligned}\boldsymbol{J}(\bar{\boldsymbol{g}}_\ell(\boldsymbol{\alpha}_\ell)) = -\tau_\ell \operatorname{diag}\{H_a(\widetilde{\boldsymbol{\mathcal{W}}}_{\boldsymbol{\alpha}_\ell}\boldsymbol{\mu})\widetilde{\boldsymbol{\mathcal{W}}}_{\boldsymbol{\alpha}_\ell}\boldsymbol{\lambda}\}\boldsymbol{G}\boldsymbol{J}(\widetilde{\boldsymbol{\mathcal{W}}}_{\boldsymbol{\alpha}_\ell}\boldsymbol{\mu}) \\ +\tau_\ell H_a(\widetilde{\boldsymbol{\mathcal{W}}}_{\boldsymbol{\alpha}_\ell}\boldsymbol{\mu})\boldsymbol{J}(\widetilde{\boldsymbol{\mathcal{W}}}_{\boldsymbol{\alpha}_\ell}\boldsymbol{\lambda})\end{aligned} \tag{6.11}$$

where $\boldsymbol{G} \in \mathbb{R}^{n_\mathrm{b}, n_\mathrm{v}}$ represents the line integral matrix where an element (i, j) is the length of intersection of the line connecting the two detectors corresponding to the bin i with voxel j, $H_a(\widetilde{\boldsymbol{\mathcal{W}}}_{\boldsymbol{\alpha}_\ell}\boldsymbol{\mu})$ is the attenuation-corrected system matrix using $\widetilde{\boldsymbol{\mathcal{W}}}_{\boldsymbol{\alpha}_\ell}\boldsymbol{\mu}$ as attenuation map (as in Bousse et al. 2016a) and $\forall \boldsymbol{f} = \boldsymbol{\mu}$ or $\boldsymbol{\lambda}$, $\boldsymbol{J}(\widetilde{\boldsymbol{\mathcal{W}}}_{\boldsymbol{\alpha}_\ell}\boldsymbol{f})$ is the Jacobian matrix associated to $\widetilde{\boldsymbol{\mathcal{W}}}_{\boldsymbol{\alpha}_\ell}\boldsymbol{f}$ with respect to $\boldsymbol{\alpha}_\ell$, already expressed in Equation (6.7).

The gradient $\nabla\Phi$, corresponding to the regularised motion estimation step, is equal to $\nabla L + \nabla V$, where ∇L is the concatenation of all subgradients $\nabla_{\boldsymbol{\alpha}_\ell} L$ and ∇V is the gradient of V.

Regularised Image Reconstruction :

The image update maximises the motion-dependent penalised log-likelihood (Equation 6.5), using either:

- The modified Ordered-Subsets Expectation Maximisation scheme from De Pierro 1995, that will be referred as "Mod-OSEM", with a quadratic penalty on the emission image. The update needs therefore as parameters: the number of Mod-OSEM and motion-compensated Mod-OSEM ("MC-Mod-OSEM") iterations numOSEMIter, the number of subsets numSubs and the penalty weighting factor β.

- Block sequential regularized expectation maximization (BSREM) (Ahn et al. 2003). The standard BSREM reconstruction was also modified to incorporate the motion-compensated BSREM ("MC-BSREM"). More details on the implementation are given in Appendix B.3. The parameters of the update are the number of subsets numSubs and the penalty weighting factor β.

JRM Regularisation Summary :

We will consider the following 3 JRM regularisation configurations:

- *Reference regularisation*: $U_{\mathrm{QP}}(\boldsymbol{\lambda}) + V_{\mathrm{def}}(\boldsymbol{\theta})$.

- *Smoothing regularisation*: $U_{\mathrm{QP}}(\boldsymbol{\lambda}) + V_{\mathrm{QP}}(\boldsymbol{\theta})$.

- *Edge-preserving regularisation*: $U_{\mathrm{RD}}(\boldsymbol{\lambda}) + V_{\mathrm{STV}}(\boldsymbol{\theta})$.

For all penalties U and V, the neighbourhood sizes were set to $3 \times 3 \times 3$ (either in the image grid for U or in the grid of control points for V). A padding using nearest values was used for values at the edges of the images.

6.2.4 Method Extensions

In this part, extensions to standard and mass-preserving JRM will be discussed and assessed on patient data. Firstly, a method directly derived from standard JRM from Bousse et al. 2016a will be introduced for dynamic PET data. Then, the handling of multiple bed positions will be discussed for standard and mass-preserving JRM.

6.2.4.1 Dynamic Acquisitions

Background :

It is challenging to adapt correction methods dedicated for static PET imaging to dynamic PET imaging. For example, if one wants to assess the motion from non-AC images, one could:

1. Reconstruct each separate dynamic frame at each respiratory gate. Afterwards standard registration methods could be applied and a mean deformation field at each gate could be found from all registrations. However such a method would have the deficiency of using limited number of counts (especially just after injection of the tracer).

2. Reconstruct a larger number of dynamic frames together to avoid the problem of low counts and possible missing gates. Another major drawback is that the contrast between respiratory gated images might be quite different and registering such images would require careful attention to the cost function used in the registration, in addition to the general problems linked to non-AC image registration.

More accurate methods could take into account the noise model of the PET data, e.g., by estimating the deformations between respiratory gates which would maximise the log-likelihood at each dynamic frame. Static JRM (from Section 6.2)

could be used at each frame separately, however as the early frames are very short, noise is likely to be an issue. This would also be computationally expensive.

More generally, a good motion-compensating method for dynamic PET should remain relatively simple.

Extensive work has been done for head motion, which is applicable to dynamic data. Because it is considered rigid, it is possible to use motion tracking (e.g., RPM) or estimating motion from non-AC images. This is most particularly available for PET/MR scanners, where multiple MR sequences can be acquired during the PET acquisition (Gillman et al. 2017).

However, in the lung, correction for respiratory motion in dynamic PET acquisitions is more challenging and few correction techniques exist.

Yu et al. 2016 adapted a method presented for static data in Liu et al. 2011; Chan et al. 2013 to dynamic data. This work corrects single organ or tumour motion, assumed to be rigid, by correlating the displacement of its centroid to the respiratory surrogate signal. This is justified by the observation of a linear correlation between the surrogate respiratory signal and the displacement along the superior-inferior, anterior-posterior and left-right axes. The centroids are determined using a semi-automatic segmentation on gated AC PET images. Contrary to standard MCIR, introduced in Section 4.3.4, the motion model deforms the system matrix instead of the emission and/or attenuation images. Because of rapid changes within the radiotracer distribution, the beginning of the dynamic acquisition is skipped to construct the correlation (first three minutes). Although providing good results for tumour and kidney studies, as the motion is assumed rigid, the method cannot be translated to diffuse lung diseases such as IPF. Chan et al. 2018 extended the work in Yu et al. 2016 to respiratory motion correction, by allowing non-rigid (B-spline parameterised) motion in the method.

Proposed Method:

Similarly to Yu et al. 2016 and Chan et al. 2018, we assume that the data can be gated according to a surrogate signal, where the deformation between the gates does not depend on time. We can then first estimate the motion and subsequently tracer kinetics.

The listmode data from the entire dynamic acquisition is binned into

respiratory-gated dynamic PET sinograms $\boldsymbol{g} = \{\boldsymbol{g}_\ell^m\}_{(\ell,m)\in[\![1,n_\mathrm{g}]\!]\times[\![1,n_\mathrm{f}]\!]}$ (where n_g denotes the number of gates and n_f the number of time frames) $\boldsymbol{g}_\ell^m$, each following a Poisson distribution:

$$\forall(\ell,m)\in[\![1,n_\mathrm{g}]\!]\times[\![1,n_\mathrm{f}]\!],\quad \boldsymbol{g}_\ell^m \sim \mathrm{Poisson}(\bar{\boldsymbol{g}}_\ell^m(\boldsymbol{\lambda}^m,\varphi_\ell,\boldsymbol{\mu}))\,,$$

where $\bar{\boldsymbol{g}}_\ell^m$ is the expected number of counts at gate ℓ and frame m, whose value at detection bin $i\in[\![1,n_\mathrm{b}]\!]$ is:

$$[\,\bar{\boldsymbol{g}}_\ell^m(\boldsymbol{\lambda}^m,\varphi_\ell,\boldsymbol{\mu})\,]_i = \tau_{\ell,m}\, a_i(\boldsymbol{\mathcal{W}}_{\varphi_\ell}\boldsymbol{\mu}) H_i \boldsymbol{\mathcal{W}}_{\varphi_\ell}\boldsymbol{\lambda}^m + s_{i,\ell,m}\,,$$

which depends on the activity image $\boldsymbol{\lambda}^m$ at a time frame m, the attenuation image $\boldsymbol{\mu}$ and φ_ℓ a deformation field corresponding to the gate ℓ. $\boldsymbol{\mathcal{W}}_{\varphi_\ell}$ is the (standard) warping operator defined by the deformation φ_ℓ, $\tau_{\ell,m}$ is the gate/frame duration, $a_i(\boldsymbol{\mathcal{W}}_{\varphi_\ell}\boldsymbol{\mu})$ is the attenuation term along the line of response corresponding to the bin i and H_i is the detection bin system response and $s_{i,\ell,m}$ is the background term. Note that in this model $\boldsymbol{\lambda}^m$ and $\boldsymbol{\mu}$ are affected by the same motion and that the warping operator is not mass-preserving (the mass-preserving model for patient data is only used in the present work in Section 6.4.3). If we assume that the changes in radioactivity distribution between all gates are negligible within each time frame, then the optimisation problem from Equation (6.6) can be extended to:

$$\left(\left\{\hat{\boldsymbol{\lambda}}^1,\ldots,\hat{\boldsymbol{\lambda}}^m\right\},\hat{\boldsymbol{\varphi}}\right) \in \arg\max_{\{\boldsymbol{\lambda}^1,\ldots,\boldsymbol{\lambda}^m\},\,\boldsymbol{\varphi}} \sum_m \Phi_m(\boldsymbol{\lambda}^m,\boldsymbol{\varphi},\boldsymbol{\mu})\,. \tag{6.12}$$

Solving Problem (6.12) is however computationally expensive. We therefore propose a more tractable method: the gated data are summed over the frame index m, forming $\boldsymbol{g}_\ell = \sum_{m=m_\mathrm{ini}}^{n_\mathrm{f}} \boldsymbol{g}_\ell^m$. We denote $\boldsymbol{\varphi} = \{\varphi_\ell\}_{\ell\in[\![1,n_\mathrm{g}]\!]}$. The method uses the implementation of JRM in Bousse et al. 2016a as for a static acquisition, resulting in the following optimisation problem:

$$(\hat{\boldsymbol{\lambda}},\hat{\boldsymbol{\varphi}}) \in \arg\max_{\boldsymbol{\lambda},\,\boldsymbol{\varphi}} \Phi(\boldsymbol{\lambda},\boldsymbol{\varphi},\boldsymbol{\mu})\,, \tag{6.13}$$

where $\Phi(\boldsymbol{\lambda},\boldsymbol{\varphi},\boldsymbol{\mu})$ is the (penalised) log-likelihood, using a B-spline parameterisation of the deformation fields. Here $\hat{\boldsymbol{\lambda}}$ is an time-averaged motion-compensated image,

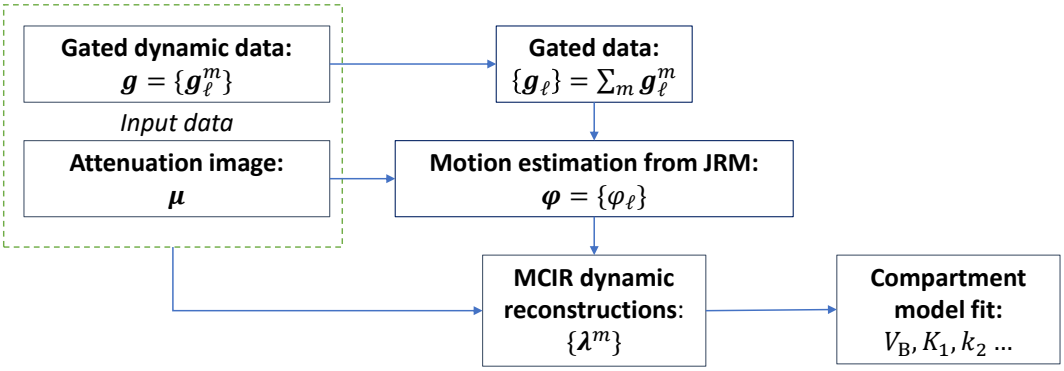

Figure 6.1: Overview of the method

which will not be used in the next step as at this stage we are only interested in the estimated motion $\hat{\varphi}$.

The final step is using standard MCIR (MC-Mod-OSEM, Section 6.2.3.4) at each dynamic frame from the previously estimated deformation fields.

A summary of the proposed method is shown in Figure 6.1.

In Yu et al. 2016 and Chan et al. 2018, the motion estimation was based on pre-reconstructed images, which are affected by misalignment between PET gates and μ map(s) (even in the ideal case of CINE-CT data). The novelty of our method relies in optimising jointly the activity image and the deformation—which should contribute to fewer errors linked to the use of a wrong attenuation map in the reconstruction.

The main caveat about optimising the time-averaged $\hat{\boldsymbol{\lambda}}$ image is when discrepancies exist in the radioactivity between respiratory gates: in this case Equations (6.12) and (6.13) are not strictly valid anymore. In practice, in the region of the heart or major blood vessels (e.g., aorta), rapid concentration changes are observed just after injection, therefore the assumption that the radioactivity distribution is the same for all gates at a given dynamic frame does not hold in the early part of a dynamic lung PET acquisition. It is only (approximately) true for either short time frames (compared to the kinetics) or when the radioactivity concentration is almost stable, otherwise this could induce some motion mis-estimation, as JRM could try to compensate for the discrepancies by warping.

To investigate this, in the following, the proposed method will be assessed both when using the entire acquisition and when using the later part of the acquisition only (skipping 1 min of the dynamic acquisition for the motion estimation).

6.2.4.2 Multi-Bed Position Handling for Static Acquisitions

For most scanners still used in clinical settings, with relatively short axial FOV (≈ 15 cm, e.g., 15.7 cm for GE PET/CT Discovery 710, Bettinardi et al. 2011), static PET/CT lung acquisitions often consist of two bed positions (i.e., two consecutive acquisitions with an overlap), to be able to capture the entire lung. Indeed, the mean vertical height of the diaphragm (defined as the mean distance from the base of the vertebra T1 to the diaphragm) is approximately of 23 cm at maximum expansion (Bellemare et al. 2001). Recent scanners with longer axial FOV should alleviate the need of using two bed positions for thorax acquisitions. For example, the recent Siemens Biograph Vision PET/CT has an axial FOV of 25.6 cm (Van Sluis et al. 2019) while for the GE Discovery MI with 5 rings it is 25 cm. However, such data were not available for the current study.

JRM can be used separately for each bed position. This is however an issue for joint reconstruction if the attenuation map is of the same dimension as the PET image during the optimisation. For example, if the CTAC acquisition corresponds to an end-expiration state, the JRM optimisation will:

- for the bed position corresponding to the apex of the lungs, push some of the attenuation map outside of the axial FOV for the other respiratory gates. This should not be an issue if the control grid is large enough.

- for the bed position corresponding to the lower part of the lungs, try to warp voxels from outside the FOV into the FOV. However, a single bed position implementation of JRM does not have access to the corresponding μ values. This could be an important issue, where the optimisation might fail at the edges of the axial FOV.

Several possibilities can be investigated to handle multi-bed positions:

- *Ideal solution*: optimisation of all bed positions in the same motion estimation. The joint reconstruction would therefore lead to the reconstruction of an image and the estimation of the deformation for the entire axial field of view (for all bed positions).

  This however requires careful modifications to take into account the differences in sensitivity and decay factors in the overlap between bed positions.

In addition, for a 2-bed position acquisition, the optimisation problem would require approximately twice as much memory, which might not be viable on the UCL systems ($\approx 64\,\text{Gb}$ would be required for patient data in the current implementation).

- *Intermediate solution*: use an attenuation map which has larger dimensions than the activity image, so the issues of warping nonexistent attenuation values almost disappear if we assume there is not much motion outside of the entire axial FOV corresponding to the two bed positions. This solution was not adopted as it would require substantial modifications to the current implementation.

- *Acceptable solution*: The presented joint reconstruction can be used separately at each bed position. With the estimated deformations, an average displacement field can then be created corresponding to the entire axial field of view of the two bed positions (accounting for differences in sensitivity and decay within overlaps of the two bed positions). Then, a pseudo 4D-CT is created from the two sets of displacement fields (which are averaged within the overlap). If we denote $\boldsymbol{D}_1^C$ and $\boldsymbol{D}_2^C$ the displacement matrices along C-axis (where $C \in \{X, Y, Z\}$) corresponding only to voxels in the overlap between the two bed positions, the averaged displacement matrix in the overlap can be expressed as:

$$\bar{\boldsymbol{D}}^C = \frac{w_1 \boldsymbol{D}_1^C + w_2 \boldsymbol{D}_2^C}{w_1 + w_2} \,,$$

where w_1 and w_2 are weighting factors accounting for acquisition durations, decay factors and slice sensitivies. Finally, standard MCIRs from known deformation are used for the two bed positions, using the 4D μ maps instead of warping a single μ map. There might still be an issue within the overlap (if the motion estimation failed for one of the bed positions) and should be assessed carefully.

The latter solution was the one used in this thesis. Warped μ maps and Jacobian determinant images from the two bed positions will be consolidated.

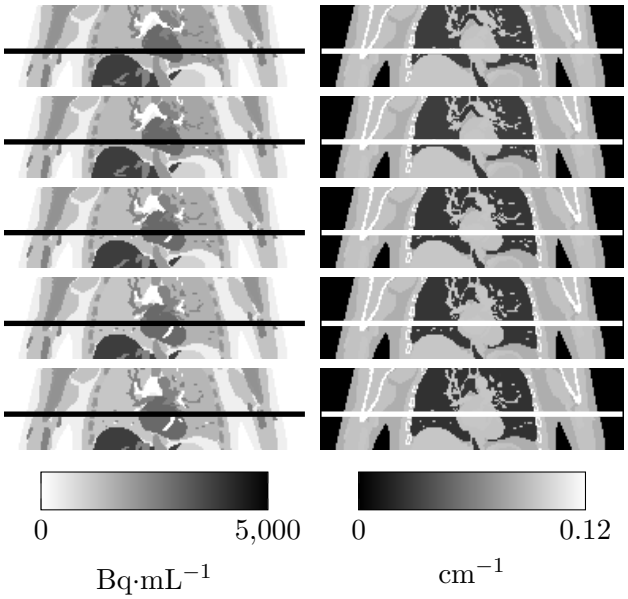

Figure 6.2: Modified XCAT images used for the simulation: emission images (left) and attenuation images (right) from end-inspiration (top) to end-expiration (right)

6.3 Static PET JRM: XCAT Lung Simulations

6.3.1 Data Generation

Five sets of lung XCAT images were generated, corresponding to five different respiratory gates ($n_{\mathrm{g}} = 5$). The corresponding activity and attenuation images are denoted $\{\boldsymbol{\lambda}_\ell\}_{\ell\in[\![1,n_{\mathrm{g}}]\!]}$ and $\{\boldsymbol{\mu}_\ell\}_{\ell\in[\![1,n_{\mathrm{g}}]\!]}$, respectively (where $\ell = 1$ is the end-inspiration and $\ell = 5$ is the end-expiration), mimicking displacement gating. The values in the activity images correspond to an FDG acquisition 60-min post-injection.

Additionally, to simulate density changes in lungs obeying mass preservation, the emission and density values were changed uniformly in the lung, depending on the total volume change compared to the mid-expiration state (gate 3). The changes in density and activity concentration were as follows: gate 1: -11%, gate 2: -6.9%, gate 3: 0%, gate 4: $+8.2\%$, gate 5: $+11.5\%$. The resulting images are shown in Figure 6.2.

Once the activity and activity images created, the gated projection data were obtained via forward projection of the activity images and separate attenuation correction factors were computed for each gate. Scatters and randoms were added with a level similar to a usual lung acquisition (about 60% of the total number of detected counts). In absence of realistic single scatter simulation (SSS) from

the XCAT μ maps, the true gated background sinograms were considered uniform and the same for all gates. Poisson noise was added to the projection data in the results presented (number of prompts $\approx 3 \cdot 10^7$), to simulate the acquisitions from the Coagulation Study cohort (injected activity 177 MBq, weight 75 kg, total acquisition duration 250 s). A GE Discovery 710 scanner geometry was used to simulate single bed position data (using GE proprietary projectors callable in a MATLAB package). The background term does not depend on the respiratory gate in the simulation, unlike for patient data, therefore it is accurately known within the entire joint reconstruction.

In the following XCAT simulations, numMotionEstimation (Table 6.1) was set to 30 at the first JRM iteration, and then set to 15. For the image reconstruction, 8 subsets were used. All data were reconstructed with GE proprietary projectors in MATLAB.

6.3.2 Regularisation Selection

In this part, the input attenuation image corresponds to the end-expiration state $\boldsymbol{\mu}_5$, to avoid warping voxels from outside of the FOV. This also corresponds to the best case scenario where the gated reconstruction used to initialise the activity image at the start of JRM is already aligned with the μ map. A total of 3 numJRMIter (Table 6.1) were used. All regularisation configurations summarised in Section 6.2.3.4 were tested in this part (i.e., "reference", "smoothing" and "edge-preserving" regularisation). For the standard and smoothing regularisation, i.e., when Mod-OSEM or MC-Mod-OSEM image reconstructions were used, 6 iterations were chosen. The penalty weights corresponding to the image reconstruction (either QP or RD) are considered fixed in these simulations and were tuned visually to achieve a satisfactory overall image quality.

6.3.2.1 Noise Realisations

The two JRM models are tested with the regularising penalties described in Section 6.2.3.1. For each penalty configuration, 5 weights for $V(\boldsymbol{\theta})$ are tested on 30 different noise realisations. For all reconstructions, the background sinograms—considered uniform—are known accurately during the entire reconstruction.

The minimal and maximal weights of the motion estimation step for each configuration were determined approximately using preliminary tuning, to correspond

to weak regularisation and strong regularisation, respectively.

6.3.2.2 Methodology

The image variance and squared bias in all attenuation images and only in the lung were studied to select the best regularisation configuration for each model and to compare the two models. Because of the differences in the image reconstruction algorithm used, no measure was computed on the activity images. The attenuation image squared bias, using gate-dependent ROIs $\mathcal{V}_g$, is given as:

$$\text{Bias}^2 = \frac{1}{n_\text{g}} \frac{1}{K} \sum_{g=1}^{n_\text{g}} \frac{1}{|\mathcal{V}_g|} \sum_{j \in \mathcal{V}_g} \left(\sum_{\kappa=1}^{K} \left[\boldsymbol{\mu}_g^{[\kappa]} \right]_j - [\boldsymbol{\mu}_g]_j \right)^2 , \tag{6.14}$$

and the attenuation image variance as:

$$\text{Var} = \frac{1}{n_\text{g}} \frac{1}{K-1} \sum_{g=1}^{n_\text{g}} \frac{1}{|\mathcal{V}_g|} \sum_{j \in \mathcal{V}_g} \sum_{\kappa=1}^{K} \left(\left[\boldsymbol{\mu}_g^{[\kappa]} \right]_j - m_j(\boldsymbol{\mu}_g) \right)^2 , \tag{6.15}$$

where $|\mathcal{V}_g|$ is the number of voxels in $\mathcal{V}_g$ (here $\forall g \; \mathcal{V}_g$ is either the entire image or the gate-dependent XCAT lung mask) and

$$m_j(\boldsymbol{\mu}_g) = \frac{1}{K} \sum_{\kappa=1}^{K} \left[\boldsymbol{\mu}_g^{[\kappa]} \right]_j$$

and $K = 30$, $\boldsymbol{\mu}_g^{[\kappa]}$ is the estimated $\boldsymbol{\mu}$ at a respiratory gate g and at the κ-th noise realisation.

These measures of variances and squared biases were used to assess the best regularisation configuration (using a scatter plot), for each model. The regularisation is then adapted to patient data.

Due to difference in resolution effects between the simulations and the patient data (e.g., very sharp edges in the simulated μ map whereas the μ maps for patient data are preliminary smoothed), we have seen that values of the regularisation parameters are not directly comparable. For this reason, the regularisation weights were not tuned.

In addition to the bias-variance study, the different JRM variants will be assessed from reconstructions using intermediate weights of each regularisation configuration (corresponding to only one of the 30 noise realisations, randomly selected).

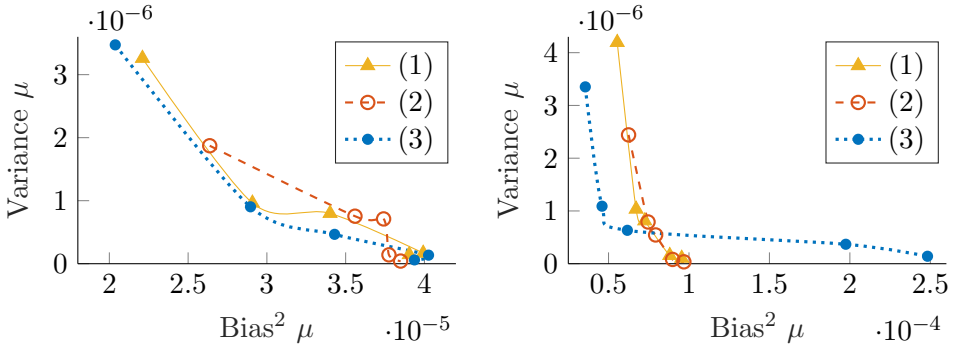

(a) Entire image **(b)** Lung only

Figure 6.3: Tradeoff between variance and the (squared) bias in the μ images, in (a) the entire image and in (b) the lung only, for standard JRM and different regularisation configurations (legend labels: (1) reference, (2) smoothing, (3) edge-preserving, as summarised in 6.2.3.4.

(a) $\boldsymbol{\lambda}_{\text{ref}}$ **(b)** $\boldsymbol{\lambda}_{\text{sm}}$ **(c)** $\boldsymbol{\lambda}_{\text{pr}}$ **(d)** $\boldsymbol{\lambda}^{\star}$

Figure 6.4: Coronal views of (d) the true activity image $\boldsymbol{\lambda}^{\star}$ and the motion-compensated images using either (a) the reference regularisation $\boldsymbol{\lambda}_{\text{ref}}$, (b) the smoothing regularisation $\boldsymbol{\lambda}_{\text{sm}}$ or (c) the edge-preserving regularisation $\boldsymbol{\lambda}_{\text{pr}}$, as summarised in 6.2.3.4).

The reconstructed activity images $\boldsymbol{\lambda}$ and the warped attenuation images $\mathcal{W}_{\varphi_\ell}\boldsymbol{\mu}$ will be compared to true activity and attenuation images. The estimated Jacobian determinant images will also be validated against simulated density and activity distribution changes.

6.3.2.3 Results

Standard JRM :

The results of the tradeoff study (i.e., comparing variances and squared biases in the μ images) are presented as scatter plots in Figure 6.3. Overall, the different regularisation schemes achieve similar results for both image variances and biases, even though the edge-preserving results show a slight improvement.

Figure 6.4 shows the reconstructed activity images compared to the true activity image (using intermediate penalty weights for the motion estimation). Differences between the reconstructed images and the true image—outside of noise—are not conspicuous: despite the model inconsistencies (by construction of the simulated

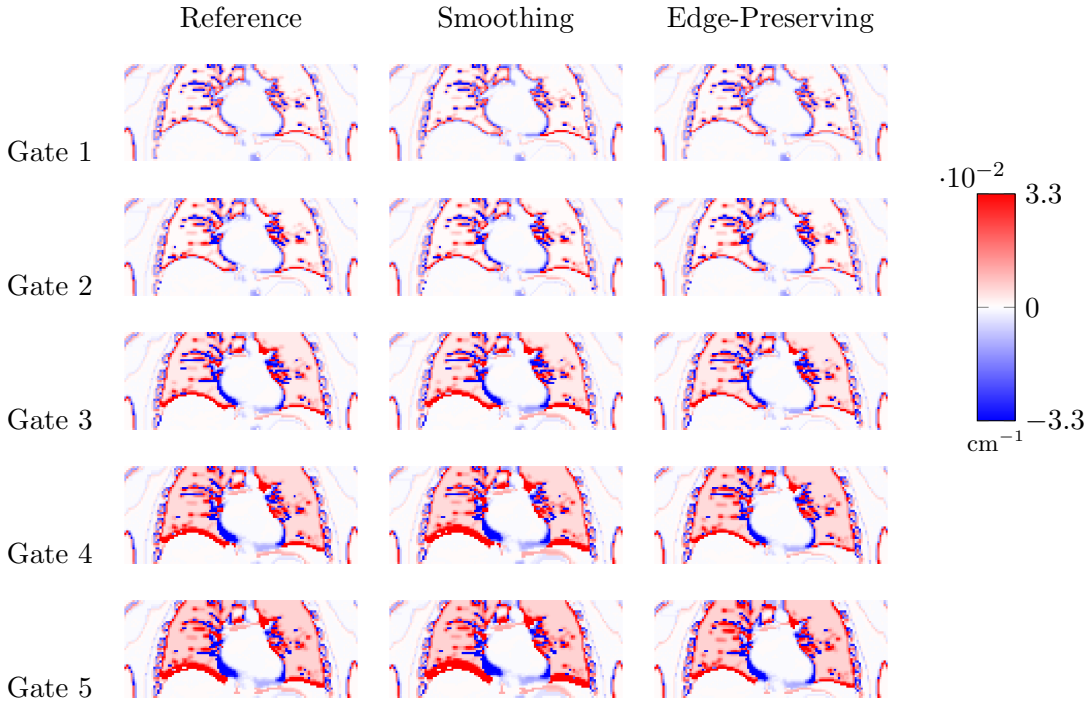

Figure 6.5: Coronal views of the difference images between the true attenuation map and the warped end-expiration attenuation map, for all respiratory gates, using standard JRM deformation fields obtained with the regularisation configurations introduced in 6.2.3.4: reference (left), smoothing (centre) and edge-preserving (right) regularisation.

data), standard JRM seems to have succeeded in reconstructing an accurate motion-compensated image. This is confirmed from the mean relative errors in the true lung mask (reference: true activity image): -3.5% for the reference regularisation, -2.9% for the smoothing regularisation and -0.4% for the edge-preserving regularisation.

Now, if we visually compare the warped μ-maps for all the respiratory gates against the true μ-maps (Figure 6.5) and the Jacobian determinant images against the true density and radioactivity concentration changes (Figure 6.6, it becomes evident that, although the final activity image seems adequate for these XCAT simulated data, JRM did not manage to find deformation fields resulting in Jacobian determinant images which are close to the changes, especially near the base of the lungs, e.g., in the liver.

Mass-Preserving JRM :

The scatter plots showing the image variances versus the squared biases in the warped μ maps are shown in Figure 6.7. Overall and in the lung, the edge-preserving regularisation achieves lower biases than both smoothing and reference regularisation

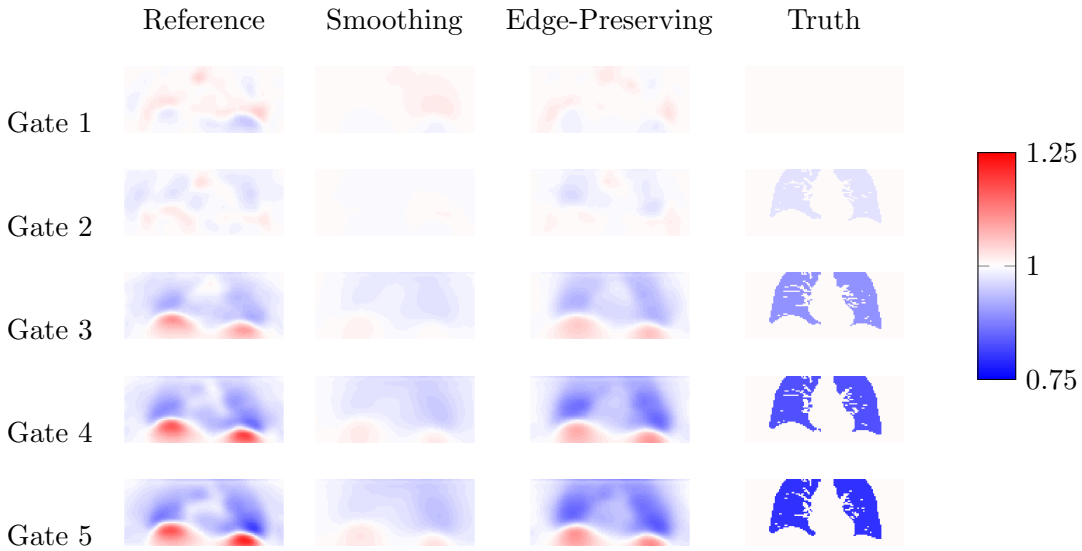

Figure 6.6: Coronal views of the Jacobian determinant images, at each respiratory gate, computed from the deformation fields estimated using standard JRM and either the reference (1st column), the smoothing (2nd column) or the edge-preserving (3rd column) regularisation, compared to the ground-truth (4th column).

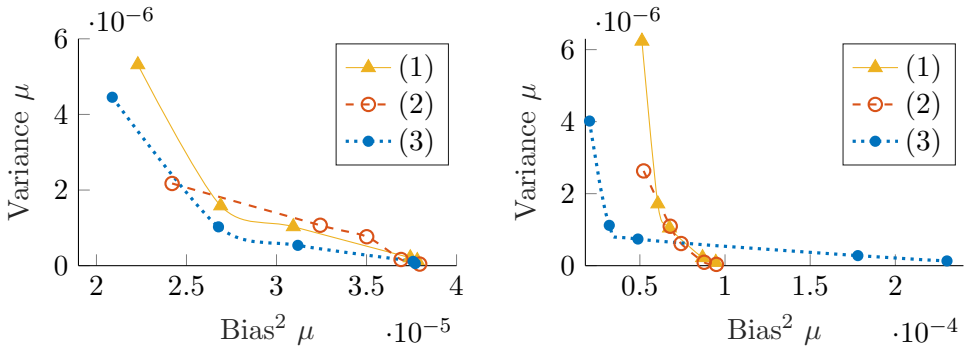

(a) Entire image **(b)** Lung only

Figure 6.7: Tradeoff between variance and the (squared) bias in the μ images, in (a) the entire image and in (b) the lung only, for mass-preserving JRM and different regularisation configurations (legend labels: (1) reference, (2) smoothing, (3) edge-preserving, as summarised in 6.2.3.4).

configurations. The variances are however quite similar to the reference regularisation.

The reconstructed activity images in Figure 6.8 are very similar to those in Figure 6.4, i.e., for these simulated data, we do not see clear benefits of using the mass-preserving model in JRM. The mean relative errors in the lung mask are close to the ones of the standard JRM: -2.8% for the reference regularisation, -2.8% for the smoothing regularisation and $+0.4\%$ for the edge-preserving regularisation.

(a) $\boldsymbol{\lambda}_{\text{ref}}$ (b) $\boldsymbol{\lambda}_{\text{sm}}$ (c) $\boldsymbol{\lambda}_{\text{pr}}$ (d) $\boldsymbol{\lambda}^{\star}$

Figure 6.8: Coronal views of (d) the true activity image $\boldsymbol{\lambda}^{\star}$ and the motion-compensated images using either (a) the reference regularisation $\boldsymbol{\lambda}_{\text{ref}}$, (b) the smoothing regularisation $\boldsymbol{\lambda}_{\text{sm}}$ or (c) the edge-preserving regularisation $\boldsymbol{\lambda}_{\text{pr}}$, as summarised in 6.2.3.4.

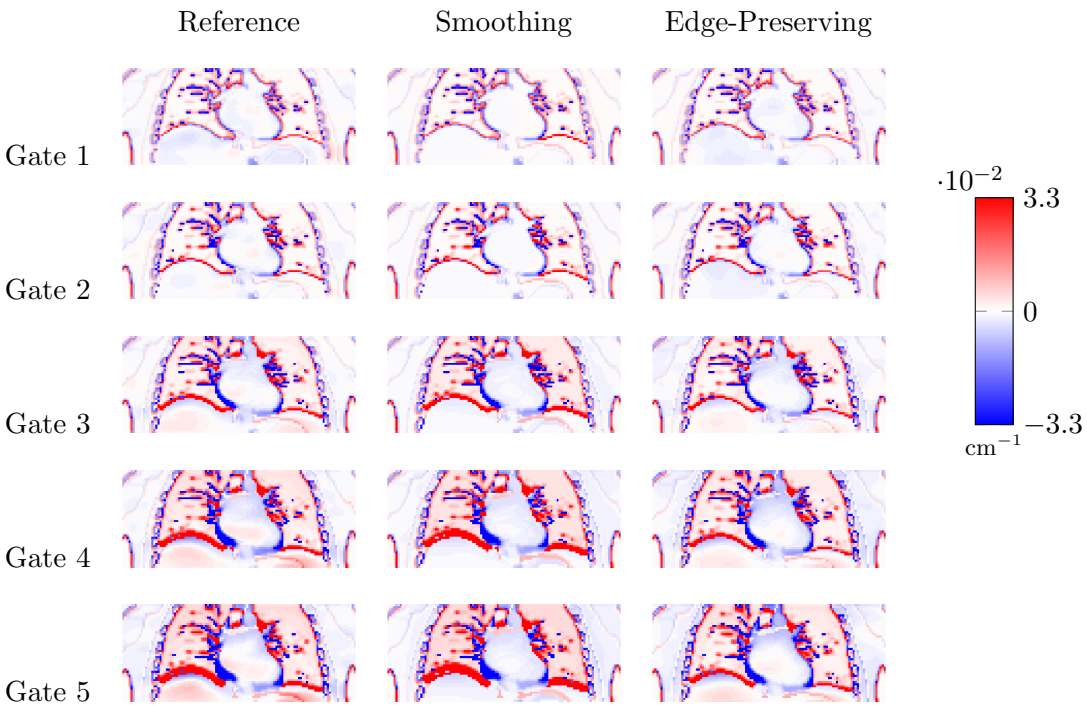

Figure 6.9: Coronal views of the difference images between the true attenuation map and the warped end-expiration attenuation map, for all respiratory gates, using mass-preserving JRM deformation fields obtained with the regularisation configurations introduced in 6.2.3.4: reference (left), smoothing (centre) and edge-preserving (right) regularisation.

However, when comparing the deformation fields via the differences between the warped and the true μ maps (Figure 6.9), we can observe that mass-preserving JRM decreases errors in the μ maps. This can also be seen in Figure 6.10, where the Jacobian determinant maps are visually closer to true changes (as constructed in the simulation), even though they do not match completely.

Standard JRM vs Mass-Preserving JRM :

The results for the two different JRM models (using edge-preserving regularisation) were compared.

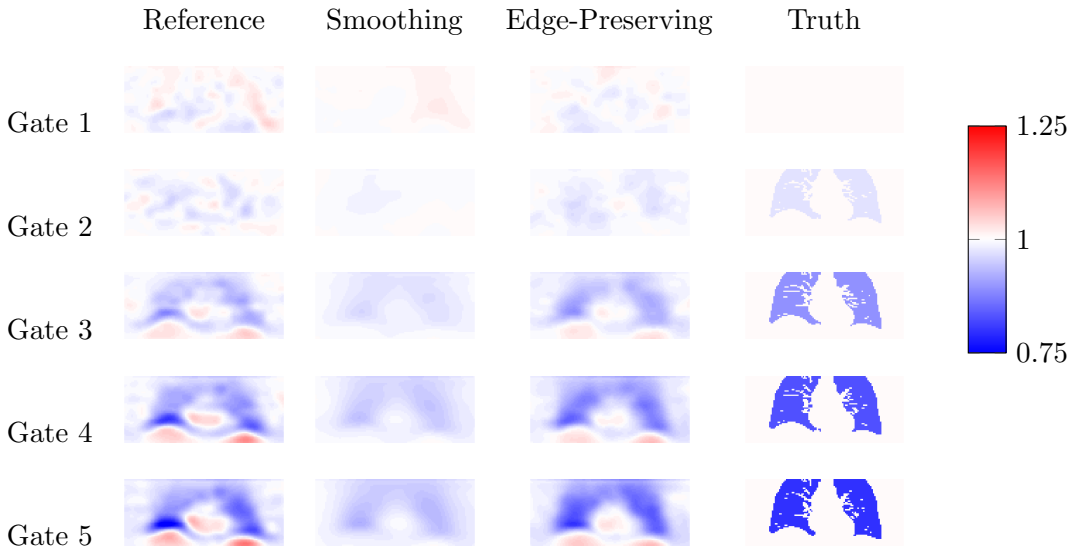

Figure 6.10: Coronal views of the Jacobian determinant images, at each respiratory gate, computed from the deformation fields estimated using mass-preserving JRM and either the reference (1st column), the smoothing (2nd column) or the edge-preserving (3rd column) regularisation, compared to the ground-truth (4th column).

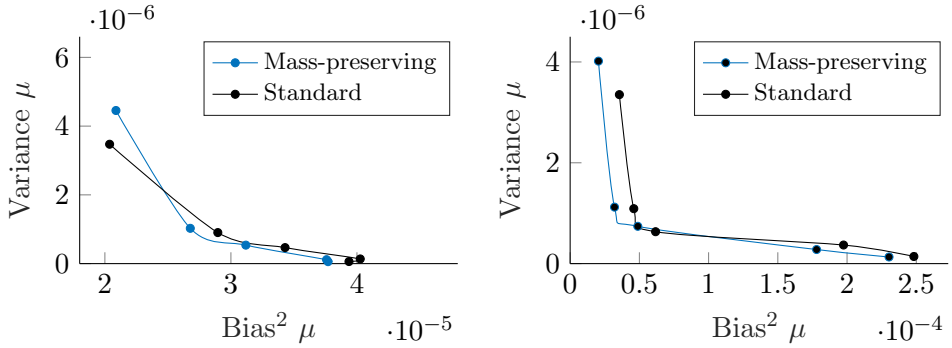

(a) Entire image **(b)** Lung only

Figure 6.11: Tradeoff between variance and the (squared) bias in the μ images, in (a) the entire image and in (b) the lung only, between the two JRM models, using an edge-preserving JRM regularisation.

As can be observed in Figure 6.11, in the lung, the bias at matched variance is considerably lower for mass-preserving JRM, whereas this is not the case in the entire image.

6.3.3 Influence of Initialisation

In this part, the same XCAT phantom was used for five different input μ maps, corresponding to the five μ maps from the XCAT simulation. The same noise seed and reconstruction parameters were utilised for these different initial μ maps, with

10 main JRM iterations (numJRMIter).

In all simulations, the initial gated reconstruction (see Algorithm 1) is performed using the end-expiration data, as it will also be the case for the patient data. This means that—apart from the case where the input μ map is the end-expiration map—the initial λ image presents motion artefacts.

We show the impact of the initial μ map by plotting the mean value in the lung of the Jacobian determinant image over the 10 iterations, at all gates. We note that for the same respiratory gate, the mean values—depending on the input μ map—should not converge to the same value, since the Jacobian determinant is a measure of relative change with respect to the initial μ map. The plots are displayed in Figure 6.12. Plots show that the convergence rate highly depends on the input μ map.

The mean value of the Jacobian determinant in the lung for the gate corresponding to the input μ map is particularly of interest: the value should indeed converge to ≈ 1 in all cases. In the Figure 6.12f, we can observe that the "worse" the initial gated reconstruction used in JRM is (i.e., the more misaligned with the end-expiration gate the μ map is), the slower the convergence. The reasoning behind this is that when the mass-preserving model is used, in the motion estimation step, the Jacobian determinant can compensate not only for motion but also for the error in the activity image (which is warped). This is particularly visible when iterating only once mass-preserving JRM, where the estimated Jacobian determinant images reflect largely the errors in the preliminary gated reconstruction (results not shown here).

From this simulation study, we can conclude that mass-preserving JRM would highly benefit from a better initialisation of the deformation fields or/and of the initial activity image.

6.3.4 Influence of Errors in Background Term

Finally, the effect of errors in the background term and most particularly in the estimate of the scatter sinogram is studied here.

In this part, the input attenuation map corresponds to the end-expiration state, as in Section 6.3.2 to avoid problems due to initialisation.

The simulated errors in the background sinograms are the following:

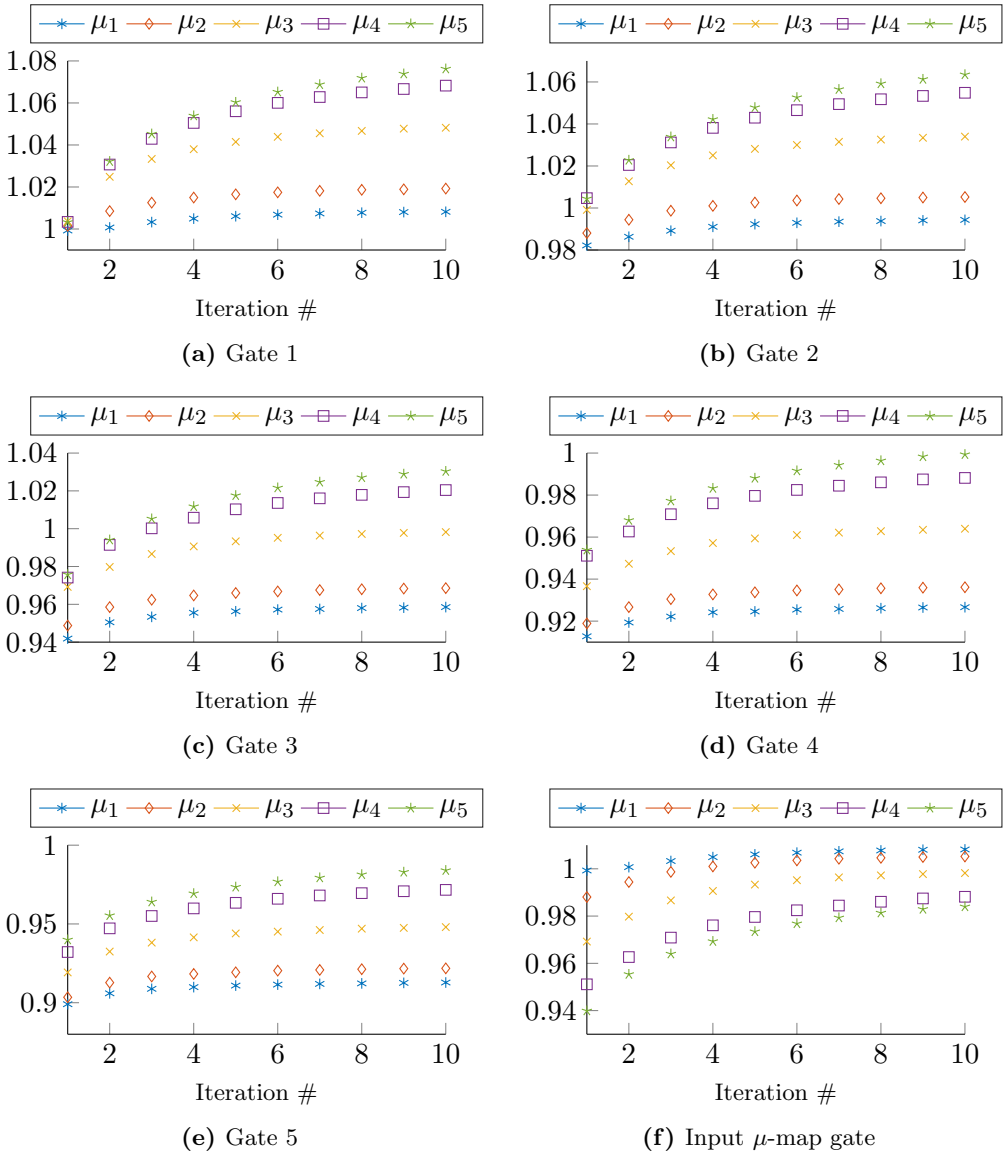

Figure 6.12: Mean Jacobian determinant value in the lung calculated at different respiratory gate (a-e: gate 1 to 5 and f: same gate as input μ map) over the iterations, depending on the initial μ map: $\boldsymbol{\mu}_1$ to $\boldsymbol{\mu}_5$ (indices: 1 corresponds to end-expiration, 5 to end-inspiration and 2, 3 and 4 are intermediary gates).

Simulation	1st simulation	2nd simulation	reference simulation
Entire image	8.755×10^{-10}	8.741×10^{-10}	8.736×10^{-10}
Lung only	1.084×10^{-9}	1.063×10^{-9}	1.092×10^{-9}

Table 6.2: Mean squared errors in the entire image and in the lung only, for the different simulations.

- 1st simulation – small errors: -3%, -2%, 0%, $+2\%$, $+3\%$, respectively for gates from end-expiration to end-inspiration.
- 2nd simulation – large errors: -10%, -5%, 0%, $+5\%$, $+10\%$, respectively for gates from end-expiration to end-inspiration.

The results of these two simulations are compared with a simulation from Section 6.3.2, using the same reconstruction parameters ("reference simulation").

Firstly, the impact of (uniform) errors in the background sinograms is evaluated using the mean squared error (MSE) in the reconstructed activity image (reference: the true activity images). The MSE in the entire image and in the lung only are given in Table 6.2.

Visually the reconstructed activity images are almost identical (outside of differences in noise), which confirms the very close numbers found in the table.

Furthermore, the warping was assessed from the estimated Jacobian determinant images. The images were highly similar (not shown here), which is in agreement with the previous validation.

The results in the section seem to indicate that mass-preserving JRM is not sensitive to uniform errors in the background sinograms. This will be further tested with patient data for non-uniform background errors in Section 6.4.3.2.

6.4 Patient Data

6.4.1 Available Data: Coagulation Study Cohort

A total of 11 IPF patients were part of the entire cohort, among whom 2 were control patients where the acquisition protocol slightly modified (see below). We will refer as "treatment patients" patients who underwent the anticoagulation treatment and "control patients" who did not. For each patient, two days of acquisition (we will refer to each as "substudy") were performed:

1. **Pre-Treatment**: In the case of the treatment patients, the anticoagulation

treatment starts the day after the Pre-Treatment substudy.

2. **Post-Treatment**: The substudy takes place approximately 3 to 4 weeks after the Pre-Treatment substudy.

Each substudy comprises two PET scans (both with listmode acquisition enabled), acquired in the following order:

1. **Dynamic Acquisition**: The FDG radiotracer is given to the patient just after the start of the acquisition. The acquisition protocol was different for the 9 treatment patients and the 2 control patients:

   - Treatment patients: a preliminary CTAC acquisition was undergone before a 14 min dynamic acquisition (12x5 s,12x10 s,6x20 s,5x60 s,2x120 s).
   - Control patients: a CINE-CT acquisition was performed before a 25 min dynamic acquisition (12x5 s,12x10 s,6x20 s,5x60 s,4x120 s,1x300 s,1x240 s). The 37 first frames coincide with the dynamic frames of the treatment patients.

2. **Static Acquisition**: A CTAC acquisition precedes a 2-bed position lung acquisition (2 min per bed position). The static PET data were acquired approximately 60 min after the radiotracer injection.

Only data from patients whose respiration was monitored with a Varian RPM system was used in the following analysis. All patients were instructed to breathe shallowly during the CTAC and CINE-CT acquisitions.
CTAC and CINE-CT protocols:

- The CTAC image (used for JRM) was reconstructed by the scanner software from a multislice helical acquisition (slice thickness: 3.75 mm, pitch: 1.375, voltage: 120 kVp, current: 40 mA, revolution time: 0.8 s).
- The CINE-CT data were acquired using a step-and-shoot (4 bed positions) technique to cover the lung PET bed position (slice thickness: 5 mm, voltage: 120 kVp, current: 10 mA, revolution time: 0.5 s). The cine duration was set to one respiratory period of the patient + an additional 1 s.

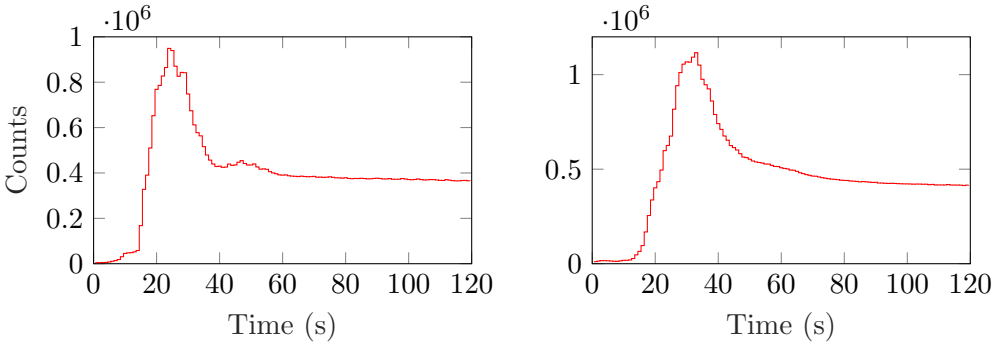

(a) Patient 1 **(b)** Patient 2

Figure 6.13: Counts per second during the first two minutes of a dynamic acquisition for the two studied patients, (a) Patient 1 and (b) Patient 2.

As part of the Coagulation Study, 11 dynamic acquisitions and 3 static acquisitions were used in this thesis. The patient data in this chapter were reconstructed using GE proprietary projectors in MATLAB.

6.4.2 Dynamic PET Reconstruction

The main reconstruction parameters (Table 6.1) were the following: numJRMIter = 6, numSubs = 8, numOSEMIter = 6, numMotionEstimation = 20 at the first JRM iteration, then numMotionEstimation = 10. The penalty weights were approximately tuned in order to obtain adequate images and registration visually.

6.4.2.1 Skipping Duration for Motion Estimation

Two patient acquisitions were selected and processed using the algorithm presented in Section 6.2.4.1 using either the entire acquisition or skipping the initial part of the acquisition for the motion estimation.

In the second case, the skipped duration was estimated from plotting the number of counts per second in the listmode data for all patients of the Coagulation Study cohort. The plots for the two studied patients here are shown in Figure 6.13. For all patients, the count rate varies very quickly at the start of the acquisition but stabilises after approximately 30 to 40 s (although a small bump in the curves can usually be identified, corresponding to the first re-circulation of the radiotracer).

The skipped duration was therefore chosen as 1 min, corresponding to the first 12 dynamic frames of the acquisition, as a tradeoff between removing rapid changes in radiotracer distribution and keeping as many counts as possible.

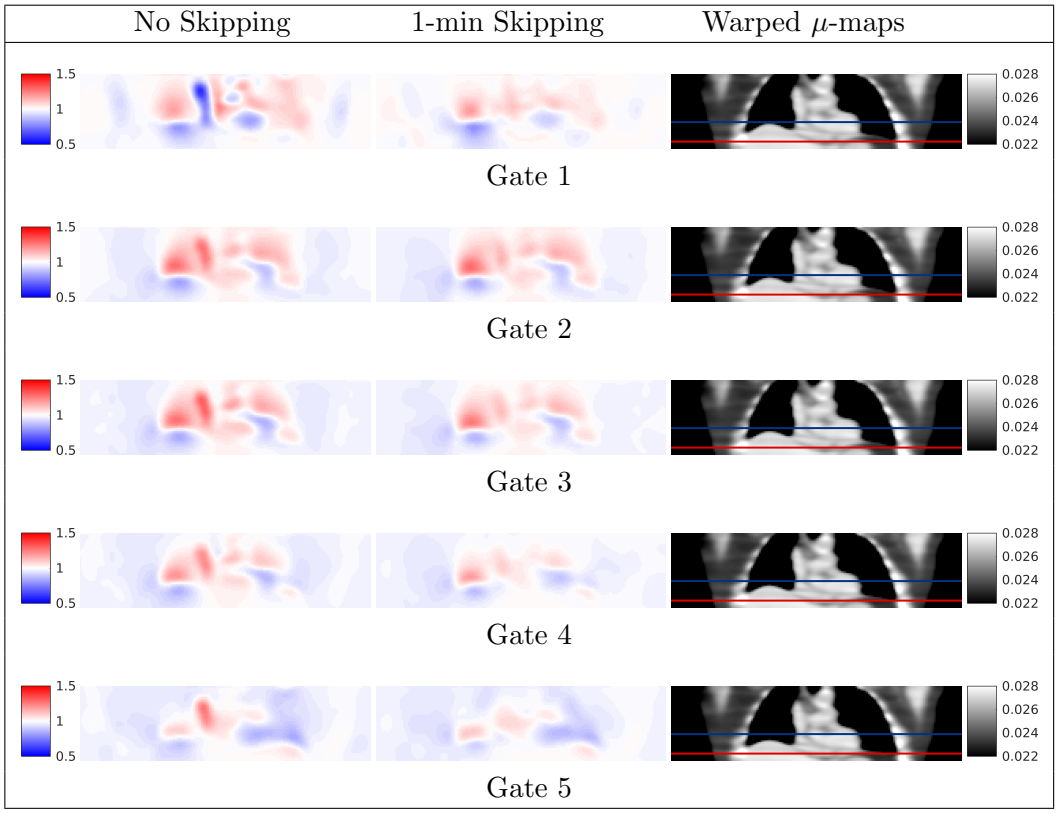

Figure 6.14: 1st Patient: Jacobian determinants for all respiratory gates determined from the entire acquisition (left column) or from a part of the acquisition (middle column), compared to the warped μ-map at each gate (left column). The blue and red lines in the warped μ-map images are visual landmarks for motion assessment.

First patient :

Coronal views of the Jacobian determinant images corresponding to the first patient are shown in Figure 6.14. Both methods have similar results, although we can observe that the values of the Jacobian determinant in the ascending aorta are closer to 1 (as expected), especially for gate 1, when the first minute is skipped.

Second patient :

For the second patient larger discrepancies were observed in some regions, such as the aorta – see Figure 6.15. A skipped duration of 1 minute might not be enough for this patient, as we can still distinguish the aorta in the Jacobian determinant images.

Summary of Results :

From the results presented for the two patients, we can conclude that it is necessary to skip the early part of the dynamic acquisition in order to obtain realistic

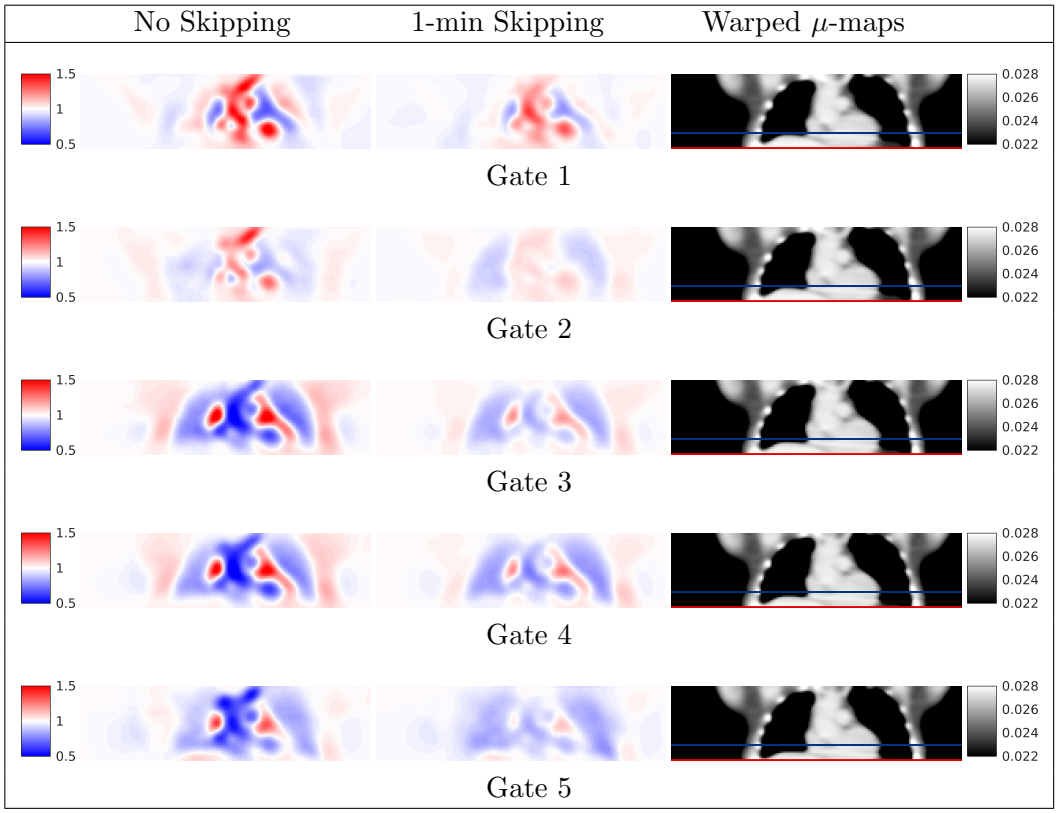

Figure 6.15: 2nd Patient: Jacobian determinants for all respiratory gates determined from the entire acquisition (left column) or from a part of the acquisition (middle column), compared to the warped μ-map at each gate (left column). The blue and red lines in the warped μ-map images are visual landmarks for motion assessment.

deformation fields. This is similar to Yu et al. 2016; Chan et al. 2018, where they skipped three minutes of the acquisition. Here we have shown that it is necessary to skip at least one minute for a standard dynamic FDG acquisition to obtain accurate motion fields.

Although it is usually necessary to discard the early part of the dynamic acquisition to estimate the motion, we can still apply the motion fields to the frames which were initially excluded, as we assume the relation between the motion and the surrogate respiratory signal stays consistent over the entire dynamic acquisition. Rapid distribution changes between time frames are not a problem anymore for the second stage using MCIR, since the frames are reconstructed separately.

6.4.2.2 Validation using Residuals of Compartmental Modelling

The 1-tissue compartment model described in Appendix A to obtain blood volume fractions is used to estimate kinetic parameters from the obtained dynamic MCIR

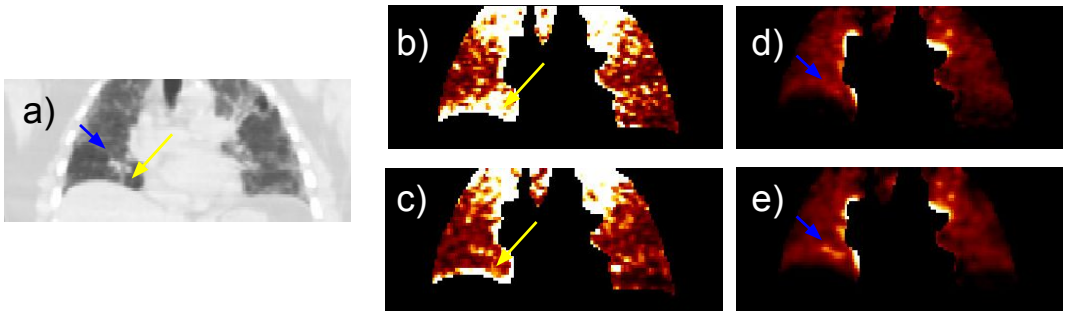

Figure 6.16: a) CT image; residuals of the kinetic model fits from: b) standard OSEM, c) MCIR OSEM; V_B images: c) standard OSEM and d) MCIR OSEM, within the dilated lung mask. The yellow arrows show increased residuals near the diaphragm and the blue arrows show lung structures.

reconstructions. The fit was performed on the images corresponding to the first 14 min of the acquisition, i.e., using all images for the treatment patients or the first 37 images for the control patients (see Section 6.4.1). The "residuals" of the model fitting in the lung are used to demonstrate the goodness of fit. In continuous settings, the residual at a voxel i would be given as:

$$\mathrm{Res}^i = \int_{t_0}^{t_1} (C^i(t) - C_{\mathrm{CM}}(t, \Psi_i))^2 \, \mathrm{d}t \tag{6.16}$$

where t_0 and t_1 represent the acquisition start and end times, respectively, Ψ_i is the set of estimated kinetic parameters from the compartment model fit at a voxel i, $C^i(t)$ and $C_{\mathrm{CM}}(t, \Psi_i)$ the measured and estimated concentration at time t given Ψ_i, respectively. Since the voxel concentrations C^i are discrete data, the previous Formula (6.16) becomes in discrete settings:

$$\mathrm{Res}^i = \sum_{\tau=\tau_1}^{\tau_{n_\mathrm{f}}} \left(\boldsymbol{C}^i_\tau - \boldsymbol{C}_{\mathrm{CM}}(\tau, \Psi_i)\right)^2 \tag{6.17}$$

where τ represents a time frame (τ_1 is the first frame, τ_{n_f} is the last frame), $\boldsymbol{C}^i_\tau$ and $\boldsymbol{C}_{\mathrm{CM}}(\tau, \Psi_i)$ are approximates of C^i and $C_{\mathrm{CM}}(\cdot, \Psi_i)$, respectively, over the time interval defined by τ.

Figure 6.16 shows the residual and the blood volume images, obtained from a reversible 1-tissue compartment model with either the MCIR OSEM images or the ungated OSEM images. We observed that the mean residual in the lung was reduced by 18.7% after motion compensation on average for all acquisitions.

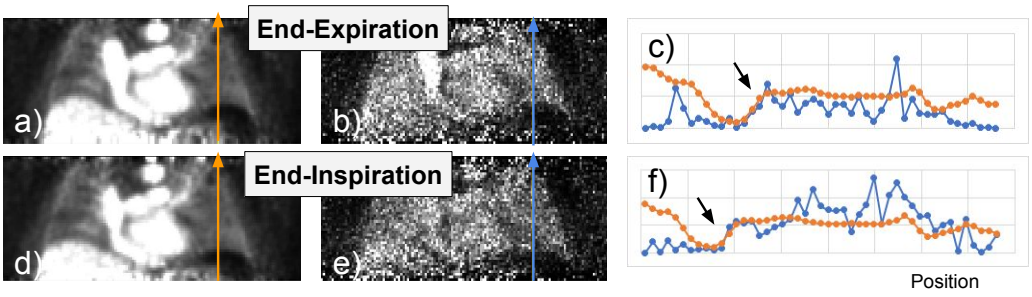

Figure 6.17: Comparison of warped JRM images and non-AC gated reconstructions, along a superior-inferior profile: at end-expiration: a) warped JRM, b) non-AC, c) profiles, and at end-inspiration: d) warped JRM, e) non-AC, f) profiles. The black arrows show the matched diaphragm locations for the two gates.

The blood volume images also show an improvement for the MCIR images, where some structures are better delineated (such as blood vessels).

6.4.2.3 Visual Validation against non-AC PET Images

To assess the accuracy of the motion estimation from JRM, non-AC OSEM reconstructions (6 iterations, 8 subsets) were performed on the respiratory gated data $\{\boldsymbol{g}_\ell\}$ (entire dynamic acquisition). The position of the diaphragm is then compared to its position as given by JRM, warping the JRM-reconstructed average image to end-expiration and end-inspiration. The visual assessment for one of the patients is given in Figure 6.17.

6.4.2.4 Visual Validation against CINE-CT Data

A third method was used to validate the method: by comparing to gated CINE-CT data. As stated in Section 4.2.3, image artefacts are common for reconstructed gated CT from CINE-CT acquisitions, and it is unlikely that PET and CT gates match completely, for instance due to motion between the CT and PET acquisitions. Nevertheless, this comparison can give an idea on how much the lungs dilate extend during respiration and is often used to assess motion-compensating methods.

For 4 dynamic PET acquisitions (corresponding to the 2 control patients) of the Coagulation Study cohort, a CINE-CT acquisition was performed before the radiotracer injection, in place of the standard CTAC acquisition.

Case 1 – Good Alignment between CINE-CT and PET Acquisition :

The warped μ maps correspond closely to the μ maps created from the CINE-CT acquisition as well as the non-AC images, see Figure 6.18. We can however notice that the densities at end-inspiration are higher than they should be in the JRM

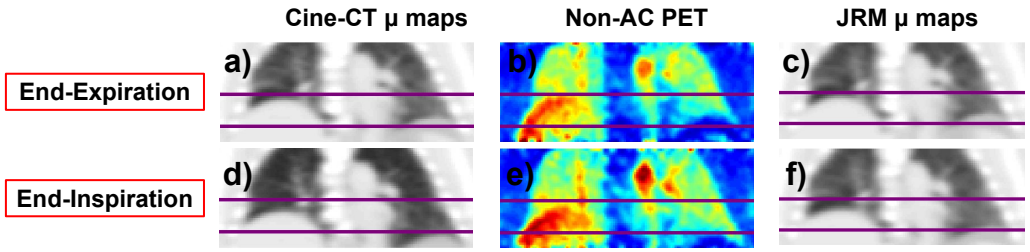

Figure 6.18: End-Expiration: a) μ map from CINE-CT, b) non-AC, c) warped μ map; End-Inspiration: d) μ map from CINE-CT, e) non-AC, f) warped μ map.

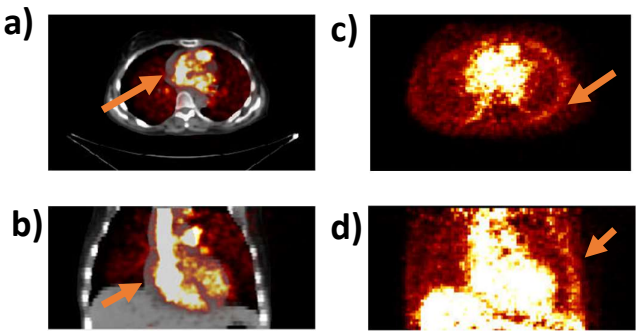

Figure 6.19: Visual artefacts identified on early (a) and b)) and late (c) and d)) frames of the PET reconstructed images, in axial and coronals views.

warped μ maps. Indeed, the warping did not include the Jacobian determinant of the deformation fields in this section.

Case 2 – Gross Patient Motion :

One of the patients moved between the CINE-CT and the PET acquisitions (shift of approximately 1 cm along the right-left direction), producing conspicuous artefacts on the reconstructed images (ribs/around the heart), which are clearly visible from the early frames. The re-positioning of the patient was confirmed by the physician in charge of the acquisition. Figure 6.19 shows an early dynamic frame overlayed on the CT image (used to derive the attenuation map) and a late dynamic frame, in both coronal and axial views. The early frame corresponds to $\approx$ 20 to 25 s after tracer injection and the late frame to 510 to 570 s after injection.

The presented method mostly realigned the μ map to the PET gates (as compared to the non-AC reconstructions), as shown in Figure 6.20.

6.4.3 Static PET Reconstruction

We determined in Section 6.3 the best type of regularisation for the mass-preserving JRM (i.e., edge-preserving regularisation). The penalty weights were tuned for pa-

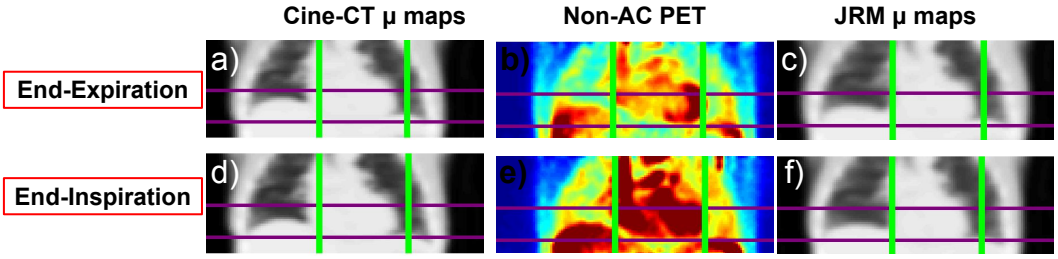

Figure 6.20: End-Expiration: a) μ map from CINE-CT, b) non-AC, c) warped μ map; End-Inspiration: d) μ map from CINE-CT, e) non-AC, f) warped μ map.

tient data to obtain Jacobian determinant images visually similar to those of simulated data in Section 6.3. From the validation study, a similar regularisation weighting was used for the standard JRM implementation (i.e., quadratic regularisation on both the activity image and the deformation parameters).

Three patient datasets from the Coagulation Study cohort were reconstructed using:

1. Standard JRM (as described in Bousse *et al.* i.e., using the reference regularisation).

2. Mass-preserving JRM, using edge-preserving regularisation, with average scatter sinogram computed from input attenuation map.

3. Mass-preserving JRM, using edge-preserving regularisation, with re-estimation of the scatter sinograms at each respiratory gate.

Although results from Section 6.3.3 indicate that a greater number of iterations for numJRMIter should be needed for the mass-preserving JRM, due to computational limitations only 4 iterations were used here to obtain preliminary results.

The results were only visually assessed using reconstructed images gated non-AC reconstructions (OSEM 8 subsets, 6 iterations, 6-mm FWHM 2D Gaussian postfilter + 1-4-1 weighted z-axis postfilter).

They were not compared against gated AC images, as problems with the MATLAB reconstruction toolbox were found, making the reconstructed images not fully quantitative (differences between the images reconstructed with the scanner and those reconstructed with the toolbox). It will be discussed in more detail in the discussion of this chapter.

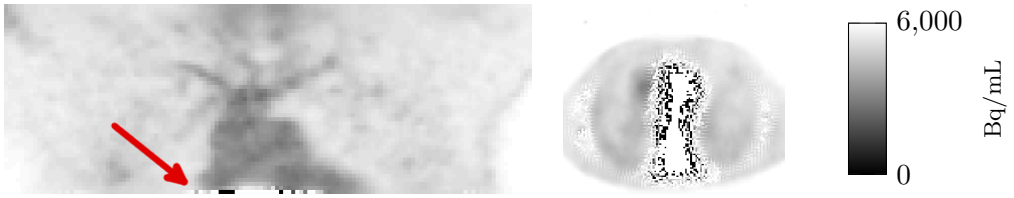

(a) (b)

Figure 6.21: (a) Coronal and (b) axial views of a MC-BSREM reconstructed activity image depicting visual artefacts at the edges of the FOV. The red arrow indicate the axial slices where the artefact can be seen.

6.4.3.1 Problems linked to MC-BSREM

Block sequential regularized expectation maximization (BSREM) is a penalised reconstruction using a gradient-based step (see Section 2.3.1.2). Unlike Newton or quasi-Newton methods, the step size is heuristically fixed for the entire image to ensure a fast overall convergence while avoiding as much as possible artefacts due to large step sizes. For motion-compensated BSREM (MC-BSREM, Paragraph 6.2.3.4), the step size was adapted to also include the number of respiratory gates (cf. Appendix B.3.2).

However, although BSREM and MC-BSREM did not show any visible problem on simulated data, "grid" artefacts were present on the reconstructed patient data, as can be visualised in Figure 6.21.

This issue might be linked to differences in detection sensitivity (which is lower at the edges of the axial FOV). For this reason, motion estimation using mass-preserving JRM in this part was impacted. Section 6.4.3.1

6.4.3.2 Gate-Dependent Background Sinograms and Impact for JRM

The scatter sinograms corresponding to end-expiration and end-inspiration gates, computed using the deformation fields estimated after all JRM iterations are compared to the "rescaled" scatter sinogram, which approximates the scatter sinogram from ungated data and a given μ map (as described in Section 6.2.1).

The mean relative differences between the estimated gate-dependent and averaged scatter sinograms are given in Table 6.3.

Similarly to the results presented for simulated data in Section 6.3.4, the changes in the scatter sinograms (and therefore background sinograms) did not have a large impact on the reconstructed activity image and the estimation of the deformation

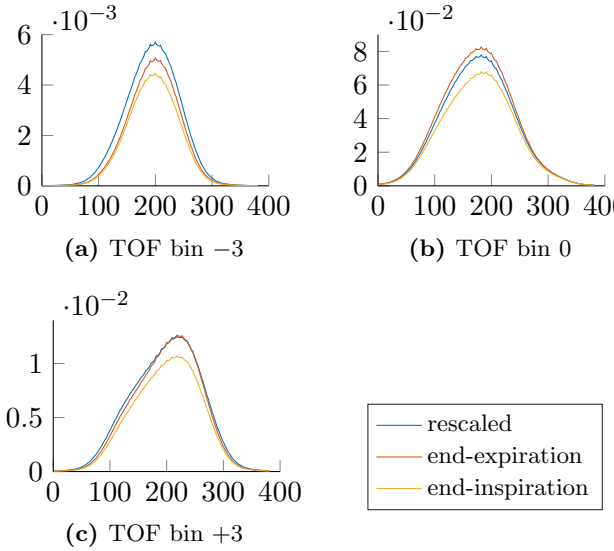

(a) TOF bin −3 **(b)** TOF bin 0

(c) TOF bin +3

Figure 6.22: Normalised scatter profiles corresponding to one of the patient datasets for rescaled scatter, end-expiration scatter and end-inspiration scatter, at three different TOF bins (−3,0,+3, for TOF bins sorted from −5 to +5, cf. Appendix B), averaging over all views. The normalisation accounted for the gate durations.

	gate 1 – BP 0	gate 1 – BP 1	gate 5 – BP 0	gate 5 – BP 1
Patient 1	−1.33%	−1.48%	−1.09%	−1.24%
Patient 2	−3.27%	−3.66%	−2.37%	−3.92%
Patient 3	−2.65%	−1.96%	−1.48%	−3.15%

Table 6.3: Mean relative differences between the estimated scatted sinograms at end-inspiration and end-expiration and the rescaled scatter sinogram, using a gate-specific rescaling factor. In the table, gate 1 indicates end-expiration, gate 5 end-inspiration. BP 0 corresponds to the lower-thorax bed position and BP 1 the upper-thorax bed position.

fields. An example is provided in Figure 6.23 for an upper-chest acquisition, showing relative differences mostly under 5%.

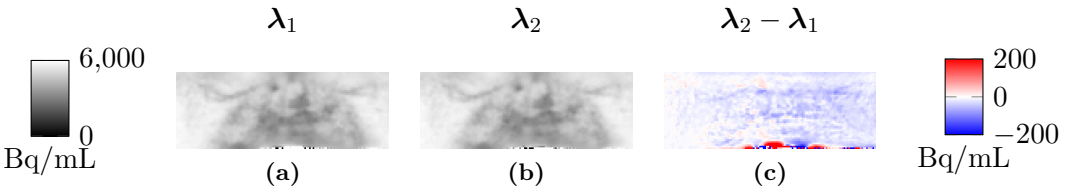

(a) **(b)** **(c)**

Figure 6.23: Coronal views of the activity images $\boldsymbol{\lambda}_1$ and $\boldsymbol{\lambda}_2$ reconstructed with mass-preserving JRM, either (a) with re-estimation of gate-dependent scatter sinograms or (b) using rescaled scatter sinograms, respectively, and of (c) the difference image $\boldsymbol{\lambda}_2 - \boldsymbol{\lambda}_1$.

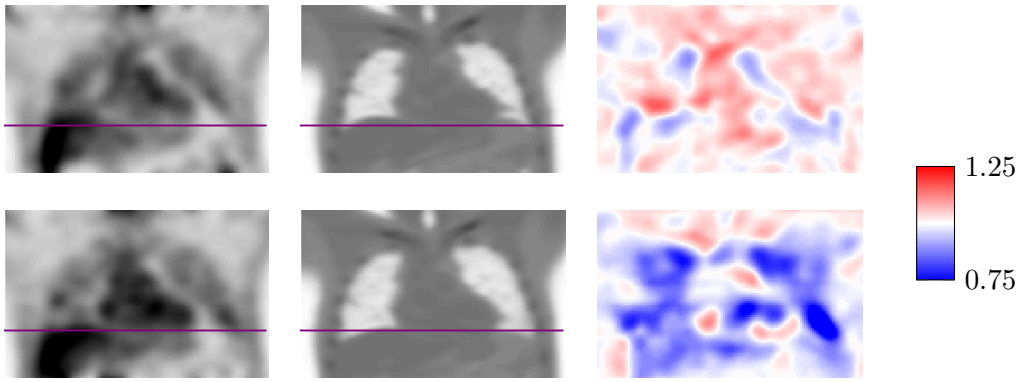

Figure 6.24: Coronal views of the consolidated non-AC image (1st column), warped μ map using deformation fields from standard JRM (2nd column), Jacobian determinant image from standard JRM (3rd column), either at end-expiration (1st row) or end-inspiration (2nd row). Visual assessment is helped using a horizontal purple line. Units for the μ maps and the non-AC images are not provided as only visual assessment is needed here.

6.4.3.3 Motion Estimation and Jacobian Determinant

We assess the estimation of motion by comparing the warped μ maps against the non-AC images and by visually analysing the Jacobian determinant images, both at end-expiration and end-inspiration. All figures in this section show images for one of the patients, which were "consolidated" (i.e., averaged from separate results corresponding to the two bed positions). Figure 6.24 shows the results for standard JRM and Figure 6.25) are the results of mass-preserving JRM (with re-estimation of the scatter sinogram at each gate).

Both JRM methods manage to obtain realistic deformation fields (diaphragm at end-expiration is higher than at end-inspiration) and the motion from JRM seems to follow closely the motion observed in the non-AC images. Visually the warped μ maps appear similar, but differences in the Jacobian determinant images are conspicuous. The Jacobian determinant images obtained from mass-preserving JRM have unexpected low values in the heart and in the liver for all respiratory gates. Mass-preserving JRM seems therefore to be more impacted by the problems in the reconstruction toolbox than standard JRM. For ungated PET data, the MATLAB toolbox values in the liver were found consistently lower than the values reconstructed by the scanner software; mass-preserving JRM seems to try and compensate for those problems by tuning the Jacobian determinant values. Results on other patient datasets (not shown here) show similar results.

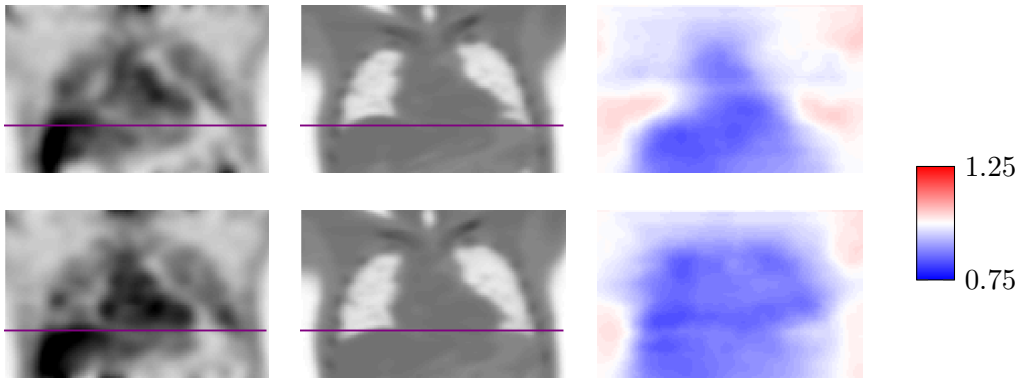

Figure 6.25: Coronal views of the consolidated non-AC image (1st column), warped μ map using deformation fields from mass-preserving JRM (2nd column), Jacobian determinant image from mass-preserving JRM (3rd column), either at end-expiration (1st row) or end-inspiration (2nd row). Visual assessment is helped using a horizontal purple line. Units for the μ maps and the non-AC images are not provided as only visual assessment is needed here.

6.5 Conclusion and Discussion

In this chapter, methods based on the implementation of JRM from Bousse et al. 2016a were presented and assessed.

Firstly, a mass-preserving version of JRM was introduced and mathematically formulated. This model was based on the assumptions that respiratory motion affects both displacement of the tissue and changes in density and activity concentration, mostly in the lungs. The same approximation for the changes as in Chapter 4 was utilised: the volume changes estimated from the Jacobian determinant of the deformation.

In this mass-preserving reconstruction algorithm, regularisation is of great importance to be able to obtain both realistic deformation fields and realistic Jacobian determinant images. The incorporation of the Jacobian determinant in the cost function otherwise allows JRM to overfit the PET data noise. Similarly as in Chapter 4, the quadratic regularisation on the deformation parameters is replaced by regularisation applied on the Jacobian determinant images. Following the results from the registration on patient data in Section 4.6.3.1, standard and mass-preserving versions of JRM were assessed with different types of regularisation in Section 6.3.2 using lung XCAT simulated data. Density and activity concentration changes were added to the XCAT original images, by multiplying by the volume gain or loss between a given respiratory gate and the mid-expiration gate.

Mass-preserving JRM has shown promising results for the simulation data, especially in the lung where, at comparable variance, biases on warped μ maps were reduced and the estimated maps of density changes (i.e., the Jacobian determinant images) more representative of the simulated density changes. The reconstructed activity images from both standard and mass-preserving JRM methods were however almost identical (for a given regularisation configuration). This means that despite less accurate motion estimation, standard JRM can reconstruct a motion-compensated activity representation similar to mass-preserving JRM. The impact of incorrect initialisation in mass-preserving JRM was also evaluated with such simulations. The study showed that the optimisation will converge slowly when a μ-map far from the end-expiration is used as input, as it creates quantitative artefacts in the initial gated activity image. In the motion estimation of mass-preserving JRM, the incorporation of the Jacobian determinant in the model adds a degree of freedom such that the errors can be compensated not only by realigning the data, but also by modifying the image intensity. Mass-preserving JRM is still expected to converge towards an adequate solution but initial iterations are more impacted by a wrong initialisation as for standard JRM: this is particularly observable after one or two iterations of mass-preserving JRM, where the Jacobian determinant images reflect both motion and AC mismatches. As for uniform errors in the background/scatter sinograms, they were found to have little impact on the motion estimation and the final reconstructed image in simulations.

In Section 6.2.4.1, the implementation of JRM for static PET data of Bousse *et al.* was first extended to dynamic PET data. The modified method consists in accumulating the gated projection data corresponding to the different dynamic frames, in order to estimate the motion during the entire dynamic acquisition. The standard JRM is then applied to these projection data. While the activity image—representing the average concentration during the covered dynamic period—is discarded, the deformation fields obtained are used separately to reconstruct all dynamic frames. This strategy is similar to the one applied in another motion-compensating technique (Yu et al. 2016; Chan et al. 2018). We have also skipped the start of the acquisition, where the radioactivity distribution is rapidly changing, for the motion estimation: keeping the fast kinetics in the projection data led to

local problems in the deformation fields. The rate of the initial changes depends on the injection rate of the radiotracer and blood flow. The duration of the part to skip can be approximately determined by checking when the count rate starts to slowly decrease in the listmode data during the entire acquisition. The method was evaluated on 11 FDG dynamic acquisitions in Section 6.4.2, using three different techniques: (i) comparison of the warped images with non-AC gated images for general alignment of the lungs, (ii) comparison of the warped μ maps with 4D CT images created from a CINE-CT acquisition (when available) and (iii) using the residuals of compartmental modelling applied in the lung. The estimated motion was visually very consistent with the observed motion from the non-AC and 4D CT images. This was confirmed with the results from compartmental modelling, where the mean residual in the lung was reduced by 18.7% on average. The skipped duration was estimated to 60 s in our dataset. It might however not be sufficient for other datasets, for example if the radiotracer is administered more slowly or for different types of radiotracer, with slower kinetics. A possibility would be to apply the method to different parts of the acquisition, to verify the stability of the results.

The mass-preserving model has not been tested on dynamic JRM, because of the kinetics involved during the dynamic frames. However, as we concluded that it was required to remove the very early part of the dynamic acquisition to obtain realistic deformation fields even without introducing the Jacobian, mass preservation might be applicable. This would however need more validation. More generally, the outcome of using mass preservation in the reconstruction of the PET images is uncertain in the dynamic case. Indeed, mass preservation does not apply for fluids, including blood, as they are considered (almost) incompressible. Not accounting for density and activity concentration changes in the reconstruction however affect the compartmental modelling fit, inducing biases in measurement of kinetic parameters, as suggested in other work on brain (Mérida et al. 2017; Cabello et al. 2019). This will need to be investigated in future work, for example reconstructing the (dynamic) control patient data (from the Coagulation Study cohort) with different initial μ maps (using gated CINE-CT data).

JRM was then extended to 2-bed lung position acquisitions. Lung PET scans often need to be acquired in two steps, in order to cover the entire lungs, referred

as bed positions (i.e., step-and-shoot acquisitions with an axial translation of the bed). In this case, the current joint reconstruction optimises the two acquisitions separately. As discussed in Section 6.2.4.2, a better optimisation should however try and estimate the deformation fields and the activity image corresponding to the entire scanning axial length. Three patient datasets (static 2-bed position listmode data), acquired approximately one hour post-injection, were reconstructed with, on the one hand, the standard JRM approach and, on the other hand, mass-preserving JRM (either with rescaled average background sinograms or with gated background sinograms, recomputed from estimated deformation fields). Re-estimating the scatter backgrounds at each respiratory gate had negligible impact on the estimated motion and image. The motion was assessed only visually against non-AC images, as bugs in the patient data reconstruction software, impacting image quantification, were found. A static acquisition from the Coagulation Study cohort was indeed reconstructed with the current version of the GE reconstruction MATLAB package using the same TOF OSEM reconstruction parameters as the ones which were used to reconstruct the data with the scanner reconstruction software. The mean relative errors in spherical ROIs (radius: 3 mm, volume: 14124.5 mm^3) drawn using ITK-SNAP (Yushkevich et al. 2006) in the right lung, the liver and cardiac region (using the image reconstructed with the scanner software as reference) were computed as +3.5%, −4.5% and −6.7%, respectively. In addition, a large cubic ROI ($300 \times 240 \times 180\,mm^3$) was drawn covering most of the patient thorax to investigate the overall impact of the bug on quantification, the mean relative error was of −2.2%. These measures show that the errors caused by the bugs in the software are not global but location-dependent. As the overall error in the thorax is relatively small, the most-likely source is the implementation of the scatter estimation. Using multiple patient data, the non-TOF scatter sinograms were compared by collapsing all TOF bins from the TOF scatter sinograms together to create a non-TOF sinogram; the scatter sinogram differences were negligible (less than 0.01%), which imply that the bug lies either only in the TOF scatter estimation or in both TOF and non-TOF scatter estimations).

In spite of those problems, all JRM methods managed to recover the general outline of respiratory motion, where non-AC images were in good agreement with

warped μ maps, e.g., near the diaphragm. The Jacobian determinant images computed from the deformation fields corresponding to mass-preserving JRM however contained unexpected values, especially in the cardiac and hepatic areas, most likely linked to the quantification problems arising from the bugs in the toolbox used. When fixed, the motion correction methods could be assessed by comparing the quantification of gated images (selecting the PET respiratory gate which is visually the closest to the input CT gate). Other techniques could also be used to validate the output of the joint reconstruction, such as using gated MLAA reconstructions, using denoising from a convolutional neural network (Hwang et al. 2019a; Hwang et al. 2019b (this has not been properly validated yet) or from CINE-CT acquisitions. Although image artefacts are often present in gated CT images and the respiratory gates between CT and PET might not coincide (Section 4.2.3, Yamamoto et al. 2008), the latter could provide information on the amount of density changes expected between respiratory gates, such as between end-inhalation and end-expiration gates.

In this work, standard emission reconstruction algorithms were used to compute the activity images, i.e., OSEM and BSREM. Both algorithms showed however relatively slow convergence. A more efficient algorithm, such as the fast quasi-Newton algorithm using L-BFGS-B with preconditioning presented in Tsai et al. 2018b, could have been used to accelerate convergence. BSREM also demonstrated problems when large step sizes were used, especially at the edges of the axial FOV. Additionally, the number of iterations for the different steps (image reconstruction, motion estimation and number of alternations) were not tuned, which could also be beneficial (Tsai et al. 2018a).

In addition, the current implementation of both standard and mass-preserving JRM in MATLAB is not optimal and reconstructions run over multiple days on CPU. On the UCL cluster, a typical motion estimation update for one gate lasts between $7,000\,\text{s}$ to $16,000\,\text{s}$ and a MCIR update using BSREM up to $40,000\,\text{s}$ (leading to each JRM main update to run for approximately one day). These high figures could be reduced with more optimal code and the use of GPU-based computation—the proprietary GE software used in this thesis however does not have this functionality, use single-threaded projectors and cannot be modified. Note that the additional compu-

tation time due to the addition of the Jacobian determinant in the mass-preserving JRM was negligible compared to the computation time related to back-projecting and forward-projecting (including the calculation of warped images). Rewriting the reconstruction algorithm in a more optimised fashion will be subject of future work.

Finally, the mass-preserving reconstruction method presented in this chapter could also be extended to PET/MR imaging, provided that the input JRM μ map is a good representation of the attenuation distribution at a given respiratory state. Since standard methods used in PET/MR imaging to derive μ maps are often prone to errors (Lillington et al. 2019), more sophisticated methods would therefore be required—potential candidates are MLAA or deep learning based μ maps. Standard JRM methods have been used for these data (e.g., Bousse et al. 2017 uses the same implementation as in Bousse et al. 2016a, on which our mass-preserving method is based) and showed that it was also possible to estimate respiratory motion, despite inaccuracies in the MR-based input μ map. The results from this chapter are in good agreement with this assessment, since both standard and mass-preserving JRM methods managed to realign the lungs, although there were issues in the estimated scatter sinograms and consequently also in the model.

Chapter 7

General Conclusions and Future Work

7.1 Main Conclusions

Idiopathic pulmonary fibrosis (IPF) is a progressive pathology affecting the lungs, with an increased rigidity of the tissue in the pathological/fibrotic regions due to the build up of scarring and local remodelling. The breathing of the patient is worsened. As its aetiology is unknown, great effort is being made to get an understanding of its progression. PET imaging could be a way to provide physiological information for IPF. Imaging the lung is however challenging, as the quantitative image quality suffers from several uncertainties and artefacts. The thorax and abdominal regions are indeed highly affected by motion, such as the motion caused by respiration. Furthermore, IPF brings global changes in the lung architecture, especially at the base of the lungs, which become more rigid and dense; this implies that the resolution is spatially variant.

In **Chapter 3**, positron range was investigated in density-varying media, such as in the fibrotic lung. Indeed, in absence of a dedicated correction method, the reconstructed PET images do not represent directly the radioactivity distribution (where the positrons are emitted by the radiotracer), but the distribution of annihilation events per second. Because of the overall lower density of the lung compared to other organs, positron range is generally larger in the lung and represents a major difficulty for tracers labelled with high-energy radionuclides, such as ^{82}Rb or ^{68}Ga. Its effect on the reconstructed PET images is often neglected, as positron range is typically in the range of a few millimeters or less in common regions of the body, and is rarely compensated for. Monte Carlo simulations were used in this thesis to characterise the effect. The results showed that for ^{18}F-FDG PET acquisitions

in the fibrotic lung, the impact should be minimal on the quantification, especially if we assume that the low-density regions have lower uptake than high-density regions, due to differences in air fraction (Holman et al. 2015). For a future lung study involving a tracer labelled with a higher energy radionuclide (such as ^{68}Ga-PSMA or ^{82}Rb), caution should be taken when analysing measures from the images, if no correction method is used.

In **Chapter 4** another main challenge of PET lung imaging was introduced: respiratory motion. In healthy patients, the most mobile part of the lung is located near the diaphragm, which moves approximately 1.5 – 2 cm. When no correction technique is used, static and dynamic lung PET acquisitions are therefore affected by this motion, which compromises both image visual quality and quantitative measures, especially at the base of the lungs. A basic approach is to not use the values of regions that are too close to the diaphragm. However, as the base of the lungs usually coincides with the pathological regions of an IPF lung, it might then be impossible to predict the disease evolution or treatment response for some patients in early stage of IPF. Aside from the displacement of tissues, the density and the radiotracer concentration in the lung are also modified by respiration, mainly by the dilation or expansion of the lungs. Respiratory motion has been discussed in many studies and different strategies can be used to compensating for it. Nonetheless, the density changes occurring during the respiration are rarely accounted for, as motion compensation is generally used in PET reconstruction for tumour detection and cancer staging, where the effects of lung compression and extension are likely to be negligible. However, they cannot be neglected in lung diseases such as IPF. More generally, the impact of respiratory motion on image reconstruction was demonstrated in this chapter, using patient data, for both static and dynamic PET reconstructions. A way to estimate the changes linked to compression and extension of the lung is by using the Jacobian determinant of deformation fields, which represents a measure of (local) volume change. When the Jacobian determinant is included within the optimisation cost function, the estimated deformation fields can be more accurate. In this chapter, a simple mass-preserving mage registration technique based on a sum of squared differences (SSD) cost was tested on reconstructed PET images and on μ maps. Regularisation is needed to avoid overfitting of noise by

the Jacobian determinant: this was accomplished by smoothing both the Jacobian image and the deformation fields. Accounting for density or activity concentration changes showed great improvement in the registered images, compared to standard SSD registration. The results on μ maps were found visually comparable to those from a standard registration. This preliminary study demonstrated the feasibility of using a mass-preserving model to estimate motion, which laid the foundations for the mass-preserving motion correction technique of Chapter 6.

More generally, model inconsistencies in the reconstruction were discussed in **Chapter 5**. We focused on inconsistencies due to attenuation mismatches only (i.e., the attenuation map used in the reconstruction is incorrect) in TOF PET reconstructions. Such mismatches can lead to quantitative errors in the PET reconstructed images, in both TOF and non-TOF reconstructions. Previous literature predicted that the use of more accurate time information for TOF leads to improved image SNR and reduced errors in quantification where the mismatch is (Conti 2011) – we have however found that when using a standard maximum-likelihood reconstruction, such as MLEM, the errors do not disappear but are only moved to the rest of the image. The results showed on the one hand the benefits of TOF reconstruction over non-TOF reconstruction in the region of a density attenuation mismatch, i.e., when the density is wrongly estimated in a region of the attenuation map. On the other hand, in neighbouring regions, the quantification errors are worsened in the TOF case. These findings are relevant in lung PET/CT imaging, where the attenuation map is usually known precisely in the aorta (where little motion is expected at shallow breathing), but not necessarily in the lung (especially when no mass-preserving motion-compensating strategy is adopted). For example, in compartmental modelling, where blood and/or plasma radiotracer concentration are needed in the fit, the aorta is often used as the location to draw a region of interest (ROI) and thereby obtain an image-derived input function. TOF PET reconstructions were expected to improve such compartmental model fits by reducing errors in the lung; the results presented in sections 5.3.3 and 5.3.4 however demonstrate increased errors in the aorta or ventricles, even when a standard (non-mass-preserving) motion-compensating method is used to align the attenuation map with the respiratory gate (as the lung density depends on the breathing state). Generally, we

have shown that even at high TOF time resolution, using an accurate attenuation map within the PET reconstruction is essential to obtain robust quantitative measures. When the attenuation map is not known precisely enough (as is usually the case for lung imaging), the attenuation images would need to be systematically re-estimated, for example via maximum likelihood reconstruction of activity and attenuation (MLAA) or by incorporating density and activity concentration changes (for example using the Jacobian determinant presented in Chapter 4) in the motion-compensating reconstruction.

Finally, in **Chapter 6**, two methods for accurate respiratory motion correction were presented. Both aim to estimate the motion between respiratory gates and reconstruct an activity image corresponding to a single μ map (computed from a CT acquisition). They are built upon an existing motion-compensating technique published in Bousse et al. 2016a.

The first method is dedicated to dynamic PET acquisitions. The latter—commonly used in the brain—estimate kinetic measures from the variation of the tracer radiodistribution over time, such as the fractional blood volume (i.e., the fraction of blood per voxel, cf. Appendix A) or other quantitative parameters related to the underlying biological processes. In the lung, the extraction of such measures is likely to be useful for increasing the understanding of the disease processes, such as IPF, even though ultimately static PET would be more desirable for clinical application. The use of dynamic PET data in the lung is however more challenging than in the head because of respiratory and cardiac motion. When 4D anatomical images (such as CT or MR images) are available, it may be possible to use MCIR to obtain "motion-less" PET images. However, either this involves high dose to the patient (when using CINE-CT or similar techniques) or low contrast (when using standard MR sequences) and these are rarely used. The presented method creates PET images which are aligned with the input μ map (here derived from a standard low-dose CTAC acquisition). It is a direct extension of Bousse et al. 2016a; the difference lies in the use of the sum of gated projection data from dynamic time frames instead of static PET gated projection data. While the reconstructed activity image—representing an average motion-compensated activity—can be discarded, the estimated deformations between the respiratory gates are used afterwards for

frame-wise MCIR, i.e., reconstructing all dynamic time frame separately.

The second method is aimed at compensating for motion in static PET acquisitions. The standard model in Bousse et al. 2016a is modified to take into account the density and activity concentration changes occurring during the respiration. The method uses the mass-preserving model introduced in the Chapter 4 within a motion-dependent log-likelihood. A validation study was carried out on simulated data first (using XCAT lung images, in which the density and activity were changed uniformly within the lung), which compared different types of regularisation for mass-preserving motion estimation via log-likelihood maximisation. The stability of the optimisation was also studied by carrying out two simple simulations: one accounting for uniform errors in the background sinograms and one testing different input attenuation maps. Whereas errors in background sinograms were found to have little impact for mass-preserving JRM, a wrong initialisation of the activity image (and therefore using a μ-map far from end-expiration) demonstrated that the convergence of JRM is slowed down. This can indeed be explained by the fact that the mass-preserving model can partly compensate for attenuation corrected (AC) errors in the preliminary activity image by adjusting the activity voxel values directly in the Jacobian determinant. For this reason, it would be recommended to initialise the deformation fields or/and the first activity image from another technique. Afterwards, standard and mass-preserving JRM were used on static patient data (using the extension for 2-bed position data presented in Section 6.2.4.2). The mass-preserving JRM results showed that such a model can globally align structures, but the current implementation and formulation lead to issues in the Jacobian determinant and near the edges of the axial FOV. While we know that the artefacts near the edges are caused by the choice of block sequential regularized expectation maximization (BSREM) to reconstruct the data, the origin of the unexpected values in the Jacobian determinant images is unknown. They could be due to a wrong initialisation of the activity image (i.e., when the CTAC used to derive the μ map is not at end-expiration), which would agree with previous observations on simulated data. Another possibility is that the current mass-preserving model allows too much freedom to maximise the penalised log-likelihood in the motion estimation step and that spatial constraints should be added, to encourage expansion and contraction

mainly in the lungs. Re-estimating the scatter sinograms at each respiratory gate did not improve on the results.

7.2 Summary of Contributions

The following points summarise the challenges addressed and highlight the novel contributions presented in this thesis:

- Positron range was studied in the fibrotic lung and lung tumour using Monte Carlo simulations. It was shown that the effect leads to an increased fraction of positron annihilations versus emissions in denser tissues. The demonstrated effect was found to be of low importance for quantification using ^{18}F-labelled radiotracers, such as ^{18}F-FDG which is used for the patient data of this thesis. It is however non-negligible for other radionuclides, such as ^{68}Ga or ^{82}Rb.

- A new regularisation scheme, designed to estimate deformation fields between respiratory states, was introduced to specifically tackle the problem that mass-preserving motion estimation is more sensitive to noise.

- The effects of using an incorrect μ map in PET reconstruction were studied in both non-TOF and TOF reconstructions at increasing TOF resolution, showing the local and global quantification errors produced by the perturbation in the attenuation. A theoretical prediction was derived for the case of very high TOF resolution.

- A practically feasible method for respiratory motion correction in dynamic PET acquisitions was presented, building on previous work for static PET data. Preliminary evaluation showed the potential for more accurate maps of kinetic parameters.

- A method previously developed to estimate jointly activity and motion was modified to incorporate the mass-preserving model. The preliminary results on simulated data show that the method should provide robust results, however could be still improved, e.g., by using spatial constraints to encourage dilation and contraction mostly in the lungs.

Even though this work is focused on IPF, most of the methods presented here would also be relevant for the study of others diseases, such as chronic obstructive

pulmonary disease (COPD); the disease also involves a structural change of the lung parenchyma, including localised density changes compared to healthy lung. However, the pathological tissues are not located in the same region as in IPF, therefore proposed techniques, such as motion correction or image registration, should give different results.

7.3 Future Work

Many parts of the work presented in this thesis could be extended or assessed in a more detailed manner.

Firstly, the study on positron range in Chapter 3 showed the possible problems of using high-energy radionuclides to label radiotracers for PET lung analysis, in the context of studying a spatially-varying pathology such as IPF. An existing compensation method (B. Bai et al. 2003; Alessio and MacDonald 2008; Szirmay-Kalos et al. 2012; Rahmim et al. 2008; Lehnert et al. 2011; Cal-González et al. 2015) could potentially be applied in the context of IPF to reduce the bias demonstrated in Chapter 3. However, apart from when using kernels obtained directly from Monte Carlo simulations (Lehnert et al. 2011), which is computationally expensive, these techniques might not be able to handle positron range effect on the PET images with sufficient precision for IPF or other diffuse lung diseases. Deep learning also could potentially provide a solution for positron range correction, by learning blurring kernels from Monte Carlo point source simulations.

In Chapters 4 and 6, the motion was parameterised using cubic B-splines. Although it is a common choice of parametrisation, B-spline motion fields can lead to issues in registration, such as the deformation being locally non-invertible (i.e., the Jacobian determinant can be < 0 in some regions), with possible folding (Chun et al. 2009). Regularising the Jacobian determinant image in order to keep the values above 0 is an option to avoid such non-local invertibility, however was not sufficient (waves in the warped images were observed for patient data, when JRM was used with such regularisation). An additional regularisation on the B-spline coefficients had to be added to the regularisation on the Jacobian determinant images to obtain satisfactory deformation fields. A more complex and computationally expensive transformation model, such as a fluid material model (Christensen et al. 1996), could be used to ensure one-to-one mapping and smooth deformation fields;

it would not allow sliding motion, which might be a problem e.g., near the edges of the lungs, however the impact should be minimal at PET resolution.

In Chapter 5, model inconsistencies were studied in the context of TOF PET reconstruction, with a particular focus on errors due attenuation corrected (AC) mismatches (i.e. incorrect μ map used in the reconstruction). Since recent work has demonstrated the importance of re-estimating the scatter sinogram in MLAA (Rezaei et al. 2019), the same study as for the AC mismatch could be carried out for errors in the background term in TOF reconstruction. In Chapter 6, these errors were assessed for mass-preserving JRM, where small scale fluctuations due to respiration in the background sinograms (expected to be $< 5\%$) had little impact on the estimation of motion and on reconstructed images.

Our evaluation shows that the deformation estimated by the mass-preserving JRM should be more reliable and realistic in comparison with the standard JRM, although this needs further validation. Indeed, such a mass-preserving model is not completely correct as it relies on tissues being fully compressible. However, blood is considered as mostly incompressible and accounts for at least 8% in the lung (Table 2.6). Furthermore, the proportion of fluid exchanges might vary among respiratory states and, more generally, the radiotracer kinetics are not accounted for. If the method is validated, it could be used to obtain an additional biomarker of IPF, using the Jacobian determinant to estimate the local compressibility of lung tissue, as the pathological regions of the lungs are denser and less compressible. Although this biomarker can already be computed, usually from CT data (Han et al. 2017; Guo et al. 2017), but at the cost of high radiation exposure to the patient. PET/CT might provide this information during free breathing, in addition to other measures derived from the PET data. However the mass-preserving joint reconstruction would require more validation and fine tuning of regularisation and optimisation scheme.

The evaluation for the mass-preserving JRM for static JRM was preliminary and needs to be extended for patient data acquisitions. This would however require quantitative reconstructions for the available patient data—it could be achieved by either fixing the bug related to scatter correction in the reconstruction software used in this thesis or obtaining a more recent version compatible with our scanner, the GE Discovery 710. Another possibility would be the use of other patient datasets from

a different scanner. In this context, the results from the mass-preserving method could be further validated—potential methods could use:

- Gated MLAA-based μ maps: if the remaining non-uniqueness in the μ maps estimated by MLAA can be fixed (Defrise et al. 2012; Rezaei et al. 2019), it should be possible to compare directly the gated MLAA-based μ maps and the JRM warped μ maps, for example within large ROIs in the lungs at each respiratory gate.

- Gated static reconstruction using a single gate μ map: after selecting the PET respiratory gate which is the closest to the respiratory state of the input μ map, the JRM recontructed activity image could be validated against the corresponding gated reconstructed image.

- 4D μ maps from a CINE-CT acquisition: provided the CT respiratory gates follow closely the PET respiratory gates, the warped μ maps should be directly comparable to the 4D CT-based μ maps. A similar visual assessment of the estimated motion as in 6.4.2.4 could be used, although the values in the warped μ maps could also be validated against the values in the 4D CT-based μ maps thanks to the mass-preserving model.

- Several JRM results using different μ maps (for example from CTAC and HRCT acquisitions) as inputs for JRM: assuming the use of identical respiratory gating of the PET data, the estimated gated μ and activity images from JRM should not depend on the input μ map.

- Several JRM results using different respiratory gates of the PET data: the final reconstructed image should not depend on the gating. When only part of the PET data is used with mass-preserving JRM (for example only data close to end-expiration or end-inspiration), the reconstructed activity image should be comparable to the image which would be reconstructed from the entire PET acquisition, when it might not be the case for standard JRM.

Generally, the methods presented for JRM in static and dynamic acquisitions—in Chapter 6—suffered from large computational times and rather slow convergence. Apart from optimising the implementation, modifications to the algorithm could

have been made. The activity image reconstruction could be modified to use a fast quasi-Newton algorithm via L-BFGS-B and preconditioning (Tsai et al. 2018b). Another way to achieve faster convergence would be to initialise coarsely the deformation fields from another method; JRM would therefore tune the deformation instead of estimating it *ex nihilo*. Using such an approach, we could hope to realign the data with a couple iterations and avoid problems due to bad initialisation, as presented in Section 6.3.3. This will be investigated in future work, via for example regularised mass-preserving registration (within the activity hull) of the input attenuation sinogram to gated MLAA-derived attenuation sinograms (where, according to Defrise et al. 2012, the latter are estimated up to a constant sinogram). Using such a method instead of a simpler method (such as non-AC image registration and selection of the closest PET gate to the input μ map) would eliminate the need of having an attenuation map aligned or almost aligned with one of the respiratory gates (in the same way as what JRM does). Very preliminary results on patient data showed that this could indeed lead to good initialisation for JRM and will be further evaluated.

The method described for dynamic PET acquisitions assumes that the relation between the motion and the respiratory signal stays consistent throughout the entire dynamic acquisition. Such acquisitions are however usually lengthy (sometimes up to an hour); patient breathing patterns might change during this period. Furthermore, it should be noted that the method relied on displacement gating from an RPM respiratory trace, using a reflective marker block placed on the chest/abdomen of the patient. In the event that the block is not placed in a steady way, it could change position on the patient, which could result in counts from data from different respiratory states being binned in the same gate. The longer the acquisition, the more likely the variation in block position. This means that robustness of respiratory gating for long dynamic acquisitions and more generally the joint reconstruction would need to be asserted. It would be possible to use the presented method on two separate parts of the dynamic data and verify that the deformation fields are consistent. Additionally, in the method for dynamic data presented in this thesis, the regularisation configuration was kept the same as in the original paper from Bousse et al. 2016a, i.e., it uses a quadratic penalty on the deformation parameters

and on the image values. A more adequate regularisation could have been used so that a rapid change of radioactivity is not compensated and mis-identified as motion during the optimisation. A possibility would be to use the Jacobian determinant, hypothesising that the Jacobian determinant values cannot be too far from 1, e.g., by penalising $\log(\det \boldsymbol{\mathcal{J}}_{\varphi})$ (for a deformation φ), similar to what can be done in the NiftyReg software (Modat et al. 2010) or the work in Rühaak et al. 2013. This however requires careful assessment of the penalty weights.

The joint reconstruction method for dynamic data here could easily be modified for "direct" parametric reconstruction (Meikle et al. 1998; Kamasak et al. 2003). We could, for example, have developed a method similar to Jiao et al. 2017; the method is also derived from the same implementation of JRM chosen here and aimed at correcting for (rigid) head motion. The cost function of the joint reconstruction is however optimised with respect to kinetic parameters, by the means of basis functions to express the activity distribution as a function of the kinetic parameters. Respiratory motion can however not be considered rigid and more motion gates would need to be considered, which would make such method likely computationally very expensive. Nonetheless, using the present method, a direct reconstruction could be performed after the deformation fields were preliminary determined.

Another possibility to improve the deformation fields obtained within JRM from the methods of Chapter 6 would be to incorporate some "temporal consistencies" between the respiratory gates, e.g., from temporal regularisation or constraints (Wu et al. 2013) or by incorporating a realistic motion model (McClelland et al. 2017). Such changes would however increase the computational time and should be assessed carefully.

It should be noted that all respiratory signals used in the joint reconstruction methods in Chapter 6 were derived from an external monitoring device. In order to make JRM methods more widely used, another possibility would be to use directly the PET listmode data to derive a surrogate for respiration. Common techniques in static PET acquisition are PCA (Thielemans et al. 2011; Bertolli et al. 2017), CoM (Bundschuh et al. 2007) or SAM (Schleyer et al. 2009). Such methods to derive data-driven signals could potentially be extended to dynamic PET acquisitions, with careful handling of the preliminary part with rapid kinetics (especially in the

blood vessels), as in Schleyer et al. 2014.

Finally, a study more in depth of the impact of motion and AC mismatches could have been carried out for dynamic data reconstruction. The motion-compensating method for dynamic acquisitions presented in 6 could have been used for a more reliable validation of compartmental modelling in the lung as a "test-retest" strategy. The dynamic acquisitions corresponding to the two control patients of the Coagulation Study (Section 6.4.1) were indeed reconstructed using this strategy and kinetic modelling was fitted on the images (indirect reconstruction). As the kinetic maps are automatically aligned with the input attenuation map, it is possible to align the images using a standard CT registration. However, even when realigned, the results are dependent on the initial attenuation map used in the reconstruction (respiratory state and general posture), especially since the mass-preserving warping operator was not used in this method.

More generally, the question of whether we should use a mass-preserving model in PET is linked to the measures that we wish to report in clinical or research studies: should they represent values at end-inspiration, end-expiration, full-inspiration, an average for free breathing? Values vary during respiration (Holman et al. 2016), sometimes up to 20%. This impact both stability and repeatability of measures. Mass-preserving JRM, via warping including such respiratory changes, might have the premise to answer this open question, e.g., by reporting accurately all measures at end-expiration.

7.4 Publications and Presentations Arising from this Work

7.4.1 Papers in Peer-Reviewed Journals

The contribution to the different journal articles is explained following each entry.

7.4.1.1 First Author

Published/Accepted for Publication:

- *E.C. Emond*, A.M. Groves, B.F. Hutton, K. Thielemans, *Effect of Positron Range on PET Quantification in Diseased and Normal Lungs*, Physics in Medicine and Biology, 2019

(The presented publication contains all personal work, using HRCT data provided by A.M. Groves, under supervision of B.F. Hutton and K. Thielemans)

- *E.C. Emond*, A. Bousse, M. Machado, J. Porter, A.M. Groves, B.F. Hutton, K. Thielemans, *Effect of Attenuation Mismatches in Time of Flight PET Reconstruction*, Physics in Medicine and Biology, 2020
  (The theory and the results were personal contributions, with help from A. Bousse for the mathematical demonstrations. The patient data were provided by J. Porter and A.M. Groves. The study was carried out under supervision of B.F. Hutton and K. Thielemans.)

Work in Progress :

- *E.C. Emond*, A. Bousse, L. Brusaferri, A.M. Groves, B.F. Hutton, K. Thielemans, *Improved PET/CT Respiratory Motion Compensation by Incorporating Changes in Lung Density*, submitted to IEEE Transactions on Radiation and Plasma Medical Sciences
  (The theory and the results were personal contributions, with help from A. Bousse and L. Brusaferri for writing the publication. The study was carried out under supervision of A. Bousse, B.F. Hutton and K. Thielemans.)

7.4.1.2 Co-Authored

Published/Accepted for Publication :

- N. Efthimiou, *E. Emond*, P. Wadhwa, C. Cawthorne, C. Tsoumpas, K. Thielemans, *Implementation and validation of time-of-flight PET image reconstruction module for listmode and sinogram projection data in the STIR library*, Physics in Medicine and Biology, 2018 *(fixing and validating all TOF code on sinogram projection data using simulated data and GATE Monte Carlo data)*

- A. Bousse, M. Courdurier, *É. Émond*, K. Thielemans, B.F. Hutton, P. Irarrazaval, D. Visvikis, *PET Reconstruction with non-Negativity Constraint in Projection Space: Optimization Through Hypo-Convergence*, IEEE Transactions on Medical Imaging, 2020 *(advice regarding clinical data reconstruction and participation in writing the publication)*

- P. Wadhwa, K. Thielemans, N. Efthimiou, K. Wangerin, N. Keat, *E. Emond*, T. Deller, O. Bertolli, D. Deidda, G. Delso, M. Tohme, F. Jansen, R.N. Gunn, W. Hallett, C. Tsoumpas, *PET Image Reconstruction Using Physical and Mathematical Modelling For Time of Flight PET-MR Scanners in the STIR Library*, Methods, 2020 *(technical help with TOF STIR code)*

- L. Brusaferri, A. Bousse, *E.C. Emond*, R. Brown, Y-J Tsai, D. Atkinson, S. Ourselin, C.C. Watson, B.F. Hutton, S. Arridge, K. Thielemans, *Joint Activity, Attenuation and Scatter Estimationfrom Multiple Energy Window Data in non-TOF3D PET: a preliminary study*, published in the Early Access of IEEE Transactions on Radiation and Plasma Medical Sciences, 2020 *(technical help and advice, help with formal writing of the publication)*

Work in Progress :

- N. Efthimiou, K. Thielemans, *E. Emond*, C. Cawthorne, S.J. Archibald and C. Tsoumpas, *Use of non-Gaussian time-of-flight kernels for image reconstruction of Monte Carlo simulated data of ultra-fast PET scanners*, submitted to EJNMMI Phys *(initiated the work regarding the inaccuracy of the standard Gaussian TOF kernel at high time resolution, help with proofreading the paper)*

- D.L. Chen, S. Ballout, L. Chen, J. Cheriyan, E.R. Chilvers, G. Choudhury, A. Denis-Bacelar, *E. Emond*, K. Erlandsson, M. Fisk, F. Fraioli, A.M. Groves, R.N. Gunn, J. Hatazawa, B.F. Holman, B.F. Hutton, H. Iida, S. Lee, W. MacNee, K. Matsunaga, D. Mohan, D. Parr, A. Rashid Nasab, G. Rizzo, R. Stockley, D. Subramanian, R. Tal-Singer, K. Thielemans, N. Tregay, E.J.R. van Beek, L. Vass, M.V. Melo, J.W. Wellen, J. Wevrett, I. Wilkinson, F.J. Wilson, T. Winkler, *Consensus recommendations on the use of 18F-FDG PET/CT in diffuse lung diseases (lead of the "reconstruction" section, help with coordination and preparatory meetings)*

- B.F. Holman, *E.C. Emond*, H. Iida, K. Koshino, L. Millner, R. Endozo, T. Win, J.C. Porter, A.M. Groves, B.F. Hutton, K. Thielemans, *Accurate Determination of Blood Volume in the Lung using short PET/CT Dynamic Studies (validation against porcine data of the method, see Appendix A of this thesis)*

7.4.2 Conference Contributions

7.4.2.1 First Author

- *E. Emond*, B. Holman, B. Hutton, K. Koshino, H. Iida, K. Thielemans, *Comparison of blood volume estimated from dynamic 18F-FDG-PET and 15O-CO-PET within porcine lungs*, SNMMI 2017 (Denver, USA)
- N. Efthymiou, *E.C. Emond**, C. Cawthorne, C. Tsoumpas, K. Thielemans, *Reconstruction of Time-Of-Flight Projection Data with the STIR reconstruction framework* (*: joint first author), IEEE NSS/MIC 2017 (Atlanta, USA)
- *E.C. Emond*, A.M. Groves, B.F. Hutton, K. Thielemans, *Evaluation of Positron Range in the Fibrotic Lung*, EANM Annual Meeting 2018 (Düsseldorf, Germany)
- *E.C. Emond*, A. Bousse, A.M. Groves, B.F. Hutton, K. Thielemans, *Dependence of Error Propagation due to an Incorrect Attenuation Map on PET Time-of-Flight Resolution*, EANM Annual Meeting 2019 (Barcelona, Spain)
- *E.C. Emond*, A. Bousse, M. Machado, J. Porter, K. Erlandsson, A.M. Groves, B. F. Hutton, K. Thielemans , *Respiratory Motion Correction in Dynamic PET with a Single Attenuation Map*, IEEE NSS/MIC 2019 (Manchester, UK)
- *E.C. Emond*, A. Bousse, L. Brusaferri, A.M. Groves, B.F. Hutton, K. Thielemans, *Mass Preservation for Respiratory Motion Registration in Both PET and CT*, IEEE NSS/MIC 2019 (Manchester, UK)

7.4.2.2 Co-Authored

- E. Ovtchinnikov, D. Atkinson, C. Kolbitsch, B.A. Thomas, O. Bertolli, C. da Costa-Luis, N. Efthimiou, R. Fowler, E. Pasca, P. Wadhwa, *E. Emond*, J. Matthews, A.J. Reader, C. Tsoumpas, C. Prieto, M. Turner, K. Thielemans, *SIRF: Synergistic Image Reconstruction Framework*, IEEE NSS/MIC 2017 (Atlanta, USA)
- L. Brusaferri, A. Bousse, N. Efthymiou, *E. Emond*, D. Atkinson, S. Ourselin, B. Hutton, S. Arridge, K. Thielemans, *Potential benefits of incorporating energy information when estimating attenuation from PET data*, IEEE NSS/MIC 2017 (Atlanta, USA)

- N. Efthymiou, *E. Emond*, C. Cawthorne, K. Thielemans, C. Tsoumpas, *Incorporation of Time-of-Flight in STIR image reconstruction toolkit*, IPEM "PET Update: current status and future developments" 2017 (York, UK)

- P. Wadhwa, K. Thielemans, O. Bertolli, N. Efthimiou, *E. Emond*, B.A. Thomas, M. Tohme, G. Delso, W. Hallett, R. Gunn, D. Buckley, C. Tsoumpas, *Implementation and Validation of Image Reconstruction for PET Data from GE SIGNA PET/MR Scanners In the STIR Library*, IEEE NSS/MIC, 2018 (Sydney, Australia)

- N. Efthimiou, *E. Emond*, C. Cawthorne, C. Tsoumpas, K. Thielemans, *Estimation of Timing Resolution for very fast Time-Of-Flight detectors in Monte Carlo simulations*, IEEE NSS/MIC, 2018 (Sydney, Australia)

- P. Wadhwa, K. Thielemans, N. Efthimiou, O. Bertolli, *E. Emond*, B.A. Thomas, M. Tohme, K.A. Wangerin, G. Delso, W. Hallett, R.N. Gunn, D. Buckley, C. Tsoumpas, *Implementation of Image Reconstruction for GE SIGNA PET/MR PET Data in the STIR Library*, IEEE NSS/MIC, 2018 (Sydney, Australia)

- P. Wadhwa, N. Efthimiou, K. Thielemans, *E. Emond*, K. Wangerin, G. Delso, S.J. Archibald, W. Hallett, R. Gunn, D. Buckley, C. Tsoumpas, *Validation of Time-of-Flight Image Reconstruction for GE SIGNA PET/MR scanner Using STIR Toolkit*, PSMR 2019 (Munich, Germany)

- R. Twyman, S. Arridge, B.F. Hutton, *E.C. Emond*, L. Brusaferri, S. Ahn, K. Thielemans, *Iterative PET Image Reconstruction using Adaptive Adjustment of Subset Size and Random Subset Sampling*, IEEE NSS/MIC, 2019 (Manchester, UK)

- L. Brusaferri, *E.C. Emond*, D. Atkinson, S. Ourselin, B.F. Hutton, S. Arridge, K. Thielemans, *Joint reconstruction of activity and attenuation in non-TOF PET using a synergistic prior to enforce structural similarities*, IEEE NSS/MIC, 2019 (Manchester, UK)

- A.C. Whitehead, *E.C. Emond*, N. Efthimiou, A. Akintonde, B.F. Hutton, J. McClelland, K. Thielemans, *Impact of Time-of-Flight on Respiratory Mo-*

tion Modelling using Non-Attenuation-Corrected PET, IEEE NSS/MIC, 2019 (Manchester, UK)

7.4.3 Others

- Presentation at the STIR user's meeting during the IEEE NSS/MIC 2017 conference (Atlanta, USA), *Time-of-Flight within STIR: Overview and Results of Tests using GATE Simulations*

- A. Bousse and E. Emond*, *Respiratory Motion Correction in PET/CT and PET/MR* (*: joint first author), invited presentation at SIAM 2018 (Bologna, Italy)

- Chairing position at IEEE NSS/MIC 2019 (Manchester, UK), session: "Data Corrections and Quantitative Imaging Techniques"

Appendix A

Estimating Blood Volume from Dynamic Studies

This appendix provides additional details on compartmental modelling, which was introduced in Section 2.3.4. Compartmental modelling is then used for a validation study on porcine data.

A.1 Time Activity Curves and Input Function

TACs are used to obtain a compartmental model fit. They represent the radiotracer concentration in a ROI at a specific interval of the acquisition and are obtained from consecutive measures on the dynamic PET reconstructed images. We can distinguish between two types of TACs for lung kinetic analysis:

- blood TAC, a curve describing the radiotracer concentration in blood,
- lung TAC, a curve representing the change of concentration for a single voxel of the image or for a small ROI.

The input function (IF) of the compartmental model can be obtained from arterial or venous sampling, or more recently from image-derived methods or from population-based IFs (Gunn et al. 2001). Arterial sampling is considered as the gold standard for brain imaging to obtain an accurate estimation of the input function, but it is very invasive, so an increasing number of methods incorporate an IDIF nowadays. A drawback of IDIFs is that the blood TAC, used to fit the IDIF, is for the whole blood and not for the plasma, which can reduce the quantitative accuracy. To be able to capture the initial arrival of the bolus, the early frames of the dynamic

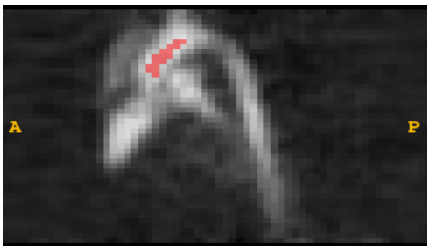

Figure A.1: Segmentation of the Ascending Aorta (AA) for a pig (see Section A.3.3).

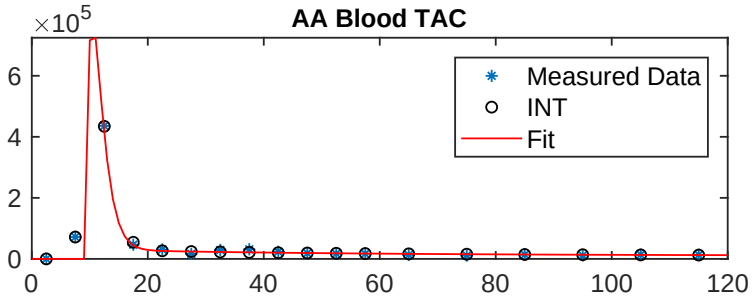

Figure A.2: AA blood TAC and its respective fit for one of the patients of the Coagulation Study in the first 2 minutes of the acquisition (see Section 6.4.1).

acquisition must be short ($\approx 5\,\mathrm{s}$, Holman 2017). As the number of counts in the short frames is very low, the reconstructed images are very noisy.

For any studies within the Institute of Nuclear Medicine of University College Hospital (London, UK), as no arterial sampling is available, IDIFs will be used. The measured blood TAC is fit to a model (see Feng et al. 1993):

$$\begin{aligned} \mathrm{IF}(t) = &\quad (A_1 t - A_2 - A_3)\mathrm{e}^{\lambda_1(t-\tau)} + A_2\mathrm{e}^{\lambda_2(t-\tau)} + A_3\mathrm{e}^{\lambda_3(t-\tau)}\,, \quad \text{when } t \geq \tau \\ = &\quad 0\,, \quad \text{when } t < \tau \end{aligned} \tag{A.1}$$

where λ_1, λ_2, λ_3, A_1, A_2, A_3 are fitting constants and τ is a time delay constant.

In this work, the ROIs used to determine the IDIFs are drawn, using the *ITK-SNAP* software (Yushkevich et al. 2006), on the Ascending Aorta (AA), as some studies have shown it to be the most accurate structure to draw blood regions (van der Weerdt et al. 2001; de Geus-Oei et al. 2006; Holman 2017). An example for a porcine AA is given in Figure A.1.

The Figure A.2 shows the TAC for a blood ROI situated in the AA, along with its fit to the predefined model in Equation (A.1).

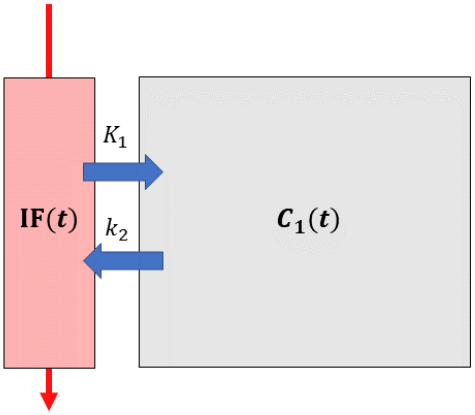

Figure A.3: Representation of a 1-Tissue Compartmental Model

A.2 Reversible 1-Tissue Compartmental Model

The 1-tissue compartment model, also referred as 2-compartment model, is a simple model composed only of the blood/plasma compartment and one tissue compartment, it is represented in Figure A.3. In this work, it will be used to estimate the fractional blood volume images.

The equation associated to the tissue compartment (compartment 1) is the following:

$$\frac{\mathrm{d}C_1}{\mathrm{d}t}(t) = K_1 \mathrm{IF}(t) - k_2 C_1(t) \tag{A.2}$$

where K_1 is the rate constant for entry of tracer from the plasma to the tissue and k_2 is the rate constant for return of tracer from the tissue to the plasma.

The solution of Equation (A.2) is the following:

$$C_1(t) = K_1 \mathrm{e}^{-k_2 t} \otimes \mathrm{IF}(t) \tag{A.3}$$

The concentration of a lung ROI C_{ROI} at a time t is given by:

$$C_{\mathrm{ROI}}(t) = V_{\mathrm{B}}\,\mathrm{IF}(t) + (1 - V_{\mathrm{B}}) K_1 \mathrm{e}^{-k_2 t} \otimes \mathrm{IF}(t) \tag{A.4}$$

where V_{B} represents the (fractional) blood volume.

A.2.1 Irreversible 2-Tissue Compartmental Model

A representation of the model is given in Figure A.4. For an irreversible model, $k_4 = 0$.

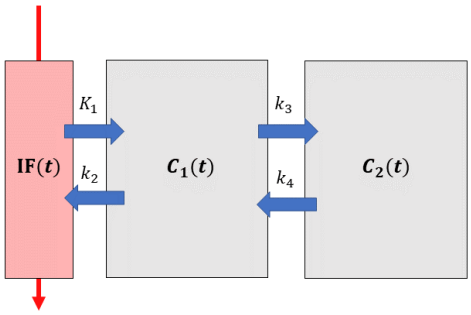

Figure A.4: Representation of a 2-Tissue Compartmental Model

The equations linked to the irreversible 2-tissue model are the following:

$$\begin{aligned} \frac{\mathrm{d}C_1}{\mathrm{d}t}(t) &= K_1 \mathrm{IF}(t) - (k_2 + k_3)\, C_1(t) \\ \frac{\mathrm{d}C_2}{\mathrm{d}t}(t) &= k_3 C_1(t) \end{aligned} \tag{A.5}$$

The solutions of the previous system of equations (A.5) are:

$$\begin{aligned} C_1(t) &= K_1 \mathrm{e}^{-(k_2+k_3)\,t} \otimes \mathrm{IF}(t) \\ C_2(t) &= \frac{K_1 k_3}{k_2 + k_3} \left(1 - \mathrm{e}^{-(k_2+k_3)\,t}\right) \otimes \mathrm{IF}(t) \end{aligned}$$

For a lung ROI TAC, we have $C_{\mathrm{ROI}}(t) = V_{\mathrm{B}}\, \mathrm{IF}(t) + (1 - V_{\mathrm{B}})(C_1(t) + C_2(t))$ i.e.:

$$C_{\mathrm{ROI}}(t) = V_{\mathrm{B}}\, \mathrm{IF}(t) + (1 - V_{\mathrm{B}}) \left[K_1 \mathrm{e}^{-(k_2+k_3)\,t} + K_i \left(1 - \mathrm{e}^{-(k_2+k_3)\,t}\right)\right] \otimes \mathrm{IF}(t) \tag{A.6}$$

where $K_i = \frac{K_1 k_3}{k_2 + k_3}$ represents the radiotracer influx rate from the blood/plasma compartment to the trapped compartment (Gunn et al. 2001).

This model has been used to estimate K_{I} for FDG in IPF patients, in the hope it can provide some information on the tissue kinetics and be a biomarker (Holman 2017).

A.3 Fractional Blood Volume Model

Estimating the fractional blood volume is essential in the lung to obtain the tracer concentration for the lung tissue only (Section 2.4.2.3). Two methods to estimate the blood fractions will be discussed in this part:

- The gold standard method, based on carbon monoxide imaging.

- An alternative method, based on compartmental modelling.

A.3.1 Gold Standard

To obtain fractional blood volume images, the gold standard is considered to be using carbon monoxide (CO) as the active molecule, either labelled with ^{11}C or ^{15}O. The method is very simple to use and, although tested first for the brain (Grubb Jr et al. 1978; Martin et al. 1987), can be applied to other parts of the body, such as the lungs (Rhodes and Hughes 1995).

It relies on the assumption that CO stays bound to haemoglobin during the whole acquisition (after a brief initial period for equilibration). The CO concentration is then directly proportional to the amount of blood in a tissue. If we know the fraction of haemoglobin in blood ("haematocrit") in the small veins (within the tissue) and in large veins (in regions which contain only blood, such as the aorta or one of the ventricles), we can obtain a robust measure of the fractional blood volume within the region.

At a time t, large enough so that CO is distributed homogeneously, the fractional blood volume V_{B} can be estimated as:

$$V_{\mathrm{B}} = \frac{C_{\mathrm{v}}(t)}{\mathrm{IF}(t) \cdot \mathrm{HCR}} \tag{A.7}$$

where $C_{\mathrm{v}}(t)$ is the CO concentration in the lung at a voxel at time t, and HRC is the haematocrit ratio (estimated at ≈ 0.9 in the human lungs, Rhodes and Hughes 1995).

The major drawback of using CO imaging to assess fractional blood volume is the necessity to have a cyclotron in close proximity to the PET scanner because of the short half-life of the radionuclide. It remains unavailable for most imaging facilities.

A.3.2 Alternative Model

The idea of the alternative model is to acquire a dynamic PET acquisition and could be used for most common tracers, e.g. FDG, to overcome the low availability of CO imaging. The model corresponds to a 1-tissue reversible compartment model. It is applied to the early part of the study. It requires to start the PET acquisition just before injecting the tracer to the patient, to be able to capture the bolus.

The model of Section A.2 is then used to determined V_B, taking into account the variable time delay δt between the IF and a voxel (or small ROI) in the lung (Holman et al. 2017):

$$C_{\mathrm{v}}(t) = V_{\mathrm{B}}\,\mathrm{IF}(t+\delta t) + (1-V_{\mathrm{B}})K_1\,\mathrm{e}^{-k_2 t} \otimes \mathrm{IF}(t+\delta t) \tag{A.8}$$

The voxel-wise δt is used to take the variability of the radiotracer arrival time within the blood to the lungs into account (Holman 2017). This model will be referred as the "alternative model" in the following Section A.3.3.

A.3.3 Validation

Data for six healthy pigs were acquired on a PET scanner for two separate studies: first a ^{15}O-CO acquisition and then a ^{18}F-FDG dynamic acquisition. The ^{15}O-CO acquisition was preceded by a transmission scan, to estimate the attenuation map. The study was with adequate break times in between all parts of the study so that acquisitions are not affected by the previous ones. The pigs were sedated and ventilated during the whole study to minimise all motion-related problems (Teramoto et al. 2011).

The methods described in Sections A.3.1 and A.3.2 were used on the reconstructed images (using the estimated haematocrit ratio 0.9 in the whole human lungs, Rhodes and Hughes 1995). The results presented here (Emond et al. 2017) are the fractional blood volume images using a blood TAC drawn on the Ascending Aorta.

Axial views of the two types of blood volume images can be found in Figure A.5.

Because the reconstructed images were not motion corrected and there was a long gap between the acquisitions ($\approx 3\,\mathrm{h}$), the images were compared on a regional level, drawing six ellipsoidal ROIs ($\approx 1.2\,\mathrm{cm}^3$) on different parts of the lungs: 2 in the upper part of the right and left lungs, 2 in the dorsal base of the right and left

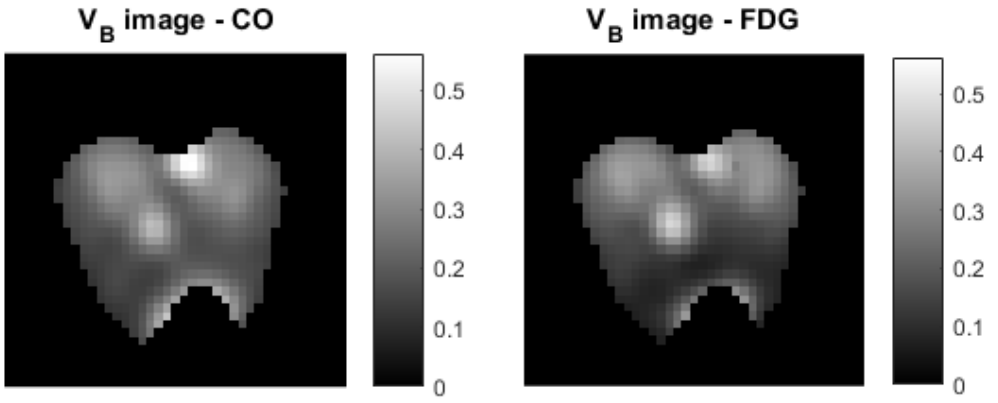

Figure A.5: Fractional blood volume images computed from the gold standard using ^{15}O-CO images (left) and from the alternative method using early frames of a ^{18}F-FDG dynamic acquisition (right)

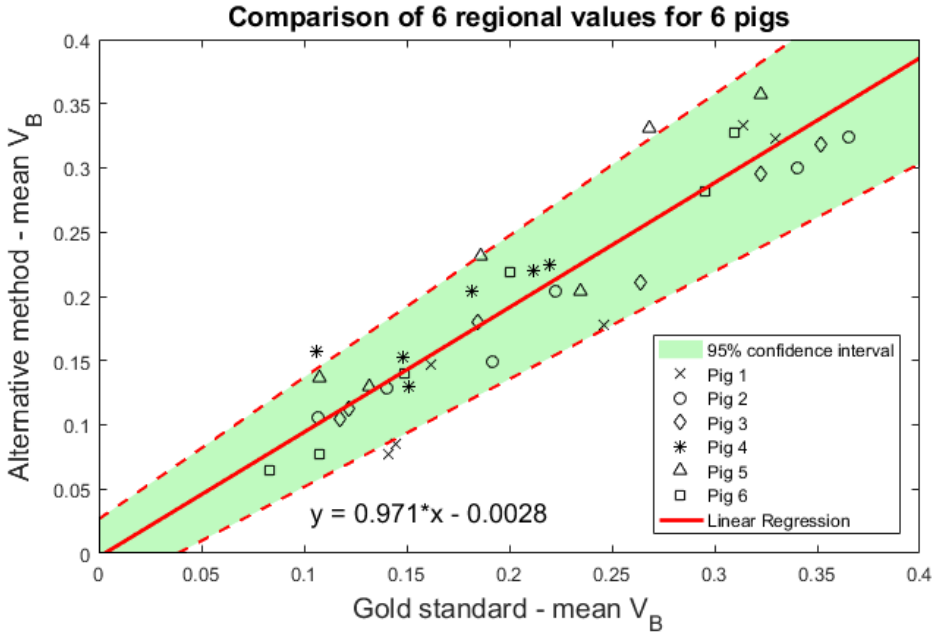

Figure A.6: Scatter plot for the mean fractional blood volume values within the 6 ROIs

lungs and 2 in the ventral base of the right and left lungs.

Figure A.6 shows the scatter plot, along with its respective linear regression line, for the mean fractional blood volume values within the six ellipsoids (lung ROIs).

The Pearson's correlation coefficient between the ^{15}O -CO and ^{18}F-FDG V_B estimates was found to be ≈ 0.94. The linear regression (gradient and intercept approximately 1 and 0 respectively) and correlation coefficient results show the strong relationship between the blood volume images computed from the ^{18}F-FDG and

^{15}O-CO dynamic images.

N.B.: The validation study used PET data reconstructed with transmission scans, therefore the attenuation map was equally affected by motion in the lungs as FDG data, which is similar to current methods using averaged CT images to compute the attenuation map (Section 4.3.1). As pointed out in Chapter 5, AC mismatch could have a large impact on the quantification and therefore needs to be assessed. More generally, pulmonary compartmental modelling require a careful validation in human diseased lungs.

Appendix B

Software Development

This appendix briefly describes the main software development performed during this PhD.

B.1 TOF implementation in STIR

STIR is an open source and freely distributed image reconstruction framework (Thielemans 2012, `http://stir.sourceforge.net`). It is widely used by many research groups around the world and provides analytical and iterative reconstruction algorithms, for both PET projection data and listmode, as well as dynamic and motion compensating reconstructions or scatter estimation.

However, at the start of this PhD, TOF data was not supported in STIR. Its support will be added in an imminent release of the software. Some details of the implementation (Efthimiou et al. 2018) can be found below, in which I contributed its projection data support as well as helping with the validation on GATE Monte Carlo and data from the GE SIGNA PET/MR scanner (Palak et al. 2018; Wadhwa et al. 2019).

Implementation of Time-of-Flight Projection Data

Introduction

Projection data in the current version of STIR only have 3 spatial dimensions. To extend the projection data to TOF, a fourth dimension was added, which led to some changes in several C++ classes of STIR:

- STIR scanners in **Scanner** can now hold three more parameters: the number of TOF bins (*max_num_of_timing_bins*), the TOF width in ps (*size_timing_bin*) and the timing resolution of the scanner in ps (*timing_resolution*).

- a projection data object can have a fourth dimension (when the scanner is compatible with TOF), so **ProjData** and **ProjDataInfo** were extended to support it.

- in the calculation of the system matrix in **ProjMatrixByBin**.

- in the forward-projector **ForwardProjectorByBin** and back-projectors **BackProjectorByBin**.

- several utilities were extended to support TOF (such as *lm_to_projdata* to create projection data from a listmode file, *poisson_noise* to add Poisson noise to the data and *stir_math* to perform basic operations on images and projection data)

Note that the reconstruction algorithms were not modified, aside from inserting extra loops over the TOF dimension.

Validations

To validate the changes within the software, we used both analytical simulations (forward-projecting an image, including attenuation, using STIR) and Monte Carlo simulations, using the GATE toolkit (Appendix C). We show results using the scanner characteristics from the GE Discovery PET/CT 690 as an example but other scanners have already been implemented. This scanner has a TOF resolution of 550 ps, 55 TOF bins of width 89 ps. TOF mashing was applied to reduce the number of TOF bins to 11 in some of the simulations.

Poisson noise was added in the analytical simulations, at a level comparable to a real acquisition.

In order to validate the calculation of the TOF system matrix, subset sensitivity images (backprojection of 1s) were calculated using on the one hand the non-TOF backprojector and on the other hand several TOF backprojectors (varying timing resolutions of 300, 400, 500 and 550 ps, with 11 TOF bins, i.e. TOF mashing factor 5). They were then compared and the results showed that the mean difference was $0.0012 \pm 0.0007\%$, which is negligible. Also, as an additional check we summed the forward projected data over the TOF dimension to form a non-TOF sinogram. The difference between the newly created non-TOF sinogram and the original non-TOF sinogram is also negligible (less than 0.001% for all timing resolutions used).

To further validate the TOF projection matrix, GATE was used to simulate 12 point sources in different locations. The scanner TOF characteristics were modified to simulate a close to perfect time resolution (time resolution: 75 ps, 275 TOF bins of width 17.8 ps). We compared the centre of mass of maximum probability backprojections of the ROOT data with the location of the point sources, as shown for two of the point source simulations on the Figure B.1. In all cases, the centre of mass was placed within the image resolution range of the original position.

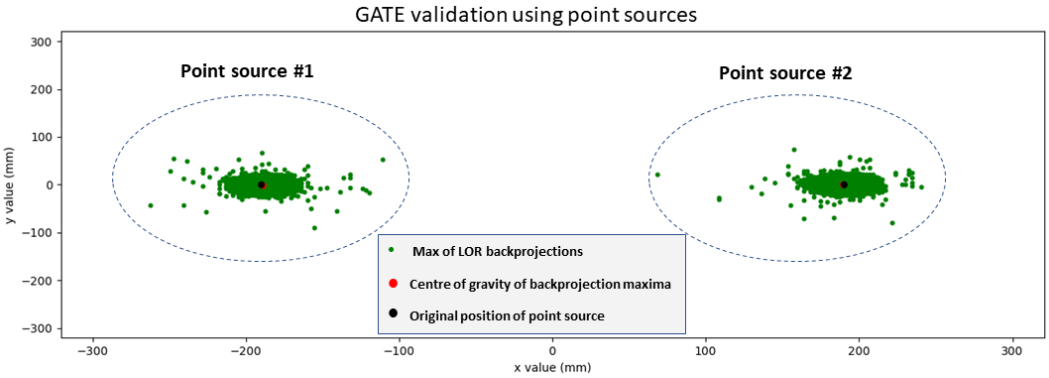

Figure B.1: Centre of mass of maximum probability backprojections of the ROOT data with the location of the point sources.

Forward projection to non-TOF and TOF sinograms (with 5 TOF bins) of an emission image consisting of an oblique plane, located near the centre of the FOV (L40xW15xH0.8 cm^3), are shown in Figure B.2.

Additional validation on reconstructed images is reported in Efthimiou et al. 2018.

Figure B.2: TOF sinograms of an oblique plane.

B.2 Utilities for Positron Range Estimation

The positron emission energy spectra for the different radionuclides presented in Chapter 3 were obtained using Formula (3.3) using Mathematica (Wolfram Research 2017).

Software was written to process the Monte Carlo data (see appendix C). The emission and annihilation images were obtained using Python 3.6. This includes: (1) reading coordinates from ROOT/GATE, (2) for all emission events finding the location of the positron annihilation events and (3) discarding emission events which did not annihilate.

B.3 Joint Motion Reconstruction

B.3.1 GE Patient Data: GEPETToolbox

Improvement of the TOF code to match as closely as possible non-TOF reconstruction implementation, with more flexible function calls.

B.3.2 Joint Reconstruction Package: "pm_jrm"

This internal MATLAB package was created by Alexandre Bousse for Joint Image Reconstruction/Motion Estimation (Bousse et al. 2016a) with the aim to improve the joint reconstruction by including density and activity changes within the motion estimation and image reconstruction of the joint optimisation, see 6.

Change in system model :

The modifications to the system model described in sections 4.4 and 6.2.3 were added to the implementation, including addition of C/mex files to compute the Jacobian matrices and related analytical derivatives. The gradients were validated using finite differences.

Quantification :

The pre-existing implementation of the joint reconstruction was not quantitative, as many factors/corrections were not properly or at all taken into account. Therefore, only studies on tumour delineations were shown in previous publications.

Main code changes: decay correction, normalisation, correct gate times (τ_i from Bousse et al. 2016a instead of previously implemented gate fractions (gate time over total time)) were added to the pre-existing implementation.

The changes were carefully validated using unit tests for both TOF and non-TOF

reconstructions (using either the entire acquisition or a random sampling to test the gate times), against the reconstructions from a GE proprietary reconstruction package.

Reconstructions :

Additionally to the previously implemented De Pierro modified OSEM (De Pierro 1995), block sequential regularized expectation maximization (BSREM), described in Ahn et al. 2003, was added to the package. The α parameter in the publication was empirically set to 2. A few considerations were taken into account:

- In the absence of implementation of FBP, one OSEM iteration from pre-corrected counts is used to obtain the image $\boldsymbol{\lambda}_{\text{ini}}$ and to compute the number "t" from Ahn et al. 2003 (used to threshold the negative values in the emission image after an iteration such that for an image value $f_j \leq 0 \rightarrow f_j = t$). We use $t = 0.001 \max \boldsymbol{\lambda}_{\text{ini}}$. Additionally, we use an upper threshold set to $T = 2 \max \boldsymbol{\lambda}_{\text{ini}}$.

- Step size at an iteration k: similarly as in Ahn et al. 2003, we chose the step size as $\alpha_k = \frac{1}{\frac{k}{15}+1}$ for standard BSREM reconstruction. For MCIR BSREM reconstructions, the step size was lowered to avoid issues near the edges of the field of view: $\alpha_k = \frac{1}{n_{\text{g}}} \frac{1}{\frac{k}{15}+1}$, where n_{g} is the number of respiratory gates.

- Stopping criteria: the reconstruction stops either (i) when reaching a maximum number of iterations equal to 300/numSubs (TOF reconstruction) or 1000/numSubs (non-TOF reconstruction), where numSubs is the number of subsets, or (ii) when the median difference between two updates is lower than 0.1%.

Regularisation :

In addition to the existing quadratic prior, the two additional priors described in Section 2.3.2.4 were also included in the implementation. All changes were validated using finite differences.

Scripts for GE Discovery 710 Data :

In the package, scripts were created to automatise entire joint reconstructions used in this PhD. The main steps are the following:

1. Creation of calibration and background files.

2. Gating from RPM/PCA and unlisting of the data.

3. Joint reconstruction (TOF or non-TOF).

4. Non-AC and AC reconstruction.

5. Final OSEM reconstructions and writing to DICOM images.

B.4 Compartmental Modelling: "inm-DynamicLung"

This internal MATLAB package (initiated by Holman 2017) was completely refactored (removal of hard-coded scripts to create "generic" flexible functions, which can be adapted to different studies) and several functionalities were added:

+ Two compartment models: reversible 2-tissue compartment models for FDG and water imaging (perfusion studies).

+ Computation of blood volume maps from CO maps.

+ Tools to modify/create DICOM images, so that they can be read on GE Advanced Workstations.

The previous compartment model fitting being unstable, the general fit scheme was modified:

- The time delay is preliminary fitted to the early part of the scan only ($\approx 120\,\mathrm{s}$).

- The previously existing optimisation scheme, using the average radioactivity per 2D slice to initialise the fit parameters for that specific slice, was replaced. To favour continuity between the voxel fits, a preliminary fit is performed for each voxel. A moving mean filter (of size $3 \times 3 \times 3$) is applied on the parameter maps, to initialise the parameters of the final compartment model fit.

- From the preliminary fit, the supposed blood regions are excluded from the main fit (when the computed blood fractions were computed as more than 0.75).

- Central differences are used in place of forward differences to compute gradient estimates in the *fmincon* optimisation (for non-linear optimisation as Equations (A.4) and (A.6)).

A more complex optimisation scheme could be used, ideally using 3D fits with spatial regularisation for continuous maps, however this was out of scope for this PhD.

Appendix C

GATE Settings and Database

GATE is an open-source software package, developed by the OpenGATE collaboration (`http://www.opengatecollaboration.org`), dedicated to realistic simulations in medical imaging and radiotherapy, and is often used in PET simulations (Jan et al. 2004).

A "material" in GATE is meant to describe all the types of tissues in a body, such as the lung, the blood, the liver, etc. Each material is represented by its name, its mass density in g.cm^{-3} and the atoms comprising it, as well as their fraction. GATE is released with a default material database, however this needed to be modified to include new materials for our simulations in Chapter 3, to represent different densities in the lung. They are defined below.

C.1 Lung Tumour Material in GATE

```
LungTumour:   d=1.028 g/cm3 ; n=8
        +el: name=Hydrogen    ; f=0.106
        +el: name=Carbon      ; f=0.284
        +el: name=Nitrogen    ; f=0.026
        +el: name=Oxygen      ; f=0.578
        +el: name=Phosphor    ; f=0.001
        +el: name=Sulfur      ; f=0.002
        +el: name=Chlorine    ; f=0.002
        +el: name=Potassium   ; f=0.001
```

C.2 Fibrotic Lung Materials in GATE

```
LungTissue:   d=0.89 g/cm3 ; n=9
       +el: name=Hydrogen   ; f=0.106
```

```
        +el: name=Carbon     ; f=0.096
        +el: name=Nitrogen   ; f=0.019
        +el: name=Oxygen     ; f=0.765
        +el: name=Sodium     ; f=0.003
        +el: name=Phosphor   ; f=0.003
        +el: name=Sulfur     ; f=0.004
        +el: name=Chlorine   ; f=0.003
        +el: name=Potassium  ; f=0.001
```

```
Lung-800:    d=0.26 g/cm3 ; n=3
         +mat: name=Air                ; f=0.74
         +mat: name=Blood              ; f=0.16
         +mat: name=LungTissue         ; f=0.1
Lung-750:    d=0.289 g/cm3 ; n=3
         +mat: name=Air                ; f=0.7067
         +mat: name=Blood              ; f=0.16
         +mat: name=LungTissue         ; f=0.1333
Lung-700:    d=0.319 g/cm3 ; n=3
         +mat: name=Air                ; f=0.6734
         +mat: name=Blood              ; f=0.16
         +mat: name=LungTissue         ; f=0.1666
Lung-650:    d=0.348 g/cm3 ; n=3
         +mat: name=Air                ; f=0.6401
         +mat: name=Blood              ; f=0.16
         +mat: name=LungTissue         ; f=0.1999
Lung-600:    d=0.378 g/cm3 ; n=3
         +mat: name=Air                ; f=0.6068
         +mat: name=Blood              ; f=0.16
         +mat: name=LungTissue         ; f=0.2332
Lung-550:    d=0.408 g/cm3 ; n=3
         +mat: name=Air                ; f=0.5735
         +mat: name=Blood              ; f=0.16
         +mat: name=LungTissue         ; f=0.2665
Lung-500:    d=0.437 g/cm3 ; n=3
         +mat: name=Air                ; f=0.5402
         +mat: name=Blood              ; f=0.16
         +mat: name=LungTissue         ; f=0.2998
Lung-450:    d=0.467 g/cm3 ; n=3
         +mat: name=Air                ; f=0.5069
         +mat: name=Blood              ; f=0.16
```

```
        +mat: name=LungTissue                ; f=0.3331
Lung-400:    d=0.496 g/cm3 ; n=3
        +mat: name=Air                       ; f=0.4736
        +mat: name=Blood                     ; f=0.16
        +mat: name=LungTissue                ; f=0.3664
Lung-350:    d=0.526 g/cm3 ; n=3
        +mat: name=Air                       ; f=0.4403
        +mat: name=Blood                     ; f=0.16
        +mat: name=LungTissue                ; f=0.3997
Lung-300:    d=0.555 g/cm3 ; n=3
        +mat: name=Air                       ; f=0.407
        +mat: name=Blood                     ; f=0.16
        +mat: name=LungTissue                ; f=0.433
Lung-250:    d=0.585 g/cm3 ; n=3
        +mat: name=Air                       ; f=0.3737
        +mat: name=Blood                     ; f=0.16
        +mat: name=LungTissue                ; f=0.4663
Lung-200:    d=0.615 g/cm3 ; n=3
        +mat: name=Air                       ; f=0.34
        +mat: name=Blood                     ; f=0.16
        +mat: name=LungTissue                ; f=0.5
```

Bibliography

Agostinelli, S. et al. (2003). "GEANT4 – a simulation toolkit". In: *Nuclear Instruments and Methods in Physics Research A* 506, pp. 250–303. DOI: 10.1016/S0168-9002(03)01368-8.

Ahn, S. et al. (2003). "Globally convergent image reconstruction for emission tomography using relaxed ordered subsets algorithms". In: *IEEE Transactions on Medical Imaging* 22.5, pp. 613–626. ISSN: 02780062. DOI: 10.1109/TMI.2003.812251.

— (2014). "Analysis of the effects of errors in attenuation maps on PET quantitation in TOF PET". In: *IEEE Nuclear Science Symposium and Medical Imaging Conference*.

Alessio, A.M. et al. (2004). "PET/CT scanner instrumentation, challenges, and solutions". In: *Radiologic Clinics of North America* 42.6, pp. 1017–1032.

Alessio, A.M. and L. MacDonald (2008). "Spatially variant positron range modeling derived from CT for PET image reconstruction". In: *IEEE Nuclear Science Symposium Conference Record*.

Alvarez, R.E. and A. Macovski (1976). "Energy-selective reconstructions in X-ray computerized tomography." In: *Physics in medicine and biology* 21.5, pp. 733–744.

Ashburner, J. et al. (1999). "High-dimensional image registration using symmetric priors". In: *NeuroImage* 9.6 I, pp. 619–628. ISSN: 10538119. DOI: 10.1006/nimg.1999.0437.

Bai, B. et al. (2003). "Positron range modeling for statistical PET image reconstruction". In: *2003 IEEE Nuclear Science Symposium. Conference Record*

(IEEE Cat. No.03CH37515) 4.2, pp. 2501–2505. ISSN: 10957863. DOI: 10.1109/NSSMIC.2003.1352400.

Bai, W. and M. Brady (2004). "Motion correction and attenuation correction for respiratory gated PET images". In: *IEEE Transactions on Medical Imaging* 30.2, pp. 351–365.

— (2009). "Regularized B-spline deformable registration for respiratory motion correction in PET images". In: *Physics in Medicine and Biology* 54.9, pp. 2719–2736.

Bailey, D. (2004). "Transmission scanning in emission tomography". In: *Eur. J. Nuc. Med.* 25.7, pp. 774–787.

Bardinet, E. et al. (1996). "Tracking and motion analysis of the left ventricle with deformable superquadrics". In: *Medical Image Analysis* 1.2, pp. 129–149. ISSN: 13618415. DOI: 10.1016/S1361-8415(96)80009-0.

Baur, M. et al. (2019). "Correction of beam hardening in X-ray radiograms". In: *Review of Scientific Instruments* 90.2, pp. 1–11. ISSN: 10897623. DOI: 10.1063/1.5080540.

Bé, M.-M. et al. (2016). *Table of Radionuclides*. Vol. 8. Monographie BIPM-5. Pavillon de Breteuil, F-92310 Sèvres, France: Bureau International des Poids et Mesures. ISBN: 978-92-822-2264-5. URL: http://www.bipm.org/utils/common/pdf/monographieRI/Monographie_BIPM-5_Tables_Vol8.pdf.

Bellemare, J.-F. et al. (2001). "Thoracic dimensions at maximum lung inflation in normal subjects and in patients with obstructive and restrictive lung diseases". In: *Chest* 119.2, pp. 376–386. ISSN: 00123692. DOI: 10.1378/chest.119.2.376.

Bertolli, O. et al. (2017). "Sign determination methods for the respiratory signal in data-driven PET gating". In: *Physics in Medicine and Biology* 62.8, pp. 3204–3220.

Bettinardi, V. et al. (2011). "Physical Performance of the new hybrid PET/CT Discovery-690". In: *Medical Physics* 38.10, pp. 5394–5411. ISSN: 00942405. DOI: 10.1118/1.3635220.

Beyer, T. et al. (2003). "Dual-modality PET/CT imaging: The effect of respiratory motion on combined image quality in clinical oncology". In: *European Journal of Nuclear Medicine and Molecular Imaging* 30.4, pp. 588–596.

Blanco, A. (2006). "Positron Range Effects on the Spatial Resolution of RPC-PET". In: *IEEE Nuclear Science Symposium Conference Record*.

Bousse, A. et al. (2016a). "Maximum-likelihood joint image reconstruction/motion estimation in attenuation-corrected respiratory gated PET/CT using a single attenuation map". In: *IEEE Transactions on Medical Imaging* 35.1, pp. 217–228.

— (2016b). "Maximum-likelihood joint image reconstruction and motion estimation with misaligned attenuation in TOF-PET/CT". In: *Physics in Medicine and Biology* 61.3, pp. L11–L19.

— (2017). "Evaluation of a Direct Motion Estimation/Correction Method in Respiratory-Gated PET/MRI with Motion-Adjusted Attenuation". In: *Medical Physics* 44.6, pp. 2379–2390. DOI: 10.1002/mp.12253.

Bousse, A., M. Courdurier, et al. (2020). "PET Reconstruction with non-Negativity Constraint in Projection Space : Optimization Through Hypo-Convergence". In: *IEEE Transactions on Medical Imaging* 39.1, pp. 75–86. DOI: 10.1109/TMI.2019.2920109.

Brookhaven National Laboratory (2019). *National Nuclear Data Center*. http://www.nndc.bnl.gov. Accessed: 2019-05-21.

Bruehlmeier, M. et al. (2004). "Assessment of Hypoxia and Perfusion in Human Brain Tumors Using PET with 18F-Fluoromisonidazole and 15O-H2O". In: *Journal of Nuclear Medicine* 45.11, pp. 1851–1859.

Brusaferri, L. et al. (2019). "Effects of detected photon energies and phantom size on MLAA from scattered and unscattered data". In: *8th Conference on PET/MR and SPECT/MR [Accepted Conference Abstract]*.

Bundschuh, R.A. et al. (2007). "Postacquisition detection of tumor motion in the lung and upper abdomen using list-mode PET data: A feasibility study". In:

Journal of Nuclear Medicine 48.5, pp. 758–763. ISSN: 01615505. DOI: 10.2967/jnumed.106.035279.

Burgos, N. et al. (2016). "Effect of scatter correction when comparing attenuation maps: Application to brain PET/MR". In: *2014 IEEE Nuclear Science Symposium and Medical Imaging Conference, NSS/MIC 2014*. DOI: 10.1109/NSSMIC.2014.7430775.

Cabello, J. et al. (2019). "Impact of non-uniform attenuation correction in a dynamic [18F]-FDOPA brain PET/MRI study". In: *EJNMMI Research* 9.1. ISSN: 2191219X. DOI: 10.1186/s13550-019-0547-0.

Cachier, P. et al. (2003). "Iconic feature based nonrigid registration: The PASHA algorithm". In: *Computer Vision and Image Understanding* 89.2-3, pp. 272–298. ISSN: 10773142. DOI: 10.1016/S1077-3142(03)00002-X.

Cal-González, J. et al. (2010). "Validation of PeneloPET positron range estimations". In: *IEEE Nuclear Science Symposium Conference Record*.

Cal-González, J. et al. (2013). "Positron range estimations with PeneloPET". In: *Physics in Medicine and Biology* 58.15, pp. 5127–5152.

— (2015). "Tissue-Dependent and Spatially-Variant Positron Range Correction in 3D PET". In: *IEEE Transactions on Medical Imaging* 34.11, pp. 2394–2403. ISSN: 1558254X. DOI: 10.1109/TMI.2015.2436711.

Cao, K. et al. (2012). "Improving intensity-based lung CT registration accuracy utilizing vascular information". In: *International Journal of Biomedical Imaging* 2012. ISSN: 16874188. DOI: 10.1155/2012/285136.

Castell, F. and G.J.R. Cook (2008). "Quantitative techniques in 18FDG PET scanning in oncology". In: *British Journal of Cancer* 98.10, pp. 1597–1601.

Cates, J.W. and C.S. Levin (2018). "Evaluation of a TOF-PET detector design that achieves ¡= 100 ps coincidence time resolution". In: *2017 IEEE Nuclear Science Symposium and Medical Imaging Conference, NSS/MIC 2017 - Conference Proceedings*. DOI: 10.1109/NSSMIC.2017.8532998.

Chan, C. et al. (2013). "Event-by-event respiratory motion correction for PET with 3D internal-1D external motion correlation". In: *Medical Physics* 40.11, p. 112507. URL: http://dx.doi.org/10.1118/1.4826165.

— (2018). "Non-Rigid Event-by-Event Continuous Respiratory Motion Compensated List-Mode Reconstruction for PET". In: *IEEE Transactions on Medical Imaging* 37.2, pp. 504–515. ISSN: 1558254X. DOI: 10.1109/TMI.2017.2761756.

Chang, S. et al. (1999). "Five different anti-prostate-specific membrane antigen (PSMA) antibodies confirm PSMA expression in tumor-associated neovasculature". In: *Cancer Research* 59.13, pp. 3192–3198.

El-Chemaly, S. et al. (2008). "Lymphatics in Lung Disease Souheil". In: *Ann N Y Acad Sci.* Pp. 195–202.

Chen, D. et al. (2017). "Quantification of Lung PET Images: Challenges and Opportunities". In: *Journal of Nuclear Medicine* 58.2, pp. 201–207.

Cherry, S.R. et al. (2018). "Total-body PET: Maximizing sensitivity to create new opportunities for clinical research and patient care". In: *Journal of Nuclear Medicine* 59.1, pp. 3–12. ISSN: 2159662X. DOI: 10.2967/jnumed.116.184028.

Christensen, G.E. et al. (1996). "Deformable templates using large deformation kinematics". In: *IEEE Transactions on Image Processing* 5.10, pp. 1435–1447. ISSN: 10577149. DOI: 10.1109/83.536892.

Chun, S.-Y. et al. (2009). "A simple penalty that encourages local invertibility and considers sliding effects for respiratory motion". In: 7259, 72592U. ISSN: 16057422. DOI: 10.1117/12.811181.

Conti, M. (2011). "Focus on time-of-flight PET: The benefits of improved time resolution". In: *European Journal of Nuclear Medicine and Molecular Imaging* 38.6, pp. 1147–1157.

Coultas, D.B. et al. (1994). "The epidemiology of Interstitial Lung Diseases". In: *American Journal of Respiratory and Critical Care Medicine* 150.4, pp. 967–972.

Cuplov, V. et al. (2018). "Issues in quantification of registered respiratory gated PET/CT in the lung". In: *Physics in Medicine and Biology* 63.1, pp. 3148–3163.

de Geus-Oei, L. et al. (2006). "Comparison of Image-Derived and Arterial Input Functions for Estimating the Rate of Glucose Metabolism in Therapy-Monitoring 18F-FDG PET Studies Lioe-Fee". In: *Journal of Nuclear Medicine* 47.6, pp. 945–949.

De Pierro, A.R. (1995). "Modified expectation maximization algorithm for penalized likelihood estimation in emission tomography". In: *IEEE Transactions on Medical Imaging* 14.1, pp. 132–137.

De Pierro, A.R. et al. (2001). "Fast EM-like methods for maximum "a posteriori" estimates in emission tomography". In: *IEEE Transactions on Medical Imaging* 20.4, pp. 280–288. ISSN: 02780062. DOI: 10.1109/42.921477.

Defrise, M. et al. (1989). "Three-dimensional image reconstruction from complete projections". In: *Phys. Med. Biol.* 34.5, pp. 573–587.

— (2012). "Time-of-flight PET data determine the attenuation sinogram up to a constant". In: *Phys. Med. Biol.* 57.4, pp. 885–899.

Delbeke, D. et al. (2006). "Procedure Guideline for Tumor Imaging with 18F-FDG PET/CT 1.0*". In: *Journal of Nuclear Medicine* 47.5, pp. 885–895.

Dempster, A. et al. (1977). "Maximum likelihood from incomplete data via the EM algorithm". In: *Journal of the Royal Statistical Society Series B Methodological* 39.1, pp. 1–38.

Dennis, Jr., J.E. et al. (1977). "Quasi-Newton Methods, Motivation and Theory". In: *SIAM Review* 19.1, pp. 46–89. ISSN: 0036-1445. DOI: 10.1137/1019005.

Derenzo, S.E. (1979). "Precision measurement of annihilation point spread distributions for medically important positron emitters". In: *International Conference on Positron Annihilation.*

Dittrich, A.S. et al. (2012). "Modeling 18F-FDG Kinetics during Acute Lung Injury: Experimental Data and Estimation Errors". In: *PLoS ONE* 7.10.

Driessen, R.S. et al. (2017). "Myocardial perfusion imaging with PET". In: *International Journal of Cardiovascular Imaging* 33.7, pp. 1021–1031. ISSN: 15730743. DOI: 10.1007/s10554-017-1084-4.

Efthimiou, N. et al. (2018). "Implementation and validation of time-of-flight PET image reconstruction module for listmode and sinogram projection data in the STIR library". In: *Physics in Medicine and Biology*. ISSN: 0031-9155. DOI: 10.1088/1361-6560/aaf9b9. URL: http://iopscience.iop.org/article/10.1088/1361-6560/aaf9b9.

Emond, E. et al. (2017). "Comparison of blood volume estimated from dynamic 18F-FDG-PET and 15O-CO-PET within porcine lungs". In: *Journal of Nuclear Medicine* 58.supplement 1, p. 698. URL: http://jnm.snmjournals.org/content/58/supplement_1/698.abstract.

— (2019). "Effect of positron range on PET quantification in diseased and normal lungs". In: *Physics in Medicine and Biology*, p. 205010. ISSN: 0031-9155. DOI: 10.1088/1361-6560/ab469d.

Erdi, Y.E. et al. (2004). "The CT motion quantitation of lung lesions and its impact on PET-measured SUVs". In: *Journal of nuclear medicine* 45.8, pp. 1287–1292.

Erlandsson, K. et al. (2001). "Low-Statistics Reconstruction with AB-EMML 1". In:

Evans, R.D. (1955). *The Atomic Nucleus*.

Feng, D. et al. (1993). "Models for computer simulation studies of input functions for tracer kinetic modeling with positron emission tomography". In: *International Journal of Bio-Medical Computing* 32.2, pp. 95–110.

Fessler, J.A. (1994). "Penalized weighted least squares image reconstruction for Positron Emission Tomography". In: *IEEE Transactions on Medical Imaging* 13.2, pp. 290–300.

Fessler, J.A. and A.O. Hero (1995). "Penalized Maximum Likelihood Image Reconstruction using Space Alternating Generalized EM Algorithms". In: *IEEE Transactions on Image Processing* 10.4, pp. 1417–1429.

Fletcher, J.W. and P.E. Kinahan (2010). "PET/CT Standardized Uptake Values (SUVs) in Clinical Practice and Assessing Response to Therapy". In: *NIH Public Access* 31.6, pp. 496–505.

Gaertner, F.C. et al. (2012). "Radiolabelled RGD peptides for imaging and therapy". In: *European Journal of Nuclear Medicine and Molecular Imaging* 39.1, pp. 126–138.

Geramifar, P. et al. (2013). "Respiratory-induced errors in tumor quantification and delineation in ct attenuation-corrected PET images: Effects of tumor size, tumor location, and respiratory trace: A simulation study using the 4D XCAT phantom". In: *Molecular Imaging and Biology* 15.6, pp. 655–665. ISSN: 15361632. DOI: 10.1007/s11307-013-0656-5.

Gigengack, F. et al. (2012). "Motion Correction in Dual Gated Cardiac PET Using Mass-Preserving Image Registration". In: *IEEE Transactions on Medical Imaging* 31.3, pp. 698–712.

Gillman, A. et al. (2017). "PET motion correction in context of integrated PET/MR: Current techniques, limitations, and future projections: Current". In: *Medical Physics* 44.12, e430–e445. ISSN: 00942405. DOI: 10.1002/mp.12577.

Goerres, G.W. et al. (2003). "Respiration-induced attenuation artifact at PET/CT: technical considerations." In: *Radiology* 226.3, pp. 906–910.

Gorbunova, V. et al. (2012). "Mass preserving image registration for lung CT". In: *Medical Image Analysis* 16.4, pp. 786–795. ISSN: 13618415. DOI: 10.1016/j.media.2011.11.001.

Grootjans, W. et al. (2014). "Amplitude-based optimal respiratory gating in positron emission tomography in patients with primary lung cancer". In: *European Radiology* 24.12, pp. 3242–3250.

Groves, A. et al. (2009). "Idiopathic pulmonary fibrosis and diffuse parenchymal lung disease: implications from initial experience with 18F-FDG PET/CT." In: *Journal of Nuclear Medicine* 50.4, pp. 538–545.

Grubb Jr, R.L. et al. (1978). "Measurement of regional cerebral blood volume by emission tomography". In: *Annals of Neurology* 4.4, pp. 322–328.

Guerrero, T. et al. (2006). "Dynamic ventilation imaging from four-dimensional computed tomography". In: *Physics in Medicine and Biology* 51.4, pp. 777–791.

Gunn, R.N. et al. (2001). "Positron Emission Tomography Compartmental Models". In: *Journal of Cerebral Blood Flow & Metabolism* 21, pp. 635–652.

— (2002). "Positron Emission Tomography Compartmental Models: A Basis Pursuit Strategy for Kinetic Modeling". In: *Journal of Cerebral Blood Flow & Metabolism* 22, pp. 1425–1439.

Guo, F. et al. (2017). "Thoracic CT-MRI coregistration for regional pulmonary structure-function measurements of obstructive lung disease". In: *Medical physics* 44.5, pp. 1718–1733. ISSN: 24734209. DOI: 10.1002/mp.12160.

Han, L. et al. (2017). "A hybrid patient-specific biomechanical model based image registration method for the motion estimation of lungs". In: *Medical Image Analysis* 39, pp. 87–100. ISSN: 13618423. DOI: 10.1016/j.media.2017.04.003. URL: http://dx.doi.org/10.1016/j.media.2017.04.003.

Heußer, T. et al. (2017). "MLAA-based attenuation correction of flexible hardware components in hybrid PET/MR imaging". In: *EJNMMI Physics* 4.1. ISSN: 21977364. DOI: 10.1186/s40658-017-0177-4.

Hill, D.L.G. et al. (2001). "Medical image registration". In: *Physics in Medicine and Biology* 46.1, R1–R45.

Holman, B.F. (2017). "Improving Quantification of PET/CT Biomarkers for Evaluation of Disease Progression and Treatment Effectiveness in Pulmonary Fibrosis". In:

Holman, B.F. et al. (2015). "Improved correction for the tissue fraction effect in lung PET/CT imaging". In: *Physics in Medicine and Biology* 60.18, pp. 7387–7402. ISSN: 0031-9155. DOI: 10.1088/0031-9155/60/18/7387. URL: http://dx.doi.org/10.1088/0031-9155/60/18/7387.

Holman, B.F. et al. (2016). "The effect of respiratory induced density variations on non-TOF PET quantitation in the lung". In: *Physics in Medicine and Biology* 61.8, pp. 3148–3163.

— (2017). "Method to determine the voxel-wise blood volume in the lung from dynamic PET data". In: *Journal of Nuclear Medicine* 58.supplement 1, p. 1310. URL: http://jnm.snmjournals.org/content/58/supplement_1/1310.abstract.

— (2018). "Improved quantitation and reproducibility in multi-PET/CT lung studies by combining CT information". In: *EJNMMI Physics* 5.1, pp. 1–14. ISSN: 21977364. DOI: 10.1186/s40658-018-0212-0.

Hudson, H.M. and R.S. Larkin (Jan. 1994). "Calculation of positron range and its effect on the fundamental limit of positron emission tomography system spatial resolution". In: *IEEE Transactions on Medical Imaging* 13.4.

Hutton, B.F., H.M. Hudson, and F.J. Beekman (Jan. 1997). "Calculation of positron range and its effect on the fundamental limit of positron emission tomography system spatial resolution". In: *European Journal of Nuclear Medicine* 24.7, pp. 797–808.

Hwang, D. et al. (2019a). "Data-driven respiratory phase-matched attenuation without CT". In: *2019 IEEE Nuclear Science Symposium and Medical Imaging Conference - Conference Proceedings (in press)*.

— (2019b). " Generation of PET Attenuation Map for Whole-Body Time-of-Flight 18 F-FDG PET/MRI Using a Deep Neural Network Trained with Simultaneously Reconstructed Activity and Attenuation Maps ". In: *Journal of Nuclear Medicine* 60.8, pp. 1183–1189. ISSN: 0161-5505. DOI: 10.2967/jnumed.118.219493.

Inoue, K. et al. (2009). "18FDG uptake associated with CT density on PET/CT in lungs with and without chronic interstitial lung diseases". In: *Annals of Nuclear Medicine* 39.3, pp. 277–281.

Jacobson, M.W. and J.A. Fessler (2003). "Joint estimation of image and deformation parameters in motion-corrected PET". In: *IEEE Nuclear Science Symposium Conference Record*.

Jahani, N. et al. (2014). "Assessment of regional non-linear tissue deformation and air volume change of human lungs via image registration". In: *Journal of Biomechanics* 47.7, pp. 1626–1633.

Jakoby, B.W. et al. (2011). "Physical and clinical performance of the mCT time-of-flight PET/CT scanner". In: *Physics in Medicine and Biology* 56.8, pp. 2375–2389. ISSN: 00319155. DOI: 10.1088/0031-9155/56/8/004.

Jan, S. et al. (2004). "GATE - Geant4 Application for Tomographic Emission: a simulation toolkit for PET and SPECT". In: *Physics in Medicine & Biology* 49.19, pp. 4543–4561.

Jiao, J. et al. (2017). "Direct Parametric Reconstruction with Joint Motion Estimation/Correction for Dynamic Brain PET Data". In: *IEEE Transactions on Medical Imaging* 36.1, pp. 203–213. ISSN: 1558254X. DOI: 10.1109/TMI.2016.2594150.

Jødal, L. et al. (2012). "Positron range in PET imaging: an alternative approach for assessing and correcting the blurring". In: *Phys. Med. Biol.* 57.12, pp. 3931–3943.

Jødal, L et al. (2014). "Positron range in PET imaging : non-conventional isotopes". In: *Phys. Med. Biol* 59.1, pp. 7419–7434. DOI: 10.1088/0031-9155/59/23/7419.

Johnson, V. (1994). "A Note on Stopping Rules in EM-ML Reconstructions of ECT Images". In: *IEEE Transactions on Medical Imaging* 13.3, pp. 569–571.

Jones, H.A. et al. (1998). "Pulmonary fibrosis correlates with duration of tissue neutrophil activation". In: *American Journal of Respiratory and Critical Care Medicine* 158.2, pp. 620–628.

Jones, H.A. et al. (2002). "Dissociation Between Respiratory Burst Activity and Deoxyglucose Uptake in Human Neutrophil Granulocytes: Implications for In-

terpretation of 18F-FDG PET Images". In: *Journal of Nuclear Medicine* 43.5, pp. 620–628.

Kamasak, M.E. et al. (2003). "Direct Reconstruction of Kinetic Parameter Images from Dynamic PET Data". In: *IEEE Transactions on Medical Imaging* 24.5, pp. 636–650.

Kemerink, G.J. et al. (2011). "Effect of the positron range of 18F, 68Ga and 124I on PET/CT in lung-equivalent materials". In: *European Journal of Nuclear Medicine and Molecular Imaging* 38.5, pp. 940–948. ISSN: 16197070. DOI: 10.1007/s00259-011-1732-1.

Kinahan, P. et al. (2006). "Compensating For Patient Respiration in PET / CT Imaging with the Registered and Summed Phases (RASP) Procedure". In: *3rd IEEE International Symposium on Biomedical Imaging: Nano to Macro*.

Kinahan, P.E. et al. (1998). "Attenuation correction for a combined 3D PET / CT scanner". In: *Medical Physics* 25.10, pp. 2046–2053.

— (Nov. 2004). "Analytic Image Reconstruction Methods". In: *Emission Tomography: The Fundamentals of PET and SPECT*. Elsevier Inc., pp. 421–442. ISBN: 9780080521879. DOI: 10.1016/B978-012744482-6.50023-5.

Klein, G.J. et al. (1996). "Non-Rigid Summing of Gated PET Via Optical Flow". In: *Nuclear Science Symposium*.

Kolthammer, J.A. et al. (2015). "Performance evaluation of the Ingenuity TF PET/CT scanner with a focus on high count-rate conditions". In: *Physics in Medicine and Biology* 59.14, pp. 3843–3859.

Kotasidis, F.A. et al. (2016). "Impact of time-of-flight on indirect 3D and direct 4D parametric image reconstruction in the presence of inconsistent dynamic PET data". In: *Physics in Medicine and Biology* 61.9, pp. 3443–3471. ISSN: 13616560. DOI: 10.1088/0031-9155/61/9/3443.

Lambrou, T. et al. (2011a). "The importance of correction for tissue fraction effects in lung PET: Preliminary findings". In: *European Journal of Nuclear Medicine*

and Molecular Imaging 38.12, pp. 2238–2246. ISSN: 16197070. DOI: 10.1007/s00259-011-1906-x.

Lambrou, T. et al. (2011b). "The importance of correction for tissue fraction effects in lung PET: preliminary findings". In: *European Journal of Nuclear Medicine and Molecular Imaging* 38, pp. 2238–2246.

Lammertsma, A.A. (2017a). "Forward to the Past: The Case for Quantitative PET Imaging". In: *Journal of Nuclear Medicine* 58.7, pp. 1019–1024. ISSN: 0161-5505. DOI: 10.2967/jnumed.116.188029.

— (2017b). "Forward to the Past: The case for Quantitative PET Imaging". In: *Journal of Nuclear Medicine* 58.7, pp. 1019–1024.

Lange, K. and R. Carson (1984). "EM Reconstruction Algorithms for Emission and Transmission Tomography". In: *Journal of Computer Assisted Tomography* 8.2, pp. 306–316.

Lavalaye, J.E. et al. (2009). "Imaging of fibrogenesis in patients with idiopathic pulmonary fibrosis with cis-4-[18F]-Fluoro-L-Proline PET". In: *Molecular Imaging and Biology* 22.2, pp. 123–127.

Leahy, R.M. and J. Qi (2000a). "Imaging of fibrogenesis in patients with idiopathic pulmonary fibrosis with cis-4-[18F]-Fluoro-L-Proline PET". In: *Statistics and Computing* 10.2, pp. 147–165.

— (2000b). "Statistical approaches in quantitative positron emission tomography". In: *Statistics and Computing* 10.2, pp. 147–165. ISSN: 09603174. DOI: 10.1023/A:1008946426658.

Lecoq, P. (2017). "Pushing the Limits in Time-of-Flight PET Imaging". In: *IEEE Transactions on Radiation and Plasma Medical Sciences* 1.6, pp. 473–485. ISSN: 2469-7311. DOI: 10.1109/trpms.2017.2756674.

Lehnert, W. et al. (2011). "Analytical positron range modelling in heterogeneous media for PET Monte Carlo simulation". In: *Phys. Med. Biol.* 56.11, pp. 3313–3335.

Levin, C.S. and E.J. Hoffman (1999). "Calculation of positron range and its effect on the fundamental limit of positron emission tomography system spatial resolution". In: *Physical in Medicine and Biology* 44.3, pp. 781–799.

Li, T. et al. (2006). "Model-based image reconstruction for four-dimensional PET". In: *Medical Physics* 33.5, pp. 1288–1298. ISSN: 00942405. DOI: 10.1118/1.2192581.

Lillington, J. et al. (2019). "PET/MRI Attenuation Estimation in the Lung: A Review of Past, Present, and Potential Techniques". In: *Medical Physics* 47.2, pp. 790–811. DOI: 10.1002/mp.13943.

Liu, C. et al. (2010). "Quiescent period respiratory gating for PET/CT". In: *Medical Physics* 37.9, pp. 5037–5043.

— (2011). "Respiratory motion correction for quantitative PET/CT using all detected events with internal-external motion correlation". In: *Medical Physics* 38.5, pp. 2715–2723. ISSN: 00942405. DOI: 10.1118/1.3582692.

Llacer, J. (1993). "Results of a clinical receiver operating characteristic study comparing filtered backprojection and maximum likelihood estimator images in FDG PET studies". In: *J. Nuc. Med.* 34.7, pp. 1198–1203.

Manjeshwar, R. et al. (2006). "Motion Compensated Image Reconstruction of Respiratory Gated PET/CT". In: *3rd IEEE International Symposium on Biomedical Imaging: Nano to Macro, 2006.* 2, pp. 674–677. DOI: 10.1109/isbi.2006.1625006.

Martin, W.R. et al. (1987). "Cerebral Blood Volume Measured with Inhaled C ¡sup¿15¡/sup¿ O and Positron Emission Tomography". In: *Journal of Cerebral Blood Flow & Metabolism* 7.4, pp. 421–426.

Martinez, F.J. et al. (2011). "The future of chronic obstructive pulmonary disease treatment - Difficulties of and barriers to drug development". In: *The Lancet* 378, pp. 1027–1037.

Mattes, D. et al. (2003). "PET-CT image registration in the chest using free-form deformations". In: *IEEE Transactions on Medical Imaging* 22.1, pp. 120–128. ISSN: 02780062. DOI: 10.1109/TMI.2003.809072.

Matthies, H. and G. Strang (1979). "The Solution of Nonlinear Finite Element Equations". In: *International Journal for Numerical Methods in Engineering* 14.1, pp. 1613–1626. ISSN: 00457949. DOI: 10.1016/0045-7949(92)90243-S.

McClelland, J.R. et al. (2017). "A generalized framework unifying image registration and respiratory motion models and incorporating image reconstruction, for partial or full imaging data". In: *Physics in medicine and biology* 62.Iccr 2016, pp. 4273–4292. ISSN: 0031-9155. DOI: 10.1042/BJ20101136.

Mehranian, A. et al. (2017). "MR-guided joint reconstruction of activity and attenuation in brain PET-MR". In: *NeuroImage* 162, pp. 276–288. ISSN: 10959572. DOI: 10.1016/j.neuroimage.2017.09.006.

Meikle, S.R. et al. (1998). "Parametric image reconstruction using spectral analysis of PET projection data". In: *Physics in Medicine and Biology* 43.3, pp. 651–666. ISSN: 00319155. DOI: 10.1088/0031-9155/43/3/016.

Melcher, C. (2000). "Scintillation crystals for PET". In: *Journal of Nuclear Medicine* 41.6, pp. 1051–1055.

Meltzer, E.B. and P.W. Noble (2008). "Idiopathic pulmonary fibrosis". In: *Orphanet Journal of Rare Diseases* 3.1, pp. 1–15.

Mérida, I. et al. (2017). "Multi-atlas attenuation correction supports full quantification of static and dynamic brain PET data in PET-MR". In: *Physics in Medicine and Biology* 62.7, pp. 2834–2858. ISSN: 13616560. DOI: 10.1088/1361-6560/aa5f6c.

Mettivier, G. et al. (2011). "The effect of count statistics on the convergence value in OSEM reconstruction in PET and TOF PET". In: *IEEE Nuclear Science Symposium Conference Record*.

Mettler, F.A. and M.J. Guiberteau (2012). "Essentials of Nuclear Medicine Imaging". In: *Elsevier Health* 31.

Modat, M. et al. (2010). "Fast free-form deformation using graphics processing units". In: *Computer Methods and Programs in Biomedicine* 98.3, pp. 278–284. ISSN: 01692607. DOI: 10.1016/j.cmpb.2009.09.002.

— (2014). "Global image registration using a symmetric block-matching approach". In: *Journal of Medical Imaging* 1.2, pp. 1–6. ISSN: 2329-4302. DOI: 10.1117/1.jmi.1.2.024003.

More, JJ et al. (1994). "Line Search Algorithms Sufficient Decrease". In: *ACM Transaction on Mathematical Software* 20.3, pp. 286–307.

Moreno, F and H.A. Lyons (1961). "Effect of body posture on lung volumes." In: *Journal of applied physiology* 16.4, pp. 27–29.

Morey, A.M. and D.J. Kadrmas (2013). "Effect of varying number of OSEM subsets on PET lesion detectability". In: *Journal of Nuclear Medicine Technology* 41.4, pp. 268–273. ISSN: 00914916. DOI: 10.2967/jnmt.113.131904.

Moses, W.W. (2011). "Fundamental Limits of Spatial Resolution in PET William". In: *Nuclear Inst. and Methods in Physics Research, A* 648.Supplement 1, S236–S240.

Moses, W.W. and S.E. Derenzo (1999). "Prospects for time-of-flight pet using LSO scintillator". In: *IEEE Transactions on Nuclear Science* 46.3, pp. 474–478.

Mumcuoğlu, E.Ü. et al. (1996). "Bayesian reconstruction of PET images : methodology and performance analysis". In: *Phys. Med. Biol.* 41.9, pp. 1777–1807.

Musse, O. et al. (2001). "Topology preserving deformable image matching using constrained hierarchical parametric models". In: *IEEE Transactions on Image Processing* 10.7, pp. 1081–1093. ISSN: 10577149. DOI: 10.1109/83.931102.

Nakamura, H. et al. (2015). "Standardized Uptake Values in the Primary Lesions of Non-Small- Cell Lung Cancer in FDG-PET / CT Can Predict Regional Lymph Node Metastases". In: *Annals of Surgical Oncology* 22, pp. 1388–1393. DOI: 10.1245/s10434-014-4351-9.

Navaratnam, V. et al. (2011). "The rising incidence of idiopathic pulmonary fibrosis in the UK". In: *Thorax* 66.6, e3–e19.

Nehmeh, S.A. et al. (2007). "Deep-Inspiration Breath-Hold PET/CT of the Thorax". In: *Journal of Nuclear Medicine* 48.1, pp. 22–27.

Nehmeh, S.A. and Y.E. Erdi (2008). "Respiratory Motion in Positron Emission Tomography/Computed Tomography: A Review". In: *Seminars in Nuclear Medicine* 38.3, pp. 167–176.

Nehmeh, S.A. and pthers (2002). "Effect of respiratory gating on reducing lung motion artifacts in PET imaging of lung cancer". In: *Medical Physics* 29.3, pp. 366–371. ISSN: 00942405. DOI: 10.1118/1.1448824.

Nocedal, J. (Jan. 1980). "Updating quasi newton matrices with limited storage". In: *Mathematics of Computation* 35.151, pp. 951–958. ISSN: 0025-5718. DOI: 10.1090/S0025-5718-1980-0572855-7.

Nocedal, J. and S. Wright (2006). *Numerical optimization*. Springer Science & Business Media.

Nocedal, J. and S.J. Wright (1999). *Numerical Optimization*. ISBN: 0387987932.

Nuyts, J. et al. (1999). "Simultaneous maximum a posteriori reconstruction of attenuation and activity distributions from emission sinograms". In: *IEEE Transactions on Medical Imaging* 18.5, pp. 393–403.

— (2002). "A concave prior penalizing relative differences for maximum-a-posteriori reconstruction in emission tomography". In: *Transactions on Nuclear Science* 49.1, pp. 56–60.

Nyflot, M.J. et al. (2015a). "Impact of CT attenuation correction method on quantitative respiratory-correlated (4D) PET / CT imaging". In: *Medical Physics* 42.1, pp. 110–120.

— (2015b). "Impact of CT attenuation correction method on quantitative respiratory-correlated (4D) PET/CT imaging". In: *Medical Physics* 42.1, pp. 110–120. ISSN: 00942405. DOI: 10.1118/1.4903282.

Oliveira, F.P.M. et al. (2014). "Medical image registration : A review". In: *Computer Methods in Biomechanics and Biomedical Engineering* 17.2, pp. 73–93. ISSN: 1025-5842.

Ollinger, J.M. (1996). "Model-based scatter correction for fully 3D PET". In: *Physics in Medicine and Biology* 41.1, pp. 153–176. ISSN: 00319155. DOI: 10.1088/0031-9155/41/1/012.

Pace, D.F. et al. (2011). "Deformable Image Registration of Sliding Organs Using Anisotropic Diffusive Regularization Danielle". In: *Proc Int Symp Biomed Imaging*, pp. 407–413. ISSN: 15378276. DOI: 10.1038/jid.2014.371. eprint: NIHMS150003.

Palak, W. et al. (2018). "Implementation of Image Reconstruction for GE SIGNA PET/MR PET Data in the STIR Library". In: *2018 IEEE Nuclear Science Symposium and Medical Imaging Conference, NSS/MIC 2018 - Proceedings*, pp. 3–5. DOI: 10.1109/NSSMIC.2018.8824341.

Pan, T. et al. (2004). "4D-CT imaging of a volume influenced by respiratory motion on multi-slice CT". In: *Medical Physics* 31.2, pp. 333–340. ISSN: 00942405. DOI: 10.1118/1.1639993.

— (2005). "Attenuation Correction of PET Images with Respiration-Averaged CT Images in PET/CT". In: *Journal of Nuclear Medicine* 46, pp. 1481–1487.

— (2019). "Performance evaluation of the 5-Ring GE Discovery MI PET/CT system using the national electrical manufacturers association NU 2-2012 Standard". In: *Medical Physics* 46.7, pp. 3025–3033. ISSN: 00942405. DOI: 10.1002/mp.13576.

Pépin, A. et al. (2014). "Management of respiratory motion in PET/computed tomography: The state of the art". In: *Nuclear Medicine Communications* 35.2, pp. 113–122.

Postmus, P.E. et al. (2017). "Early and locally advanced non-small-cell lung cancer (NSCLC): ESMO Clinical Practice Guidelines for diagnosis, treatment and follow-up†". In: *Annals of Oncology* 28.4, pp. 1–21.

Qi, J. et al. (1998). *High Resolution 3D Bayesian Image Reconstruction using the microPET Small Animal Scanner.*

Qiao, F. et al. (2006). "A motion-incorporated reconstruction method for gated PET studies". In: *Physics in Medicine and Biology* 51.15, pp. 3769–3783.

Raghu, G. et al. (2011). "An Official ATS/ERS/JRS/ALAT Statement: Idiopathic pulmonary fibrosis: Evidence-based guidelines for diagnosis and management". In: *American Journal of Respiratory and Critical Care Medicine* 183.2, pp. 788–824.

— (2015). "An Official ATS/ERS/JRS/ALAT Clinical Practice Guideline: Treatment of Idiopathic Pulmonary Fibrosis. An Update of the 2011 Clinical Practice Guideline". In: *American Journal of Respiratory and Critical Care Medicine* 192.2, e3–e19.

Rahmim, A. et al. (2008). "Resolution modeled PET image reconstruction incorporating space-variance of positron range: Rubidium-82 cardiac PET imaging". In: *IEEE Nuclear Science Symposium Conference Record*, pp. 3643–3650. ISSN: 10957863. DOI: 10.1109/NSSMIC.2008.4774108.

Rahmin, A. et al. (2013). "Resolution modeling in PET imaging: Theory, practice, benefits, and pitfalls". In: *Medical Physics* 40.6.

Rakvongthai, Y. et al. (2017). "MR-based Motion Correction for Quantitative PET in Simultaneous PET-MR Imaging". In: *PET Clinics* 12.3, pp. 321–327.

Rausch, I. et al. (2015). "Performance evaluation of the Biograph mCT Flow PET/CT system according to the NEMA NU2-2012 standard". In: *EJNMMI Physics* 2.1, pp. 1–17. ISSN: 21977364. DOI: 10.1186/s40658-015-0132-1. URL: http://dx.doi.org/10.1186/s40658-015-0132-1.

Reichert, J.M. and V.E. Valge-Archer (2007). "Development trends for monoclonal antibody cancer therapeutics." In: *Nat. Rev. Drug Discov.* 6.5, pp. 349–356. ISSN: 1474-1776. DOI: 10.1038/nrd2241.

Reinhardt, J.M. et al. (2008). "Registration-based estimates of local lung tissue expansion compared to xenon CT measures of specific ventilation". In: *Medical Image Analysis* 12.6, pp. 752–763.

Rezaei, A. et al. (2012a). "Simultaneous Reconstruction of Activity and Attenuation in Time-of-Flight PET". In: *IEEE Transactions on Medical Imaging* 31.12, pp. 2224–2233.

— (2012b). "Simultaneous Reconstruction of Activity and Attenuation in Time-of-Flight PET". In: 31.12, pp. 2224–2233.

— (2016). "Simultaneous reconstruction of the activity image and registration of the CT image in TOF-PET". In: *Physics in Medicine and Biology* 61.4, pp. 1852–1874. ISSN: 13616560. DOI: 10.1088/0031-9155/61/4/1852.

— (2017). "Data driven time alignment for TOF-PET". In: *IEEE Nuclear Science Symposium and Medical Imaging Conference Record*.

— (2019). "A Quantitative Evaluation of Joint Activity and Attenuation Reconstruction in TOF-PET/MR Brain Imaging". In: *Journal of Nuclear Medicine*. ISSN: 0161-5505. DOI: 10.2967/jnumed.118.220871.

Rhodes, C.G. and J.M.B. Hughes (1995). "Pulmonary studies using positron emission tomography". In: *European Respiratory Journal* 8.6, pp. 1001–1017.

Rich, D.A. (1997). "A brief history of positron emission tomograph". In: *Journal of Nuclear Medicine Technology* 25.1, pp. 4–11.

Roncoli, E. and S.R. Cherry (2011). "Application of Silicon Photomultipliers to Positron Emission Tomography". In: *Annals of Biomedical Engineering* 39.4, pp. 1358–1377.

Rudin, L. D. et al. (1992). "Nonlinear total variation based noise removal algorithms". In: *Physica D: Nonlinear Phenomena* 60.1, pp. 259–268.

Rueckert, D. et al. (1999). "Nonrigid registration using free-form deformations: application to breast MR images." In: *IEEE Trans. Med. Imag.* 18.8, pp. 712–721.

Rühaak, J. et al. (2013). "Highly accurate fast lung CT registration". In: *Medical Imaging 2013: Image Processing* 8669.March 2013, 86690Y. ISSN: 16057422. DOI: 10.1117/12.2006035.

Ruthenborg, R.J. et al. (2014). "Regulation of Wound Healing and Fibrosis by Hypoxia and Hypoxia-Inducible Factor-1". In: *Mol. Cells* 37.9, pp. 637–643.

Salomon, A. et al. (2011). "Simultaneous reconstruction of activity and attenuation for PET/MR". In: *IEEE Transactions on Medical Imaging* 30.3, pp. 804–813.

Schleyer, P.J. et al. (2009). In: *Physics in Medicine and Biology* 54.7, pp. 1935–1950. ISSN: 00319155. DOI: 10.1088/0031-9155/54/7/005.

— (2014). "Extracting a respiratory signal from raw dynamic PET data that contain tracer kinetics". In: *Physics in Medicine and Biology* 59.15, pp. 4345–4356. ISSN: 13616560. DOI: 10.1088/0031-9155/59/15/4345.

Schroeder, T. et al. (2008). "Modeling Pulmonary Kinetics of 2-Deoxy-2-[18F]fluoro-d-glucose During Acute Lung Injury". In: *Academic Radiology* 15.6, pp. 763–775.

— (2011). "Method to determine the voxel-wise blood volume in the lung from dynamic PET data". In: *Journal of Nuclear Medicine* 48.11, pp. 1889–1896.

Schwarz, A.J. and M.O. Leach (2000). "Management of respiratory motion in PET/-computed tomography: The state of the art". In: *Phys. Med. Biol.* 45, pp. 2105–2116.

Shah, K. et al. (2002). "Position-sensitive avalanche photodiodes for gamma-ray imaging". In: *IEEE Transactions on Nuclear Science* 49.4, pp. 1051–1055.

Sharma, R. et al. (2015). "Multicenter Reproducibility of 18F-Fluciclatide PET Imaging in Subjects with Solid Tumors". In: *Journal of Nuclear Medicine* 56.12, pp. 1855–1861.

Shepp, L.A. and Y. Vardi (1982). "Maximum Likelihood Reconstruction in Positron Emission Tomography". In: *IEEE Trans. Medical Imaging* 2.1, pp. 113–122.

Shibuya, K. (2007). "Limit of Spatial Resolution in FDG-PET due to Annihilation Photon Non-Collinearity". In: *World Congress on Medical Physics and Biomedical Engineering 2006*.

Simon, B.A. (2000). "Non-invasive imaging of regional lung function using x-ray computed tomography". In: *Journal of clinical monitoring and computing* 16.5–6, pp. 433–442.

Spagnolo, P. et al. (2015). "Idiopathic pulmonary fibrosis: An update". In: *Annals of Medicine* 47.1, pp. 15–27.

Spanoudaki, V.C. and C.S. Levin (2010). "Photo-detectors for time of flight positron emission tomography (ToF-PET)". In: *Sensors* 10, pp. 10484–10505.

Spinks, T.J. et al. (1992). "Physical performance of a positron tomograph for brain imaging with retractable septa". In: *Physics in Medicine and Biology* 37.8, pp. 1637–1655. ISSN: 00319155. DOI: 10.1088/0031-9155/37/8/002.

Sureshbabu, W. et al. (2005). "PET/CT Imaging Artifacts". In: *Journal of Nuclear Medicine Technology* 33.3, pp. 156–161.

Surti, S. (2015). "Update on time-of-flight PET imaging". In: *Journal of Nuclear Medicine* 56.1, pp. 98–105. ISSN: 01615505. DOI: 10.2967/jnumed.114.145029.

Szirmay-Kalos, L. et al. (2012). "Fast positron range calculation in heterogeneous media for 3D PET reconstruction". In: *IEEE Nuclear Science Symposium Conference Record*.

Teramoto, N. et al. (2011). "Experimental pig model of old myocardial infarction with long survival leading to chronic left ventricular dysfunction and remodeling as evaluated by PET". In: *Journal of nuclear medicine : official publication, Society of Nuclear Medicine* 52.5, pp. 761–768. DOI: 10.2967/jnumed.110.084848. URL: http://www.ncbi.nlm.nih.gov/pubmed/21498524.

Thielemans, K. (2012). "STIR: Software for Tomographic Image Reconstruction Release 2". In: *Phys. Med. Biol.* 57.4, pp. 867–883.

Thielemans, K. et al. (2007). "A new algorithm for scaling of PET scatter estimates using all coincidence events". In: *IEEE Nuclear Science Symposium Conference Record* 5, pp. 3586–3590. ISSN: 10957863. DOI: 10.1109/NSSMIC.2007.4436900.

— (2008). "Image-based correction for mismatched attenuation in pet images". In: *IEEE Nuclear Science Symposium Conference Record*.

Thielemans, K. et al. (2009). "Mass-Preserving Image Registration Using Free-Form Deformation Fields". In: *IEEE Nuclear Science Symposium Conference Record*, pp. 2490–2495.

— (2011). "Device-less gating for PET/CT using PCA". In: *IEEE Nuclear Science Symposium Conference Record*, pp. 3904–3910. ISSN: 10957863. DOI: 10.1109/NSSMIC.2011.6153742.

Thorwarth, D. et al. (2005). "A kinetic model for dynamic [18F]-Fmiso PET data to analyse tumour hypoxia". In: *Physics in Medicine and Biology* 50.10, pp. 2209–2224.

Tong, S. et al. (2010). "Image reconstruction for PET/CT scanners: past achievements and future challenges". In: *Imaging Med.* 5.2, pp. 529–545.

Travis, W.D. et al. (2015). "The 2015 World Health Organization Classification of Lung Tumors: Impact of Genetic, Clinical and Radiologic Advances since the 2004 Classification". In: *Journal of Thoracic Oncology* 10.9, pp. 1243–1260.

Tsai, Y.J. et al. (2018a). "Algorithms for Solving Misalignment Issues in Penalized PET/CT Reconstruction Using Anatomical Priors". In: *2018 IEEE Nuclear Science Symposium and Medical Imaging Conference, NSS/MIC 2018 - Proceedings*, pp. 1–3. DOI: 10.1109/NSSMIC.2018.8824558.

— (2018b). "Fast Quasi-Newton Algorithms for Penalized Reconstruction in Emission Tomography and Further Improvements via Preconditioning". In: *IEEE Transactions on Medical Imaging* 37.4, pp. 1000–1010. ISSN: 1558254X. DOI: 10.1109/TMI.2017.2786865.

Tzouvelekis, A. et al. (2014). "Comparative expression profiling in pulmonary fibrosis suggests a role of hypoxia-inducible factor-1alpha in disease pathogenesis". In: *American Journal of Respiratory and Critical Care Medicine* 176.11, pp. 1108–1119.

Unser, M. et al. (1993). "B-Spline Signal Processing: Part II – Efficient Design and Applications". In: *IEEE Transactions on Signal Processing* 41.2, pp. 834–848.

van der Weerdt, A.P. et al. (2001). "Image-derived input functions for determination of MRGlu in cardiac (18)F-FDG PET scans". In: *Journal of Nuclear Medicine* 42.11, pp. 1622–1629.

Van Slambrouck, K. et al. (2014). "Reconstruction scheme for accelerated maximum likelihood reconstruction: The patchwork structure". In: *IEEE Transactions on Nuclear Science* 61.1, pp. 173–181. ISSN: 00189499. DOI: 10.1109/TNS.2013.2287637.

Van Sluis, J. et al. (2019). "Performance characteristics of the digital biograph vision PET/CT system". In: *Journal of Nuclear Medicine* 60.7, pp. 1031–1036. ISSN: 2159662X. DOI: 10.2967/jnumed.118.215418.

Vandemeulebroucke, J. et al. (2012). "Automated segmentation of a motion mask to preserve sliding motion in deformable registration of thoracic CT". In: *Medical Physics* 39.2, pp. 1006–1015. ISSN: 00942405. DOI: 10.1118/1.3679009.

Verschakelen, J.A. et al. (1993). "Differences in CT density between dependent and nondependent portions of the lung: Influence of lung volume". In: *American Journal of Roentgenology* 161.4, pp. 713–717.

Wadhwa, P. et al. (2019). "Validation of Time-of-Flight Image Reconstruction for GE SIGNA PET/MR scanner Using STIR Toolkit". In: *8th Conference on PET/MR and SPECT/MR [Accepted Conference Abstract]*.

Wallace, W.E. et al. (2002). "Cis-4-[(18)F]fluoro-L-proline PET imaging of pulmonary fibrosis in a rabbit model". In: *Journal of Nuclear Medicine* 43.3, pp. 413–420.

Wang, H. et al. (May 2015). "Expression of Prostate-Specific Membrane Antigen in Lung Cancer Cells and Tumor Neovasculature Endothelial Cells and Its Clinical Significance". In: *PLOS ONE* 10.5, pp. 1–8. DOI: 10.1371/journal.pone.0125924.

Watson, C.C. (2007). "Extension of Single Scatter Simulation to Scatter Correction of Time-of-Flight PET". In: *IEEE Transactions on Nuclear Science* 54.5, pp. 1679–1686.

Watson, C.C. et al. (1996). "A Single Scatter Simulation Technique for Scatter Correction in 3D PET". In: *3D image Reconstruction in Radiation and Nuclear Medicine*, pp. 256–268.

Werner, R.A. et al. (2019). "Moving into the next era of PET myocardial perfusion imaging: introduction of novel 18 F-labeled tracers". In: *International Journal of Cardiovascular Imaging* 35.3, pp. 569–577. ISSN: 15730743. DOI: 10.1007/s10554-018-1469-z.

Win, T. et al. (2012a). "18F-Fluorodeoxyglucose positron emission tomography pulmonary imaging in idiopathic pulmonary fibrosis is reproducible: Implications for future clinical trials". In: *European Journal of Nuclear Medicine and Molecular Imaging* 39.3, pp. 521–528.

— (2012b). "18F-Fluorodeoxyglucose positron emission tomography pulmonary imaging in idiopathic pulmonary fibrosis is reproducible: Implications for future clinical trials". In: *European Journal of Nuclear Medicine and Molecular Imaging* 39.3, pp. 521–528. ISSN: 16197070. DOI: 10.1007/s00259-011-1986-7.

Wolfram Research, Inc. (2017). *Mathematica, Version 11.2*.

Wu, G. et al. (2013). "Estimating the 4D respiratory lung motion by spatiotemporal registration and super-resolution image reconstruction". In: *Medical Physics* 40.3, pp. 1–17. ISSN: 00942405. DOI: 10.1118/1.4790689.

Xu, D.M. et al. (2008). "Limited value of shape, margin and CT density in the discrimination between benign and malignant screen detected solid pulmonary nodules of the NELSON trial". In: *European Journal of Radiology* 68.2, pp. 347–352. ISSN: 0720048X. DOI: 10.1016/j.ejrad.2007.08.027.

Yamamoto, T. et al. (2008). "Retrospective Analysis of Artifacts in Four-Dimensional CT Images of 50 Abdominal and Thoracic Radiotherapy Patients". In: *International Journal of Radiation Oncology Biology Physics* 72.4, pp. 1250–1258. ISSN: 03603016. DOI: 10.1016/j.ijrobp.2008.06.1937.

Yang, Y. et al. (2016). "A Prototype High-Resolution Small-Animal PET Scanner Dedicated to Mouse Brain Imaging". In: *Journal of Nuclear Medicine* 57.7, pp. 1130–1135. ISSN: 0161-5505. DOI: 10.2967/jnumed.115.165886.

Yilmaz, C. et al. (2011). "Quantification of Regional Interstitial Lung Disease from CT-derived Fractional Tissue Volume. A Lung Tissue Research Consortium Study". In: *Academic Radiology* 18.8, pp. 1014–1023.

Yin, Y. et al. (2009). "Mass preserving nonrigid registration of CT lung images using cubic B-spline". In: *Med. Phys.* 36.9, pp. 4213–4222. DOI: 10.1118/1.3193526.

Yu, Y. et al. (2016). "Event-by-event continuous respiratory motion correction for dynamic PET imaging". In: *Journal of Nuclear Medicine* 57.7, pp. 1084–1090. ISSN: 2159662X. DOI: 10.2967/jnumed.115.167676.

Yushkevich, P.A. et al. (2006). "User-Guided 3D Active Contour Segmentation of Anatomical Structures: Significantly Improved Efficiency and Reliability". In: *Neuroimage* 31.3, pp. 1116–1128.

Zhu, C. et al. (1994). *L-BFGS-B – Fortran Subroutines for Large-Scale Bound Constrained Optimization.*